Measurement of

Cabibbo-suppressed

τ lepton decays and

the determination of $|V_{us}|$

Stefan Schenk

DISSERTATION

submitted to the
Combined Faculties for the Natural Sciences and Mathematics
of the Ruperto-Carola University of Heidelberg, Germany
for the degree of

doctor rerum naturalium

presented by

Dipl.-Phys. Stefan Schenk

born in Würselen, Germany

Oral examination: July 07$^{\text{th}}$, 2008

Measurement of

Cabibbo-suppressed τ lepton decays

and the determination of $|V_{us}|$

Referees: Prof. Dr. Ulrich Uwer

Prof. Dr. Johanna Stachel

Abstract

This work presents simultaneous branching fraction measurements of the decay modes $\tau^- \to K^- n\pi^0 \nu_\tau$ with $n = 0, 1, 2, 3$ and $\tau^- \to \pi^- n\pi^0 \nu_\tau$ with $n = 3, 4$. The analysis is based on a data sample of 427×10^6 $\tau^+\tau^-$ pairs recorded with the $B\textsc{a}B\textsc{ar}$ detector, which corresponds to an integrated luminosity of $464.4\,\text{fb}^{-1}$. The measured values are $\mathcal{B}(\tau^- \to K^- \nu_\tau) = (6.57 \pm 0.03 \pm 0.11) \times 10^{-3}$, $\mathcal{B}(\tau^- \to K^- \pi^0 \nu_\tau) = (4.61 \pm 0.03 \pm 0.11) \times 10^{-3}$, $\mathcal{B}(\tau^- \to K^- \pi^0 \pi^0 \nu_\tau) = (5.05 \pm 0.17 \pm 0.44) \times 10^{-4}$, $\mathcal{B}(\tau^- \to K^- \pi^0 \pi^0 \pi^0 \nu_\tau) = (1.31 \pm 0.43 \pm 0.40) \times 10^{-4}$, $\mathcal{B}(\tau^- \to \pi^- \pi^0 \pi^0 \pi^0 \nu_\tau) = (1.263 \pm 0.008 \pm 0.078) \times 10^{-2}$ and $\mathcal{B}(\tau^- \to \pi^- \pi^0 \pi^0 \pi^0 \pi^0 \nu_\tau) = (9.6 \pm 0.5 \pm 1.2) \times 10^{-4}$, where the uncertainties are statistical and systematic, respectively. All measurements are compatible with the current world averages whereas the uncertainties are significantly smaller by a factor of up to five. The determination of $\mathcal{B}(\tau^- \to \pi^- \pi^0 \pi^0 \pi^0 \pi^0 \nu_\tau)$ is the first measurement of this branching fraction. The measured branching fractions are combined with the current world averages. Using the new averages, an updated determination of $|V_{us}|$ from hadronic τ decays yields $|V_{us}| = 0.2146 \pm 0.0025$, which improves previous measurements by $19\,\%$. Its uncertainty is comparable to the one of the current world average from semileptonic kaon decays.

Kurzfassung

In der vorliegenden Arbeit werden die Verzweigungsverhältnisse der Zerfälle $\tau^- \to K^- n\pi^0 \nu_\tau$ mit $n = 0, 1, 2, 3$ und $\tau^- \to \pi^- n\pi^0 \nu_\tau$ mit $n = 3, 4$ gemessen. Der verwendete Datensatz von 427×10^6 $\tau^+\tau^-$-Paaren wurde mit dem $B\textsc{a}B\textsc{ar}$-Detektor aufgezeichnet und entspricht einer integrierten Luminosität von $464.4\,\text{fb}^{-1}$. Die gemessenen Verzweigungsverhältnisse sind $\mathcal{B}(\tau^- \to K^- \nu_\tau) = (6.57 \pm 0.03 \pm 0.11) \times 10^{-3}$, $\mathcal{B}(\tau^- \to K^- \pi^0 \nu_\tau) = (4.61 \pm 0.03 \pm 0.11) \times 10^{-3}$, $\mathcal{B}(\tau^- \to K^- \pi^0 \pi^0 \nu_\tau) = (5.05 \pm 0.17 \pm 0.44) \times 10^{-4}$, $\mathcal{B}(\tau^- \to K^- \pi^0 \pi^0 \pi^0 \nu_\tau) = (1.31 \pm 0.43 \pm 0.40) \times 10^{-4}$, $\mathcal{B}(\tau^- \to \pi^- \pi^0 \pi^0 \pi^0 \nu_\tau) = (1.263 \pm 0.008 \pm 0.078) \times 10^{-2}$ und $\mathcal{B}(\tau^- \to \pi^- \pi^0 \pi^0 \pi^0 \pi^0 \nu_\tau) = (9.6 \pm 0.5 \pm 1.2) \times 10^{-4}$, wobei die ersten Unsicherheiten statistischer und die zweiten systematischer Natur sind. Alle Messungen sind mit den aktuellen Weltmittelwerten kompatibel, wobei die Unsicherheiten um bis zu einen Faktor fünf kleiner sind. Die Bestimmung von $\mathcal{B}(\tau^- \to \pi^- \pi^0 \pi^0 \pi^0 \pi^0 \nu_\tau)$ ist die erste Messung dieses Verzweigungsverhältnisses. Die gemessenen Verzweigungsverhältnisse werden mit den aktuellen Weltmittelwerten kombiniert. Eine aktualisierte Bestimmung von $|V_{us}|$ aus hadronischen τ-Zerfällen unter Verwendung der neuen Mittelwerte ergibt $|V_{us}| = 0.2146 \pm 0.0025$. Dies stellt eine Verbesserung bisheriger Messungen um $19\,\%$ dar. Die Unsicherheit ist mit der des aktuellen Weltmittelwertes aus semileptonischen Kaonzerfällen vergleichbar.

Contents

Introduction

The parameters of the Cabibbo-Kobayashi-Maskawa (CKM) quark mixing matrix [1, 2] are fundamental parameters of the Standard Model of Particle Physics and cannot be predicted theoretically. A precise determination of all elements of the CKM matrix is an important test of the restrictions that are imposed by the Standard Model. One of these constraints is the unitarity of the quark mixing matrix.

The amplitude of the flavor-changing weak $s \to u$ transition is proportional to the element V_{us} of the CKM matrix. This element can thus be measured in kaon decays. The current world average of $|V_{us}|$ is solely based on measurements of semileptonic kaon decays [3]. The precision of these measurements is of the order of $1\,\%$. After long-standing deviations [3], current results are now compatible with the unitarity condition for the first row of the CKM matrix. However, the determination of $|V_{us}|$ from semileptonic kaon decays is limited by the theoretical precision of the form factor calculations that are needed to extract $|V_{us}|$ from the measurements [3]. Different methods of calculating the form factors yield results that deviate by up to $2\,\%$ [3].

Hadronic τ decays into final states with net strangeness provide a method to measure $|V_{us}|$ that is both theoretically and experimentally independent of semileptonic kaon decays [4, 5]. All τ decays into final states with net strangeness involve the creation of a $\overline{u}s$ quark pair from the QCD vacuum:
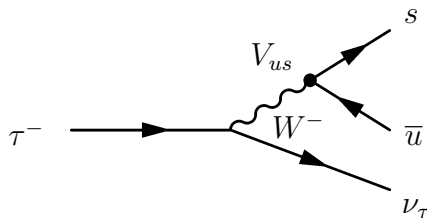
Their inclusive rate is thus proportional to $|V_{us}|^2$ and can be used to extract $|V_{us}|$. Experimentally, the inclusive rate is measured as the sum of all exclusive final states with net strangeness, i.e., containing an odd number of kaons. Additional information can be inferred from a measurement of the invariant mass spectra of the final states. This necessitates the exclusive reconstruction of all final state particles. A precise measurement of the invariant mass spectra might allow for a simultaneous determination of $|V_{us}|$ and the strange-quark mass m_s [4, 5].

Current measurements of $|V_{us}|$ based on the world averages of the τ branching fractions of final states with net strangeness differ by 2.5 standard deviations from the measurements using semileptonic kaon decays and thus from unitarity [3, 6, 7]. The uncertainties of the measurements using τ decays are completely dominated by the

experimental uncertainties of the branching fractions of the τ lepton into final states with net strangeness [4–6]. Improved determinations of the contributing τ branching fractions are essential to further investigate the observed deviation. So far, most measurements of τ branching fractions are dominated by analyses of the LEP and CLEO collaborations [3]. Their measurements of the Cabibbo-suppressed modes with net strangeness are statistically limited.

The *BaBar* experiment at the PEP-II collider located at the Stanford Linear Accelerator Center near San Francisco provides a huge data sample of τ decays. In the center of the *BaBar* detector, electrons collide with positrons at a center-of-mass energy of 10.58 GeV, which corresponds to the mass of the $\Upsilon(4S)$ resonance [8]. The $\Upsilon(4S)$ resonance decays almost entirely into $B\bar{B}$ pairs [3]. Due to the huge number of produced B mesons, PEP-II is called a B factory. As the cross section for the production of $\tau\tau$ pairs is comparable to the one for $B\bar{B}$ pairs [9], PEP-II is also a τ factory. During its operating time, the *BaBar* experiment has recorded a data set of approximately 488×10^6 $\tau\tau$ pairs.

Within this work, a subset of 427×10^6 $\tau\tau$ pairs—corresponding to an integrated luminosity of $464.4\,\mathrm{fb}^{-1}$—is used to measure the branching fractions of the decay modes

$$\tau^- \to K^- n\pi^0 \nu_\tau \quad \text{with} \quad n = 0, 1, 2, 3\,.$$

They contribute a significant fraction to the total branching fraction of the τ lepton into final states with net strangeness and to its uncertainty.

It is also interesting to note that the current PDG world average of the branching fraction of the decay mode $\tau^- \to K^- \nu_\tau$ differs by 1.3 standard deviations from a prediction based on lepton universality and the measurement of the decay mode $K^- \to \mu^- \overline{\nu}_\mu$ [3, 10]. A possible deviation between these two values could indicate new physics beyond the Standard Model [7]. A more precise measurement of the branching fraction $\mathcal{B}(\tau^- \to K^- \nu_\tau)$ is needed to clarify this issue.

In addition to the above four decay channels, the branching fractions of the modes

$$\tau^- \to \pi^- n\pi^0 \nu_\tau \quad \text{with} \quad n = 3, 4$$

are also measured within this analysis. They represent significant backgrounds to the kaon modes. For the decay mode containing four π^0 mesons, the branching fraction has not been measured so far. Only the branching fraction of the combined decay channel $\tau^- \to h^- \pi^0 \pi^0 \pi^0 \pi^0 \nu_\tau$ with $h = \pi, K$ has been measured [3].

All of the branching fractions measured within this work are averaged with the current PDG world averages—if available. On the basis of the updated world averages for the decay modes $\tau^- \to K^- n\pi^0 \nu_\tau$ with $n = 0, 1, 2, 3$, an updated value of the inclusive branching fraction of the τ lepton into final states with net strangeness is determined. This value is used to perform an updated measurement of $|V_{us}|$ from hadronic τ decays.

Chapter 1

Theoretical background and experimental status

This chapter presents the theoretical background and the current experimental status of hadronic τ decays and the determination of $|V_{us}|$. Section 1.1 briefly summarizes today's knowledge of fundamental interactions with a specific focus on the properties and consequences of the quark mixing matrix. The experimental status of hadronic τ decays is described in Section 1.2. Section 1.3 summarizes the theoretical description of hadronic τ decays within the framework of perturbative QCD. Finally, Section 1.4 presents methods to measure the element $|V_{us}|$ of the quark mixing matrix, as well as current experimental results.

1.1   The Standard Model

The *Standard Model of Particle Physics* summarizes today's knowledge of fundamental particles and their interactions [11–13]. It is a gauge field theory, which includes three of the four known fundamental forces, the electromagnetic, weak and strong interactions. Gravity, the fourth fundamental force, cannot yet be described in a consistent way with the three field theories. The main building blocks of the Standard Model are fundamental *fermions* (spin-1/2 particles, *matter*) and interaction fields, which are mediated by *gauge bosons* (spin-1 vector bosons).

Fermions can be divided into two sectors. *Quarks* carry strong charge (*color*), while *leptons* are color-neutral and do not interact strongly. In contrast, all fermions carry weak charge and participate in the weak interaction. Both sectors occur in three *generations* following a mass hierarchy. Each generation contains two quark and two lepton states (*up*- and *down*-type quarks, *neutrinos* and (charged) *leptons*). Thus, the Standard Model contains six quarks and six leptons, i. e., six *flavors* per sector, as summarized in Table 1.1. Additionally, an anti-fermion exists for each fermion flavor. Apart from their flavor quantum numbers, corresponding particles from different generations have identical quantum numbers and only differ by their masses. All (known) stable matter is made from fermions of the first generation. However, all fermions listed in Table 1.1 have been observed experimentally.

The three forces of the Standard Model form a gauge group of the type $\text{SU}_C(3) \times$

Table 1.1: Fermion content of the Standard Model and its division into three generations. The approximate particle masses are given in parenthesis [3]. For the light quarks, u, d, s, these are *current-quark* masses at a scale $\mu \approx 2\,\text{GeV}$. The c and b quark masses are *running* masses in the $\overline{\text{MS}}$ scheme, while the t mass is obtained from the direct observation of top events. Within the original Standard Model, neutrinos are massless. However, the observation of neutrino oscillations provides evidence that at least two neutrino flavors have non-zero masses [3].

	Type	1st generation		2nd generation		3rd generation	
Quarks	up	u	$(2\,\text{MeV}/c^2)$	c	$(1.25\,\text{GeV}/c^2)$	t	$(174\,\text{GeV}/c^2)$
	down	d	$(5\,\text{MeV}/c^2)$	s	$(95\,\text{MeV}/c^2)$	b	$(4.2\,\text{GeV}/c^2)$
Leptons	neutrino	ν_e	(0)	ν_μ	(0)	ν_τ	(0)
	lepton	e	$(511\,\text{keV}/c^2)$	μ	$(106\,\text{MeV}/c^2)$	τ	$(1.78\,\text{GeV}/c^2)$

$\text{SU}_T(2) \times \text{U}_Y(1)$. The symbol C denotes the color of the strong interaction and T the *weak isospin*. The *weak hypercharge* Y is defined as $Y = Q - T_3$, where Q is the electric charge and T_3 the third component of the weak isospin. Thus, $\text{U}_Y(1)$ is the symmetry group of the weak hypercharge. The group $\text{SU}_T(2) \times \text{U}_Y(1)$ is the gauge group of the electroweak unified theory by Glashow, Salam and Weinberg [14–16].

The Standard Model also contains a spin-0 boson, which is responsible for the masses of the fermions and gauge bosons (*Higgs boson*). Unlike all other building blocks of the Standard Model, it has not (yet) been observed directly. Table 1.2 summarizes the (gauge) boson content of the Standard Model as well as their masses. Tables 1.1 and

Table 1.2: Boson content of the Standard Model and the approximate particle masses. All gauge bosons are spin-1 (vector) bosons, while the Higgs particle is a spin-0 (scalar) boson. In the Standard Model, photon and gluons are massless. The given Z^0 mass is the mass parameter of the Z^0 Breit-Wigner resonance. The cited limit on the mass of the scalar Standard Model Higgs boson H^0 is given at $95\,\%\,\text{CL}$ and obtained from direct searches at the LEP experiments [3].

Interaction	(Gauge) bosons	Mass
Electromagnetic	photon (γ)	0
Weak	$W^\pm$	$80\,\text{GeV}/c^2$
	Z^0	$91\,\text{GeV}/c^2$
Strong	gluons $(g_1, \ldots, g_8)$	0
—	Higgs boson (H^0)	$> 114\,\text{GeV}/c^2$

1.2 show huge differences in the observed mass scales, both between the fermions and the gauge bosons.

1.1.1 The electroweak interaction

The electroweak interaction is mediated by the $W^\pm$ and Z^0 bosons (weak part) and the photon γ (electromagnetic part). All left-handed fermion fields are doublets with respect to the weak isospin, while right-handed fermion fields are isospin singlets. Table 1.3 summarizes the (electroweak) flavor quantum numbers of leptons and quarks. In the original Standard Model, neutrinos are massless and thus only interact weakly. Since right-handed neutrinos would be isospin singlets, they would not interact at all and hence do not exist in the limit of massless neutrinos. This changes since neutrinos obtain finite masses as indicated by neutrino oscillations [3, 12].

Table 1.3: Weak flavor quantum numbers of leptons and quarks. The symbol T denotes the weak isospin, T_3 is its third component, $Y = Q - T_3$ the weak hypercharge, where Q is the electric charge in units of the elementary charge e. The subscripts L and R indicate left- and right-handed states. Weak isospin doublets are surrounded by brackets. The quarks d', s' and b' are related to the quarks d, s and b of well-defined mass via the quark mixing matrix (Equation 1.1). Table taken from Reference [12].

Generations			T	T_3	Y	Q
$\begin{pmatrix} \nu_{e\mathrm{L}} \\ e_\mathrm{L} \end{pmatrix}$ $\begin{pmatrix} \nu_{\mu\mathrm{L}} \\ \mu_\mathrm{L} \end{pmatrix}$ $\begin{pmatrix} \nu_{\tau\mathrm{L}} \\ \tau_\mathrm{L} \end{pmatrix}$			$1/2$	$+1/2$ $-1/2$	$-1/2$ $-1/2$	0 -1
e_R	μ_R	τ_R	0	0	-1	-1
$\begin{pmatrix} u_\mathrm{L} \\ d'_\mathrm{L} \end{pmatrix}$ $\begin{pmatrix} c_\mathrm{L} \\ s'_\mathrm{L} \end{pmatrix}$ $\begin{pmatrix} t_\mathrm{L} \\ b'_\mathrm{L} \end{pmatrix}$			$1/2$	$+1/2$ $-1/2$	$+1/6$ $+1/6$	$+2/3$ $-1/3$
u_R	c_R	t_R	0	0	$+2/3$	$+2/3$
d_R	s_R	b_R	0	0	$-1/3$	$-1/3$

The quark eigenstates of the weak interaction—as summarized in Table 1.3— are not identical to the states of well-defined mass from Table 1.1. The weak eigenstates of the down-type quarks $(\boldsymbol{d'}, \boldsymbol{s'}, \boldsymbol{b'})^\mathsf{T}$ can be described as a rotation of their mass eigenstates $(\boldsymbol{d}, \boldsymbol{s}, \boldsymbol{b})^\mathsf{T}$, where $^\mathsf{T}$ indicates a transposed matrix:

$$\begin{pmatrix} \boldsymbol{d'} \\ \boldsymbol{s'} \\ \boldsymbol{b'} \end{pmatrix} = \boldsymbol{V}_\mathrm{CKM} \begin{pmatrix} \boldsymbol{d} \\ \boldsymbol{s} \\ \boldsymbol{b} \end{pmatrix} . \tag{1.1}$$

The matrix $\boldsymbol{V}_\mathrm{CKM}$ is called *quark mixing* or *Cabibbo-Kobayashi-Maskawa (CKM) matrix* [1, 2]. In principle, the rotation could also be attributed to the up-type quarks. However, it has traditionally always been located in the down-type sector.

The occurrence of the quark mixing matrix is due to the fact that both up-type and down-type quarks acquire mass [12]. Within the Standard Model, the two corresponding mass matrices cannot be diagonalized simultaneously. Since only the charged leptons are massive within the original Standard Model, no mixing matrix occurs for the lepton sector. The effects of the quark mixing can be illustrated by considering the part of the electroweak Lagrangian density that describes the coupling of the fermions to the gauge bosons, i. e., the interactions [12]:

$$\mathcal{L}^{\text{ew}}_{\text{int}} = -e\bigg\{ \mathbf{A}_\mu \boldsymbol{\mathcal{J}}^\mu_{\text{em}} \; + \; \frac{1}{\sin\theta_{\text{W}}\cos\theta_{\text{W}}} \mathbf{Z}_\mu \boldsymbol{\mathcal{J}}^\mu_{\text{NC}}$$
$$+ \; \frac{1}{\sqrt{2}\sin\theta_{\text{W}}} \left[\mathbf{W}^+_\mu \boldsymbol{\mathcal{J}}^\mu_{\text{CC}} + \mathbf{W}^-_\mu \boldsymbol{\mathcal{J}}^{\mu\dagger}_{\text{CC}} \right] \bigg\}. \qquad (1.2)$$

The symbols $\mathbf{A}_\mu$, $\mathbf{Z}_\mu$ and $\mathbf{W}^\pm_\mu$ denote the photon, Z^0 and $W^\pm$ fields, e is the positron charge and θ_{W} the weak mixing angle. A † marks a Hermitian conjugate operator. Using Equation 1.1, the electromagnetic (em), neutral (NC) and charged (CC) weak currents take the following form [12]:

$$\boldsymbol{\mathcal{J}}^\mu_{\text{em}} \;=\; \sum_{\ell=e,\mu,\tau} -\overline{\boldsymbol{\ell}}\,\gamma^\mu\,\boldsymbol{\ell} + \sum_{q=u,c,t,d,s,b} Q_q\,\overline{\boldsymbol{q}}\,\gamma^\mu\,\boldsymbol{q}\,,$$

$$\boldsymbol{\mathcal{J}}^\mu_{\text{NC}} \;=\; \sum_{\ell=e,\mu,\tau} \left\{ \overline{\boldsymbol{\nu}}_\ell\,\gamma^\mu \frac{1}{2}\frac{1-\gamma_5}{2}\,\boldsymbol{\nu}_\ell - \overline{\boldsymbol{\ell}}\,\gamma^\mu \left(-\frac{1}{2}\frac{1-\gamma_5}{2} + \sin^2\theta_{\text{W}} \right)\boldsymbol{\ell} \right\}$$
$$+ \sum_{q=u,c,t,d,s,b} \overline{\boldsymbol{q}}\,\gamma^\mu \left(T_3\frac{1-\gamma_5}{2} - Q_q\sin^2\theta_{\text{W}} \right)\boldsymbol{q}\,, \qquad (1.3)$$

$$\boldsymbol{\mathcal{J}}^\mu_{\text{CC}} \;=\; (\overline{\boldsymbol{\nu}}_{e\text{L}}, \overline{\boldsymbol{\nu}}_{\mu\text{L}}, \overline{\boldsymbol{\nu}}_{\tau\text{L}})\,\gamma^\mu \begin{pmatrix} \boldsymbol{e}_{\text{L}} \\ \boldsymbol{\mu}_{\text{L}} \\ \boldsymbol{\tau}_{\text{L}} \end{pmatrix} + (\overline{\boldsymbol{u}}_{\text{L}}, \overline{\boldsymbol{c}}_{\text{L}}, \overline{\boldsymbol{t}}_{\text{L}})\,\gamma^\mu \begin{pmatrix} \boldsymbol{d}'_{\text{L}} \\ \boldsymbol{s}'_{\text{L}} \\ \boldsymbol{b}'_{\text{L}} \end{pmatrix}$$

$$=\; (\overline{\boldsymbol{\nu}}_{e\text{L}}, \overline{\boldsymbol{\nu}}_{\mu\text{L}}, \overline{\boldsymbol{\nu}}_{\tau\text{L}})\,\gamma^\mu \begin{pmatrix} \boldsymbol{e}_{\text{L}} \\ \boldsymbol{\mu}_{\text{L}} \\ \boldsymbol{\tau}_{\text{L}} \end{pmatrix} + (\overline{\boldsymbol{u}}_{\text{L}}, \overline{\boldsymbol{c}}_{\text{L}}, \overline{\boldsymbol{t}}_{\text{L}})\,\gamma^\mu \boldsymbol{V}_{\text{CKM}} \begin{pmatrix} \boldsymbol{d}_{\text{L}} \\ \boldsymbol{s}_{\text{L}} \\ \boldsymbol{b}_{\text{L}} \end{pmatrix}\,.$$

The symbol $\boldsymbol{\ell}$ and $\boldsymbol{\nu}_\ell$ with $\ell = e, \mu, \tau$ denote the lepton fields, $\boldsymbol{q}'$ the weak and $\boldsymbol{q}$ the mass eigenstates of the relevant quarks fields, where $q = u, c, t, d, s, b$. Their adjoint fields are marked by a bar. The quark charges in units of the positron charge are named Q_q and T_3 is the third component of their isospin (Table 1.3). The γ^μ are the Dirac matrices and γ_5 is defined as $\gamma_5 \equiv i\gamma^0\gamma^1\gamma^2\gamma^3$. The subscript L denotes left-handed fermion states.

Equation 1.3 shows that the inequality of the weak and the mass eigenstates of the down-type quarks, i. e., the occurrence of the CKM matrix, results in *flavor-changing (FC) charged quark currents*, e. g.,

$$\begin{aligned} d &\rightarrow u + W^- \quad (V_{11} \equiv V_{ud})\,, \\ \text{FC}: \quad s &\rightarrow u + W^- \quad (V_{12} \equiv V_{us})\,, \\ \text{FC}: \quad b &\rightarrow u + W^- \quad (V_{13} \equiv V_{ub})\,. \end{aligned} \qquad (1.4)$$

The amplitudes of the given reactions are proportional to the indicated matrix elements V_{uj}. Due to the structure of the flavor-changing charged quark currents in Equation 1.3, the matrix elements are intuitively named

$$\boldsymbol{V}_{\text{CKM}} \equiv \begin{pmatrix} V_{ud} & V_{us} & V_{ub} \\ V_{cd} & V_{cs} & V_{cb} \\ V_{td} & V_{ts} & V_{tb} \end{pmatrix}. \tag{1.5}$$

This work is aimed at the precise measurement of the element $|V_{us}|$.

Because of the unitarity of the CKM matrix, $\boldsymbol{V}_{\text{CKM}}(\boldsymbol{V}_{\text{CKM}})^{\dagger} = \boldsymbol{1}$, flavor-changing neutral currents at tree level do not exist in the Standard Model. Similarly, due to the absence of a mixing matrix in the lepton sector, no flavor-changing charged lepton currents occur within the Standard Model. This changes since neutrinos have mass. A lepton mixing matrix has to be introduced and flavor mixing occurs in charged lepton currents. This results, e.g., in neutrino oscillations. Thus, the observation of neutrino oscillations [3] indicates that neutrinos indeed have finite masses. In contrast to the quark sector, the lepton mixing matrix is usually associated with the neutrinos (i.e., the up-type leptons). It is called the *neutrino mixing* or *Pontecorvo-Maki-Nakagawa-Sakata (PMNS) matrix*.

1.1.2 Properties of the quark mixing matrix

The quark mixing matrix $\boldsymbol{V}_{\text{CKM}}$ describes a basis transformation of the mass into the weak (isospin) eigenstates of the down-type quarks:

$$\begin{pmatrix} \boldsymbol{d'} \\ \boldsymbol{s'} \\ \boldsymbol{b'} \end{pmatrix} = \begin{pmatrix} V_{ud} & V_{us} & V_{ub} \\ V_{cd} & V_{cs} & V_{cb} \\ V_{td} & V_{ts} & V_{tb} \end{pmatrix} \begin{pmatrix} \boldsymbol{d} \\ \boldsymbol{s} \\ \boldsymbol{b} \end{pmatrix}. \tag{1.6}$$

By definition, the CKM matrix is unitary, $\boldsymbol{V}_{\text{CKM}}(\boldsymbol{V}_{\text{CKM}})^{\dagger} = \boldsymbol{1}$, which results in the following unitarity conditions:

$$\sum_{k=1}^{3} V_{ki}^{*} V_{kj} = \delta_{ij} \quad \text{with} \quad \delta_{ij} = \begin{cases} 1: & i = j \\ 0: & i \neq j \end{cases}. \tag{1.7}$$

The unitarity reflects the fact that an up-type quark q_u must transform into a down-type quark q_d if a charged current interaction occurs. It cannot disappear within the Standard Model and any deviation from unitarity indicates physics beyond the Standard Model.

The unitarity conditions leave nine free parameters for the nine complex matrix elements V_{ij}. Five of these parameters can be absorbed into the unobservable phases of the quark fields, as the Lagrangian density is invariant under phase transformations [12]. The four remaining parameters are three mixing angles θ_{ij} with $i \neq j$ and one *CP*-violating phase δ. This *Kobayashi-Maskawa phase* is responsible for all *CP*-violating phenomena in flavor-changing processes within the Standard Model [2, 3, 12].

A standard parametrization of the quark mixing matrix is [3, 17]

$$\boldsymbol{V}_{\mathrm{CKM}} = \begin{pmatrix} c_{12}c_{13} & s_{12}c_{13} & s_{13}e^{-i\delta} \\ -s_{12}c_{23} - c_{12}s_{23}s_{13}e^{i\delta} & c_{12}c_{23} - s_{12}s_{23}s_{13}e^{i\delta} & s_{23}c_{13} \\ s_{12}s_{23} - c_{12}c_{23}s_{13}e^{i\delta} & -c_{12}s_{23} - s_{12}c_{23}s_{13}e^{i\delta} & c_{23}c_{13} \end{pmatrix}, \tag{1.8}$$

where $s_{ij} \equiv \sin\theta_{ij}$ and $c_{ij} \equiv \cos\theta_{ij}$.

The four parameters are free parameters of the Standard Model and have to be determined experimentally. The experiments show that $s_{13} \ll s_{23} \ll s_{12} \ll 1$. This hierarchy of the CKM matrix can be expressed by the *Wolfenstein parametrization* [3, 17], which defines:

$$\begin{aligned} \lambda &\equiv s_{12} = \frac{|V_{us}|}{\sqrt{|V_{ud}|^2 + |V_{us}|^2}}, \\ A\lambda^2 &\equiv s_{23} = \lambda \left| \frac{V_{cb}}{V_{us}} \right|, \\ A\lambda^3 (\rho + i\eta) &\equiv s_{13}e^{i\delta} = V_{ub}^*. \end{aligned} \tag{1.9}$$

The matrix then takes the following form [3]:

$$\boldsymbol{V}_{\mathrm{CKM}} = \begin{pmatrix} 1 - \frac{\lambda^2}{2} & \lambda & A\lambda^3 (\rho - i\eta) \\ -\lambda & 1 - \frac{\lambda^2}{2} & A\lambda^2 \\ A\lambda^3 (1 - \rho - i\eta) & -A\lambda^2 & 1 \end{pmatrix} + \mathcal{O}(\lambda^4). \tag{1.10}$$

Experimentally [3],

$$\begin{aligned} \lambda &\approx 0.22 \quad \Rightarrow \quad \mathcal{O}(\lambda^4) \approx 10^{-3}, \\ A &\approx 0.82. \end{aligned} \tag{1.11}$$

The unitarity condition that involves the matrix element V_{us} is

$$|V_{ud}|^2 + |V_{us}|^2 + |V_{ub}|^2 = 1 \tag{1.12}$$

with the following estimates of the contributing matrix elements [3]:

$$\begin{aligned} |V_{ud}| &\approx 1 - \frac{\lambda^2}{2} \approx 0.98, \\ |V_{us}| &\approx \lambda \approx 0.22, \\ |V_{ub}| &\approx A\lambda^3 \sqrt{\rho^2 + \eta^2} \approx 3.5 \times 10^{-3}. \end{aligned} \tag{1.13}$$

1.1.3   The strong interaction

In analogy to the optical theory of colors, the strong interaction is also called *Quantum Chromodynamics (QCD)*. The charge of the strong interaction is named *color* and, in contrast to one single electric charge/anti-charge pair, comprises three pairs, *red/anti-red, green/anti-green and blue/anti-blue*. Of the two fermion sectors, only the quarks carry

color and feel the strong force. Leptons are color singlets, i. e., they are *color-neutral (white)* and do not interact strongly. Due to the three colors, the quarks are color triplets and the underlying symmetry group of QCD is the $\mathrm{SU}_C(3)$ group of colors. This results in eight gauge bosons, the *gluons*, which mediate the interaction. Because of the *non-Abelian* character of QCD, gluons carry color themselves and interact strongly, in contrast to the photon of *Quantum Electrodynamics (QCD)*. Each gluon carries one color and one anti-color [12].

Another specific feature of QCD is *confinement*. Free quark systems (*hadrons*) must be color-neutral (white). This is caused by the dependence of the effective coupling constant α_S on the momenta which are involved in the interaction. At large momenta, i. e., small distances, α_S is small, but it increases with decreasing momentum, i. e., increasing distances [10]:

$$\begin{aligned} \alpha_S(m_\tau^2 \approx 1.78^2 \, \mathrm{GeV}^2/c^4) &\approx 0.344 \,, \\ \alpha_S(m_Z^2 \approx 91^2 \, \mathrm{GeV}^2/c^4) &\approx 0.1212 \,. \end{aligned} \tag{1.14}$$

Hence, free quarks or gluons do not exist. Only bound, color-neutral quark and gluon states are observable. In analogy to the theory of colors, two types of color-neutral quark states exist. Firstly, di-quark systems that are made of color/anti-color pairs (*mesons*, $q_C q'_{\overline{C}}$). Secondly quark triplets, in which each quark carries a different color (*baryons*, $q_r q'_g q''_b$).

Due to the potentially large value of the coupling constant α_S, *perturbation theory* can only be applied to calculate QCD processes in regions where α_S is sufficiently small, i. e., in interactions with large transferred momenta. Otherwise, large *non-perturbative* corrections invalidate the use of perturbation theory.

1.2   Experimental status of hadronic τ decays

Experimentally, hadronic τ decays are described by the branching fractions of *exclusive* decays into specific final states and the invariant mass spectra of the latter. The branching fraction of a mode $\tau \to i$ is defined as the ratio of its decay width Γ_i to the total width Γ of the τ lepton,

$$\mathcal{B}_i \equiv \frac{\Gamma_i}{\Gamma} \,. \tag{1.15}$$

It is measured as the number of decays of the type $\tau \to i$ relative to the number of all τ lepton decays, $\mathcal{B}_i = N_i/N_\tau$ (Chapter 6).

In the following, the experimental status of the branching fraction measurements is presented for the decay modes which are most important to this analysis. A more detailed review may be found in Reference [10]. Since leptonic τ decays are complementary to all hadronic modes and are known with good precision, they provide the most precise means to determine the total hadronic branching fraction of the τ lepton. The current experimental situation of leptonic τ decays is reviewed before presenting actual measurements of hadronic τ decays.

1.2.1 Branching fractions of leptonic τ decays

The current world averages for the leptonic τ branching fractions [3] are[1]

$$
\begin{aligned}
\mathcal{B}_e &\equiv \mathcal{B}(\tau^- \to e^- \overline{\nu}_e \nu_\tau) &=& (17.82 \pm 0.05)\,\% \,, \\
\mathcal{B}_\mu &\equiv \mathcal{B}(\tau^- \to \mu^- \overline{\nu}_\mu \nu_\tau) &=& (17.33 \pm 0.05)\,\% \,.
\end{aligned}
\tag{1.16}
$$

Lepton universality can be used to further improve the knowledge of the leptonic branching fractions as discussed in the following paragraphs.

Within the standard $V - A$ theory, the decay width of a lepton $L = \mu, \tau$ into a lepton $\ell = e, \mu$ and the corresponding neutrinos can be calculated [10] using

$$
\Gamma(L^- \to \ell^- \overline{\nu}_\ell \nu_L(\gamma)) = \frac{G_L G_\ell}{192\pi^3} f\left(\frac{m_\ell^2}{m_L^2}\right) \delta_W^L \delta_\gamma^L
\tag{1.17}
$$

with

$$
\begin{aligned}
G_\ell &\equiv \frac{g_\ell^2}{4\sqrt{2} m_W^2} \,, \\
\delta_W^L &\equiv 1 + \frac{3}{5} \frac{m_L^2}{m_W^2} \,, \\
\delta_\gamma^L &\equiv 1 + \frac{\alpha(m_L)}{2\pi}\left(\frac{25}{4} - \pi^2\right) \,, \\
f(x) &\equiv 1 - 8x + 8x^3 - x^4 - 12x^2 \ln x \,.
\end{aligned}
$$

The symbols g_ℓ denote the weak leptonic couplings, m_W is the mass of the W boson, m_L the one of the lepton L and $\alpha(m_L)$ the electromagnetic fine structure constant at the L mass scale. Numerically, the W-propagator and radiative corrections are small, both for τ leptons and muons: $\delta_W^\tau \approx 1 + 2.9 \times 10^{-4}$, $\delta_\gamma^\tau \approx 1 - 43.2 \times 10^{-4}$, $\delta_W^\mu \approx 1 + 1.0 \times 10^{-6}$ and $\delta_\gamma^\mu \approx 1 - 42.4 \times 10^{-4}$.

Using lepton universality, $g_e = g_\mu = g_\tau$, the ratio of the two leptonic τ branching fractions can be calculated from the corresponding decay widths according to Equations 1.15 and 1.17 [10]:

$$
r_{\mu e} \equiv \frac{\mathcal{B}_\mu}{\mathcal{B}_e} = \frac{f\left(m_\mu^2/m_\tau^2\right)}{f\left(m_e^2/m_\tau^2\right)} = 0.972565 \pm 0.000009 \,.
\tag{1.18}
$$

The world averages as of 2004 are used for the lepton masses [10, 18] and the uncertainty is dominated by the uncertainty of the τ mass. Equation 1.18 facilitates an independent measurement of the electronic branching fraction on the basis of the muonic one:

$$
\mathcal{B}_e^{(\mu)} \equiv \frac{\mathcal{B}_\mu}{r_{\mu e}} = (17.82 \pm 0.05)\,\% \,,
\tag{1.19}
$$

where the exact numerical agreement with the measurement from Equation 1.16 should be considered as being accidental.

---

[1]Whenever a particle or decay mode is given, the charged conjugate particle or mode is also implied.

The electronic branching fraction of the τ lepton can also be obtained from a measurement of the τ lepton and muon masses and lifetimes τ_τ and τ_μ. Assuming $\tau - \mu$ universality in weak charged currents and applying Equations 1.15 and 1.17 to both the electronic τ lepton and muon decays yields

$$
\begin{aligned}
\mathcal{B}_e^{(\mu \to e)} &\equiv \frac{\mathcal{B}(\tau^- \to e^- \overline{\nu}_e \nu_\tau)}{\mathcal{B}(\mu^- \to e^- \overline{\nu}_e \nu_\mu)} \\
&= \frac{\tau_\tau}{\tau_\mu} \left(\frac{m_\tau}{m_\mu}\right)^5 \frac{f\left(m_e^2/m_\tau^2\right)}{f\left(m_e^2/m_\mu^2\right)} \frac{\delta_W^\tau \delta_\gamma^\tau}{\delta_W^\mu \delta_\gamma^\mu} = (17.81 \pm 0.07)\,\% \,.
\end{aligned}
\tag{1.20}
$$

Here, the electronic branching fraction of the muon is $\mathcal{B}(\mu^- \to e^- \overline{\nu}_e \nu_\mu(\gamma)) = 1$ and the Heisenberg uncertainty principle is used to express the total decay width Γ via the lifetime τ, $\Gamma = \hbar/\tau$. Again, the world averages as of 2004 are used for the lepton masses and lifetimes [10, 18].

The direct measurement of the electronic τ branching fraction (Equation 1.16) and the two derived values (Equations 1.18, 1.20) are in good agreement. Their combination results in the *universality-improved* value of the electronic τ branching fraction,

$$
\mathcal{B}_e^{(\mathrm{uni})} = (17.818 \pm 0.032)\,\% \,.
\tag{1.21}
$$

1.2.2   Branching fractions of hadronic τ decays

The most precise measurement of the total branching fraction of the τ lepton into hadronic final states $\mathcal{B}_{\mathrm{had}} \equiv \mathcal{B}(\tau^- \to X_{\mathrm{had}}^- \nu_\tau)$ can be calculated as follows:

$$
\begin{aligned}
\mathcal{B}_{\mathrm{had}}^{(\mathrm{uni})} &= 1 - \mathcal{B}_e - \mathcal{B}_\mu = 1 - (1 + r_{\mu e})\,\mathcal{B}_e^{(\mathrm{uni})} \\
&= (64.853 \pm 0.063)\,\% \,.
\end{aligned}
\tag{1.22}
$$

Table 1.4 summarizes the current world averages of the measured branching fractions of the τ lepton into hadronic final states with net strangeness, i.e., with an odd number of kaons. The summary is taken from Reference [10] and is based on measurements by the ALEPH, OPAL and CLEO collaborations [3, 19–23]. Recent measurements from the BABAR and Belle collaborations are included as described in Reference [7].

In analogy to the electronic τ branching fraction (Equation 1.20), the branching fraction $\mathcal{B}_K \equiv \mathcal{B}(\tau^- \to K^- \nu_\tau)$ can be determined from the branching fraction of the decay $K^- \to \mu^- \overline{\nu}_\mu$ under the assumption of $\tau - \mu$ universality in charged weak currents [10]:

$$
\begin{aligned}
\mathcal{B}_K^{(\mathrm{uni})} &= \frac{\tau_\tau \mathcal{B}(K^- \to \mu^- \overline{\nu}_\mu)}{\tau_K} \frac{m_\tau^3}{2 m_K m_\mu^2} \left(\frac{1 - m_K^2/m_\tau^2}{1 - m_\mu^2/m_K^2}\right)^2 \delta_{\tau/K} \\
&= (7.15 \pm 0.03) \times 10^{-3} \,.
\end{aligned}
\tag{1.23}
$$

The world averages as of 2004 are used for the branching fraction of the mode $K^- \to \mu^- \overline{\nu}_\mu$ as well as for the τ and K masses (m_τ, m_K) and lifetimes (τ_τ, τ_K). The symbol $\delta_{\tau/K}$ denotes a small radiative correction factor, $\delta_{\tau/K} = 1.0090 \pm 0.0022$ [10]. The measured branching fraction from Table 1.4 differs by 1.3 standard deviations from

Table 1.4: World averages for the branching fractions of τ decays into final states with net strangeness, taken from References [7, 10]. The averages are based on measurements by the ALEPH, OPAL and CLEO collaborations [3, 19–23], as well as recent analyses of the *BaBar* and Belle collaborations [24, 25]. The *BaBar* measurement of the mode $\tau^- \to K^- \pi^0 \nu_\tau$ [26] is not included in the world average for this channel as it is superseded by the more precise measurement performed within this work (Chapter 6). The value for the $\tau^- \to (\overline{K}\pi\pi)^- \nu_\tau$ branching fraction takes into account measurements from ALEPH and CLEO, as well as estimates for unseen final states using isospin relations. The estimate for the very small mode $\tau^- \to (\overline{K}\pi\pi\pi)^- \nu_\tau$ is obtained from an empirical observation of pionic modes and Cabibbo suppression.

Mode	$\mathcal{B}\,[10^{-3}]$	
$\tau^- \to K^- \nu_\tau$	6.85	$\pm$ 0.23
$\tau^- \to K^- \pi^0 \nu_\tau$	4.54	$\pm$ 0.30
$\tau^- \to \pi^- \overline{K}^0 \nu_\tau$	8.31	$\pm$ 0.28
$\tau^- \to K^- \pi^0 \pi^0 \nu_\tau$	0.58	$\pm$ 0.24
$\tau^- \to \pi^- \overline{K}^0 \pi^0 \nu_\tau$	3.6	$\pm$ 0.4
$\tau^- \to K^- \pi^+ \pi^- \nu_\tau$	2.80	$\pm$ 0.16
$\tau^- \to K^- \eta \nu_\tau$	0.27	$\pm$ 0.06
$\tau^- \to (\overline{K}\pi\pi)^- \nu_\tau$	0.74	$\pm$ 0.30
$\tau^- \to K_1(1270)^- \nu_\tau \to K^- \omega \nu_\tau$	0.67	$\pm$ 0.21
$\tau^- \to (\overline{K}\pi\pi\pi)^- \nu_\tau$ & $\tau^- \to K^{*-} \eta \nu_\tau$	0.40	$\pm$ 0.12
$\tau^- \to K^- K^+ K^- \nu_\tau$	0.016	$\pm$ 0.002
$\tau^- \to X_S^- \nu_\tau = \sum$	28.78	$\pm$ 0.79

the predicted value in Equation 1.23. If confirmed, this could be an indication of the violation of lepton universality and thus physics beyond the Standard Model. The measurement of the mode $\tau^- \to K^- \nu_\tau$ within this analysis is an important step to clarify this issue.

Using the predicted value instead of the measurement from Table 1.4, the total branching fraction of τ decays into *strange* final states $\mathcal{B}_{\mathrm{S}} \equiv \mathcal{B}(\tau^- \to X_S^- \nu_\tau)$ becomes

$$\mathcal{B}_{\mathrm{S}}^{(\mathrm{uni})} = (29.08 \pm 0.75) \times 10^{-3}\,. \tag{1.24}$$

The branching fractions of the τ lepton into final states without net strangeness have been measured precisely by the ALEPH, OPAL and CLEO collaborations [3, 19–23]. However, the most precise determination of the *total* branching fraction of the τ lepton into *non-strange* final states $\mathcal{B}_{\mathrm{NS}} \equiv \mathcal{B}(\tau^- \to X_{NS}^- \nu_\tau)$ is obtained from the total hadronic

and the total strange branching fractions (Equations 1.22, 1.24, Table 1.4):

$$
\begin{aligned}
\mathcal{B}_{\text{NS}} &= \mathcal{B}_{\text{had}}^{(\text{uni})} - \mathcal{B}_{\text{S}} &= (61.97 \pm 0.10)\,\% \,, \\
\mathcal{B}_{\text{NS}}^{(\text{uni})} &= \mathcal{B}_{\text{had}}^{(\text{uni})} - \mathcal{B}_{\text{S}}^{(\text{uni})} &= (61.95 \pm 0.10)\,\% \,.
\end{aligned}
\tag{1.25}
$$

1.2.3 Hadronic decay rate of the τ lepton

For the theoretical treatment of hadronic τ decays and the extraction of $|V_{us}|$ in the following sections, the hadronic decay rate is defined as the hadronic decay width normalized to the electronic one:

$$
\begin{aligned}
R_\tau &\equiv \frac{\Gamma(\tau^- \to X_{\text{had}}^- \nu_\tau)}{\Gamma(\tau^- \to e^- \overline{\nu}_e \nu_\tau)} = \frac{\mathcal{B}(\tau^- \to X_{\text{had}}^- \nu_\tau)}{\mathcal{B}(\tau^- \to e^- \overline{\nu}_e \nu_\tau)} \\
&\equiv R_{\tau,\text{NS}} + R_{\tau,\text{S}} \,,
\end{aligned}
\tag{1.26}
$$

where $R_{\tau,\text{NS}}$ and $R_{\tau,\text{S}}$ are the corresponding decay rates into *non-strange* and *strange* final states.

Their values are obtained using the universality-improved electronic branching fraction $\mathcal{B}_e^{(\text{uni})}$ [27]:

$$
\begin{aligned}
R_\tau^{(\text{uni})} &= \frac{1 - \mathcal{B}_e - \mathcal{B}_\mu}{\mathcal{B}_e} = \frac{1}{\mathcal{B}_e^{(\text{uni})}} - (1 + r_{\mu e}) \\
&= 3.640 \pm 0.010 \,, \\
R_{\tau,\text{S}} &= \frac{\mathcal{B}_{\text{S}}}{\mathcal{B}_e^{(\text{uni})}} \\
&= 0.1615 \pm 0.0044 \,, \\
R_{\tau,\text{NS}} &= R_\tau^{(\text{uni})} - R_{\tau,\text{S}} = \frac{1}{\mathcal{B}_e^{(\text{uni})}} - (1 + r_{\mu e}) - \frac{\mathcal{B}_{\text{S}}}{\mathcal{B}_e^{(\text{uni})}} \\
&= 3.478 \pm 0.011 \,.
\end{aligned}
\tag{1.27}
$$

If lepton universality in the leptonic weak currents is used to calculate the branching fraction $\mathcal{B}(\tau^- \to K^- \nu_\tau)$, the result changes to [27]

$$
\begin{aligned}
R_{\tau,\text{S}}^{(\text{uni})} &= 0.1632 \pm 0.0042 \,, \\
R_{\tau,\text{NS}}^{(\text{uni})} &= 3.477 \pm 0.011 \,.
\end{aligned}
\tag{1.28}
$$

1.2.4 Spectral functions of hadronic τ decays

Spectral functions in τ decays describe the structure of the hadronic final states. They represent the probability to produce a given hadronic final state from the QCD vacuum as a function of its invariant mass-squared s. For a hadronic τ decay into a vector (axial-vector) final state $\tau^- \to V^-(A^-)\nu_\tau$ with or without net strangeness, the spectral functions $v_J^{(V)}(s)$ $(a_J^{(A)}(s))$ are defined according to the spin J of the hadronic system. They are obtained by dividing the normalized invariant mass-squared

distribution $(1/N_{V/A})(dN_{V/A}/ds)$ for a given hadronic mass $\sqrt{s}$ by an appropriate kinematic factor [10]:

$$
\begin{aligned}
a_0^{(A)}(s) &\equiv \frac{m_\tau^2}{6\,|V_{\mathrm{CKM}}|^2} \frac{\mathcal{B}(\tau^- \to A^- \nu_\tau)}{\mathcal{B}(\tau^- \to e\overline{\nu}_e \nu_\tau)} \frac{1}{N_A} \frac{dN_A}{ds} \left(1 - \frac{s}{m_\tau^2}\right)^{-2}, \\[2mm]
v_1^{(V)}(s)/a_1^{(A)}(s) &\equiv \frac{m_\tau^2}{6\,|V_{\mathrm{CKM}}|^2} \frac{\mathcal{B}(\tau^- \to V^-/A^- \nu_\tau)}{\mathcal{B}(\tau^- \to e\overline{\nu}_e \nu_\tau)} \\[2mm]
&\quad \times \frac{1}{N_{V/A}} \frac{dN_{V/A}}{ds} \left[\left(1 - \frac{s}{m_\tau^2}\right)^2 \left(1 + \frac{2s}{m_\tau^2}\right)\right]^{-1}.
\end{aligned}
\tag{1.29}
$$

The symbol V_{CKM} denotes the CKM matrix element appropriate to the observed decay mode $\tau^- \to V^-(A^-)\nu_\tau$ and S_{EW} are electroweak radiative corrections. In the limit of *conserved vector currents (CVC)*, the spin-0 vector spectral function vanishes. Since CVC is a very good approximation, it is set to zero for the purpose of this analysis, $v_0(s) = 0$. The main contributions to the spin-0 axial-vector spectral functions are the pion and kaon poles with $(1/N_{\pi/K})(dN_{\pi/K}/ds) = \delta(s - m_{\pi/K})$. Generally, the spectral functions are dominated by known single-particle resonances at low masses [10]. Experimentally, the spectral functions are obtained from the measured invariant mass-squared spectra by unfolding of detector effects.

Figure 1.1 shows the inclusive vector plus axial-vector spectral functions $(v^{\overline{u}s}(s) + a^{\overline{u}s}(s))$ for hadronic final states with net strangeness as measured by the ALEPH and OPAL collaborations. Both distributions clearly show the $K^{*-}(892)$ resonance at small
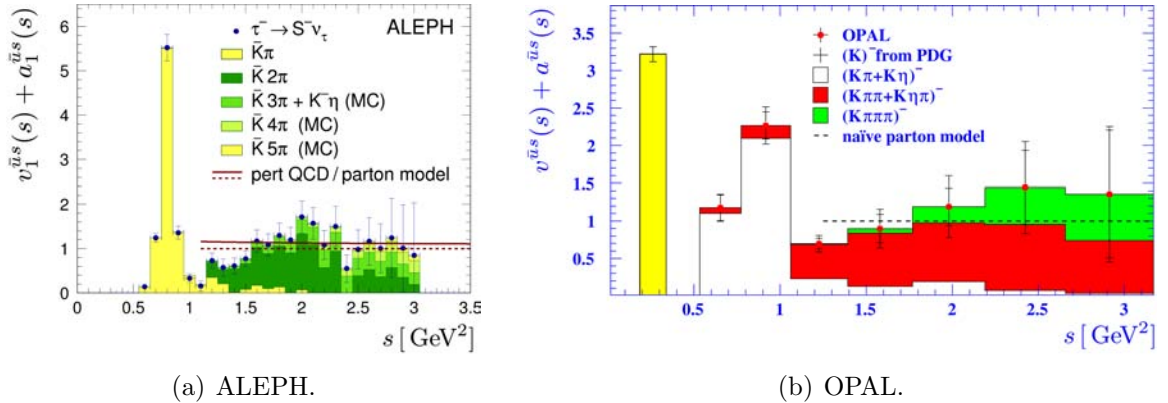
(a) ALEPH.   (b) OPAL.

Figure 1.1: Inclusive vector plus axial-vector spectral functions $(v^{\overline{u}s}(s) + a^{\overline{u}s}(s))$ for τ decays into final states with net strangeness as measured by the **(a)** ALEPH and **(b)** OPAL collaborations [19, 20], taken from Reference [10]. The contributions from the different decay modes are indicated by the colored histograms. The yellow peak in the OPAL distribution is the kaon pole, which has been scaled to the world average of the corresponding branching fraction. In case of the ALEPH plot, the kaon pole is not included and the shape of modes with three or more pions is taken from a phase-space Monte Carlo simulation.

invariant masses, while the higher mass parts are consistent with the expectation from the parton model/perturbative QCD—albeit within the large (statistical) uncertainties.

1.3 Hadronic τ decays and QCD

Hadronic τ decays are one of the most powerful testing grounds for (perturbative) Quantum Chromodynamics and an ideal laboratory for weak hadronic currents. Considering Figure 1.1, the question arises why and how hadronic τ decays can at all be described by perturbative QCD. It shows that hadronic τ decays are dominated by resonant single-particle final states such as $\tau^- \to K^{*-}(892)\nu_\tau \to (\overline{K}\pi)^- \nu_\tau$ or $\tau^- \to a_1^- \nu_\tau \to (\pi\pi\pi)^- \nu_\tau$. The corresponding QCD interaction that binds the quarks and gluons into the hadrons necessarily involves small transferred momenta, i.e., large couplings α_s, and perturbation theory is not applicable. It is indeed the *inclusive* character of the *sum* of all hadronic τ decays that allows to probe fundamental short distance physics described by perturbative QCD [10]. A more detailed description and derivation of the presented contents may be found in References [5, 10].

1.3.1 Hadronic decay rate of the τ lepton

Inclusive observables, e.g., the total hadronic τ decay rate R_τ, can be described as a function of the strong coupling constant $\alpha_s(m_\tau^2)$ at the τ mass scale using perturbation theory with small non-perturbative corrections. The scale m_τ lies in a compromise region where α_s is large enough such that R_τ is sensitive to its value, yet small enough to ensure convergence of the perturbative QCD series ($\alpha_s(m_\tau^2) \approx 0.344$). The variable R_τ is particularly suited as it is *doubly inclusive*: First, the measured distributions are integrated over all hadronic final states at a given invariant mass. Then, the spectral function is integrated over all invariant masses up to the τ mass.

Neglecting strong and electroweak corrections, the parton model predicts for $N_C = 3$ colors

$$
\begin{aligned}
R_\tau &= R_{\tau,\mathrm{NS}} + R_{\tau,\mathrm{S}} \\
&= N_C \left(|V_{ud}|^2 + |V_{us}|^2 \right) = 3 \,.
\end{aligned}
\tag{1.30}
$$

Comparing this value with the measured ones from Equations 1.27 and 1.28, a perturbative correction of approximately 21 % can be estimated. This illustrates the increased sensitivity to α_s compared to the Z^0 hadronic width, where perturbative corrections amount to approximately 4 % only [10].

Quantitatively, R_τ can be obtained from the hadronic spectral functions by integrating over the invariant mass-squared s:

$$
R_\tau = 6 \cdot S_{\mathrm{EW}} \int\limits_0^{m_\tau^2} \frac{ds}{m_\tau^2} \left(1 - \frac{s}{m_\tau^2} \right)^2 \left\{ \left(1 + \frac{2s}{m_\tau^2} \right) [v_1(s) + a_1(s)] + a_0(s) \right\} \,.
\tag{1.31}
$$

The inclusive vector (axial-vector) spectral functions $v_J(s)$ $(a_J(s))$ for the spin J of the hadronic system are defined using the spectral functions from Equation 1.29:

$$
v/a_J(s) \equiv |V_{ud}|^2 \, v/a_J^{\bar{u}d}(s) + |V_{us}|^2 \, v/a_J^{\bar{u}s}(s) \,.
\tag{1.32}
$$

Using unitarity and analyticity, the spectral functions can be connected to the *two-point correlation* (or *hadronic vacuum polarization*) functions

$$
\begin{aligned}
\Pi_{ij,U}^{\mu\nu}(q) &\equiv i \int d^4x \, e^{iqx} \left\langle 0 \left| T \left(U_{ij}^\mu(x) U_{ij}^\nu(x)^\dagger \right) \right| 0 \right\rangle \\
&= \left(-g^{\mu\nu} q^2 + q^\mu \nu^\nu \right) \Pi_{ij,U}^{(1)}(q^2) + q^\mu q^\nu \Pi_{ij,U}^{(0)}(q^2)
\end{aligned}
\tag{1.33}
$$

of vector ($U_{ij}^\mu = V_{ij}^\mu = \overline{q}_j \gamma^\mu q_i$) or axial-vector ($U_{ij}^\mu = A_{ij}^\mu = \overline{q}_j \gamma^\mu \gamma_5 q_i$) color-singlet quark currents [10]. The q_i are the involved quark flavors, q^μ is the four-momentum transfer, T denotes the time-order operator and $g^{\mu\nu}$ is the metric tensor. The imaginary part of the correlators corresponds to the spectral functions $v_J^{\overline{u}d(s)}(s)$ ($a_J^{\overline{u}d(s)}(s)$) for non-strange (strange) quark currents [10]:

$$
\Im\Pi_{\overline{u}d(s),V/A}^{(1)}(s) = \frac{1}{2\pi} v/a_1^{\overline{u}d(s)}(s), \qquad \Im\Pi_{\overline{u}d(s),A}^{(0)}(s) = \frac{1}{2\pi} a_0^{\overline{u}d(s)}(s).
\tag{1.34}
$$

Lorentz decomposition is used to separate the spin $J = 0$ and $J = 1$ parts. The correlation functions obey a dispersion relation which connects the function to its imaginary part [10]:

$$
\Pi_{ij,U}^{(J)}(q^2) = \frac{1}{\pi} \int_0^\infty ds \, \frac{\Im\Pi_{ij,U}^{(J)}(s)}{s - q^2 - i\varepsilon} + \text{ subtractions}.
\tag{1.35}
$$

Equations 1.34 and 1.35 allow the connection of the experimentally accessible spectral functions $v/a_J^{\overline{u}d(s)}(s)$ to the correlation function $\Pi_{\overline{u}d(s),V/A}^{(J)}(q^2)$, which can be derived from theory (QCD).

Inserting Equation 1.34 into Equation 1.31 yields the hadronic τ decay rate R_τ in terms of the hadronic vacuum polarization functions:

$$
R_\tau = 12\pi S_{\text{EW}} \int_0^{m_\tau^2} \frac{ds}{m_\tau^2} \left(1 - \frac{s}{m_\tau^2} \right)^2 \left\{ \left(1 + \frac{2s}{m_\tau^2} \right) \Im\Pi^{(1)}(s) + \Im\Pi^{(0)}(s) \right\}.
\tag{1.36}
$$

The inclusive two-point correlation functions $\Pi^{(J)}(s)$ for spin J are defined as

$$
\Pi^{(J)}(s) \equiv |V_{ud}|^2 \left[\Pi_{ud V}^{(J)}(s) + \Pi_{ud A}^{(J)}(s) \right] + |V_{us}|^2 \left[\Pi_{us V}^{(J)}(s) + \Pi_{us A}^{(J)}(s) \right].
\tag{1.37}
$$

The functions $\Pi^{(J)}(s)$ are analytic everywhere in the complex s plane except on the real axis, where singularities exist. Thus, Cauchy's theorem can be applied to express the line integral along the real axis in Equation 1.36 as a contour integral in the complex plane around a circle with radius $|s| = m_\tau^2$ [10]:

$$
\frac{1}{\pi} \int_0^{m_\tau^2} ds \, w(s) \Im\Pi^{(J)}(s) = -\frac{1}{2\pi i} \oint_{|s|=m_\tau^2} ds \, w(s) \Pi^{(J)}(s),
\tag{1.38}
$$

where $w(s)$ is an arbitrary analytic function and the contour integral runs counter-clockwise from $s = m_\tau^2 + i\varepsilon$ to $s = m_\tau^2 - i\varepsilon$.

The integral over all hadronic final state masses $s = 0 \ldots m_\tau^2$ in Equation 1.36 can be replaced by a contour integral at $|s| = m_\tau^2$ using Equation 1.38. This is the mathematical expression of the fact that the inclusiveness of R_τ allows its calculation from perturbative QCD although the scales of the individual resonances in the hadronic final states are small. While perturbation theory cannot be applied to the individual final states, the energy scale m_τ^2 is large enough such that $\alpha_s(m_\tau^2)$ and thus contributions form non-perturbative effects are small. In consequence, perturbation theory can be applied in form of the *Operator Product Expansion (OPE)*. In this framework, the contributions to R_τ are organized in a series of local gauge-invariant operators of increasing dimension $D = 2n$ ($n \in \mathbf{N}$) [10]:

$$R_\tau = 3 \left(|V_{ud}|^2 + |V_{us}|^2\right) S_{\text{EW}} \left\{ 1 + \delta^{(0)} + \delta'_{\text{EW}} + \sum_{D \geq 2} \delta^{(D)} \right\}$$

$$\equiv R_{\tau,\text{NS}} + R_{\tau,\text{S}}, \tag{1.39}$$

where

$$\delta^{(D)} \equiv \frac{|V_{ud}|^2}{|V_{ud}|^2 + |V_{us}|^2} \delta_{ud}^{(D)} + \frac{|V_{us}|^2}{|V_{ud}|^2 + |V_{us}|^2} \delta_{us}^{(D)} \tag{1.40}$$

is the average of the dimension D contributions with and without net strangeness. The electroweak radiative correction has the value $S_{\text{EW}} = 1.0201 \pm 0.0003$ and the residual electroweak correction is $\delta'_{\text{EW}} = 0.0010$. The symbol $\delta^{(0)}$ denotes the massless perturbative correction of dimension zero and the $\delta_{ij}^{(D)}$ are dimension $D \geq 2$ operators, which contain an implicit suppression factor $1/m_\tau^D$. For $D = 2$, $\delta^{(2)} = \delta^{(2)}(m_q)$ is the *perturbative* contribution from the quark mass m_q. While it is small for u and d quarks, $\delta_{ud}^{(2)} < 0.1\,\%$, it is much larger for the s quark due to its larger mass (Table 1.1).

The contributions to the Operator Product Expansion can be calculated up to orders of $D = 6(8)$ using perturbation theory up to third (fourth) order in α_s [10]. Estimates are used for higher-order corrections.

The longitudinal sector

The contributions of the final states with different spin $J = 0, 1$ in Equation 1.36 can also be decomposed in the following form [4, 5]:

$$R_\tau = 12\pi S_{\text{EW}} \int_0^{m_\tau^2} \frac{ds}{m_\tau^2} \left(1 - \frac{s}{m_\tau^2}\right)^2 \left\{ \left(1 + \frac{2s}{m_\tau^2}\right) \Im\Pi^{(1+0)}(s) - 2(s/m_\tau^2)\Im\Pi^{(0)}(s) \right\},$$

$$\tag{1.41}$$

where the $J = 1 + 0$ part is called *transverse* and the $J = 0$ part *longitudinal* contribution. While the perturbation series for the transverse part is well behaved and converges reasonably well—as does the longitudinal part for the non-strange sector—the longitudinal contribution in the above expression shows a bad convergence for final states with net strangeness [4, 5, 10]. This is reflected by large uncertainties of these contributions, which result mainly from higher-order perturbative corrections.

The problem can be alleviated by using a phenomenological parametrization of the $J = 0$ contribution $R_\tau^{(J=0)}$ [4, 5]. In this approach, $R_\tau^{(J=0)}$ is predicted using well-known resonances. For final states with net strangeness, $R_{\tau,\text{S}}^{(J=0)}$ is dominated by the

pseudoscalar contribution, which in turn is dominated by the well-known kaon pole. Additionally, minor higher resonances are also included, as is the small contribution from scalar resonances. The parametrization improves the uncertainty of $R_{\tau,\mathrm{S}}^{(J=0)}$ by one order of magnitude with respect to the perturbative QCD calculation [4, 5]. For completeness and with an improvement of a factor of two, the longitudinal contribution of final states without net strangeness, $R_{\tau\mathrm{NS}}^{(J=0)}$, is also parametrized. It is dominated by the pion pole.

1.3.2   Spectral moments of hadronic τ decays

Additional information on hadronic τ decays can be obtained from the *shape* of the spectral functions. The shape can be described using *spectral moments*

$$R_\tau^{kl} \equiv \int\limits_0^{m_\tau^2} ds \left(1 - \frac{s}{m_\tau^2}\right)^k \left(\frac{s}{m_\tau^2}\right)^l \frac{dR_\tau}{ds} \tag{1.42}$$

with *spectral weights* $(1 - s/m_\tau^2)^k$ and $(s/m_\tau^2)^l$ and $(k, l \in \mathbf{N})$. Thus, $R_\tau \equiv R_\tau^{00}$. All moments R_τ^{kl} can be calculated in analogy to R_τ (Equations 1.36, 1.39) using the Operator Product Expansion:

$$\begin{aligned}
R_\tau^{kl} &= 3\left(|V_{ud}|^2 + |V_{us}|^2\right) S_{\mathrm{EW}} \left\{1 + \delta^{kl(0)} + \delta'_{\mathrm{EW}} + \sum_{D \geq 2} \delta^{kl(D)}\right\} \\
&\equiv R_{\tau,\mathrm{NS}}^{kl} + R_{\tau,\mathrm{S}}^{kl}.
\end{aligned} \tag{1.43}$$

Higher moments are especially sensitive to higher-order perturbative and non-perturbative contributions to the Operator Product Expansion.

The strong coupling constant α_s from hadronic τ decays

A measurement that demonstrates the power of hadronic τ decays and their interpretation using perturbative QCD and the Operator Product Expansion is the determination of $\alpha_s(m_\tau^2)$ from the measured and predicted rate and spectral moments of τ decays into final states without net strangeness [10, 28]. The result is

$$\begin{aligned}
\alpha_s^{(\tau)}(m_\tau^2) &= 0.344 \pm 0.005_{(\mathrm{exp})} \pm 0.007_{(\mathrm{theo})} \\
&= 0.344 \pm 0.009,
\end{aligned} \tag{1.44}$$

where (τ) indicates the determination from τ decays. The total uncertainty is obtained by adding the experimental and theoretical contributions in quadrature. Evolution of the measured value to the Z^0 mass scale yields the most precise determination of $\alpha_s(m_Z^2)$:

$$\begin{aligned}
\alpha_s^{(\tau)}(m_Z^2) &= 0.1212 \pm 0.0005_{(\mathrm{exp})} \pm 0.0008_{(\mathrm{theo})} \pm 0.0005_{(\mathrm{evol})} \\
&= 0.1212 \pm 0.0011,
\end{aligned} \tag{1.45}$$

where the third uncertainty results from the evolution to the Z^0 mass scale. The measurement is in good agreement with the direct determination from the global fit to the electroweak data at the Z^0 mass scale,

$$
\begin{aligned}
\alpha_s^{(Z)}(m_Z^2) &= 0.1191 \pm 0.0027_{(\text{exp})} \pm 0.0001_{(\text{theo})} \\
&= 0.1191 \pm 0.0027 \, .
\end{aligned}
\tag{1.46}
$$

The agreement of both values over a range of two orders of magnitude of the mass scale provides a stringent test of the running of the strong coupling constant α_s and of asymptotic freedom as predicted by Quantum Chromodynamics [10, 28].

1.4 Determination of $|V_{us}|$

As Equation 1.3 shows, the amplitude of the flavor-changing us quark current is proportional to the CKM matrix element V_{us}. This is illustrated by the Feynman diagram for an $s \to u$ transition in Figure 1.2.

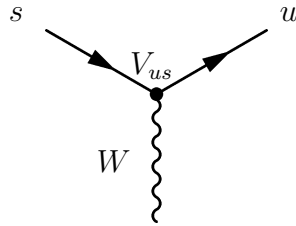**Figure 1.2:** Feynman diagram for a transition of an s quark into a u quark.

Thus, us quark currents can be used to measure $|V_{us}|$. Two methods are presented in the following sections. Firstly, the measurement of $|V_{us}|$ using semileptonic kaon decays is summarized. This is the basis for the actual world average of $|V_{us}|$ as listed in Reference [3]. Secondly, an independent method to determine $|V_{us}|$ from hadronic τ decays is outlined as presented in Reference [4]. Within this work, the second method is used to perform an updated determination of $|V_{us}|$ on the basis of the improved branching fractions of the modes $\tau^- \to K^- n\pi^0 \nu_\tau$, $n = 0, 1, 2, 3$, which are measured in this analysis.

1.4.1 Semileptonic kaon decays

Figure 1.3 shows the Feynman diagram for the semileptonic kaon decays $K^- \to \pi^0 \ell^- \overline{\nu}_\ell$ and $\overline{K}^0 \to \pi^+ \ell^- \overline{\nu}_\ell$ with $\ell = e, \mu$. The basis for the extraction of $|V_{us}|$ from semileptonic kaon decays, so called $K_{\ell 3}$ decays, $\overline{K} \to \pi \ell \overline{\nu}_\ell(\gamma)$, is the measurement of their partial decay widths

$$
\Gamma_{K_{\ell 3}} \equiv \Gamma(\overline{K} \to \pi \ell \overline{\nu}_\ell(\gamma)) \quad \text{with} \quad \ell = e, \mu \, .
\tag{1.47}
$$

Experimentally, the $\Gamma_{K_{\ell 3}}$ are obtained from a measurement of the branching fractions $\mathcal{B}_{K_{\ell 3}} \equiv \mathcal{B}(\overline{K} \to \pi \ell \overline{\nu}_\ell(\gamma))$ and the lifetimes of the corresponding kaons τ_K. The branching
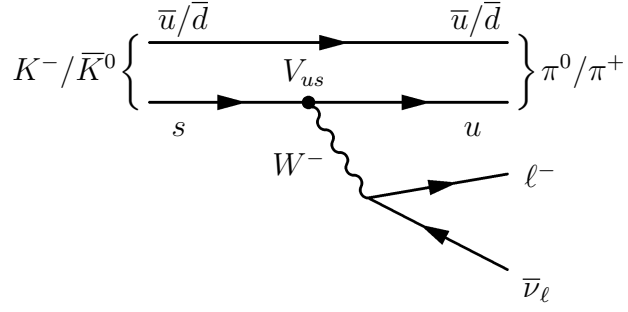
Figure 1.3: Feynman diagram of the semileptonic kaon decays $K^- \to \pi^0 \ell^- \overline{\nu}_\ell$ and $\overline{K}^0 \to \pi^+ \ell^- \overline{\nu}_\ell$ with $\ell = e, \mu$.

fraction is defined as $\mathcal{B}_i \equiv \Gamma_i / \Gamma$ (Equation 1.15), where Γ is the total decay width, $\Gamma = \hbar/\tau$.

Theoretically, the semileptonic decay widths can be calculated as follows [29]:

$$\Gamma_{K\ell 3} = \frac{G_F^2 m_K^2}{192\pi^3} C_K^2 S_{\mathrm{EW}} |V_{us}|^2 |f_+(0)|^2 I_{K\ell} \left(1 + \delta_K^{\mathrm{SU}(2)} + \delta_{K\ell}^{\mathrm{EM}}\right)^2 . \tag{1.48}$$

The symbol G_F denotes the Fermi constant, m_K is the relevant kaon mass, K denotes $K^0 \to \pi^\pm$ and $K^\pm \to \pi^0$ transitions, for which $C_K^2 = 1$ and $C_K^2 = 1/2$, respectively, and S_{EW} is the electroweak (short distance) radiative correction. The form factor $f_+(t)$ for a momentum transfer t to the $\ell\overline{\nu}_\ell$ system results from the fact that kaons and pions are not point-like particles but compound objects made from quarks and gluons. Traditionally, only the form factor $f_+(0) \equiv f_+^{K^0\pi^-}(0)$ for the transition $K^0 \to \pi^\pm$ and zero momentum transfer is explicitly used in Equation 1.48. Its momentum and mode dependence is absorbed into the correction factors $\delta_K^{\mathrm{SU}(2)}$ and $\delta_{K\ell}^{\mathrm{EM}}$, which are calculated using perturbation theory. More specifically, $\delta_K^{\mathrm{SU}(2)}$ are $\mathrm{SU}(2)$ breaking corrections that depend on the kaon species, $\delta_{K^0} = 0$, $\delta_{K^\pm} = \mathcal{O}(2.4)\,\%$. The long-distance electromagnetic corrections $\delta_{K\ell}^{\mathrm{EM}}$ depend on the meson charges and are approximately $\delta_{K^0\ell} = \mathcal{O}(0.6\,\%)$, $\delta_{K^\pm\ell} = \mathcal{O}(0.0\,\%)$. The symbol $I_{K\ell}$ denotes the phase space integral, which includes additional form factor corrections that are estimated from the experimental data.

Using Equation 1.48, the product $|f_+(0)V_{us}|$ can be obtained from a measurement of the semileptonic kaon decay widths $\Gamma_{K\ell 3}$. The world average of the different semileptonic kaon decays yields [3]

$$|f_+(0)V_{us}| = 0.21668 \pm 0.00045 \quad (0.21\,\%) , \tag{1.49}$$

where the last number is the relative uncertainty. The form factor $f_+(0)$, which is needed to extract $|V_{us}|$ from the experimental measurements of the combined quantity $|f_+(0)V_{us}|$, has to be calculated theoretically. The world average of $|V_{us}|$ as advocated by Reference [3] uses an older but still widely accepted calculation within the framework of Chiral Perturbation Theory [30]. It yields

$$f_+(0) = 0.961 \pm 0.008 \quad (0.83\,\%) . \tag{1.50}$$

The value of $|V_{us}|$ that is obtained from the measurement of Equation 1.49 with the help of this calculation is [3]

$$|V_{us}|_{K\ell 3} = 0.2255 \pm 0.0019 \quad (0.84\,\%) . \tag{1.51}$$

While recent lattice gauge theory calculations result in similar values for the form factor as Equation 1.50, a word of caution is appropriate [3, 31]. Recent evaluations on the basis of Chiral Perturbation Theory that include additional higher-order corrections yield results that deviate from Equation 1.50 by as much as 2%, giving relative uncertainties of around 1% [3, 29, 31]. For example, a recent update finds $f_+(0) = 0.974 \pm 0.012$, which implies a lower value of $|V_{us}| = 0.2225 \pm 0.0028$ [3, 31]. This fact and the relative uncertainties from the above given values of $|f_+(0)V_{us}|$, $f_+(0)$ and $|V_{us}|$ reveal a shortcoming of the measurement of $|V_{us}|$ using semileptonic kaon decays. At the current experimental precision reached for the measurements of the branching fractions of semileptonic kaon decays, all determinations of $|V_{us}|$ using this method are dominated by the theoretical uncertainty of the form factor calculation.

1.4.2 Hadronic τ decays

Hadronic τ decays into final states with net strangeness also facilitate a measurement of $|V_{us}|$. It is completely independent of the one using semileptonic kaon decays and thus allows an important cross check of the latter method. Figure 1.4 displays the Feynman diagrams of hadronic τ decays on quark level $\tau^- \to \overline{u}s\nu_\tau/\overline{u}d\nu_\tau$ and the corresponding fully leptonic τ decays $\tau^- \to \ell^-\overline{\nu}_\ell\nu_\tau$ with $\ell = e, \mu$.

(a) $\tau^- \to \overline{u}s\nu_\tau/\overline{u}d\nu_\tau$.

(b) $\tau^- \to \ell^-\overline{\nu}_\ell\nu_\tau$.
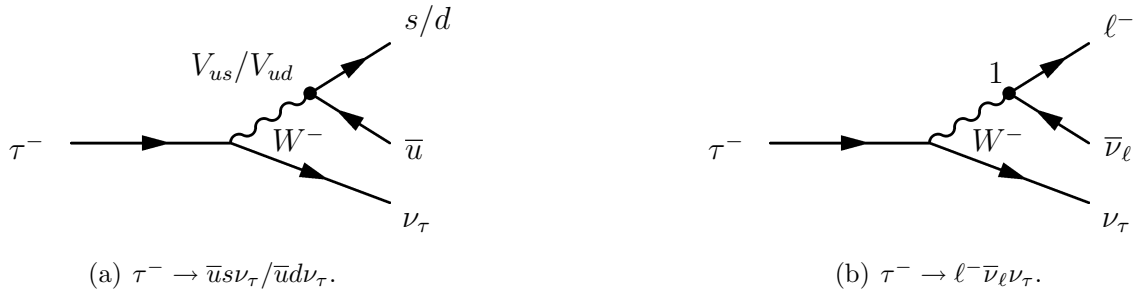
Figure 1.4: Feynman diagram of a hadronic τ decay with/without net strangeness $\tau^- \to \overline{u}s\nu_\tau/\overline{u}d\nu_\tau$ and its leptonic counterpart $\tau^- \to \ell^-\overline{\nu}_\ell\nu_\tau$ with $\ell = e, \mu$. The $\overline{u}s/\overline{u}d$ quark pair either builds only a kaon (pion) or hadronizes, e.g., into the final states $\pi^-/K^-n\pi^0$ with $n \geq 1$.

Figure 1.4(a) and Equation 1.39 show that the hadronic decay rate of the τ lepton into final states with net strangeness $R_{\tau,S}$ is directly proportional to $|V_{us}|^2$:

$$
\begin{aligned}
R_{\tau,S} &\equiv \frac{\Gamma(\tau^- \to X_S^-\nu_\tau)}{\Gamma(\tau^- \to e^-\overline{\nu}_e\nu_\tau)} \equiv \frac{\Gamma(\tau^- \to \overline{u}s\nu_\tau)}{\Gamma(\tau^- \to e^-\overline{\nu}_e\nu_\tau)} \\
&= 3\,|V_{us}|^2\,S_{\text{EW}} \left\{ 1 + \delta^{(0)} + \delta'_{\text{EW}} + \sum_{D \geq 2} \delta_{us}^{(D)} \right\},
\end{aligned}
\qquad (1.52)
$$

where the higher order corrections $\delta_{us}^{(D)}$ depend on the strange-quark mass m_s, $\delta_{us}^{(D)} = \delta_{us}^{(D)}(m_s)$.

The value of $R_{\tau,\mathrm{S}}$ can be calculated as a function of $|V_{us}|$ as outlined in Section 1.3 using perturbative QCD and phenomenological parametrizations. Thus, in principle, a measurement of $R_{\tau,\mathrm{S}}$ as summarized in Section 1.2.3 allows a determination of $|V_{us}|$ on the basis of Equation 1.52. Due to its inclusiveness, i.e., the summation over all hadronic final states, $R_{\tau,\mathrm{S}}$ does not depend on hadronic form factors—in contrast to the semileptonic kaon decay width. Only the production of the $\overline{u}s$ quark pair enters into the calculation and although the rates of the individual exclusive hadronic final states do contain form factors, they cancel in the inclusive sum of all final states with net strangeness [10]. Hence, hadronic τ decays allow a determination of $|V_{us}|$ that is completely independent of the measurement using semileptonic kaon decays.

However, a more precise determination of $|V_{us}|$ can be obtained from a measurement of the decay rates of the τ lepton both into final states without ($R_{\tau,\mathrm{NS}}$) and with ($R_{\tau,\mathrm{S}}$) net strangeness. This allows the determination of the *flavor*-$\mathrm{SU}_F(3)$ breaking difference between the CKM-normalized hadronic τ decay rates into final states without and with net strangeness [4, 5]:

$$\delta R_\tau \equiv \frac{R_{\tau,\mathrm{NS}}}{|V_{ud}|^2} - \frac{R_{\tau,\mathrm{S}}}{|V_{us}|^2} \, . \tag{1.53}$$

In the limit of flavor-$\mathrm{SU}_F(3)$ symmetry, i.e., in the limit of vanishing quark masses, this difference also vanishes. The breaking of the symmetry is mainly induced by the strange-quark mass m_s, which is much larger than the masses of the u and d quarks (Table 1.1). Thus, δR_τ basically is a function of the strange-quark mass [4, 5]:

$$\delta R_\tau = \delta R_\tau(m_s) \, . \tag{1.54}$$

It can be calculated theoretically in analogy to the terms $R_{\tau,\mathrm{S}}$ and $R_{\tau,\mathrm{NS}}$ [4, 5, 10]:

$$\delta R_\tau^{(\mathrm{theo})} = 3 S_{\mathrm{EW}} \sum_{D \geq 2} \left\{ \delta_{ud}^{(D)} - \delta_{us}^{(D)} \right\} \, . \tag{1.55}$$

Many theoretical uncertainties and especially the $D = 0$ perturbative correction $\delta^{(0)}$ cancel in this difference, allowing for a much increased precision of the calculation with respect to the ones of $R_{\tau,\mathrm{S}}$ and $R_{\tau,\mathrm{NS}}$. A QCD calculation yields [6]

$$\delta R_\tau^{(\mathrm{QCD})} = 0.227 \pm 0.054 \, , \tag{1.56}$$

where the strange-quark mass $m_s(2\,\mathrm{GeV}) = (96 \pm 10)\,\mathrm{MeV}/c^2$ from QCD sum rules and lattice QCD is the most crucial input. However, this calculation is plagued with the same convergence problems in the $J = 0$ longitudinal contribution as the calculations of $R_{\tau,\mathrm{S}}$ and $R_{\tau,\mathrm{NS}}$ (Section 1.3.1, [4, 5, 10]). Thus, the uncertainty of δR_τ is large and dominated by the longitudinal contribution $\delta R_\tau^{(\mathrm{QCD},J=0)}$ [6]:

$$\delta R_\tau^{(\mathrm{QCD},J=0)} = 0.166 \pm 0.051 \, . \tag{1.57}$$

Using a phenomenological approach for $\delta R_\tau^{(J=0)}$ as described in Section 1.3.1 results in the much more precise values [6] of

$$\begin{aligned} \delta R_\tau^{(\mathrm{pheno},J=0)} &= 0.1544 \pm 0.0037 \, , \\ \delta R_\tau^{(\mathrm{pheno})} &= 0.216 \pm 0.016 \, . \end{aligned} \tag{1.58}$$

Both are consistent with the pure QCD calculations but $\delta R_\tau^{(\text{pheno})}$ is 3.4 times more precise than its QCD counterpart. Hence, the phenomenologically improved value $\delta R_\tau^{(\text{pheno})}$ is used within this analysis.

The measurements of $R_{\tau,\text{S}}$, $R_{\tau,\text{NS}}$ and $|V_{ud}|$ can now be used to obtain $|V_{us}|$ from Equation 1.53:

$$|V_{us}| = \sqrt{\frac{R_{\tau,\text{S}}}{\frac{R_{\tau,\text{NS}}}{|V_{ud}|^2} - \delta R_\tau}} \ . \tag{1.59}$$

The values of the current world averages of $R_{\tau,\text{S}}$ and $R_{\tau,\text{NS}}$ from Equations 1.27 and 1.28 as well as the world average $|V_{ud}| = (0.97418 \pm 0.00027)$ [3] result in

$$
\begin{aligned}
|V_{us}| \quad &= \quad 0.2164 \pm 0.0005_{(\text{theo})} \pm 0.0031_{(\text{exp})} \\
&= \quad 0.2164 \pm 0.0031 \quad (1.45\,\%)\,, \\
|V_{us}|^{(\text{uni})} &= \quad 0.2176 \pm 0.0005_{(\text{theo})} \pm 0.0030_{(\text{exp})} \\
&= \quad 0.2176 \pm 0.0030 \quad (1.38\,\%)\,.
\end{aligned}
\tag{1.60}
$$

The first value uses the measured branching fraction for the mode $\tau^- \to K^- \nu_\tau$ while the second assumes the universality-improved value as described in Section 1.2.2. The values in brackets specify the relative uncertainties. Equation 1.60 shows that the theoretical uncertainty is much smaller than the experimental one—in contrast to the determination of $|V_{us}|$ from semileptonic kaon decays (Section 1.4.1) and despite the relative uncertainty of 7.5 % on δR_τ (Equation 1.58). This is due to the fact that δR_τ is only a small correction compared to $R_{\tau,\text{S}}/|V_{us}|^2$ and $R_{\tau,\text{NS}}/|V_{ud}|^2$ in Equation 1.59. Hence, the uncertainty of $|V_{us}|$ is dominated by the uncertainties of $R_{\tau,\text{S}}$ and $R_{\tau,\text{NS}}$. Both $R_{\tau,\text{S}}$ and $R_{\tau,\text{NS}}$ are determined from the branching fraction of the τ lepton into final states with net strangeness and the electronic τ branching fraction (Equation 1.27). Due to the precision of the latter (Equation 1.21), the uncertainty of $|V_{us}|$ as determined from hadronic τ decays is completely dominated by the branching fraction of the τ lepton into final states with net strangeness $\mathcal{B}_\text{S}$.

The uncertainty of $\mathcal{B}_\text{S}$ should be significantly reduced once the B factories BaBar and Belle measure all decay modes of the τ lepton into final states with net strangeness using their huge τ data samples (Section 2.3). A reduction of the uncertainty of $\mathcal{B}_\text{S}$ to 1 % would result in a relative uncertainty of $|V_{us}|$ of 0.6 % [6]. This corresponds to an improvement of a factor of 2.8 with respect to today's world average as listed in Table 1.4. It would make the determination from hadronic τ decays one of the most precise measurements of $|V_{us}|$ available. In addition, the measurement would be completely independent from other existing methods, e. g., semileptonic kaons decays.

Table 1.4 shows that the decay modes $\tau^- \to K^- n\pi^0 \nu_\tau$ with $n = 0, 1, 2, 3$ contribute a significant fraction to $\mathcal{B}_\text{S}$ and its uncertainty. Their measurement as performed in this analysis is an important step towards a reduction of the experimental uncertainties of $|V_{us}|$ as obtained from hadronic τ decays. Moreover, the measured and the universality-improved branching fraction of the mode $\tau^- \to K^- \nu_\tau$ deviate by approximately 1.3 standard deviations. Although this could very well be a statistical fluctuation, it will be enlightening to further investigate this feature by improving the experimental value of $\mathcal{B}(\tau^- \to K^- \nu_\tau)$.

Analogous to Equation 1.53, the flavor-$\mathrm{SU}_F(3)$ breaking difference of the non-strange and strange spectral moments (Equations 1.42 and 1.43) is defined as

$$\delta R_\tau^{kl} \equiv \frac{R_{\tau,\mathrm{NS}}^{kl}}{|V_{ud}|^2} - \frac{R_{\tau,\mathrm{S}}^{kl}}{|V_{us}|^2} \;. \tag{1.61}$$

It can be determined from the experimentally measured non-strange and strange spectral functions as provided, e. g., by the ALEPH and OPAL collaborations (Figure 1.1). The differences of the moments can also be calculated using the Operator Product Expansion analogous to Equation 1.55:

$$\delta R_\tau^{kl(\mathrm{theo})} = 3 S_{\mathrm{EW}} \sum_{D \geq 2} \left\{ \delta_{ud}^{kl(D)} - \delta_{us}^{kl(D)} \right\} \;. \tag{1.62}$$

Similar to δR_τ, they mainly depend on the strange-quark mass m_s. Thus, instead of using m_s as an input to calculate the moments δR_τ^{kl}, a fit of several moments δR_τ^{kl} to the experimentally measured corresponding non-strange and strange spectral moments $R_{\tau,\mathrm{NS}}^{kl}$ and $R_{\tau,\mathrm{S}}^{kl}$ allows—in principle—a simultaneous extraction of $|V_{us}|$ and m_s [4, 5].

However, a few caveats exist. Firstly, the experimentally measured moments of different orders k, l are highly correlated [10]. Secondly, independent determinations of m_s already provide a level of precision that is unlikely to be reached using τ decays [4, 5]. Thirdly—and most importantly—while the perturbative QCD series for $R_\tau \equiv R_\tau^{00}$ is reasonably well behaved at least in its $J = (1 + 0)$ part (Section 1.3.1), this is not the case for higher moments $k, l > 0$ [4, 5, 10]. These depend strongly on higher-order terms of the OPE which are less certain and induce large uncertainties. The results of the fits to several moments $k, l > 0$ show a strong dependence on the specific moments that are used [10]. This undermines the reliability of the method.

In consequence, until these *theoretical* problems are solved, the state-of-the-art and preferred, most precise method to extract $|V_{us}|$ from hadronic τ decays is the one using the 00-moment, i. e., the decay rate of the τ lepton into final states with net strangeness (Equation 1.59, [4, 5, 10]). This is the method that is used within this analysis.

1.4.3   Summary of current $|V_{us}|$ results

Figure 1.5 shows a summary of current determinations of $|V_{us}|$ as described in Sections 1.4.1 and 1.4.2 and References [3, 29, 31, 32]. *Unitarity* refers to the value obtained from the world averages of $|V_{ud}|$ and $|V_{ub}| = (4.31 \pm 0.30) \times 10^{-3}$ [3] by imposing unitarity

$$|V_{us}|^{(\mathrm{unitarity})} = \sqrt{1 - |V_{ud}|^2 - |V_{ub}|^2} = 0.2257 \pm 0.0012 \quad (0.52\,\%)\,. \tag{1.63}$$

The measurement of $\pi_{\ell 2}$ and $K_{\ell 2}$ decays $\pi^-/K^- \to \ell^- \overline{\nu}_\ell$ with $\ell = e, \mu$ allows the determination of $|V_{us}|^2/|V_{ud}|^2$. This can be converted into a measurement of $|V_{us}|$ using the world average of $|V_{ud}|$ [3, 32]. *Hyperon* decays, e. g., $\Lambda \to p\pi^-$ or $\Sigma^- \to n\pi^-$, facilitate a measurement of $|V_{us}|$ in analogy to the method using $K_{\ell 3}$ decays [31].

Similar to the extraction from semileptonic kaon decays, both methods also rely on form factors to extract $|V_{us}|$ from the measured branching fractions. Thus, all three results—$|V_{us}|$ from $K_{\ell 3}$, $K_{\ell 2}$ and hyperon decays—are dominated by the theoretical uncertainties of these calculations. As described in Section 1.4.2, the measurement
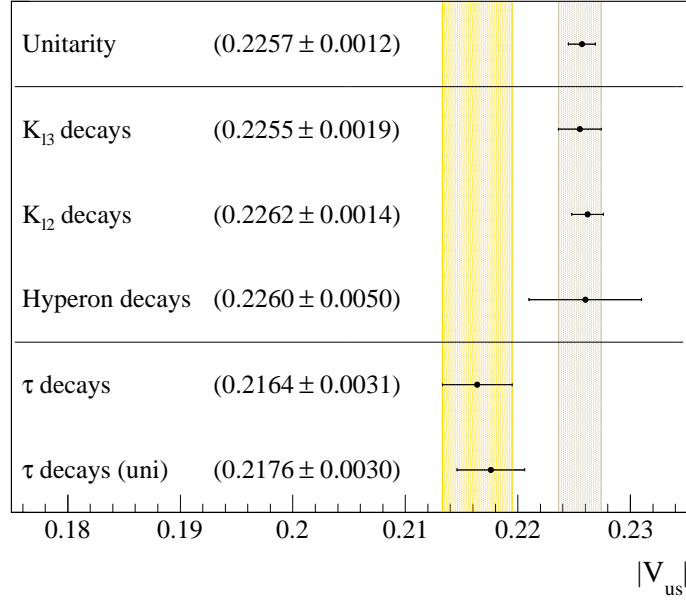
Figure 1.5: Summary of current measurements of $|V_{us}|$ [3]. *Unitarity* refers to the value obtained from the world averages of $|V_{ud}|$ and $|V_{ub}|$ by imposing unitarity (Equation 1.63). The measurement using $K_{\ell 3}$ *decays* is described in Section 1.4.1. *Hyperon* [31] and $K_{\ell 2}$ *decays* [32] provide similar methods to determine $|V_{us}|$. All three measurements are dominated by theoretical uncertainties [3, 31, 32]. The independent measurements using τ *decays* are described in Section 1.4.2 and summarized in Equation 1.60. The appendix *(uni)* denotes the method using the theoretically predicted branching fraction for the decay mode $\tau^- \to K^- \nu_\tau$ (Section 1.2.2). Both values are dominated by experimental uncertainties. The current world average [3] is marked by the grey band. The yellow band indicates the measurement from τ decays.

using hadronic τ decays is completely independent from these measurements. It is dominated by the experimental uncertainty of the branching fraction of the τ lepton into final states with net strangeness. It thus provides an excellent means to verify the theoretically dominated methods.

While the measurements from kaon and hyperon decays are all compatible with unitarity, the measurements from τ decays deviate from Equation 1.63 by 2.8 and 2.5 standard deviations respectively. This tendency was further enhanced by the recent measurements of the BABAR and Belle collaborations, which all yield smaller branching fractions than the averages of the LEP and CLEO measurements [7, 24, 25]. This resulted in a smaller value of $R_{\tau,S}$ and $|V_{us}|$ (Equation 1.59). In this context, it is particularly important to further enhance the precision of the measurements of τ decays into final states with net strangeness using the huge τ samples of the B factories. This will shed light onto the evolution of the observed deviation. Since it could also be caused by unobserved decay modes of the τ lepton, it is particularly important to precisely measure high-multiplicity final states, e.g., $\tau^- \to K^- \pi^0 \pi^0 \pi^0 \nu_\tau$. This thesis provides a contribution to all of these topics by the measurement of the branching fractions $\tau^- \to K^- n\pi^0 \nu_\tau$ with $n = 0, 1, 2, 3$ and the following extraction of $|V_{us}|$.

Chapter 2

The *BABAR* experiment

The BABAR experiment is located at the *Stanford Linear Accelerator Center* (SLAC) near San Francisco. It was operated from October 1999 until April 2008 by the Leland Stanford Junior University for the US Department of Energy. Its primary goal was the reconstruction of B meson decays and the precise measurement of CP violation in the B meson system. The B mesons are produced as $B\bar{B}$ pairs in e^+e^- collisions within the *Positron Electron Project* (PEP-II) collider facility. Due to the large cross section for the production of B meson pairs ($\sigma_{B\bar{B}} = 1.05$ nb, [33]), PEP-II is also called a *B factory* . However, the cross section for the production of $\tau^+\tau^-$ pairs is of similar size ($\sigma_{\tau\tau} = 0.919$ nb, [9]), thus PEP-II also is a τ *factory* . During its operating time, BABAR has recorded a data set of approximately 488×10^6 $\tau^+\tau^-$ pairs, of which 427×10^6 are used within this analysis.

This chapter briefly introduces the most important properties of the PEP-II collider (Section 2.1) and the BABAR detector (Section 2.2). A more detailed description may be found in References [8, 34]. The data set and the Monte Carlo simulated event samples that are used for the presented analysis are described in Section 2.3.

2.1   The PEP-II collider

The PEP-II facility is an asymmetric e^+e^- storage ring system, in which electrons with an energy of 9.0 GeV collide head-on with positrons with an energy of 3.1 GeV. The resulting center-of-mass energy is 10.58 GeV, which corresponds to the mass of the $\Upsilon(4S)$ resonance. This resonance decays into $B\bar{B}$ pairs with a probability of more than 96 % [3]. Due to the asymmetric energies of the colliding beams, the center-of-mass system is boosted with a factor $\beta\gamma = 0.56$ in the flight direction of the incoming electron beam. This facilitates the reconstruction of the decay vertices of the B mesons, which are needed to measure the relative decay length and the time dependence of the B decays.

Figure 2.1 [35] shows a schematic view of the accelerator facilities and the PEP-II ring system. Electrons and positrons are accelerated in the 3 km long *linear accelerator* (Linac). When they have reached their respective energies, they are injected into the two storage rings.[1] Both beams collide head-on in the interaction region, which is

---

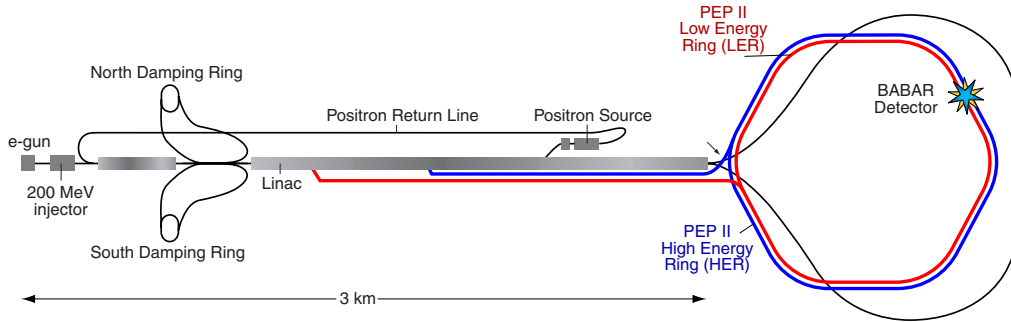[1]Because of the different energies, two storage rings are necessary.

Figure 2.1: Schematic view of the accelerator facilities and storage ring system of the PEP-II B and τ factory. The linear accelerator (Linac) is part of the Stanford Linear Collider (SLC). The BABAR detector is located around the interaction region in the upper right straight of the PEP-II hexagon. Image taken from Reference [35].

surrounded by the BABAR detector. To obtain the high rate of B mesons needed for the measurements of rare decay modes with branching fractions $\mathcal{B} \lesssim \mathcal{O}(10^{-6})$, a high luminosity is an essential prerequisite to the success of the BABAR physics program. During its operation, the original design luminosity of $3 \times 10^{33}\,\mathrm{cm}^{-2}\mathrm{s}^{-1}$ [8] has been surpassed by a factor of four, reaching a peak luminosity of $12 \times 10^{33}\,\mathrm{cm}^{-2}\mathrm{s}^{-1}$ [36].

2.2 The BABAR detector

Figure 2.2 [8] shows a schematic longitudinal section through the center of the BABAR detector. To account for the boost of the center-of-mass system, the detector is asymmetric with respect to the *forward* and *backward* directions. In this context, forward is defined as the flight direction of the incoming high energy electron beam. The detector components are arranged in a radially symmetric way around the beam axis.

The tracking system is closest to the beam pipe. It consists of the *silicon vertex tracker* (SVT), which directly surrounds the interaction point, and the *drift chamber* (DCH). They are in turn surrounded by the *Cherenkov detector* (DIRC), followed by the *electromagnetic calorimeter* (EMC). All these sub-systems are contained inside a superconducting coil, which provides a solenoidal magnetic field of 1.5 T. This facilitates the measurement of the momenta of charged particles with the tracking system. The *iron yoke* used to *return* the magnetic flux is instrumented with ionization detectors (IFR).

2.2.1 The silicon vertex tracker

In conjunction with the drift chamber, the silicon vertex tracker is used to detect charged particles and measure their momenta. In addition, both tracking devices are also used to measure the specific energy loss $\mathrm{d}E/\mathrm{d}x$ as a contribution to the identification of charged particles (Section 3.3). Figure 2.3 [8] shows a schematic longitudinal and transverse
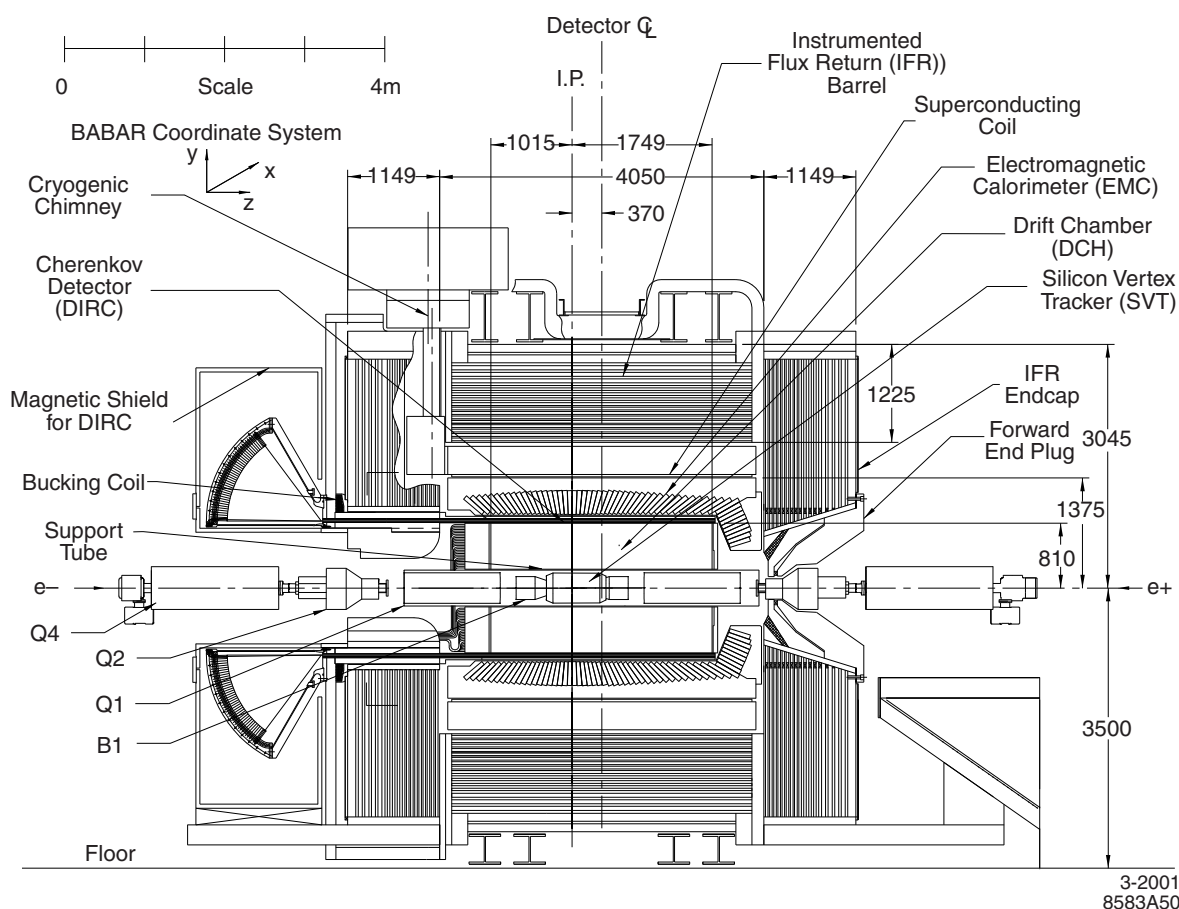
Figure 2.2: Schematic longitudinal section through the center of the *BaBar* detector. The high energy electrons (9.0 GeV) enter the detector from the left side, the low energy positrons (3.1 GeV) from the right. Thus, the center-of-mass system is boosted to the right side of the drawing. The interaction point is marked as I.P. and C_L denotes the geometric center of the *BaBar* detector, The most important components are—from the center outwards—the silicon vertex tracker, the drift chamber, the Cherenkov detector, the electromagnetic calorimeter and the instrumented flux return. The symbols Q1/2/4 and B1 denote pairs of quadrupole and dipole magnets respectively. All dimensions are given in mm unless noted otherwise. Image taken from Reference [8].

cross-section of the SVT and its arrangement around the beam pipe. The sub-detector consists of five cylindrical layers of double-sided silicon strip detectors. The outer side of each layer has strips parallel to the z-direction to allow a precise measurement of the azimuthal angle ϕ. In contrast, the strips of the inner sides are aligned perpendicular to the outer ones and thus measure the z-coordinate. The SVT covers a polar angular range of 20.1° to 150.2° [8].

As indicated by its name, the silicon vertex tracker is specifically optimized for the reconstruction of the primary and secondary decay vertices. To minimize the influence of multiple scattering on the vertex extrapolation, the innermost three layers are mounted as closely to the water-cooled beryllium beam pipe ($r \approx 27.8$ mm) as practically possible ($r_1 \approx 32$ mm). The outer two layers are located at much larger radii
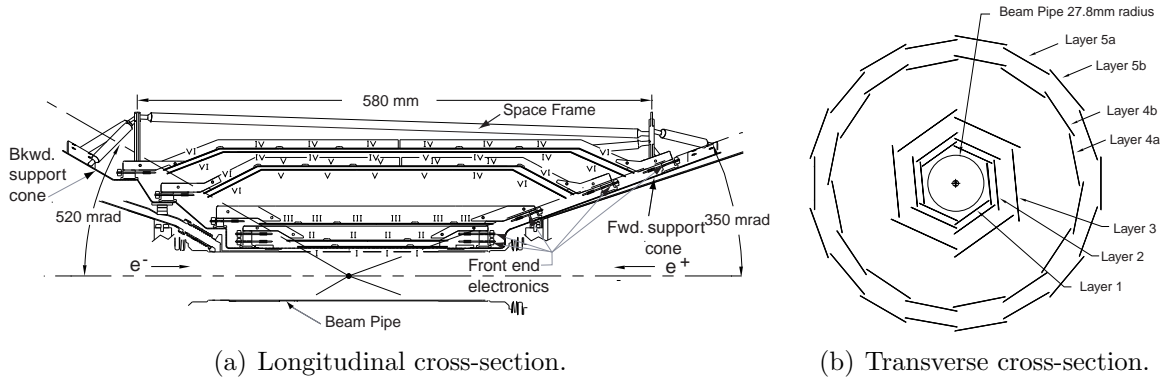
(a) Longitudinal cross-section.

(b) Transverse cross-section.

Figure 2.3: Schematic **(a)** longitudinal and **(b)** transverse cross-section of the silicon vertex tracker. The roman numerals label the six different types of sensors. The inner three layers are mounted as close to the beam pipe ($r \approx 27.8\,\text{mm}$) as possible ($r_1 \approx 32\,\text{mm}$), each consisting of six modules. The outer two layers are located at larger distances ($r_5 \approx 144\,\text{mm}$) and mainly link the SVT to the DCH tracks. They consist of 16 and 18 modules respectively. Images taken from Reference [8].

($r_5 \approx 144\,\text{mm}$) and are mainly used to link the SVT and DCH tracks. In total, the SVT provides an excellent vertex resolution of approximately $70\,\mu\text{m}$ for a fully reconstructed B meson decay [8]. This is one of the prerequisites to the successful measurements of the time-dependent CP asymmetries in B decays.

2.2.2   The drift chamber

The drift chamber provides a precise measurement of the transverse momentum of charged particles using the curvature of their trajectories in the magnetic field. Figure 2.4 [8, 35] shows a schematic longitudinal and transverse cross-section of the DCH. It is built as a multi-wire proportional chamber with an inner radius of $26.6\,\text{cm}$, an outer one of $80.9\,\text{cm}$ and a length of $280\,\text{cm}$. The volume is divided into 7104 hexagonal drift cells. The cells are arranged into ten super-layers of four layers each, thus providing up to 40 position and ionization loss measurements per trajectory. To allow position measurements along the beam axis, six super layers are *stereo layers* with alternating tilts of $\pm(45 - 76)\,\text{mrad}$. The remaining four super layers are *axial layers*. The arrangement of the layers in an alternating pattern (Figure 2.4(b)) guarantees an optimal spatial resolution. The mean resolution of a single position measurement is $125\,\mu\text{m}$ [8].

The measurement of $\mathrm{d}E/\mathrm{d}x$ in the tracking system allows a separation of pions and kaons up to momenta of $700\,\text{MeV}/c$ (Section 3.3.1, Figure 3.1(a)) in addition to the information provided by the Cherenkov detector. The resolution σ_{p_T} of the tracking system for the measurement of the transverse momentum p_T is [8]:

$$\frac{\sigma_{p_T}}{p_T} = (0.13 \pm 0.01)\,\% \cdot p_T\,[\,\text{GeV}/c\,] + (0.45 \pm 0.03)\,\% . \qquad (2.1)$$

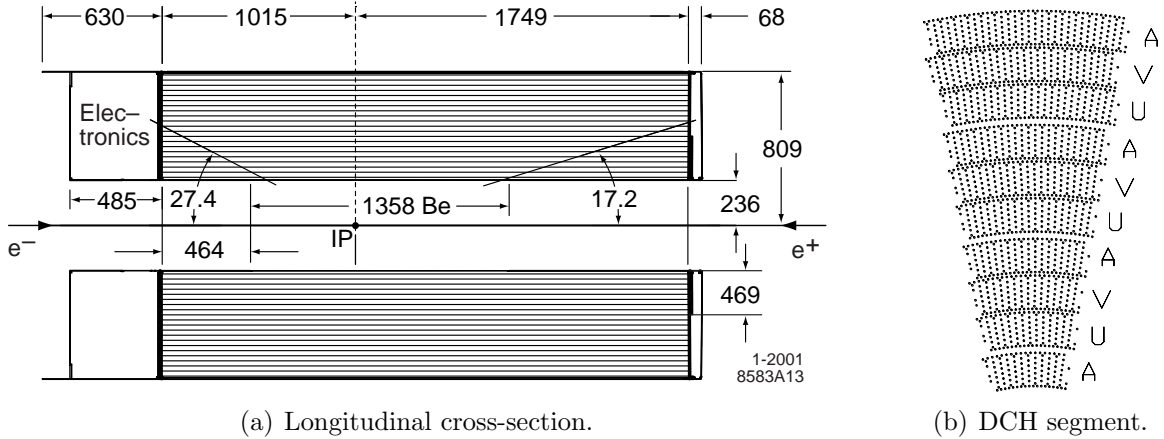(a) Longitudinal cross-section.

(b) DCH segment.

Figure 2.4: Schematic **(a)** longitudinal cross-section of the drift chamber and **(b)** transverse section of one of its segments. The interaction point—which is offset by 370 mm with respect to the geometrical center of the chamber—is marked as IP. The pattern of the axial (A) and stereo (U, V) layers is indicated in **(b)**. All dimensions are given in mm. Images taken from References [8, 35].

2.2.3 The Cherenkov detector

The Cherenkov detector is mainly used for the identification of charged particles, in particular the separation of pions and kaons. As the tracking system only provides reliable pion-kaon separation up to momenta of 700 MeV/c, this is crucial for many B analyses as well as the measurements described in this document (Sections 3.3, 4.2.2). The Cherenkov detector provides an excellent separation of pions and kaons of five standard deviations up to momenta of 2.5 GeV/c, which slowly decreases to an acceptable level of 2.5 standard deviations at 4 GeV/c [8].

To minimize the amount of material in front of the electromagnetic calorimeter and thus the reduction of its energy resolution, the Cherenkov device uses a novel design for ring-imaging Cherenkov detectors. It is designed as a *detector of internally reflected Cherenkov light* (DIRC). Only the active detector material is located between the drift chamber and the electromagnetic calorimeter, while all read-out devices are located in a *standoff box* at the rear end of the *BABAR* detector. Figure 2.5(a) [37] shows a schematic view of the construction. In total, the active detector material of the DIRC, which surrounds the drift chamber, consists of 144 bars of fused silica (quartz) with a refractive index of $n = 1.473$ [8]. The bars have a length of 4.9 m, a width of 35 mm and a thickness of 17 mm. The latter corresponds to approximately $0.17 - 0.30$ radiation lengths X_0, depending on the polar angle. Twelve bars are combined into a bar box and twelve boxes form the dodecagonal shape visible in Figure 2.5(a).

The working principle of the DIRC is illustrated in Figure 2.5(b) [35]. When a charged particle traverses the silica bars with a velocity $\beta = v/c \geq 1/n$, it emits Cherenkov light at an angle

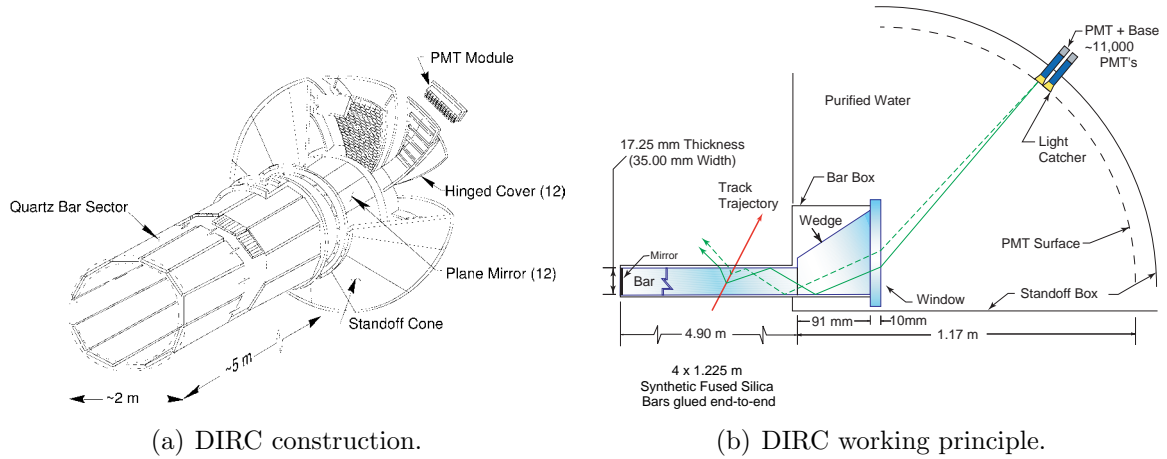$$\theta_\mathrm{C} = \frac{1}{n\beta} = \frac{\sqrt{1 + \frac{m^2 c^2}{p^2}}}{n} \, . \tag{2.2}$$

(a) DIRC construction.

(b) DIRC working principle.

Figure 2.5: **(a)** Schematic view and **(b)** working principle of the Cherenkov detector. The sketch in **(a)** shows the twelve boxes, each of which contains twelve quartz bars. It also indicates the water-filled standoff box, which is surrounded by 10572 photomultiplier tubes (PMTs). The mirrors in the standoff box are used to reflect the Cherenkov light towards the PMTs. The working principle in **(b)** is illustrated for a single quartz bar. The drawing displays the trajectory of a charged particle (red), which emits Cherenkov photons (green) inside the quartz bar (blue). The light is internally reflected and detected by the PMTs in the standoff box. Images taken from References [35, 37].

The symbol m denotes the particle's mass, p its momentum and c the velocity of light in vacuum. The position and the direction of the traversing particle as well as its momentum are measured using the tracking system. Thus, the measurement of θ_C allows the identification of the particle type. To reconstruct θ_C, the Cherenkov light is guided into the standoff box via total reflection in the quartz bars. The standoff box is filled with approximately 6000 liters of purified water. Its solenoidal surface is covered with 10572 photomultiplier tubes (PMTs), which are immersed directly into the water. Each PMT has a diameter of 29 mm and the average distance to the silica bars is 1.17 m. As reflection preserves the original emission angle, the detection of the Cherenkov photons with the PMTs allows the reconstruction of the Cherenkov angle θ_C. However, the reflections introduce discrete ambiguities in the reconstruction of the original direction of the light cone. These are resolved using additional information on the photon arrival times relative to the particle crossing as well as a sophisticated pattern recognition algorithm [8].

2.2.4 The electromagnetic calorimeter

The electromagnetic calorimeter is used to measure the energy, position and shape of electromagnetic showers. It also provides information on the energy deposits of traversing muons and hadrons. In conjunction with the tracking system, this facilitates the calculation of E/p, where E is the energy deposited in the calorimeter and p the momentum of the particle. Both the shower shape and E/p are used for the identification of charged particles (Section 3.3).

Figure 2.6 [8] displays a longitudinal cross-section of the upper half of the *BABAR* calorimeter. The EMC is designed as a scintillating crystal calorimeter. It consists
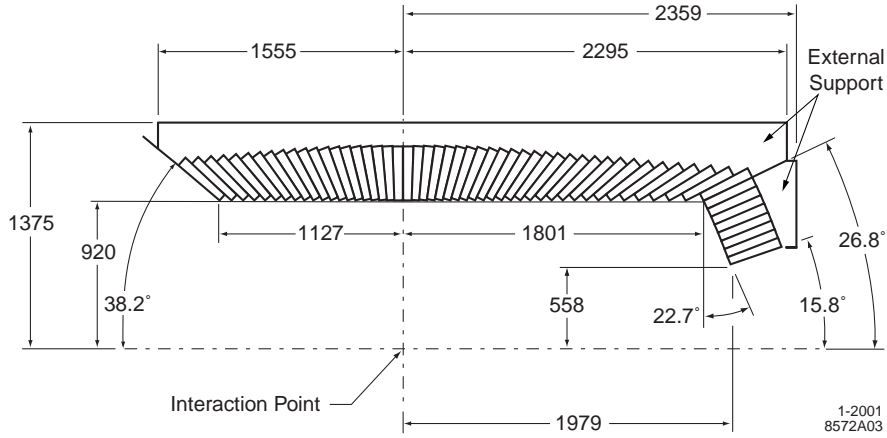

Figure 2.6: Schematic longitudinal cross-section of the upper half of the electromagnetic calorimeter. Due to the boost of the center-of-mass system, the arrangement of the crystals is asymmetric, consisting of a central barrel and a forward endcap. The detector is axially symmetric around the beam axis. Each of the 56 plotted crystals corresponds to an axially symmetric crystal ring. All dimensions are given in mm. Image taken from Reference [8].

of 6580 crystals of thallium-doped cesium iodide (CsI(Tl)). The material has been chosen partially due to its small Molière radius $R_{\mathrm{M}} \approx 3.8\,\mathrm{cm}$ and short radiation length $X_0 \approx 1.85\,\mathrm{cm}$ [8]. This allows for a compact design of the calorimeter while providing precise angular measurements and fully contained electromagnetic showers. The calorimeter consists of a central *barrel* with a length of $3\,\mathrm{m}$, an inner radius of $91\,\mathrm{cm}$ and an outer one of $136\,\mathrm{cm}$. Together with the conical *forward endcap*, it provides an angular coverage of $15.8 < \theta < 140.8°$. The length of the crystals varies between $29.8\,\mathrm{cm}$ ($16.1\,X_0$, backward barrel) and $32.6\,\mathrm{cm}$ ($17.6\,X_0$, endcap) [8]. The scintillation light is read out by two silicon photodiodes at the rear end of each crystal.

The excellent energy and angular resolutions σ_E and $\sigma_{\theta/\phi}$ can be parametrized by the empirical formulae [8]

$$\frac{\sigma_E}{E} = \frac{(2.32 \pm 0.30)\,\%}{\sqrt[4]{E\,[\,\mathrm{GeV}\,]}} \oplus (1.85 \pm 0.12)\,\%, \tag{2.3}$$

$$\sigma_\theta = \sigma_\phi = \left(\frac{3.87 \pm 0.07}{\sqrt{E\,[\,\mathrm{GeV}\,]}} + 0.00 \pm 0.04 \right)\,\mathrm{mrad}. \tag{2.4}$$

The symbol E denotes the energy measured in the calorimeter and θ and ϕ are the polar and azimuthal angles respectively.

2.2.5 The instrumented flux return

All sub-detector components described so far are located inside a solenoidal super-conducting coil. It creates a $1.5\,\mathrm{T}$ magnetic field, which is parallel to the beam axis.

The magnetic flux is *returned* using an *iron yoke*. Its components are displayed in Figure 2.7 [8]. They are arranged in a central barrel and two endcap sections, which
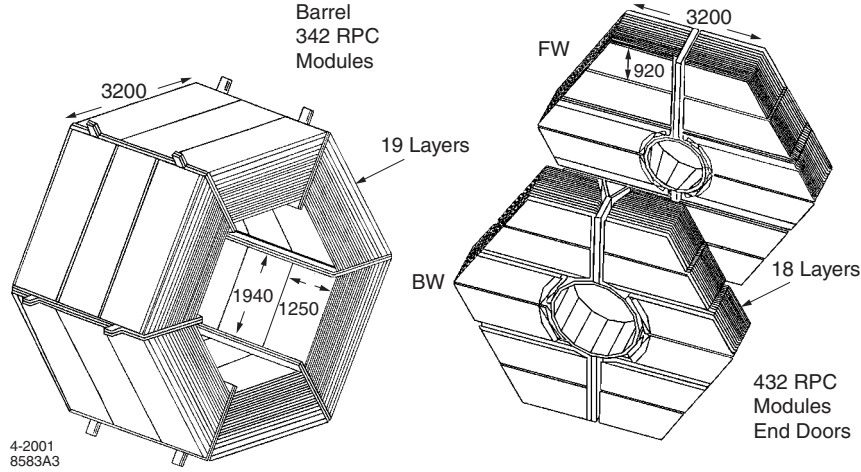

Figure 2.7: Schematic view of the instrumented flux return (IFR). The IFR is divided into a central barrel (left) and a forward and backward endcap (right). Each consists of 19 (18) layers of instrumented iron plates. During the operating time of the BABAR experiment, the original resistive plate chambers (RPCs) have been replaced with limited streamer tubes (LSTs). All dimensions are given in mm. Image taken from Reference [8].

are instrumented with 19 and 18 layers of ionization detectors between the iron plates, respectively. The *instrumented flux return* is used to detect and identify muons as well as neutral hadrons, e.g., K_L^0 mesons and neutrons. For this purpose, the thickness of the iron plates increases from 2 cm in the innermost plane to 10 cm in the outermost one. The originally installed *resistive plate chambers* (RPCs) have been replaced with *limited streamer tubes* (LSTs).

2.3   Data and Monte Carlo simulated event samples

This section introduces the data set and the Monte Carlo simulation used within this work.

2.3.1   Data

During its operating time from 1999 until 2008, the BABAR experiment has recorded an integrated luminosity of $531 \, \text{fb}^{-1}$ [38]. The majority of this data sample has been taken at a center-of-mass energy of $10.58 \, \text{GeV}$ corresponding to the $\Upsilon(4S)$ resonance (*On-Peak*). About $10\,\%$ of the data have been recorded at energies $40 \, \text{MeV}$ below the resonance (*Off-Peak*). This energy is below the threshold for $B\overline{B}$ production and the data are used to estimate backgrounds in $B\overline{B}$ analyses. The cross section for $\tau^+\tau^-$ production only changes by about $0.65\,\%$ between On-Peak and Off-Peak data [9, 39] and the kinematic properties of $\tau^+\tau^-$ events show no significant difference. In this analysis,

both On-Peak and Off-Peak data are used. The cross section difference is accounted for when scaling the Monte Carlo simulation to the data luminosity (Section 6.1). No further distinction is made between the two data samples.

The *BABAR* data sample is divided into seven *runs*. A run period is characterized by constant data taking conditions and lasts roughly one year. This analysis uses the *run I–VI* sub-sample of the *BABAR* data set. It was recorded in the years 1999–2007. Table 2.1 shows the integrated luminosity divided into run periods and On-Peak and Off-Peak samples. The given numbers for the integrated luminosities are obtained

Table 2.1: Integrated luminosities for the different run periods [40–43]. The luminosities are specified for the entire run period ($\mathcal{L}_{\sum}$) as well as separately for the On-Peak and Off-Peak fractions ($\mathcal{L}_{\text{On-Peak}}$, $\mathcal{L}_{\text{Off-Peak}}$).

Run period	$\mathcal{L}_{\sum}$ [fb^{-1}]	$\mathcal{L}_{\text{On-Peak}}$ [fb^{-1}]	$\mathcal{L}_{\text{Off-Peak}}$ [fb^{-1}]
run I	22.99 ± 0.22	20.37 ± 0.19	2.62 ± 0.02
run II	68.07 ± 0.64	61.15 ± 0.57	6.92 ± 0.07
run III	34.75 ± 0.33	32.28 ± 0.30	2.47 ± 0.02
run IV	108.56 ± 0.76	98.46 ± 0.69	10.10 ± 0.07
run V	146.6 ± 1.0	132.12 ± 0.92	14.49 ± 0.10
run VI	83.43 ± 0.58	76.16 ± 0.53	7.28 ± 0.05
run I–VI	464.4 ± 3.0	420.5 ± 2.7	43.87 ± 0.29

from the numbers of Bhabha, di-muon and two-photon events in the recorded data sample [42, 43]. The data sample analyzed within this work corresponds to an integrated luminosity of

$$\mathcal{L} = (464.4 \pm 3.0)\,\text{fb}^{-1}\,. \tag{2.5}$$

The uncertainty of the luminosity determination results from the uncertainties of the event reconstruction and selection as well as the dominant Bhabha cross section.

2.3.2 Monte Carlo simulation

Simulated events are produced using Monte Carlo methods. They are needed for the development of the event selection criteria, the calculation of the selection efficiencies and the estimation of background contributions (Section 6.2).

Reactions of the type $e^+e^- \rightarrow \tau^+\tau^-(\gamma)$ and $e^+e^- \rightarrow \mu^+\mu^-(\gamma)$ are generated with the program `kk2f` [44], where (γ) indicates a possible initial or final state photon. The decays of the τ lepton are described using the `TAUOLA` library [45]. To calculate the decays, `TAUOLA` uses the world averages of the measured branching fractions as of 2002 [46]. In the framework of this analysis, the branching fractions of all τ decay modes with a single charged track in the final state are reweighted to the actual world averages [3]. The program `EvtGen` [47] is used to generate all processes $e^+e^- \rightarrow q\bar{q}$

with $q = u, d, s, c, b$. The detector simulation is based on the `GEANT4` package [48]. All simulated events are reconstructed and selected using the same tools as for data (Chapters 3, 4). Table 2.2 contains the cross sections and the numbers of generated events for the different run periods. Since the simulated data is generated and simulated

Table 2.2: Cross sections [9, 33] and numbers of Monte Carlo generated events for the different run periods. The events of the type $e^+e^- \to \tau^+\tau^-$ do not include the decay modes listed in Table 2.3 (see text).

$e^+e^- \to$		$\tau^+\tau^-$	$\mu^+\mu^-$	$u\bar{u}, d\bar{d}, s\bar{s}$	$c\bar{c}$	$b\bar{b}$
σ[nb]		0.919 ± 0.003	1.147 ± 0.004	2.09^{a}	1.30^{a}	1.05^{a}
run I	$[\times 10^6]$	20.4	17.6	47.2	58.9	74.2
run II	$[\times 10^6]$	55.6	69.2	130.9	168.8	206.6
run III	$[\times 10^6]$	28.0	17.4	54.5	84.0	100.3
run IV	$[\times 10^6]$	89.9	79.4	213.4	252.8	335.5
run V	$[\times 10^6]$	132.3	89.5	289.8	343.6	489.1
run VI	$[\times 10^6]$	56.4	73.9	127.9	156.9	203.2
run I–VI	$[\times 10^6]$	382.5	347.0	863.7	1065.1	1408.9

[a] No estimate of the cross section uncertainties exists for these reactions. Since they only constitute a minor background in this analysis (Section 4.8), the uncertainty of the measured branching fractions due to these cross sections is negligible.

in parallel to real data taking, each Monte Carlo simulated event corresponds to a specific set of detector and beam conditions. The fraction of events simulated for each set of conditions roughly equals the fraction of real data recorded under these circumstances.

The $\tau^+\tau^-$ event sample listed in Table 2.2 does not contain all τ decay modes. Channels with small branching fractions, $\mathcal{B} \lesssim 10^{-3}$, or large uncertainties, $\Delta\mathcal{B}/\mathcal{B} \gtrsim 40\,\%$, are not included. Some signal and important background modes are affected, e. g., decays of the type $\tau^- \to K^- n\pi^0 \nu_\tau$ with $n = 2, 3$ and $\tau^- \to \pi^-\pi^0\pi^0\pi^0\pi^0\nu_\tau$. They are generated as dedicated event samples listed in Table 2.3. In each case, one τ lepton always decays into the given decay channel, while the second τ decays into one of the modes of the general event sample of $\tau\tau$ reactions. For the signal decay modes, $\tau^- \to K^- n\pi^0 \nu_\tau$ with $n = 2, 3$ and $\tau^- \to \pi^-\pi^0\pi^0\pi^0\pi^0\nu_\tau$, the available simulated events correspond to $\mathcal{O}(10)$ times the integrated data luminosity.

Bhabha scattering, $e^+e^- \to e^+e^-$, constitutes a significant background in this analysis. Due to the large cross section of approximately $40\,\mathrm{nb}$ within the acceptance of the BABAR detector and its angular distribution, the resulting background contribution is hard to simulate. Therefore, no Monte Carlo simulation is used in this analysis to estimate background from Bhabha scattering. Instead, very strict precautions are taken to reject any residual $e^+e^- \to e^+e^-$ events in the data (Section 4.5).

Table 2.3: Branching fractions [3] and numbers of generated signal and background Monte Carlo simulated $\tau\tau$ events. Only the total event numbers for run I–VI are specified. The listed decay modes are not included in the $e^+e^- \to \tau^+\tau^-$ reactions from Table 2.2.

$\tau^- \to$	$\mathcal{B}\ [\times 10^{-4}]$	Generated Events $[\times 10^3]$
$K^-\pi^0\pi^0\nu_\tau$	5.8 ± 2.4	7653
$K^-\pi^0\pi^0\pi^0\nu_\tau$	3.7 ± 2.4	7543
$\pi^-\pi^0\pi^0\pi^0\pi^0\nu_\tau$	$11.2 \pm 5.1^{\text{a}}$	7273
$\pi^-\eta\pi^0\pi^0\nu_\tau$	1.5 ± 0.5	522
$K^-\eta\nu_\tau$	2.7 ± 0.6	513
$K^-\eta\pi^0\nu_\tau$	1.8 ± 0.9	548
$\pi^-\overline{K}^0\eta\nu_\tau$	2.2 ± 0.7	636

> ᵃ This is the actual world average [3] for $\mathcal{B}(\tau^- \to h^-\pi^0\pi^0\pi^0\pi^0\nu_\tau)$. No measurement exists for $\mathcal{B}(\tau^- \to \pi^-\pi^0\pi^0\pi^0\pi^0\nu_\tau)$. Since the decay mode $\tau^- \to \pi^-\pi^0\pi^0\pi^0\pi^0\nu_\tau$ is measured in this analysis, the number is neither needed nor used any further.

Chapter 3

Particle reconstruction and identification

This chapter introduces the particle reconstruction and identification methods that are provided by the B*A*B*AR* collaboration. It also describes the reconstruction and selection of neutral pions, which is specifically developed in the framework of this thesis.

This analysis uses the Monte Carlo simulation to develop the event selection and test the understanding of the selected data (Chapter 4). Simulated events are further used to estimate the amount of remaining background in the selected data sample and to calculate absolute selection efficiencies for the determination of the branching fractions (Chapter 6). Thus, the best possible agreement between data and Monte Carlo simulation is essential for this analysis. Any discrepancies lead to systematic errors in the measurement of the branching fractions. The agreement is discussed within this chapter focusing on corrections for simulated events due to the reconstruction and identification of charged particles. They are also provided by the B*A*B*AR* collaboration. Corrections due to the reconstruction of neutral pions are developed within this analysis and discussed in detail in Chapter 5.

3.1   Charged particle reconstruction

Charged particles are reconstructed using the tracking system of the B*A*B*AR* detector. It consists of two independent subsystems, the silicon vertex tracker and the drift chamber (Sections 2.2.1, 2.2.2). Both are contained inside the 1.5 T magnetic field. Charged particles in a magnetic field are constrained to a helix-shaped trajectory. When traversing the tracking system, a charged particle ionizes the detector material and—with a certain probability—deposits a measurable amount of energy at a defined position [49]. If the energy deposit is detected, the corresponding space point is called a *hit*. A sophisticated pattern recognition algorithm combines hits that belong to one helical trajectory. The helix parameters of these *tracks* are fitted with a Kalman filter [8, 33, 50, 51]. The filter includes, amongst other things, multiple scattering, inhomogeneities of the magnetic field and energy loss in the detector material.

On top of the basic reconstruction, the distance of closest approach of a track to the primary vertex is considered to select tracks that are relevant for the presented

analysis. All final state particles considered in this work are produced directly by
the τ decay or via very short-lived resonances, e.g., ρ^- or K^{*-}. Decay modes that
proceed via longer-lived intermediate resonances, e.g., K_S^0,[1] are not to be included into
the measurements. Since the average τ flight length at the PEP-II collider is around
$250\,\mu\text{m}$—in contrast to about $5\,\text{cm}$ for a 1-GeV K_S^0 meson—the distance of closest
approach of a track to the primary vertex in the xy-plane d_0 and along the z-axis z_0
are required to fulfill the following criteria [52]:

$$
\begin{aligned}
d_0 &< 1.5\,\text{cm}\,, \\
z_0 &< 2.5\,\text{cm}\,.
\end{aligned}
\tag{3.1}
$$

These criteria assure that the measured track is compatible with coming from the
interaction point. In addition to longer-lived intermediate resonances, they also reject
tracks originating from interactions with the detector material.

Intermediate K_S^0 resonances are further suppressed by explicit identification. The
selection algorithm is described in detail in Reference [52]. It is based on the decay
mode $K_S^0 \to \pi^+\pi^-$ and combines pairs of tracks. From these track pairs, K_S^0 candidates
are selected by considering, e.g., the invariant mass of the track pair, the distance of
closest approach of the two tracks and the distance of closest approach of the vertex of
the track pair to the primary vertex. Due to the average flight length of a K_S^0 meson, its
decay vertex can be separated from the primary vertex, as opposed to the τ decay vertex.
If a track pair is consistent with originating from a K_S^0 decay, the constituent tracks
are excluded from the list of charged particles that are considered in this analysis [52].

Similar to K_S^0 mesons, Λ baryons and photon conversions are identified using the
reactions $\Lambda \to p\pi^-$ and $\gamma \to e^+e^-$ [52]. The constituent tracks are also rejected and
ignored in the remainder of this analysis.

The reconstruction efficiency of the resulting tracks[2] [53] is

$$
\varepsilon_{\text{track}} = (93.34 \pm 0.24)\,\%
\tag{3.2}
$$

in data, independent of the particle's momentum. Differences between data and Monte
Carlo simulation and the efficiency measurement are discussed in Section 3.5.

3.2 Neutral particle reconstruction

Neutral particles, e.g., π^0 and K_L^0 mesons, are measured with the electromagnetic
calorimeter and the instrumented flux return (Sections 2.2.4, 2.2.5). When traversing
these detector parts, they deposit energy by means of electromagnetic or hadronic
showers [33, 49].

Energy deposits in adjacent calorimeter crystals are combined to *clusters*. Particles
that are close together, e.g., photons from high-energetic π^0 mesons, may deposit
their energy in contiguous crystals and produce one single cluster with two local
maxima. These maxima are used to split the cluster into two *bumps* [8, 33]. Each bump
corresponds to one particle. For clusters with one single maximum, bump and cluster

---

[1]$\tau(K_S^0) = (0.8935 \pm 0.0008) \times 10^{-10}\,\text{s}$ [3].
[2]In the $B\!A\!B\!A\!R$ analysis framework, these tracks are called `GoodTracksVeryLoose`.

are identical. Care needs to be taken when splitting clusters, since local maxima are also created by shower fluctuations. These spurious local maxima are called *split-offs*. Within electromagnetic showers, they are eliminated reliably using shower shape models and are thus not separated from the cluster. Due to the irregularity and the lack of accurate shower models, hadronic split-offs cannot be treated correctly [8, 33]. The implications for this analysis are discussed in Section 5.3.2.

To identify bumps in the calorimeter as originating from neutral particles, all tracks are extrapolated into the electromagnetic calorimeter. If the position of a calorimeter bump is consistent with the track direction, it is associated with the charged particle. All remaining bumps are considered as originating from neutral particles [8, 33]. To suppress electronic noise and background from beam-gas interactions, only calorimeter bumps with an energy of more than 30 MeV are retained as neutral particles.[3]

3.3 Charged particle identification

3.3.1 Measured quantities

Charged particles are primarily reconstructed in the tracking system (Section 3.1). Their momenta are measured using the curvature of their trajectories in the magnetic field. While muons and hadrons penetrate the instrumented flux return, electrons deposit their entire energy in the electromagnetic calorimeter. In addition, the specific energy loss dE/dx in the tracking system, the Cherenkov angle measured in the DIRC and the shower shape in the electromagnetic calorimeter depend on the particle type. These properties can be used to identify charged particles and are described shortly in the following sections.

Specific energy loss

For moderately relativistic charged particles other than electrons,[4] energy loss in matter is dominated by ionization and atomic excitation. The specific energy loss dE/dx is described by the Bethe-Bloch formula as detailed in Reference [3]. Figure 3.1(a) [54] displays the measured specific energy loss of different particle types in the *BABAR* drift chamber as a function of their momentum. It illustrates that the specific energy loss can be used to differentiate between the particle types at small momenta.

Cherenkov angle

A charged particle emits *Cherenkov light* if it traverses a medium faster than the local phase velocity of light [3, 49]. The angle of the Cherenkov radiation relative to the particle's flight direction θ_C in the DIRC is shown in Figure 3.1(b) [35] as a function of the laboratory momentum of the traversing particle. A measurement of θ_C allows a good separation of pions and kaons up to momenta above 4 GeV/c. This is very important

---

[3]In the *BABAR* analysis framework, these neutral particles are called `CalorNeutral` objects.

[4]Due to their low mass, the energy loss of electrons is dominated by bremsstrahlung at small energies already, $(dE/dx)_{\text{brems}} / (dE/dx)_{\text{ion}} \sim ZE/580 \,\text{MeV}$ [49].
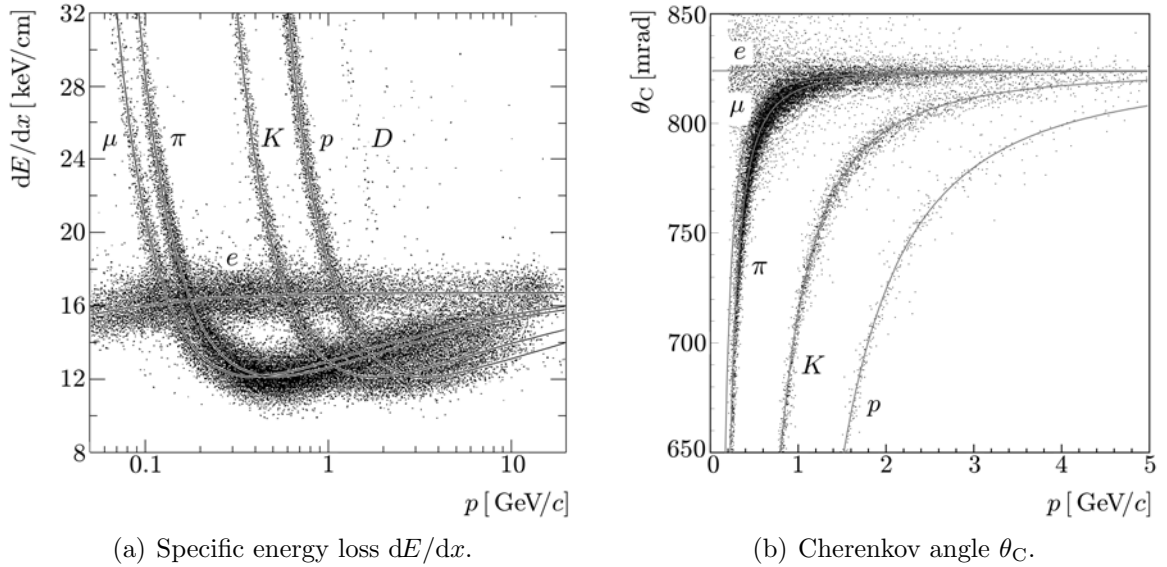
(a) Specific energy loss dE/dx.

(b) Cherenkov angle θ_{C}.

Figure 3.1: **(a)** Specific energy loss dE/dx in the *BABAR* drift chamber and **(b)** Cherenkov angle θ_{C} in the DIRC [55] as a function of the particle momentum p in the laboratory system, taken from References [35, 54].

for the discrimination of τ decay modes with net strangeness, $\tau^- \to K^- n\pi^0 \nu_\tau$, against the much more abundant decays $\tau^- \to \pi^- n\pi^0 \nu_\tau$ (Section 4.2).

Showers in the electromagnetic calorimeter

Electrons and photons produce electromagnetic showers and deposit most of their energy E in the calorimeter. A typical electromagnetic shower with an energy $E > 0.1\,\mathrm{GeV}$ has a size of more than five crystals. The electron momentum is measured with the tracking system. This facilitates the identification of electrons due to their energy-momentum ratio $E/p \approx 1$. In contrast, muons are minimum ionizing particles. They only lose a small amount of energy in isolated crystals [33, 56] ($E \approx 200\,\mathrm{MeV}$, $E/p \ll 1$). Hadrons may deposit a significant part of their energy in hadronic showers, which in some cases start already in the electromagnetic calorimeter. This leads to a significant tail in the distribution of $E/p \to 1$ and complicates the discrimination against electrons.

An additional criterion to separate hadrons from electrons is the size and shape of the calorimeter shower. Electromagnetically interacting particles deposit most of their energy in two to three crystals. Hadronic showers are less concentrated and exhibit larger energy deposits at larger distances from the bump center. A quantitative measure for the shower width is the *lateral moment LAT* [33], which is defined as

$$LAT \equiv \frac{\sum\limits_{i=3}^{N_{\mathrm{crystals}}} E_i r_i^2}{E_1 r_0^2 + E_2 r_0^2 + \sum\limits_{i=3}^{N_{\mathrm{crystals}}} E_i r_i^2} \in [0, 1]. \tag{3.3}$$

The summation includes all crystals belonging to the bump and the symbol E_i denotes

the energy deposited in crystal i, ordered such that $E_1 > E_2 > \cdots > E_{N_{\mathrm{crystals}}}$. The r_i are the distances of the crystals to the bump centroid and r_0 is the average distance between two crystals.[5] While the lateral moment is small for electromagnetic showers, it takes larger values for hadronic showers.

Showers in the instrumented flux return

In their interactions with the instrumented flux return, muons and hadrons differ with respect to the penetration depth and the transverse size of the cluster. As opposed to muons, pions and other hadrons produce extended showers. In consequence, the number of IFR layers hit and the amount of traversed material measured in hadronic interaction lengths is used to distinguish between the two particle types [33, 57].

3.3.2 Particle identification criteria

In this analysis, electrons, muons and kaons are identified. Pions are only selected as being "not kaons," i. e., they are required to fail the kaon selection criteria. The *BaBar* collaboration provides three types of particle identification algorithms [33, 58].

Cut-based methods impose a set of selection criteria on a charged particle. If the candidate passes these criteria, it is assumed to be of the tested particle type [33, 59].

Likelihood algorithms calculate a likelihood for a track to originate from a given particle type. The likelihood is based on measured quantities from different subdetectors. They are compared to the expectation values for the different particle hypotheses. A specific selection algorithm requires the likelihood to be above a certain value to assign the particle type to the track. Or else, it requests that the likelihood for a given hypothesis be larger than the ones for the other particle types [33, 56, 60].

Neural networks use a set of input variables from the *BaBar* subdetectors. They are trained to identify the wanted particle type and produce one single output variable. If the output for any particle hypothesis is larger than a preset value, this hypothesis is assigned to the charged particle [33, 57].

Electrons

This work uses a likelihood-based selection algorithm to identify electrons.[6] Input objects are tracks that have been matched to a calorimeter bump. The calculation of the likelihood [56] is based on the following quantities:

- The specific energy loss in the drift chamber,

- the number of Cherenkov photons associated with the track,

- the Cherenkov angle measured in the DIRC,

- the number of crystals in the calorimeter bump,

- the lateral moment in the calorimeter, LAT,

---

[5] At *BaBar*, $r_0 \approx 5\,\mathrm{cm}$ [33].

[6] In the *BaBar* analysis framework, this selection algorithm is called `PidLHElectrons`.

- the track-bump separation angle between the track intersection with the calorimeter front face and the bump centroid and

- E/p as measured with the calorimeter and the tracking system.

Figure 3.2(a) [58] shows the electron identification efficiency for data and Monte Carlo simulation as a function of the laboratory momentum. For data, it is approximately flat at 93 % over the entire momentum range from 0.5 to 5 GeV. The probability to misidentify a pion as an electron (pion-as-electron misidentification) is smaller than 0.1 % for all momenta (Figure 3.2(b)). Thus, the most abundant background in leptonic τ decays, $\tau^- \rightarrow \pi^- \nu_\tau$ decays,[7] is effectively eliminated. Figure 3.2(c) displays the corresponding kaon-as-electron misidentification. It is smaller than 0.4 % for momenta above 0.8 GeV. The peak of approximately 3 % at momenta $p \approx 0.6$ GeV is due to the intersection of the dE/dx curves for kaons and electrons (Figure 3.1(a)). At such low momenta, kaons do not produce Cherenkov light (Figure 3.1(b)) and the energy loss dE/dx is an important means to separate electrons from kaons. However, since most kaons in τ decays have momenta of $1 - 4$ GeV (Figure 4.14), the relatively large misidentification rate has no significant effect on the measurements of this analysis. The efficiency measurement and differences between the data and the Monte Carlo simulation are discussed in Section 3.5.
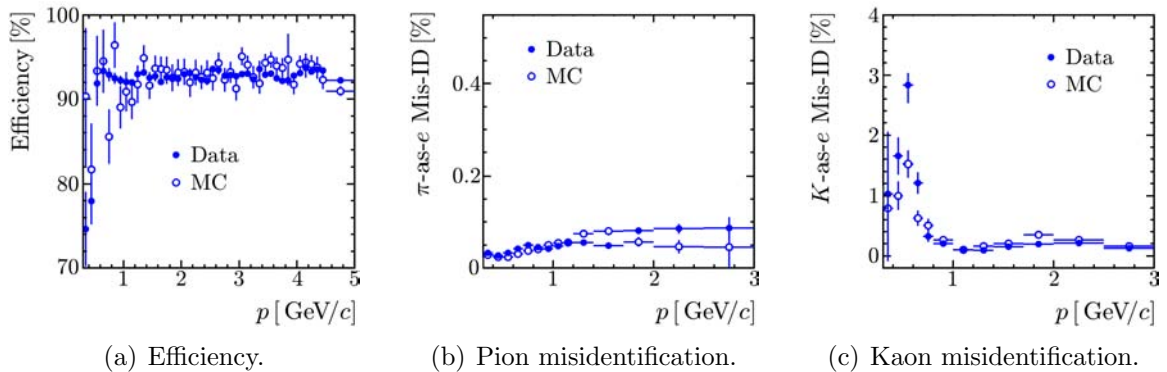

(a) Efficiency.   (b) Pion misidentification.   (c) Kaon misidentification.

Figure 3.2: (a) Efficiency, **(b)** pion-as-electron and **(c)** kaon-as-electron misidentification probability of the electron selection algorithm for data and Monte Carlo simulation as a function of the laboratory momentum p, taken from Reference [58].

In addition to the positive electron selection, this analysis uses electron identification to reject (veto) Bhabha scattering and events with two leptonic τ decays (Section 4.1). A cut-based selection algorithm is used for this purpose.[8] Its input variables [59] are

- the specific energy loss in the drift chamber,

- the number of crystals in the calorimeter bump,

- the lateral moment in the calorimeter, LAT, and

---

[7]$\mathcal{B}(\tau^- \rightarrow \pi^- \nu_\tau) = (10.83 \pm 0.11)\,\%$ versus $\mathcal{B}(\tau^- \rightarrow e^- \overline{\nu}_e \nu_\tau) = (17.82 \pm 0.05)\,\%$ [3].
[8]In the *BABAR* analysis framework, this selection algorithm is called `eMicroTight`.

- E/p as measured with the calorimeter and the tracking system.

Figure 3.3(a) [58] displays the identification efficiency of this algorithm for data and Monte Carlo simulation. Because of the looser selection criteria compared to the above described positive electron identification algorithm, the selection provides a larger efficiency of $97 - 98\,\%$ for all momenta present in electronic τ decays. This is necessary to reject the abundant Bhabha reactions $e^+e^- \to e^+e^-$, for which no suitable Monte Carlo simulation exists (Sections 2.3.2, 4.1).[9]
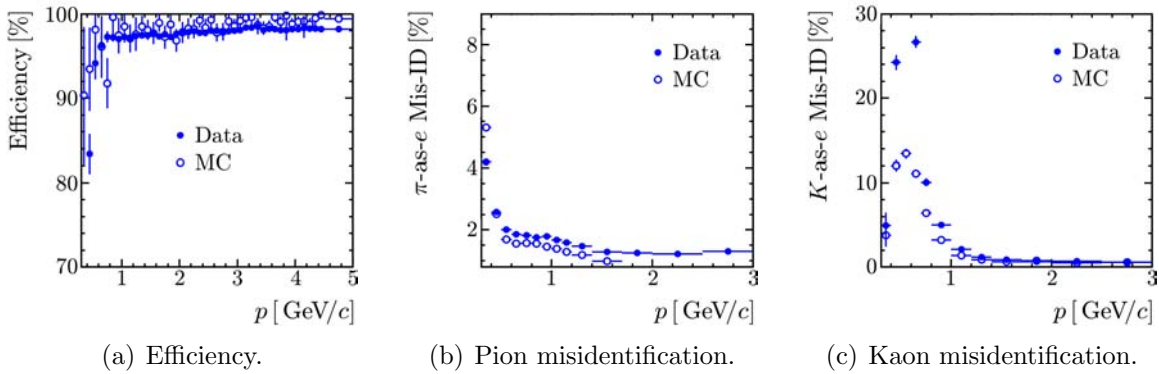

(a) Efficiency. (b) Pion misidentification. (c) Kaon misidentification.

Figure 3.3: **(a)** Efficiency, **(b)** pion-as-electron and **(c)** kaon-as-electron misidentification probability of the electron selection algorithm used as electron veto in this analysis. Both quantities are shown for data and Monte Carlo simulation as a function of the laboratory momentum p, taken from Reference [58].

But the relatively loose selection criteria needed to obtain such a high efficiency cause an increased pion-as-electron and kaon-as-electron misidentification probability (Figures 3.3(b), 3.3(c)). The pion-as-electron misidentification is around $1.5\,\%$ for large momenta $p \gtrsim 1.4\,\mathrm{GeV}$ and increases to approximately $4 - 5\,\%$ at small momenta $p \approx 0.4\,\mathrm{GeV}$. As for the peak in the kaon misidentification described above, this is due to the intersection of the $\mathrm{d}E/\mathrm{d}x$ curves of pions and electrons at $p \approx 0.2\,\mathrm{GeV}$ (Figure 3.1(a)). Similarly, the kaon-as-electron misidentification rate is below $1\,\%$ for momenta above $1.2\,\mathrm{GeV}$ and exhibits a peak at low momenta, $p \approx 0.6\,\mathrm{GeV}$. Due to the looser selection criteria, it reaches a value of approximately $25\,\%$. Since most kaons in τ decays have momenta of $1 - 4\,\mathrm{GeV}$ (Figure 4.14), the loss in kaon identification efficiency is tolerable considering the effective rejection of Bhabha scattering.

In addition to the relatively large absolute values, the misidentification rates differ by a factor of two between data and Monte Carlo simulation. This is amended by efficiency corrections for the Monte Carlo simulation. Their determination and application are discussed in Section 3.5.

---

[9]The effective production cross section at PEP-II within the acceptance of the $B\textsc{a}B\textsc{ar}$ detector is $\sigma_{ee \to ee} \approx 40\,\mathrm{nb}$ [33] compared to the total production cross section $\sigma_{ee \to \tau\tau} = (0.919 \pm 0.003)\,\mathrm{nb}$ [9].

Muons

Muons are identified using a neural network selection algorithm.[10] The calculation of
the network output [57] is based on the following input variables:

- The amount of energy deposited in the calorimeter,

- the distance traveled in the BABAR detector measured in hadronic interaction
  lengths,

- the average multiplicity of hits per IFR detector layer, as well as its standard
  deviation,

- the fit probability of the track hypothesis in the instrumented flux return and

- the fit probability of the IFR track with respect to the track extrapolation from
  the tracking system.

The performance of the muon identification is shown in Figure 3.4 [58] for data and
Monte Carlo simulation. For momenta above 1.5 GeV, the selection efficiency in data is
approximately constant at 70 %. The IFR is a key component in muon identification [33,
57] and this relatively low efficiency value is caused by the degradation of the performance
of the resistive plate chambers that instrument the flux return (Section 2.2.5). For
momenta below 1.5 GeV the efficiency decreases rapidly as the muons do not reach
the IFR chambers due to the detector material in front of it. The pion-as-muon
misidentification probability is smaller than 1.5 % over the entire momentum range up
to 5 GeV. Similarly, the kaon-as-muon misidentification is below 1 % for all momenta.
Due to the missing hadronic calorimeter in the BABAR detector, a better muon-pion
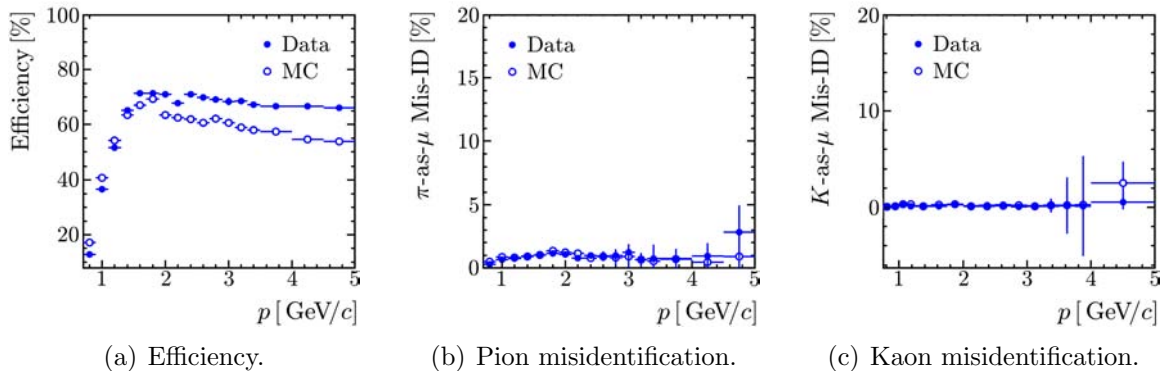and muon-kaon separation is not feasible.

(a) Efficiency.   (b) Pion misidentification.   (c) Kaon misidentification.

Figure 3.4: (a) Efficiency, **(b)** pion-as-muon and **(c)** kaon-as-muon misidentification
probability of the muon selection algorithm as a function of the laboratory momentum p,
taken from Reference [58].

While the electron efficiency is reasonably well described by the Monte Carlo
simulation, the muon efficiency shows a discrepancy of up to 20 % at large momenta.

---

[10]In the BABAR analysis framework, this selection algorithm is called `muNNTight`.

This is caused by the above degradation of the resistive plate chambers, which varies significantly with time and the position in the detector [61] and is hard to simulate. Again, corrections are used to compensate for the differences (Section 3.5).

Kaons

A likelihood-based selection algorithm is used to identify kaons.[11] The determination of the likelihood [60] is based on

- the specific energy loss in the tracking system,

- the number of Cherenkov photons contributing to the DIRC ring and

- the Cherenkov angle in the DIRC.

Due to their huge branching fractions, τ decays with pions instead of kaons are the most important backgrounds for decay modes into final states with net strangeness.[12] Thus, a small pion-as-kaon misidentification rate is crucial for this analysis. The kaon identification criteria used within this work are the tightest that are available in the *BABAR* analysis framework.

Figure 3.5 [58] shows the performance of the kaon identification for data and Monte Carlo simulation as a function of the laboratory momentum. At low momenta, $p \lesssim 600\,\text{MeV}$, kaons can be separated effectively from pions using dE/dx measurements (Figure 3.1(a)). This is reflected in the high efficiency ($\gtrsim 90\,\%$, Figure 3.5(a)) and the low pion-as-kaon misidentification rate ($< 1\,\%$, Figure 3.5(b)) in this region. Around $p \approx 700\,\text{MeV}$, both dE/dx- and DIRC-based methods are used for the kaon identification. Since neither of them provides a good separation in this region (Figure 3.1), harder selection criteria are required to keep the pion-as-kaon misidentification tolerable. Thus, the efficiency sharply drops below $70\,\%$. For momenta above $0.8\,\text{GeV}$, the kaon identification is based on the Cherenkov detector. This method provides a good kaon-pion separation up to $3\,\text{GeV}$ (Figure 3.1(b)) with an efficiency of $80 - 85\,\%$ and a pion-as-kaon misidentification of $1 - 1.5\,\%$. Above $3\,\text{GeV}$, the DIRC-based kaon-pion separation degrades quickly. Again, harder selection criteria result in a steep drop of the selection efficiency.

Pions

In this work, pions are identified as particles "not being kaons." The pion selection efficiency $\varepsilon_{\pi\text{-as-}\pi}$ and the kaon-as-pion misidentification rate $\varepsilon_{K\text{-as-}\pi}$ are given by

$$
\begin{aligned}
\varepsilon_{\pi\text{-as-}\pi} &= 1 - \varepsilon_{\pi\text{-as-}K}, \\
\varepsilon_{K\text{-as-}\pi} &= 1 - \varepsilon_{K\text{-as-}K}.
\end{aligned}
\tag{3.4}
$$

The symbol $\varepsilon_{\pi\text{-as-}K}$ denotes the pion-as-kaon misidentification rate and $\varepsilon_{K\text{-as-}K}$ is the efficiency of the kaon selection. From Figure 3.5, it follows that the pion selection efficiency is very high, $\varepsilon_{\pi\text{-as-}\pi} \approx 98 - 99\,\%$, due to the stringent kaon selection criteria.

---

[11]In the *BABAR* analysis framework, this selection algorithm is called `KMicroVeryTight`.
[12]E. g., $\mathcal{B}(\tau^- \to \pi^- \nu_\tau) = (10.83 \pm 0.11)\,\%$ versus $\mathcal{B}(\tau^- \to K^- \nu_\tau) = (6.85 \pm 0.23) \times 10^{-3}$ [3].

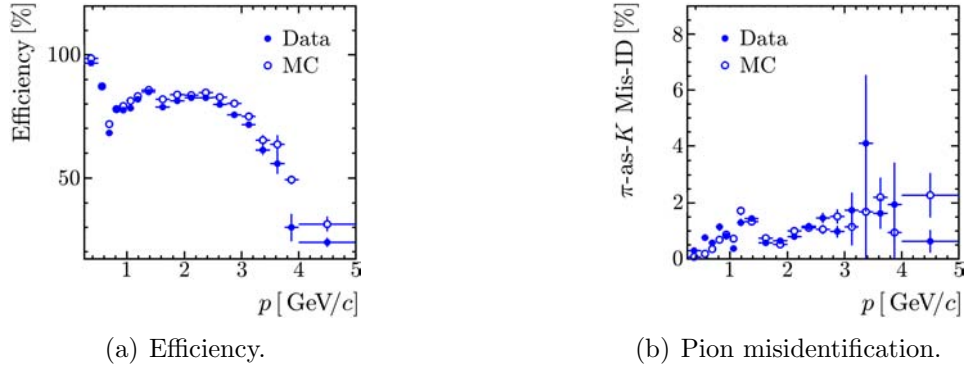(a) Efficiency.

(b) Pion misidentification.

Figure 3.5: (a) Efficiency and **(b)** pion-as-kaon misidentification probability of the kaon selection algorithm for data and Monte Carlo simulation as a function of the laboratory momentum p, taken from Reference [58].

However, these criteria also entail a large kaon-as-pion misidentification of $\varepsilon_{K\text{-as-}\pi} \approx 25 - 30\,\%$. This could be amended by using a looser kaon identification algorithm. But because of the huge ratio of the τ branching fractions into pions and kaons and the scope of this work to measure τ decays into final states with net strangeness, a clean kaon selection is more important than a high kaon reconstruction efficiency.

3.4 Neutral pion identification

Neutral pions are reconstructed in their dominant decay mode into two photons, $\mathcal{B}(\pi^0 \to \gamma\gamma) = (98.798 \pm 0.032)\,\%$ [3]. Two methods need to be considered.

Composite π^0 mesons are combined from photons that leave two separate signatures in the calorimeter, i.e., two neutral bumps as selected in Section 3.2. The properties of the π^0 mesons are obtained from the constituent photons.

In contrast, *merged* π^0 mesons are constructed from a single calorimeter object, e.g., a neutral cluster. Due to their small angular separation, photons from high-energetic π^0 mesons can produce one single cluster with one or two bumps in the calorimeter [33]. The π^0 is identified using cluster properties, e.g., the energy and the second moment[13] [62].

Since clusters with two bumps can be used both to reconstruct merged and—after being splitted (Section 3.2)—composite π^0 mesons, the two samples of π^0 mesons are not disjoint. However, due to the energy spectra of π^0 mesons in τ decays, the rate of merged π^0 mesons is small compared to the rate of composite π^0 mesons. About $7\,\%$ of all $\tau\tau$ events with a single π^0 meson contain a merged π^0. Due to the lower average π^0 energies, only $3\,\%$ of all two-π^0 final states contain a merged π^0 and the rate of events with two merged π^0 mesons is negligible.

In consequence, to reduce systematic effects, only composite π^0 mesons are considered within this analysis. The following sections describe the π^0 selection, which is designed

---

[13]The second moment S of a cluster is defined as $S \equiv 1/E \sum_i E_i \Delta\alpha_i^2$. The symbol E denotes the energy of the cluster, E_i are the energies of the constituent crystals and α_i their angular distance from the cluster centroid.

specifically for this analysis. Due to large background from spurious photons, e. g., in conjunction with a radiative Bhabha reaction, the selection variables are not shown at this stage of the analysis. Since Bhabha reactions and other QED background are not included in the Monte Carlo simulation (Section 2.3.2), no sensible comparison of data and simulated events is possible until the full event selection is performed (Chapter 4). The agreement between data and Monte Carlo simulation and systematic studies concerning the π^0 selection are discussed in Chapter 5.

3.4.1 Photon selection

A clean sample of photon candidates is needed to reconstruct composite π^0 mesons. It is obtained by additional selection criteria on top of the reconstruction of neutral calorimeter bumps as described in Section 3.2. To further eliminate calorimeter bumps from electronic noise or beam-gas interactions, the energy of photon candidates is required to be

$$E_\gamma > 0.075\,\text{GeV}\,. \tag{3.5}$$

A good measurement of the photon properties is assured by requiring that photon candidates are fully contained within the calorimeter. Only bumps whose centroid is separated by at least three crystal rings from the front or backward boundary of the calorimeter are accepted. Three crystal rings correspond to approximately four Molière radii of cesium iodide[14] (Section 2.2.4). Since 99 % of the energy of an electromagnetic shower are contained inside a cylinder with a radius of 3.5 Molière radii [3], the above requirement ensures full containment of all photon candidates considered in this analysis. It corresponds to an angular range of

$$0.37 < \theta_\gamma < 2.36\,\text{rad}\,, \tag{3.6}$$

where θ_γ is the polar angle of the photon.

To separate electromagnetic from hadronic bumps, the lateral moment (Equation 3.3) of the photon candidate is required to be (Section 3.3.1)

$$0.0 < LAT_\gamma < 0.8\,. \tag{3.7}$$

In the remaining part of this thesis, the term *photon* refers to neutral calorimeter bumps that fulfill the above selection criteria, unless explicitly mentioned otherwise. Their four-momenta are calculated using the energy and the direction of the calorimeter bump.

3.4.2 Neutral pion selection

Neutral pions are reconstructed by combining pairs of photons. The invariant mass of a photon pair is defined as

$$m_{\gamma\gamma} = \sqrt{p^\mu_{\gamma\gamma} p^{\gamma\gamma}_\mu}\,, \tag{3.8}$$

---

[14] $R_\text{M}(\text{CsI(Th)}) \approx 3.8\,\text{cm}$ [8]. The average distance between two crystals at $B\textsc{a}B\textsc{ar}$ is $r_0 \approx 5\,\text{cm}$ [33].

where $p^\mu_{\gamma\gamma} = p^\mu(\gamma_1) + p^\mu(\gamma_2)$ is the four-momentum of the π^0 candidate. It is calculated from the four-momenta of the two photons, $p^\mu(\gamma_1)$ and $p^\mu(\gamma_2)$. The invariant mass is required to be consistent with the π^0 mass, $m_{\pi^0} \approx 135\,\mathrm{MeV}/c^2$ [3]:

$$0.100 < m_{\gamma\gamma} < 0.160\,\mathrm{GeV}/c^2\,. \tag{3.9}$$

All resulting π^0 mesons are required to have an energy of

$$E_{\pi^0} = E_{\gamma_1} + E_{\gamma_2} > 0.200\,\mathrm{GeV} \tag{3.10}$$

to suppress spurious π^0 candidates made from two low-energy photons. In case two selected π^0 mesons share a common daughter photon, only one π^0 is kept. This removal of wrongly combined photon-photon pairs is essential for multi-π^0 final states. Otherwise, a sample of selected events containing n π^0 mesons would be dominated by *combinatorial background* (Section 5.2.1).

In order to decide which π^0 is kept, a kinematic fit is performed for each selected π^0 meson. Only the best fit of two π^0 mesons with a common daughter, i.e., the one with the smallest χ^2 of the kinematic fit, is kept. In the fit, the invariant photon-photon mass is constrained to the π^0 mass and the origin of the two photons is fixed to the primary vertex. Taking into account the average flight length of a τ lepton in the *BaBar* detector (Section 3.1), the average distance of the π^0 decay vertex from the primary vertex is around $250\,\mu\mathrm{m}$. This is in principle resolvable, given the excellent vertex resolution of the SVT of approximately $60\,\mu\mathrm{m}$ [8]. However, τ decays into final states containing one charged particle only—as considered in this analysis—do not allow the reconstruction of the τ decay vertex. Hence, the primary vertex is the best estimate of the τ decay vertex that is available.

The π^0 selection criteria are summarized in Table 3.1. Their efficiency and the description of the data by the Monte Carlo simulation are discussed in Chapter 5.

Table 3.1: Summary of the π^0 selection criteria. All quantities are calculated in the laboratory system.

Quantity	Selection criteria				
Photon energy			E_γ	$>$	$0.075\,\mathrm{GeV}$
Photon fiducial volume	0.37	$<$	θ_γ	$<$	$2.36\,\mathrm{rad}$
Photon lateral moment	0.0	$<$	LAT_γ	$<$	0.8
Invariant $\gamma\gamma$ mass	0.100	$<$	$m_{\gamma\gamma}$	$<$	$0.160\,\mathrm{GeV}/c^2$
π^0 energy			E_{π^0}	$>$	$0.200\,\mathrm{GeV}$

3.5 Efficiency corrections for simulated events

This work uses the Monte Carlo simulation to

- develop the event selection (Chapter 4),

- test the understanding of the selected data (Section 4.8),

- extract the π^0 efficiency correction for simulated events from any remaining differences with respect to the data in the precisely measured decay channel $\tau^- \to \pi^- \pi^0 \nu_\tau$ [3] (Chapter 5),

- estimate the amount of remaining background in the selected data sample (Chapter 6) and

- calculate absolute selection efficiencies for the determination of the branching fractions (Chapter 6).

Thus, the best possible agreement between data and Monte Carlo simulation is essential for this analysis. It is achieved by an independent determination of the tracking and charged particle identification efficiencies for data and simulated events. Any significant difference is amended by the application of corrections to the Monte Carlo simulation. Furthermore, it is crucial to obtain a thorough understanding of the systematic uncertainties resulting from efficiency differences between data and Monte Carlo simulation. They are also estimated from the efficiency studies.

3.5.1 Tracking efficiency correction

The tracking efficiency is determined in an independent study by the Charged Particles Reconstruction Working Group of the BaBar collaboration [53]. The study uses *Tau31* events, i.e., reactions of the type $e^+e^- \to \tau^+\tau^-$ in which one τ lepton decays into three charged hadrons, $\tau^- \to h^- h^+ h^- \nu_\tau$ with $h^- = \pi^-, K^-$, while the second one decays leptonically, $\tau^+ \to \ell^+ \nu_\ell \bar{\nu}_\tau$ with $\ell^+ = e^+, \mu^+$. Tau31 events are selected by requiring two charged particles that recoil against one isolated lepton. Due to charge conservation, the existence of one additional hadronic track can be inferred. This allows the determination of the track reconstruction efficiency (Equation 3.2). The ratio of the tracking efficiency in data $\varepsilon_{\text{track}}^{\text{data}}$ and Monte Carlo simulation $\varepsilon_{\text{track}}^{\text{MC}}$ is [53]

$$\eta_{\text{track}} \equiv \frac{\varepsilon_{\text{track}}^{\text{data}}}{\varepsilon_{\text{track}}^{\text{MC}}} = (1.0000 \pm 0.0021) \tag{3.11}$$

per track, independent of the particle's momentum. Hence, no correction is applied to the Monte Carlo simulation.

3.5.2 Charged particle identification efficiency correction

The Charged Particles Identification Working Group of the BaBar collaboration provides efficiencies and misidentification probabilities for all available algorithms to select electrons, muons, pions, kaons and protons [63]. They are determined from *control samples* in data and Monte Carlo simulation. A control sample consists of events in which the charged particle types are known without using any selection algorithm, solely based on topological and kinematic properties. E.g., pions and kaons are selected

from D^{*+} decays, $D^{*+} \to D^0 \pi^+_{\mathrm{slow}}$ with $D^0 \to \pi^+ K^-$. The subscript *slow* indicates the low energy of the charged pion. In a first step, pairs of charged particles—the pion and kaon candidates—are combined to a D^0, e.g., based on their invariant mass. The resulting D^0 is added to the slow pion. If the combination is consistent with being a D^{*+}, i.e., if its invariant mass is consistent with the D^{*+} mass, the pion and kaon have been identified without using any particle identification algorithms. The charge of the slow pion indicates the charge of the pion to be selected.

Figures 3.2–3.5 show the efficiencies of the selection algorithms used in this analysis along with the misidentification probabilities of the most important backgrounds as a function of the particle's momentum. While the agreement between the efficiencies in data and Monte Carlo simulation is reasonable for electrons and kaons, large deviations exist in case of the misidentification rates of the electron selection algorithms and especially for the entire muon identification. The particle identification for simulated events needs to be corrected to the efficiency and misidentification probability determined for data. The corrections for the Monte Carlo simulation are also provided by the Charged Particles Identification Working Group for all selection algorithms as a function of the run period, the particle's momentum p and its position in the detector (θ, ϕ). For each identified or vetoed charged particle, a correction factor is extracted from a table and applied as a weight to the simulated event. In case of a positive selection, i.e., the particle is required to pass the selection algorithm, the correction factor is

$$\eta_{\mathrm{PID}} \equiv \frac{\varepsilon^{\mathrm{data}}_{\mathrm{PID}}}{\varepsilon^{\mathrm{MC}}_{\mathrm{PID}}} . \tag{3.12}$$

Depending on the true particle type, the $\varepsilon^{\mathrm{data}}_{\mathrm{PID}}$ and $\varepsilon^{\mathrm{MC}}_{\mathrm{PID}}$ are the efficiencies or misidentification probabilities for the specific selection algorithm in data and Monte Carlo simulation. For a veto, i.e., the particle must fail the selection criteria, a correction of

$$\eta^{\mathrm{veto}}_{\mathrm{PID}} \equiv \frac{1 - \varepsilon^{\mathrm{data}}_{\mathrm{PID}}}{1 - \varepsilon^{\mathrm{MC}}_{\mathrm{PID}}} \tag{3.13}$$

is applied. If a particle is selected in a region of phase space for which the control samples provide no information, the average of all remaining weights for this selection algorithm is used as correction factor within this analysis. No official recipe for these cases exists within the *BaBar* collaboration.

To obtain the best possible agreement, the corrections are applied for all selection algorithms used in this analysis. I.e., the (mis)identification correction (Equation 3.12) is used for electrons, muons, and kaons, while the veto correction (Equation 3.13) is applied for the electron veto and the pion selection. The overall weight to be applied to a Monte Carlo simulated event is the product of the single particle correction factors according to Equations 3.12 and 3.13:

$$\eta^{\mathrm{event}}_{\mathrm{PID}} = \eta_{e/\mu} \cdot \eta^{\mathrm{veto}}_e \cdot \eta_{K/\pi} . \tag{3.14}$$

In addition to the efficiencies, misidentification probabilities and correction factors, the control samples also provide estimates of their uncertainties [63]. In case of a particle outside their phase space, the root mean squared width of the remaining weights is used to estimate the uncertainty. The uncertainties of the correction factors are needed to calculate the uncertainty of the branching fractions resulting from the particle identification (Section 6.5).

Chapter 4

Event selection

In e^+e^- collisions, τ leptons are produced in pairs, $e^+e^- \to \tau^+\tau^-$. Figure 4.1 displays a schematic view of a $\tau^+\tau^-$ event in the (e^+e^-) center-of-mass system. Due to momentum conservation, the two τ leptons recoil in opposite directions. One τ lepton is shown to decay according to $\tau \to \pi/K\pi^0\pi^0\nu_\tau$, while the second τ decays leptonically, $\tau \to \ell\bar{\nu}_\ell\nu_\tau$ with $\ell = e, \mu$. Because of the boost of the τ leptons in the center-of-mass system,[1] the final states of the two τ decays are well separated from each other. The neutrinos escape undetected and the event signature thus consists of the final state particles from the hadronically decaying (signal) τ lepton, which recoil against a single isolated charged lepton from the second τ decay. The utilization of such a signature to identify $\tau\tau$ reactions is called *lepton tag*. It allows the selection of $\tau\tau$ events with high purity and is therefore used within this analysis. Furthermore, all final state particles except the tag lepton can be associated with the hadronic decay of the signal τ lepton.

In this work, all decays of the signal τ lepton in the modes $\tau^- \to K^- n\pi^0\nu_\tau$ with $n = 0, 1, 2, 3$ and $\tau^- \to \pi^- n\pi^0\nu_\tau$ with $n = 1, 2, 3, 4$ are analyzed. In the remainder of this chapter, an event that contains such a decay is called *signal event*. The branching fractions of the decays $\tau^- \to K^- n\pi^0\nu_\tau$ are measured simultaneously. They are needed for the extraction of $|V_{us}|$ (Section 1.4.2). Since the branching fractions of the modes $\tau^- \to \pi^- n\pi^0\nu_\tau$ with $n = 3, 4$ are not well known[2] and since they are a major background for $\tau^- \to K^- n\pi^0\nu_\tau$ decays with multiple π^0 mesons, their branching fractions are also determined in the simultaneous measurement. The precisely measured decay modes $\tau^- \to \pi^- n\pi^0\nu_\tau$ with $n = 1, 2$ are used to determine and verify corrections to simulated events due to different π^0 selection efficiencies in data and Monte Carlo simulation (Chapter 5).[3] Similar to the corrections for charged particle reconstruction and identification (Section 3.5), these corrections are needed as the Monte Carlo simulation is, amongst other things, used to estimate remaining background after the event selection and to determine absolute selection efficiencies. Because of irreducible backgrounds from QED reactions and leptonic τ decays, the well measured mode $\tau^- \to \pi^- \nu_\tau$ cannot be analyzed—at least as long as a lepton tag is used to select $\tau\tau$ reactions.[4]

---

[1] $\sqrt{s} = 10.58\,\mathrm{GeV}$, $m_\tau = (1.77690 \pm 0.00020)\,\mathrm{GeV}/c^2$ [3], $\beta\gamma = 2.42$.

[2] $\Delta\mathcal{B}/\mathcal{B}(\tau^- \to \pi^-\pi^0\pi^0\pi^0\nu_\tau) = 9.2\,\%$, $\Delta\mathcal{B}/\mathcal{B}(\tau^- \to h^-\pi^0\pi^0\pi^0\pi^0\nu_\tau) = 46\,\%$ [3].

[3] $\Delta\mathcal{B}/\mathcal{B}(\tau^- \to \pi^-\pi^0\nu_\tau) = 0.47\,\%$, $\Delta\mathcal{B}/\mathcal{B}(\tau^- \to \pi^-\pi^0\pi^0\nu_\tau) = 1.3\,\%$ [3].

[4] $\Delta\mathcal{B}/\mathcal{B}(\tau^- \to \pi^-\nu_\tau) = 1.0\,\%$ [3].
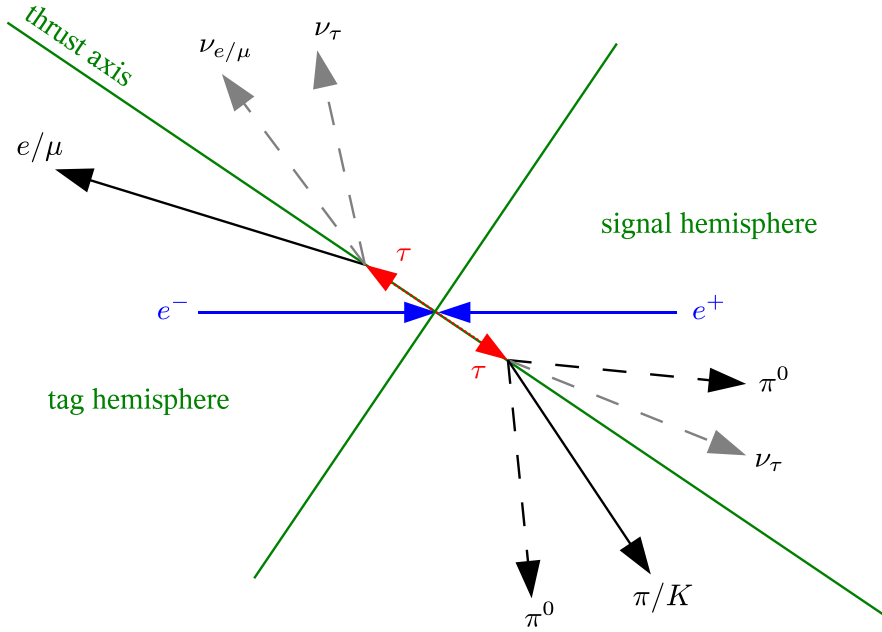
Figure 4.1: Schematic view of a reaction of the type $e^+e^- \rightarrow \tau(\rightarrow \ell\overline{\nu}_\ell\nu_\tau)\tau(\rightarrow \pi/K\pi^0\pi^0\nu_\tau)$ with $\ell = e, \mu$ in the center-of-mass system. Only the final state particles indicated in black are reconstructed either directly (charged particles, solid lines) or using their decay products (π^0 mesons, dashed lines). The event is divided into two hemispheres by a plane perpendicular to the thrust axis (Equation 4.2). Due to the boost of the τ leptons, the decay products of each τ are constrained to its respective hemisphere. Signal events (Equation 4.1) hence contain exactly one track in each hemisphere. According to the charged particle which the hemispheres contain, they are called *signal hemisphere* and *tag hemisphere*.

Due to the use of a lepton tag, the non-signal τ lepton in the event is only reconstructed in its fully leptonic decay modes, $\tau^+ \rightarrow \ell^+\nu_\ell\overline{\nu}_\tau$ with $\ell^+ = e^+, \mu^+$. Each signal event to be selected hence contains exactly two tracks, one from each τ lepton (Figure 4.1). As neutral pions are reconstructed in their dominant decay mode $\pi^0 \rightarrow \gamma\gamma$ (Section 3.4),[5] the full decay chain of such an event is:

$$
\begin{aligned}
\text{Signal decay}: \quad & \tau^- \rightarrow \pi^-/K^-\ n\pi^0\ \nu_\tau\,, \quad n = 1, 2, 3, 4\,/\,n = 0, 1, 2, 3 \\
& \quad\quad\quad\quad\quad\ \hookrightarrow\ \gamma\gamma \\
\text{Tag decay}: \quad & \tau^+ \rightarrow \ell^+\nu_\ell\overline{\nu}_\tau\,, \quad\quad\quad\quad \ell^+ = e^+, \mu^+
\end{aligned}
\tag{4.1}
$$

This chapter presents the selection of these events. It is performed in three steps. First, $e^+e^- \rightarrow \tau^+\tau^-$ reactions are selected from the *BABAR* data set. In a second step, events that contain a τ decay into any of the signal modes are selected. Finally, the remaining background is rejected. All steps are performed in parallel for data and Monte Carlo simulation. The truth information of the simulated events allows the development of the selection procedure. The selection criteria are summarized in Tables 4.2 and 4.3 and in Equation 4.27 at the end of this chapter.

---

[5]$\mathcal{B}(\pi^0 \rightarrow \gamma\gamma) = (98.798 \pm 0.032)\,\%$ [3].

4.1 Selection of $e^+e^- \to \tau^+\tau^-$ reactions

At the BABAR experiment, an e^+e^- interaction needs to pass a set of hardware and software trigger criteria in order to be recorded on disk. These criteria are designed to select reactions intended for analysis by the BABAR collaboration [64, 65]. The trigger criteria used in this analysis require a significant signal either in the drift chamber or in the calorimeter, e. g., a track with significant transverse momentum or a high-energetic cluster.

All events that pass the trigger system are classified by filter algorithms according to their topology and event category. One of the filter algorithms applied within this work is the τ filter. It is designed to select $\tau\tau$ events that contain one hadronic and one leptonic τ decay. Only events with two tracks and a total charge of zero are accepted. One of the tracks needs to have an energy-momentum ratio $E/p < 0.8$ in order to qualify for a hadronic particle (Section 3.3.1). In addition, the filter requires a significant transverse momentum and missing energy due to the undetected neutrinos in τ decays [66–68].

Since all trigger and filter criteria are superseeded by tighter selection criteria in this analysis, they are not described in detail here. The filter algorithms are mainly needed to reduce the total BABAR data sample of two petabytes to a manageable size of 1.7 terabytes. A full definition of the trigger and filter criteria may be found in References [64–68].

The following paragraphs describe the selection steps that are applied on top of the trigger and filter criteria in order to select $\tau\tau$ events. Possible backgrounds from reactions that do not contain a τ pair are:

$e^+e^- \to q\overline{q}$ with $q = u, d, s, c, b$. Due to the heavy quark masses and/or fragmentation and hadronization processes, these reactions produce a huge number of different final states. On average, these contain more charged and neutral particles than τ decays. They may however pass the selection criteria for τ decays into final states with several π^0 mesons.

$e^+e^- \to \ell^+\ell^-(\gamma)$ with $\ell = e, \mu$. These *di-lepton* events may be reconstructed as events of the type $e^+e^- \to \tau^+(\to \ell^+\nu_\ell\overline{\nu}_\tau)\tau^-(\to K^-\nu_\tau)$ if one lepton is misidentified as a kaon (Section 3.3.2).

$e^+e^- \to e^+e^-f\overline{f}$ with $f = $ fermions $= e, \mu, \pi$. These reactions may be selected as events of the type $e^+e^- \to \tau^+(\to \ell^+\nu_\ell\overline{\nu}_\tau)\tau^-(\to K^-\nu_\tau)$, e. g., if the electrons escape detection by staying inside the beam pipe, one fermion is identified as a lepton and the other one as a kaon.

Figure 4.2(a) shows a typical reconstructed Monte Carlo simulated $\tau\tau$ signal event containing a τ decay of the type $\tau^- \to K^-\pi^0\pi^0\pi^0\nu_\tau$. The second τ decays into a charged electron and two neutrinos. In contrast, Figure 4.2(b) displays a typical simulated background reaction of the type $e^+e^- \to B\overline{B}$. The two pictures illustrate the main steps in discriminating $e^+e^- \to \tau^+\tau^-$ events against this background.

Due to the low center-of-mass momentum of the heavy B mesons in $e^+e^- \to B\overline{B}$ events at the $\Upsilon(4S)$ resonance,[6] all final state particles are distributed isotropically.

---

[6] $\sqrt{s} = 10.58\,\text{GeV}$, $m_{B^0} = (5.2794 \pm 0.0005)\,\text{GeV}/c^2$, $m_{B^\pm} = (5.2790 \pm 0.0005)\,\text{GeV}/c^2$ [3].
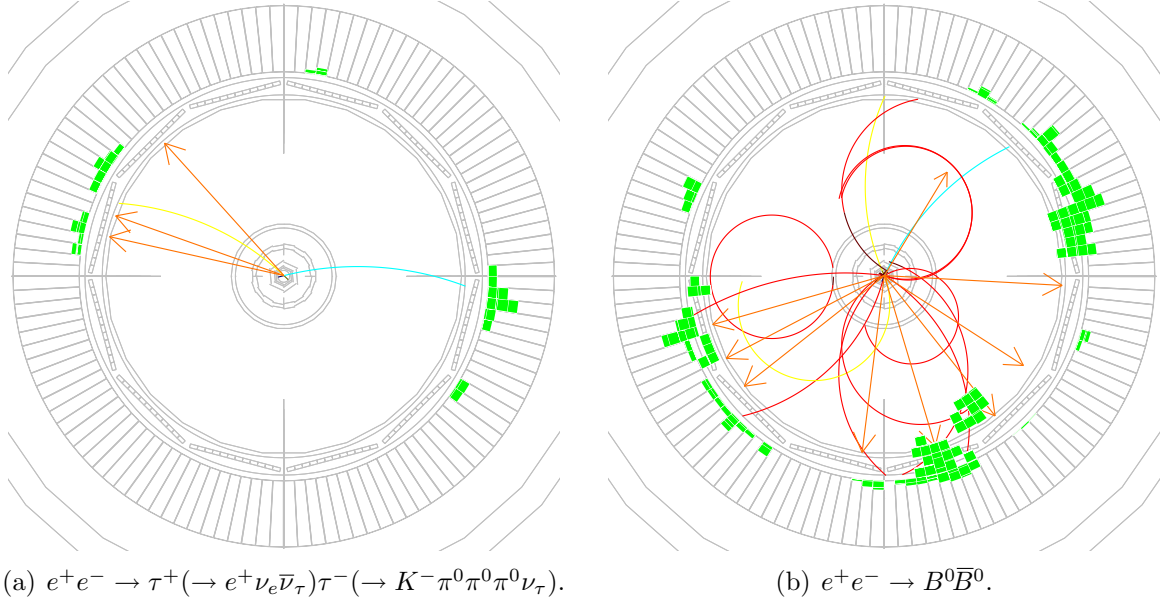
(a) $e^+e^- \to \tau^+(\to e^+\nu_e\overline{\nu}_\tau)\tau^-(\to K^-\pi^0\pi^0\pi^0\nu_\tau)$.   (b) $e^+e^- \to B^0\overline{B}^0$.

Figure 4.2: Display of an **(a)** $e^+e^- \to \tau^+(\to e^+\nu_e\overline{\nu}_\tau)\tau^-(\to K^-\pi^0\pi^0\pi^0\nu_\tau)$ signal and a **(b)** $e^+e^- \to B^0\overline{B}^0$ background event in a radial view of the *BABAR* detector (Section 2.2). Both images show Monte Carlo simulated reactions. From the center outwards, the detector sketch shows the layers of the vertex tracker, the volume of the drift chamber, the quartz bars of the Cherenkov detector and a crystal ring of the calorimeter. Reconstructed pion tracks are displayed in red. Kaons are shown in yellow and electrons in light blue. The amount of energy deposited in the calorimeter is marked in green and the orange arrows indicate the momentum direction of reconstructed π^0 mesons. Due to the low center-of-mass energies of the heavy B mesons, the final state particles in the $e^+e^- \to B^0\overline{B}^0$ event are distributed isotropically. In contrast, the $e^+e^- \to \tau^+\tau^-$ event exhibits a jet-like structure. In addition, the $B\overline{B}$ event contains more tracks than the $\tau\tau$ reaction.

In contrast, τ leptons have smaller masses[7] and large center-of-mass momenta. Their decay products are boosted and form a jet-like event structure (Figure 4.2(a)). This can be measured by the *thrust* variable T, which quantifies the maximal longitudinal projection of the center-of-mass momentum:

$$T \equiv \max_{\mathbf{n}_T} \left(\frac{\sum\limits_{i(\mathrm{FS})} |\mathbf{p}_i^{\mathrm{cms}} \cdot \mathbf{n}_T|}{\sum\limits_i |\mathbf{p}_i^{\mathrm{cms}}|} \right) \in [0.5, 1] \,. \tag{4.2}$$

The $\mathbf{p}_i^{\mathrm{cms}}$ are the center-of-mass momenta of all reconstructed final state particles (FS) and $\mathbf{n}_T$ is the *thrust axis*, i.e., the unit vector, which maximizes the sum of their longitudinal projections T. To calculate the thrust, all tracks and neutral particles as defined in Section 3.2 are used. Since longer-lived resonances like K_S^0 mesons and Λ baryons also contribute to the event balance, their daughters are added to the tracks in this specific case.

---

[7]$m_\tau = (1.77690 \pm 0.00020) \, \mathrm{GeV}/c^2$ [3].

Spherical $e^+e^- \to B\overline{B}$ events have low thrust values, while jet-like $e^+e^- \to \tau^+\tau^-$ events tend towards higher ones. To discriminate against $B\overline{B}$ events, the following selection criterion is applied:

$$T > 0.87 \, . \tag{4.3}$$

All thrust distributions are shown in Figures A.9 and A.10 (Appendix A).

The thrust axis can be used as an estimate of the $\tau\tau$ direction (Figure 4.1). An event can thus be divided into two *hemispheres* by a plane perpendicular to the thrust axis. Each hemisphere corresponds to one τ lepton. Due to the boost of the τ leptons, the decay products of each τ are constrained to its respective hemisphere. Figure 4.1 illustrates the definition for a $\tau\tau$ signal event. The hemisphere that contains the decay products of the signal τ decay is called *signal hemisphere*, while the one containing the leptonic τ decay is named *tag hemisphere*.

Figure 4.2 exemplifies that $e^+e^- \to B\overline{B}$ events contain on average more tracks than $e^+e^- \to \tau^+\tau^-$ events. Similarly, other $e^+e^- \to q\overline{q}$ reactions also contain on average more than two charged particles because of fragmentation and hadronization processes. In contrast, due to the lepton tag, signal events within this work comprehend exactly two tracks, one in each hemisphere (Figure 4.1). This is called a *1–1 topology*. All $q\overline{q}$ backgrounds are thus suppressed by requiring a reconstructed

$$1\text{--}1 \quad \text{topology} \, . \tag{4.4}$$

Because of charge conservation, an event always contains an even number of charged particles. At least two tracks have to be missed for a multi-track event to be reconstructed with a 1–1 topology. Considering the high track reconstruction efficiency (Section 3.1), the probability for this to happen is only $(1 - \varepsilon_{\text{track}})^2 \approx 0.4\,\%$. In consequence, the topological selection is a very effective criterion to reject $e^+e^- \to q\overline{q}$ decays. For the same reason, it also rejects most hadronic τ decays into final states that contain more than one charged particle.

Since the daughter tracks from the decay $K_S^0 \to \pi^+\pi^-$ are excluded from the charged particles considered in this analysis (Section 3.1), τ decays into final states with one charged particle and an additional K_S^0 decaying into two charged pions are sorted into the 1–1 topology. They need to be explicitly rejected by requiring that selected events contain no reconstructed K_S^0 candidates.

Similarly, the daughter tracks of photon conversions, $\gamma \to e^+e^-$, are also excluded from the list of tracks (Section 3.1). As their presence distorts the momentum distribution of the photon's mother particle, events containing photon conversions are explicitly rejected.

In summary, the following criteria are applied:

$$
\begin{aligned}
\text{Number of reconstructed K}_S^0 \qquad & N_{K_S^0} &=& \ 0 \, , \\
\text{Number of reconstructed photon conversions} \quad & N_{\text{conv}} &=& \ 0 \, .
\end{aligned}
\tag{4.5}
$$

The total event charge of a fully reconstructed event is zero, $Q \equiv q_1 + q_2 = 0$, where the q_i are the individual track charges. This is not necessarily the case for $e^+e^- \to q\overline{q}$ reactions. They mainly enter the 1–1 topology if several tracks escape detection. Thus, these events are further suppressed by requiring

$$\text{charge conservation} \quad Q = 0 \, . \tag{4.6}$$

To ensure a good particle identification (Sections 3.1, 3.3), both tracks are required to lie within the fiducial volume of the BABAR calorimeter and the Cherenkov detector (Section 2.2):

$$0.45 < \theta_{\text{track}} < 2.36 \, \text{rad} \, , \tag{4.7}$$

where θ_{track} is the polar angle of the considered track in the laboratory system. (Unless explicitly mentioned otherwise, all kinematic quantities within this chapter are calculated in the laboratory system.)

The leptonic τ decay is determined by requiring that at least one of the tracks passes the charged particle identification criteria for an electron or a muon. I. e., the number of reconstructed leptons ℓ in the event N_ℓ is required to fulfill

$$N_\ell \geq 1 \qquad \text{with } \ell = \text{e}, \mu \, . \tag{4.8}$$

Special care is taken if both tracks are identified as leptons.[8] The non-leptonic track is called *signal track*.

Radiative Bhabha reactions, $e^+e^- \to e^+e^-(\gamma)$, are suppressed by an *electron veto*. An event is rejected if the charged particle in the signal hemisphere passes the electron identification criteria. I. e., the number of identified electrons in the signal hemisphere N_{sig}^e is required to be

$$N_{\text{sig}}^e = 0 \, . \tag{4.9}$$

Since no appropriate Monte Carlo simulated event sample exists for Bhabha reactions (Section 2.3.2), it is particularly important to reject these events. Di-muon events are reasonably well described by the Monte Carlo simulation. Thus, because of the inefficiencies of the BABAR muon detectors and the corresponding muon selection (Section 3.3.2), no such veto is applied against events with a reconstructed muon on the signal side. They are rejected by the remaining selection criteria (Section 4.5).[9]

4.2   Selection of $\tau^- \to \pi^-/K^- n\pi^0 \nu_\tau$ decays

The event sample selected in Section 4.1 contains $\tau\tau$ events with the signal τ lepton decaying into one charged hadron and any number of additional neutral particles. Charged hadrons in τ decays are either pions and kaons or very short-lived resonances, e. g., ρ^- and K^{*-}. Other particles are excluded by the kinematic limit of the τ mass and by baryon number conservation. The resonances also decay into final states comprising pions and kaons [3]. Due to the short lifetime of the resonances, they cannot be measured directly. They can only be observed in the invariant mass spectra of their decay products. For the purpose of event reconstruction, the signal track thus is either a pion or a kaon. Neutral particles mainly comprise photons, π^0, K^0 and η mesons. The latter three are not detected directly but observed by means of their decay products (Section 3.4).

---

[8]If one track is identified as a muon and the other one as an electron, the muon is chosen as the tag lepton. If both tracks are identified as identical leptons, the negatively charged particle is considered as the tag lepton.

[9]Due to the selection of the muon as the tag lepton in case of two identified leptons, the veto also rejects fully leptonic $\tau\tau$ events of the type $e^+e^- \to \tau^+(\to e^+\nu_e\overline{\nu}_\tau)\tau^-(\to \ell^-\overline{\nu}_\ell\nu_\tau)$ with $\ell = e, \mu$.

4.2.1 Identification of charged pions and kaons

Charged kaons are identified using the selection algorithm described in Section 3.3.2. No explicit pion identification is performed. If the track in the signal hemisphere fails the kaon selection criteria, it is considered to be a pion (kaon veto).

Despite the application of the particle identification corrections (Section 3.5.2), a deviation between data and Monte Carlo simulation is observed at small kaon momenta, $p \approx 0.7\,\mathrm{GeV}/c$. This has already been noted by earlier analyses of τ decays at the BABAR experiment [69, 70]. It was found to be related to the reconstruction of the Cherenkov cone in the DIRC.

Figure 4.3 shows the Cherenkov angle of identified charged kaons θ_C in data events as a function of their laboratory momentum p. According to Reference [60], the distribution
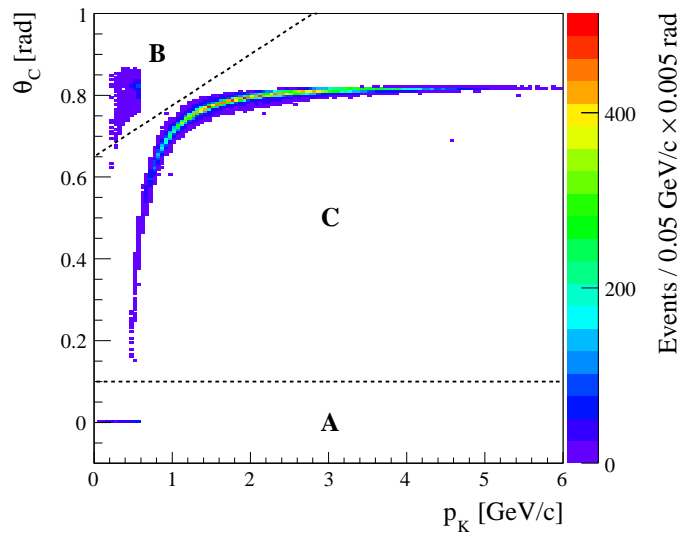
Figure 4.3: Cherenkov angle θ_C in the DIRC as a function of the kaon momentum p in the laboratory system for identified kaons from a subset of the recorded data. **A**, **B** and **C** denote the different regions discussed in the text and the dashed lines indicate the derived selection criteria.

can be divided into three regions:

A No Cherenkov cone has been reconstructed for the particles in this region. Their Cherenkov angle is set to zero, $\theta_\mathrm{C} = 0$. The kaon identification is based on the specific energy loss in the tracking system $\mathrm{d}E/\mathrm{d}x$ and is thus restricted to small momenta (Section 3.3.1).

B Identified kaons with momenta $p \approx 0.7\,\mathrm{GeV}/c$ and Cherenkov angles $\theta_\mathrm{C} \approx 0.8\,\mathrm{rad}$. These are kaons that decay shortly in front of the DIRC or interact with the detector material. The momentum and energy loss ($\mathrm{d}E/\mathrm{d}x$) measurement in the tracking system refer to the kaon, while the Cherenkov angle is measured for the secondary particle. Since the direction of the secondary particle is not well known, the measured Cherenkov angle varies significantly and may be bigger than the

allowed maximal value of 0.825 rad [55]. The kaon identification is performed using the measurement of dE/dx. Thus, only small kaon momenta occur.

C This quantitatively biggest region is the kaon band from Figure 3.1(b).

The deviation between data and Monte Carlo simulation at small kaon momenta was found to be caused by an excess of data events in the regions **A** and **B** [69, 70]. It is removed by requiring reconstructed kaons to fulfill [60, 69, 70]

$$
\begin{aligned}
\theta_{\mathrm{C}} &> 0.1 \, \mathrm{rad} \,, \\
\theta_{\mathrm{C}} &< 0.65 \, \mathrm{rad} + 0.125 \, p \, \frac{\mathrm{rad}}{\mathrm{GeV}/c} \,.
\end{aligned}
\tag{4.10}
$$

Thus, only kaons from the kaon band **C** are accepted within this analysis.

4.2.2 Separation into the decay modes $\tau^- \rightarrow \pi^-/K^- n\pi^0 \nu_\tau$

Using the above criteria to distinguish between kaons and pions, the event sample is separated into two categories according to the particle type of the track in the signal hemisphere:

$$
\begin{aligned}
&\text{Final states with net strangeness} && \tau^- \rightarrow K^- \; n \, \text{neutrals} \; \nu_\tau \,, \\
&\text{Final states without net strangeness} && \tau^- \rightarrow \pi^- \; n \, \text{neutrals} \; \nu_\tau \,.
\end{aligned}
\tag{4.11}
$$

The two event classes are further divided by considering the number of neutral pions as selected in Section 3.4. For final states with net strangeness, decays of the type $\tau^- \rightarrow K^- n\pi^0 \nu_\tau$ with $n = 0, 1, 2, 3$ are considered. Decays without net strangeness, $\tau^- \rightarrow \pi^- n\pi^0 \nu_\tau$, are analyzed in the modes with $n = 1, 2, 3, 4$. Reactions of the type $\tau^- \rightarrow K^- \pi^0\pi^0\pi^0\pi^0 \nu_\tau$ are not measured due to the low statistics expected for this decay channel. In contrast, $\tau^- \rightarrow \pi^- \nu_\tau$ decays cannot be analyzed due to the large remaining background from di-lepton, two-photon and fully leptonic $\tau\tau$ events. The resulting eight categories of selected decay modes of the signal τ lepton are summarized in Table 4.1. They are mutually exclusive to allow a simultaneous determination of all branching fractions (Chapter 6).

4.3 Graphical display of simulated distributions

All distributions in the remainder of this thesis show both data and Monte Carlo simulation. The data is displayed as black dots and the Monte Carlo simulation is splitted according to the final state X of the reaction $e^+e^- \rightarrow X$. Events of the type $e^+e^- \rightarrow \tau^+\tau^-$ are additionally splitted according to the decay mode of the signal τ lepton. Figure 4.4 shows an exhaustive legend of the displayed reactions and τ decay modes as well as their corresponding symbols and colors. The symbol $\tau^- \rightarrow$ rest refers to all decay modes of the signal τ lepton that are not explicitly listed. They contain at least three charged particles in their final state and their contribution to the selected event samples is negligible within this analysis. All listed modes and reactions are displayed as cumulative sum in the Monte Carlo simulated distributions. This allows

Table 4.1: Separation of selected events into the different decay channels of the signal τ lepton according to the numbers of pions, kaons and π^0 mesons they contain.

Signal τ decay channel	Signal track	N_{π^0}
$\tau^- \to K^- \nu_\tau$	K	$N_{\pi^0} = 0$
$\tau^- \to \pi^-/K^- \pi^0 \nu_\tau$	$\pi/\ K$	$N_{\pi^0} = 1$
$\tau^- \to \pi^-/K^- \pi^0 \pi^0 \nu_\tau$	$\pi/\ K$	$N_{\pi^0} = 2$
$\tau^- \to \pi^-/K^- \pi^0 \pi^0 \pi^0 \nu_\tau$	$\pi/\ K$	$N_{\pi^0} = 3$
$\tau^- \to \pi^- \pi^0 \pi^0 \pi^0 \pi^0 \nu_\tau$	π	$N_{\pi^0} = 4$

- Data
- $\tau^- \to K^- \nu_\tau$
- $\tau^- \to K^- \pi^0 \nu_\tau$
- $\tau^- \to K^- \pi^0 \pi^0 \nu_\tau$
- $\tau^- \to K^- \pi^0 \pi^0 \pi^0 \nu_\tau$
- $\tau^- \to \pi^- \nu_\tau$
- $\tau^- \to \pi^- \pi^0 \nu_\tau$
- $\tau^- \to \pi^- \pi^0 \pi^0 \nu_\tau$
- $\tau^- \to \pi^- \pi^0 \pi^0 \pi^0 \nu_\tau$
- $\tau^- \to \pi^- \pi^0 \pi^0 \pi^0 \pi^0 \nu_\tau$
- $\tau^- \to (\pi^-/K^-) \eta\, n\pi^0 \nu_\tau$
- $\tau^- \to (\pi^-/K^-) \overline{K}^0\, n\pi^0 \nu_\tau$
- $\tau^- \to \pi^- \overline{K}^0 (\eta/K^0) \nu_\tau$
- $e^+ e^- \to q\overline{q}$
- $e^+ e^- \to \mu^+ \mu^-$
- $\tau^- \to$ rest
- $\tau^- \to (e^-/\mu^-) \overline{\nu}_{e/\mu} \nu_\tau$
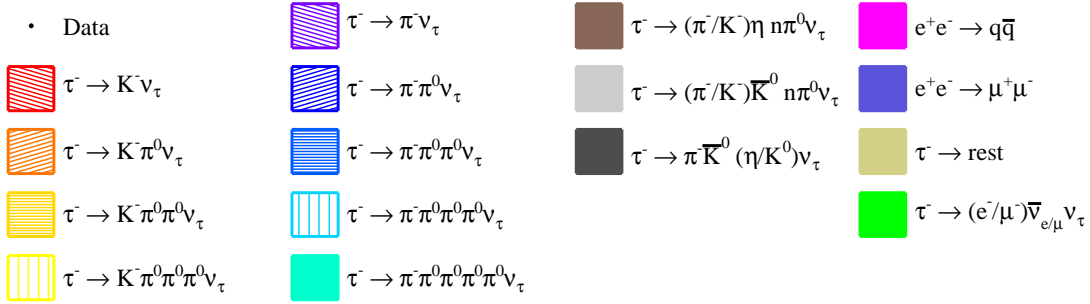
Figure 4.4: Legend for the display of data and Monte Carlo simulated distributions. The legend shows the symbols and colors that are used to display the data, the different simulated decay modes of the signal τ lepton and the simulated non-$\tau\tau$ reactions $e^+ e^- \to X$ in the remainder of this thesis.

a clear identification of the main backgrounds, e. g., in order to develop additional selection criteria or to verify the selection procedure. Some modes and reactions may however be suppressed in the legends and/or combined if they are negligible for the reconstructed decay channel displayed in the corresponding figure. Additionally, the ratio of data and Monte Carlo simulation, *Data/MC*, is shown if it is useful in the given context.

Unless explicitly mentioned otherwise, all plots in this thesis only include statistical uncertainties. The Monte Carlo simulated events are scaled to the data luminosity and the branching fractions of the measured decay modes are reweighted to the results obtained in Chapter 6. All corrections described in Section 3.5 and the π^0 efficiency correction from Sections 5.1 and 5.2 are applied to the Monte Carlo simulated events. In addition, the *split-off correction* derived in Section 5.3.2 is applied to the data distributions. When calculating the branching fractions, background due to split-offs that is not described by the Monte Carlo simulation is subtracted from the numbers of selected data events. Thus, to correctly display the level of agreement between data and simulated distributions, all data histograms in the remainder of this chapter are scaled by the corresponding correction factor $1 - f_{\text{excess}}$. The symbol f_{excess} denotes the

fractional excess of data events caused by split-offs (Table 5.1). This is a reasonable approach for most variables which are expected to be uncorrelated with the occurrence of split-offs. However, correlations may exist, e. g., for the momentum of the charged hadron in single-π^0 reactions. In any case, the scaling has no effect on the branching fractions as determined in Section 6.3.

All figures shown in the remainder of this chapter are $(n-1)$ *distributions*, i. e., all selection criteria except the one on the plotted variable are applied as summarized in Section 4.8. For most variables, only the distributions of two of the eight reconstructed decay modes $\tau^- \to \pi^- n\pi^0 \nu_\tau$ ($n = 1, 2, 3, 4$) and $\tau^- \to K^- n\pi^0 \nu_\tau$ ($n = 0, 1, 2, 3$) are displayed to illustrate the effect of the selection criteria. The histograms of the remaining decay modes are displayed in Appendix A.

4.4   Cross feed rejection

After the division of all selected events into the different decay channels, these still contain *cross feed*, i. e., an event sample with n reconstructed π^0 mesons still contains events with m real π^0 mesons, where $m \neq n$.

Figure 4.5 shows the maximal *hadron-π^0 angle* in the center-of-mass system $\alpha_{h\pi^0}^{\mathrm{cms}}$, i. e., the maximal angle between the track in the signal hemisphere and any reconstructed π^0 meson, for selected events of the type $\tau^- \to \pi^- \pi^0 \pi^0 \pi^0 \nu_\tau$ and $\tau^- \to \pi^- \pi^0 \pi^0 \pi^0 \pi^0 \nu_\tau$. As split-offs are a track related phenomenon, they only affect the reconstruction of π^0 mesons close to the charged hadron (Section 5.3.2). For events that contain multiple π^0 mesons, the *maximal* hadron-π^0 angle is thus uncorrelated with the occurrence of split-offs. Both event classes show significant cross feed, mainly from the corresponding decay channels with one or two π^0 mesons less. This can happen, e. g., if the π^- or the π^+ meson in an event of the true type $\tau^- \to \pi^- \pi^0 \pi^0 \nu_\tau$ and $\tau^+ \to \pi^+ \pi^0 \overline{\nu}_\tau$ is misidentified as a muon. The event is reconstructed as a muon tagged reaction with three neutral pions, $\tau^- \to \pi^- \pi^0 \pi^0 \pi^0 \nu_\tau$ and $\tau^+ \to \mu^+ \nu_\mu \overline{\nu}_\tau$. Since at least one of the π^0 mesons originates from the non-signal τ lepton, it is contained in the tag hemisphere (Figure 4.1). Thus, cross feed events are concentrated at large maximal hadron-π^0 angles around 2.75 rad (160°). In contrast, due to the boost of the τ lepton, π^0 mesons in correctly reconstructed decay channels are located at small angles of about 0.5 rad (30°).

Cross feed is a significant effect due to the much larger branching fraction of the decay channel with one π^0 meson less with respect to the reconstructed mode, e. g., $\mathcal{B}(\tau^- \to \pi^- \pi^0 \pi^0 \nu_\tau)/\mathcal{B}(\tau^- \to \pi^- \pi^0 \pi^0 \pi^0 \nu_\tau) \approx 10$ [3]. Given the ratio of the branching fractions $\mathcal{B}(\tau^+ \to \pi^+ \pi^0 \overline{\nu}_\tau)/\mathcal{B}(\tau^+ \to \mu^+ \nu_\mu \overline{\nu}_\tau) \approx 1.5$, τ pairs produce about 15 times more cross feed candidates of the type $\tau^- \to \pi^- \pi^0 \pi^0 \nu_\tau$ and $\tau^+ \to \pi^+ \pi^0 \overline{\nu}_\tau$ than real $\tau^- \to \pi^- \pi^0 \pi^0 \pi^0 \nu_\tau$ events with $\tau^+ \to \mu^+ \nu_\mu \overline{\nu}_\tau$. Taking into account the suppression of cross feed events with the pion-as-muon misidentification of the order of 1.5 % (Figure 3.4(b)), these candidates lead to the observed amount of cross feed in Figure 4.5(a). If the cross feed event is considered as an event of the true type $\tau^+ \to \pi^+ \pi^0 \overline{\nu}_\tau$ or $\tau^- \to \pi^- \pi^0 \pi^0 \nu_\tau$ depends on which of the two charged pions is misidentified as the muon.

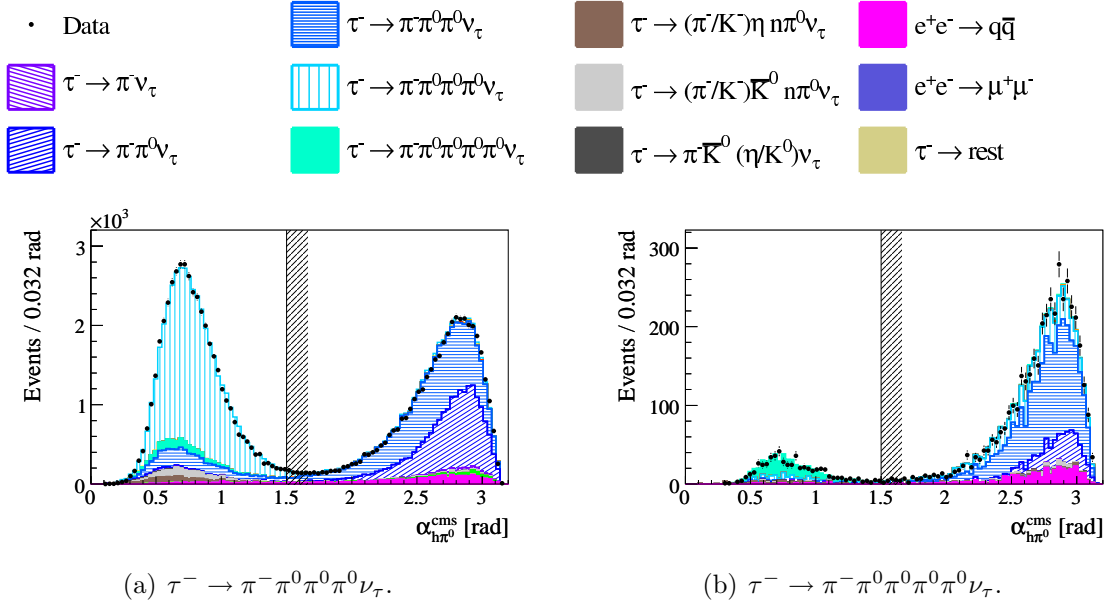Since the pion misidentification is much larger for muons than for electrons (Fig-

(a) $\tau^- \to \pi^- \pi^0 \pi^0 \pi^0 \nu_\tau$. (b) $\tau^- \to \pi^- \pi^0 \pi^0 \pi^0 \pi^0 \nu_\tau$.

Figure 4.5: Distributions of the maximal hadron-π^0 angle in the center-of-mass system $\alpha_{h\pi^0}^{\mathrm{cms}}$ for selected events of the type **(a)** $\tau^- \to \pi^- \pi^0 \pi^0 \pi^0 \nu_\tau$ and **(b)** $\tau^- \to \pi^- \pi^0 \pi^0 \pi^0 \pi^0 \nu_\tau$, using muon tagged reactions only. The selection criteria on this variable are indicated by the vertical lines.

ures 3.2, 3.4), muon tagged reactions are chosen to illustrate the effect in Figure 4.5. The distributions for the remaining decay channels are displayed in Figures A.1 and A.2. They show that similar scenarios occur for all other decay channels with multiple π^0 mesons. As indicated by Figure 4.5(b), the amount of cross feed increases strongly with the number of reconstructed π^0 mesons.

To reject cross feed from τ decays into final states with fewer neutral pions, selected π^0 mesons are restricted to a cone around the (signal) hadron track:

$$\alpha_{h\pi^0}^{\mathrm{cms}} < 1.5 \, \mathrm{rad} \, . \tag{4.12}$$

Cross feed from events with additional neutral pions occurs if a π^0 escapes detection, e.g., if one photon is outside the fiducial detector volume. This can be suppressed using the *unassociated energy in the signal event hemisphere* E_{unass}. It is defined as the sum of the energies E_i of all photons in the signal hemisphere that are not used in the reconstruction of a π^0 meson,

$$E_{\mathrm{unass}} = \sum_{i(\mathrm{unass})} E_i \, . \tag{4.13}$$

Events with additional undetected π^0 mesons contain more unassociated energy than events in which all neutral pions are reconstructed.

As an example, Figure 4.6 displays the unassociated energy for $\tau^- \to \pi^- \pi^0 \nu_\tau$ and $\tau^- \to K^- \nu_\tau$ events. Both distributions exhibit significant deviations between data and Monte Carlo simulation. But they also show that the unassociated energy is an
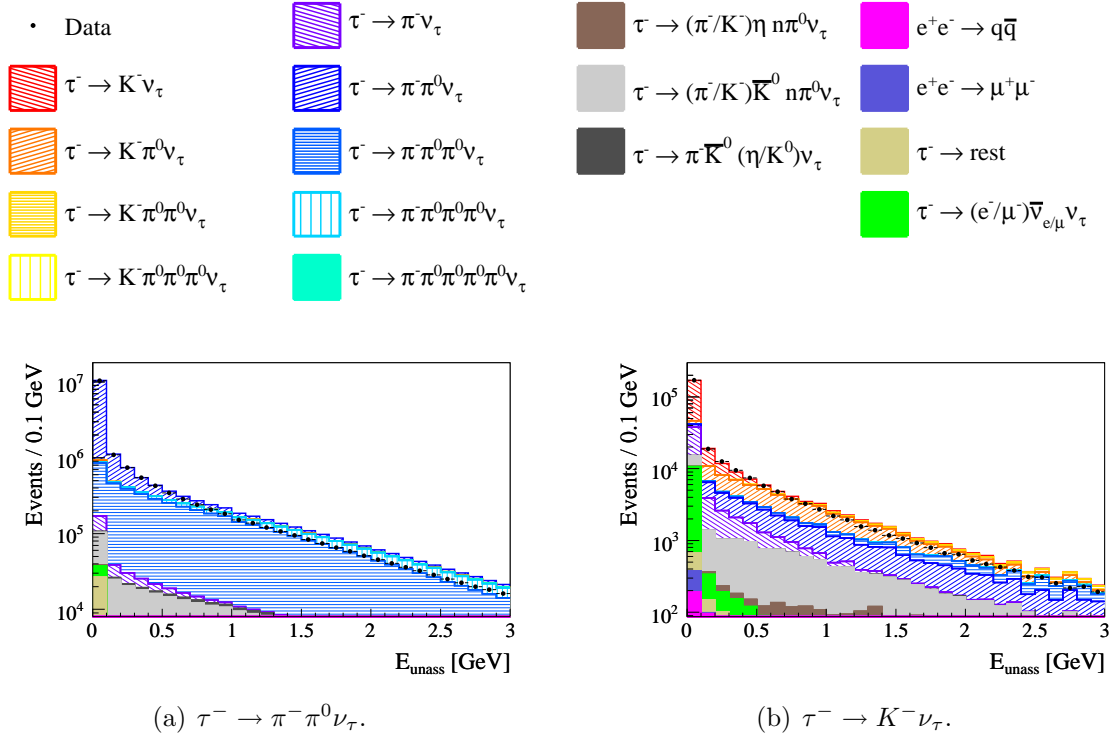
Figure 4.6: Distributions of the unassociated energy in the signal event hemisphere E_{unass} for selected events of the type **(a)** $\tau^- \to \pi^- \pi^0 \nu_\tau$ and **(b)** $\tau^- \to K^- \nu_\tau$. Only the lowest energy bin is accepted by the selection criterion.

effective means to eliminate cross feed from decay channels that contain additional π^0 mesons. The minimization of this background is essential to the determination of the π^0 efficiency correction as described in Section 5.1. Thus, all selected events are required to have

$$E_{\mathrm{unass}} < 0.1\,\mathrm{GeV}\,. \tag{4.14}$$

The selection criterion is chosen such that the uncertainty of the branching fractions due to the π^0 efficiency correction as determined in Section 5.4 is minimized. All remaining decay channels show similar distributions. They are presented in Figures A.3 and A.4.

4.5 Rejection of remaining QED backgrounds

Despite the application of the criteria to select $\tau\tau$ reactions in Section 4.1, the selected events still contain background from non-$\tau\tau$ QED processes, e.g., di-lepton reactions $e^+e^- \to \ell^+\ell^-(\gamma)$ with $\ell = e, \mu$ or two-photon processes $e^+e^- \to e^+e^- f\overline{f}$ with $f = e, \mu, \pi$. Since no suitable Monte Carlo simulation is available for Bhabha scattering and two-photon reactions (Section 2.3.2), an effective rejection of these events is essential for the success of this analysis.

Figure 4.7(a) shows the s-channel Feynman diagram for a di-lepton reaction.[10] Since

---

[10]For $e^+e^-(\gamma)$ final states, an additional t-channel diagram exists.

(a) $e^+e^- \to \ell^+\ell^-(\gamma)$.
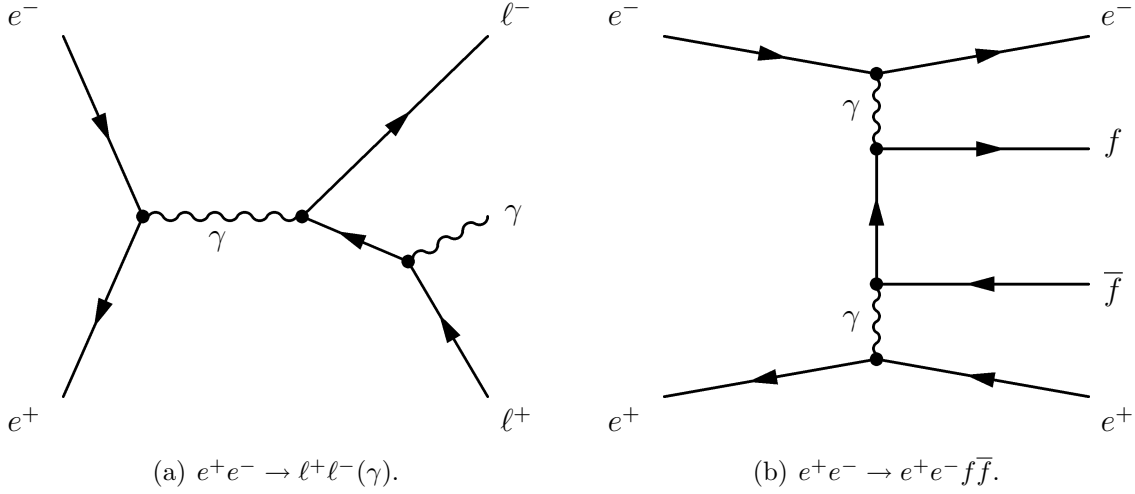
(b) $e^+e^- \to e^+e^- f\bar{f}$.

Figure 4.7: Feynman diagrams of an **(a)** $e^+e^- \to \ell^+\ell^-(\gamma)$, $\ell = e, \mu$, di-lepton and a **(b)** $e^+e^- \to e^+e^- f\bar{f}$, $f = $ fermions $= e, \mu, \pi$, two-photon background event. For $e^+e^-(\gamma)$ final states, a t-channel diagram exists in addition to the s-channel reaction shown in **(a)**. While all signal events $e^+e^- \to \tau^+(\to e^+\nu_e\overline{\nu}_\tau)\tau^-(\to \pi^-/K^-n\pi^0\nu_\tau)$ contain three undetected neutrinos in their final state, di-lepton events do not contain any undetected particles. Two-photon events are only reconstructed as signal events if two charged particles escape detection. This happens, for example, if the electrons do not leave the beam pipe.

the final state of di-lepton events does not contain any undetected neutrinos, each lepton has a center-of-mass momentum close to the individual momenta of the incoming electrons and positrons, $p_\ell^{\mathrm{cms}} \approx p_e^{\mathrm{cms}} = 5.29\,\mathrm{GeV}/c$. Differences only occur via initial and final state radiation or interactions with detector material. In contrast, leptons in signal events have significantly lower momenta because of the two final state neutrinos in leptonic τ decays, $\tau^- \to \ell^-\overline{\nu}_\ell\nu_\tau$. This is used to reject di-lepton events by requiring the reconstructed lepton to fulfill the criterion

$$p_\ell^{\mathrm{cms}} < 5.0\,\mathrm{GeV}/c. \tag{4.15}$$

Additionally, the *missing mass* is used to further suppress di-lepton events. It is defined as

$$m_{\mathrm{miss}} = \sqrt{p_{\mathrm{miss}}^\mu p_\mu^{\mathrm{miss}}}. \tag{4.16}$$

The symbol p_{miss}^μ denotes the *missing four-momentum*,

$$p_{\mathrm{miss}}^\mu = p_{ee}^\mu - \sum_{i(\mathrm{FS})} p_i^\mu, \tag{4.17}$$

where p_{ee}^μ is the total four-momentum of the incoming electron and positron and the p_i^μ are the four-momenta of all reconstructed final state particles (FS). The missing momentum is calculated using all tracks and neutral particles as defined in Sections 3.1, 3.2. As for the thrust definition, the daughters of K_S^0 mesons, Λ baryons and photon conversions are also added to the tracks.

Signal events of the type $e^+e^- \to \tau^+(\to \ell^+\nu_\ell\overline{\nu}_\tau)\tau^-(\to \pi^-/K^- n\pi^0\nu_\tau)$ comprise three neutrinos within their end products and their missing mass is significantly larger than zero. In contrast, because of the absence of any final state neutrinos, the missing mass of di-lepton events is approximately zero.

Figure 4.8 shows the missing mass distributions for events of the type $\tau^- \to \pi^-\pi^0\nu_\tau$ and $\tau^- \to K^-\nu_\tau$. For both decay modes, the comparison with the Monte Carlo
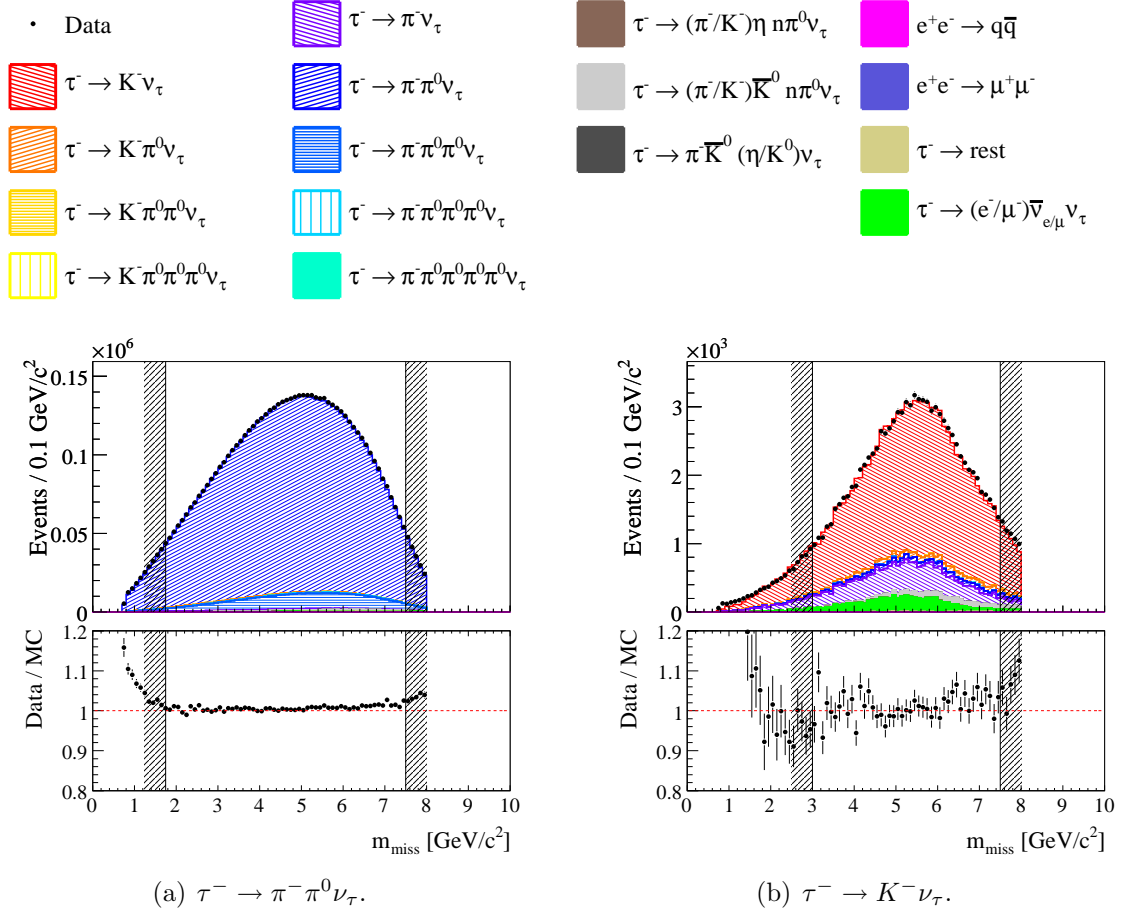
Figure 4.8: Distributions of the missing mass m_{miss} for selected events of the type **(a)** $\tau^- \to \pi^-\pi^0\nu_\tau$ and **(b)** $\tau^- \to K^-\nu_\tau$, using electron tagged reactions. The selection criteria on this variable are indicated by the vertical lines.

simulation shows an excess of data events at small missing masses—as visible in the plotted ratio histograms. This excess is due to remaining background from di-lepton reactions, $e^+e^- \to \ell^+\ell^-(\gamma)$, which are not included in the Monte Carlo simulated event samples (Section 2.3.2). Since the effect is more pronounced in electron than in muon tagged decays, only the former are displayed in Figure 4.8. The general agreement is similar for both event types. The distributions of the remaining decay modes are displayed in Figures A.5 and A.6. Because of the larger number of π^0 mesons, they are less affected by background from di-lepton events and the amount of remaining background decreases with the number of reconstructed π^0 mesons. Thus,

the background is rejected by the following decay-channel dependent selection criteria:

$$
\begin{aligned}
\tau^- &\to K^- \nu_\tau & m_{\mathrm{miss}} &> 3.00\,\mathrm{GeV}/c^2\,, \\
\tau^- &\to \pi^-/K^- \pi^0 \nu_\tau & m_{\mathrm{miss}} &> 1.75\,\mathrm{GeV}/c^2\,, \\
\tau^- &\to \pi^-/K^- \pi^0 \pi^0 \nu_\tau & m_{\mathrm{miss}} &> 1.50\,\mathrm{GeV}/c^2\,, \\
\tau^- &\to \pi^-/K^- \pi^0 \pi^0 \pi^0 (\pi^0) \nu_\tau & m_{\mathrm{miss}} &> 1.00\,\mathrm{GeV}/c^2\,.
\end{aligned}
\tag{4.18}
$$

Two-photon reactions constitute an additional class of background events. Figure 4.7(b) shows a possible Feynman diagram. At least two charged particles need to remain undetected in order to allow a reconstruction as a signal event. Due to the event kinematics, the two high-energetic electrons are most likely to remain inside the beam pipe and escape detection. Two-photon events hence tend to have large missing masses close to the kinematic limit, $m_{\mathrm{miss}} \to \sqrt{s} = 10.58\,\mathrm{GeV} - 2m_e c^2$. As these reactions are not included in the Monte Carlo simulated events samples (Section 2.3.2), remaining background from these events is visible as data excess at large missing masses in Figure 4.8. To remove these reactions, selected events are required to have

$$
m_{\mathrm{miss}} < 7.50\,\mathrm{GeV}/c^2\,.
\tag{4.19}
$$

In order to test the level of remaining QED background, Figure 4.9 displays the hadron-lepton acoplanarity $\Delta\phi_{h\ell}^{\mathrm{cms}}$, i.e., the difference in the tracks' azimuthal angles in the center-of-mass system, for selected events of the type $\tau^- \to \pi^- \pi^0 \nu_\tau$ and $\tau^- \to K^- \nu_\tau$. The distribution for $\tau^- \to \pi^- \pi^0 \nu_\tau$ decays in Figure 4.9(a) shows that the data is well described by the Monte Carlo simulation. All other decay channels with π^0 mesons in their final state exhibit a similar level of agreement (Figures A.7, A.8). In contrast, $\tau^- \to K^- \nu_\tau$ reactions (Figure 4.9(b)) display a huge excess of data events at large acoplanarities near 180° (3.14 rad). They are particularly affected by QED background that is not included in the Monte Carlo simulation and the excess is due to still remaining Bhabha background, $e^+ e^- \to e^+ e^-$, in this decay channel. Since $e^+ e^- \to e^+ e^-$ events only comprise two final state particles, these are *back-to-back*, i.e., their opening angle in the center-of-mass system is close to 180° (3.14 rad). Again, electron tagged events are used to illustrate this effect, since they exhibit the largest discrepancy. Muon tagged events display a similar but smaller deviation. The background events are removed by requiring the acoplanarity for selected events of the type $\tau^- \to K^- \nu_\tau$ to be

$$
\tau^- \to K^- \nu_\tau \quad \Delta\phi_{h\ell}^{\mathrm{cms}} < 2.95\,\mathrm{rad}\,.
\tag{4.20}
$$

4.6 Rejection of remaining $q\bar{q}$ background

Similarly to the selected samples of final states with few π^0 mesons, which still contained QED background, event samples of decay modes with multiple π^0 mesons still contain background of the type $e^+ e^- \to q\bar{q}$.

Figure 4.10(a) shows the thrust T (Equation 4.2) for selected events of the type $\tau^- \to \pi^- \pi^0 \pi^0 \pi^0 \pi^0 \nu_\tau$. A significant level of $q\bar{q}$ background is visible at low thrust values. As illustrated by the distribution for events of the type $\tau^- \to K^- \pi^0 \pi^0 \nu_\tau$ in Figure 4.10(b), remaining cross feed from non-strange reactions, i.e., $\tau^- \to \pi^- \pi^0 \pi^0 (\pi^0) \nu_\tau$, in the strange
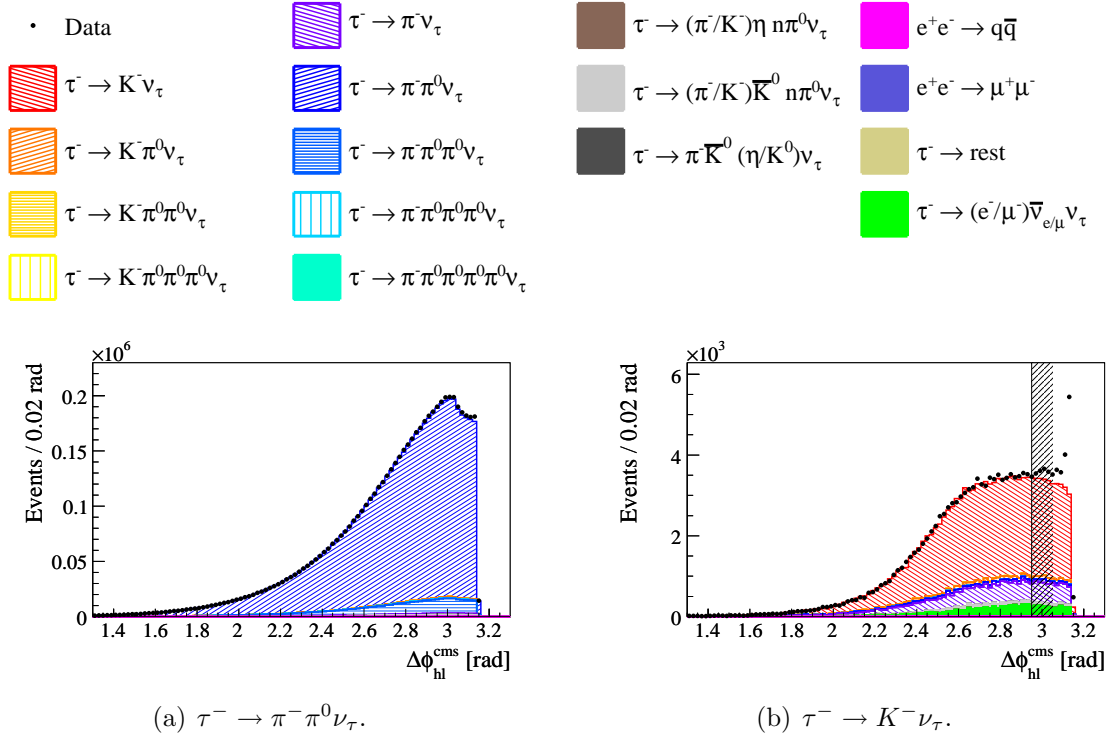
Figure 4.9: Distributions of the hadron-lepton acoplanarity $\Delta\phi_{h\ell}^{\mathrm{cms}}$ in the center-of-mass system for selected events of the type **(a)** $\tau^- \to \pi^-\pi^0\nu_\tau$ and **(b)** $\tau^- \to K^-\nu_\tau$, using electron tagged reactions. The selection criterion on this variable is indicated by the vertical line.

modes $\tau^- \to K^-\pi^0\pi^0(\pi^0)\nu_\tau$ is also enriched at small thrust values. The kinematic constraint of the τ mass and the larger kaon mass force the final state particles of decays of the type $\tau^- \to K^- n\pi^0\nu_\tau$ to be closer to the initial τ direction than in the case of $\tau^- \to \pi^- n\pi^0\nu_\tau$ reactions. Thus, the thrust value of events that contain a charged kaon is larger than the one of corresponding events with a charged pion.

Both the $q\bar{q}$ and the non-strange backgrounds are reduced by the following selection criteria:

$$
\begin{aligned}
\tau^- \to \pi^-\pi^0\pi^0\pi^0\pi^0\nu_\tau \quad & T > 0.92\,, \\
\tau^- \to K^-\pi^0\pi^0\nu_\tau \quad & T > 0.91\,, \\
\tau^- \to K^-\pi^0\pi^0\pi^0\nu_\tau \quad & T > 0.92\,.
\end{aligned}
\tag{4.21}
$$

The distribution for events of the type $\tau^- \to K^-\pi^0\pi^0\nu_\tau$ is shown alongside all other decay modes in Figures A.9 and A.10. It also displays significant background at low thrust values in contrast to all remaining modes.

4.7   Rejection of remaining $\tau\tau$ background

Remaining background from $\tau\tau$ reactions mainly consists of τ decays that produce final states similar or identical to the one of the signal decay modes, e. g., via intermediate
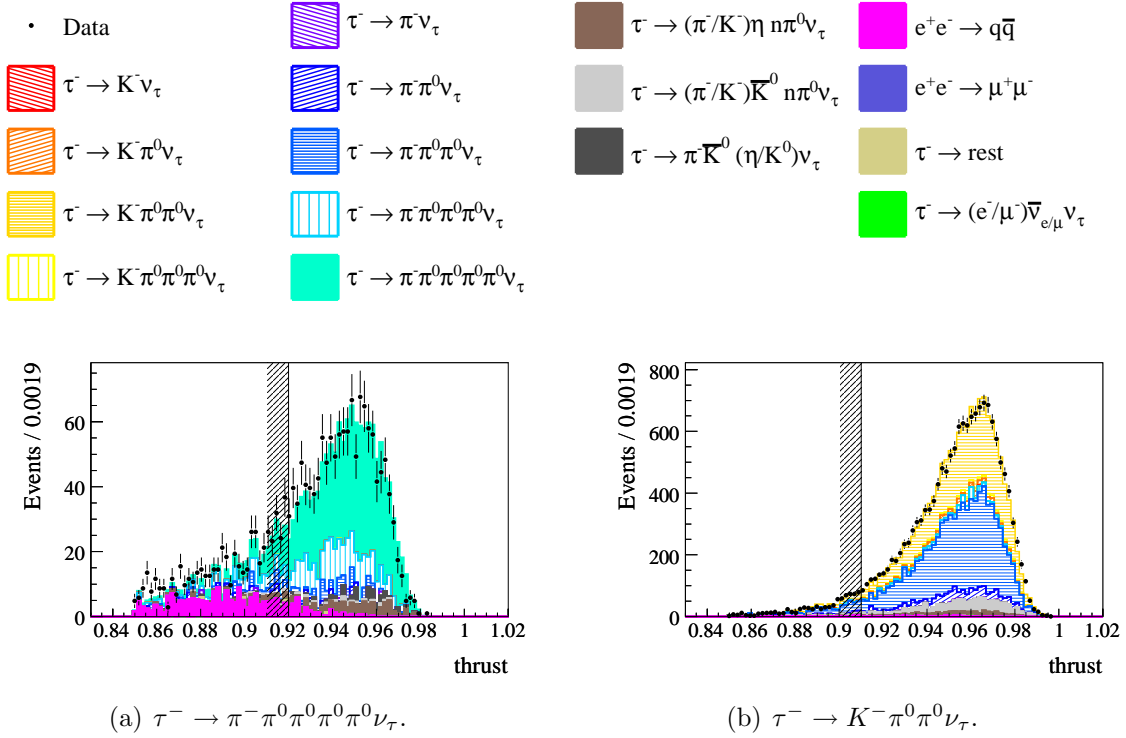
• Data	$\tau^- \to \pi^-\nu_\tau$	$\tau^- \to (\pi^-/K^-)\eta\, n\pi^0\nu_\tau$	$e^+e^- \to q\bar{q}$	
$\tau^- \to K^-\nu_\tau$	$\tau^- \to \pi^-\pi^0\nu_\tau$	$\tau^- \to (\pi^-/K^-)\overline{K}{}^0\, n\pi^0\nu_\tau$	$e^+e^- \to \mu^+\mu^-$	
$\tau^- \to K^-\pi^0\nu_\tau$	$\tau^- \to \pi^-\pi^0\pi^0\nu_\tau$	$\tau^- \to \pi^-\overline{K}{}^0\,(\eta/K^0)\nu_\tau$	$\tau^- \to$ rest	
$\tau^- \to K^-\pi^0\pi^0\nu_\tau$	$\tau^- \to \pi^-\pi^0\pi^0\pi^0\nu_\tau$		$\tau^- \to (e^-/\mu^-)\overline{\nu}_{e/\mu}\nu_\tau$	
$\tau^- \to K^-\pi^0\pi^0\pi^0\nu_\tau$	$\tau^- \to \pi^-\pi^0\pi^0\pi^0\pi^0\nu_\tau$			

(a) $\tau^- \to \pi^-\pi^0\pi^0\pi^0\pi^0\nu_\tau$.   (b) $\tau^- \to K^-\pi^0\pi^0\nu_\tau$.

Figure 4.10: Distributions of the thrust for selected events of the type **(a)** $\tau^- \to \pi^-\pi^0\pi^0\pi^0\pi^0\nu_\tau$ and **(b)** $\tau^- \to K^-\pi^0\pi^0\nu_\tau$. The selection criteria on this variable are indicated by the vertical lines.

resonances. These comprise the following decay channels:

$\boldsymbol{\tau^- \to \pi^-/K^-\overline{K}{}^0/\eta n\pi^0\nu_\tau}$ with $n = 0, 1, 2$. τ decays into final states containing neutral kaons may enter the selected event samples in two ways. Firstly, a K^0 meson that decays as a K_L^0 is not identified in this analysis due to the insufficient description of the instrumented flux return by the Monte Carlo simulation [61]. It thus escapes detection and the event is reconstructed in the corresponding mode without K^0. Secondly, an event containing a K^0 meson that decays as a K_S^0 may enter event samples with additional π^0 mesons via the decay $K_S^0 \to \pi^0\pi^0$.[11] Similarly, decays with additional η mesons may enter selected event samples via the decay $\eta \to \pi^0\pi^0\pi^0$.[12] The latter two possibilities fully enter into the selected event samples unless explicit measures against resonant multiple-π^0 final states are applied.

Since K_L^0 mesons scarcely interact in the electromagnetic calorimeter, τ decays into final states containing any K_L^0 mesons, e.g., $\tau^- \to K^-K_L^0\nu_\tau$, are not discarded by the selection criteria described so far. As their branching fractions are not well measured,[13] their subtraction from the selected data events (Section 6.1) would induce a significant uncertainty of the measured branching fractions.

---

[11]$\mathcal{B}(K^0 \to K_L^0) = \mathcal{B}(K^0 \to K_S^0) = 50\,\%$, $\mathcal{B}(K_S^0 \to \pi^0\pi^0) = (30.69 \pm 0.05)\,\%$ [3].
[12]$\mathcal{B}(\eta \to \pi^0\pi^0\pi^0) = (32.52 \pm 0.26)\,\%$ [3].
[13]E. g., $\Delta\mathcal{B}/\mathcal{B}(\tau^- \to K^-K^0\nu_\tau) = 11\,\%$ [3].

Events that contain an additional K_L^0 meson with respect to a measured decay mode are thus rejected using an estimate of the mass m_ν of the neutrino resulting from the signal τ decay:

$$m_\nu^2 = p^\mu(\nu)p_\mu(\nu) \qquad \text{with} \quad p^\mu(\nu) = p^\mu(\tau) - p^\mu(\pi/Kn\pi^0) \,. \tag{4.22}$$

The $p^\mu(\nu)$ and $p^\mu(\tau)$ are the center-of-mass four-momenta of the neutrino and the τ lepton, while $p^\mu(\pi/Kn\pi^0)$ is the center-of-mass four-momentum of all reconstructed final state particles in the signal hemisphere:

$$p^\mu(\pi/Kn\pi^0) = p^\mu(\pi/K) + \sum_{i=1}^{n} p^\mu(\pi_i^0) \,. \tag{4.23}$$

It is calculated from the four-momentum of the charged hadron $p^\mu(\pi/K)$ and those of the reconstructed π^0 mesons $p^\mu(\pi_i^0)$. The energy and momentum of the τ lepton in the center-of-mass system are known by four-momentum conservation,

$$\begin{aligned} E_\tau &= E_e \,, \\ p_\tau &= \sqrt{(E_e)^2 - m_\tau^2} \,. \end{aligned} \tag{4.24}$$

The symbol E_e denotes the center-of-mass energy of the incoming electron beam, $E_e = \sqrt{s}/2 = 5.29\,\text{GeV}$, and $m_\tau = (1.77690 \pm 0.00020)\,\text{GeV}/c^2$ is the τ mass. An estimate of the τ direction is obtained by the thrust axis $\mathbf{n}_T$:

$$p_\mu(\tau) = (E_\tau,\, p_\tau \mathbf{n}_T) \,. \tag{4.25}$$

If all final state particles except the neutrino are reconstructed, the neutrino mass should be consistent with zero, $m_\nu \approx 0$. In contrast, if an additional particle, e.g., a K_L^0, escapes detection, the neutrino mass is expected to be significantly larger than zero, $m_\nu \gg 0$.

Figure 4.11 shows the calculated squared neutrino masses for selected events of the type $\tau^- \to K^- \nu_\tau$ and $\tau^- \to K^- \pi^0 \nu_\tau$. A reasonable agreement between data and Monte Carlo simulation is observed for both decay channels except at large values. Due to the rough estimate of the τ direction using the thrust axis, a wide spread of the calculated neutrino masses is observed. In combination with the finite energy and momentum resolution, even negative values occur for the squared invariant mass m_ν^2. However, on average, events with additional K^0 mesons, $\tau^- \to K^- K^0 n\pi^0 \nu_\tau$, are concentrated at larger masses than signal events of the type $\tau^- \to K^- n\pi^0 \nu_\tau$. The excess of Monte Carlo simulated events in this region, which is observed in both decay modes, indicates that the actual world averages[14] may overestimate these branching fractions. Figure A.12 contains the distributions of the remaining modes with net strangeness, $\tau^- \to K^- \pi^0 \pi^0 \nu_\tau$ and $\tau^- \to K^- \pi^0 \pi^0 \pi^0 \nu_\tau$. They exhibit a similar behavior, although the statistical uncertainties are rather large.

---

[14]$\mathcal{B}(\tau^- \to K^- K^0 \nu_\tau) = (1.58 \pm 0.17) \times 10^{-3}$, $\mathcal{B}(\tau^- \to K^- K^0 \pi^0 \nu_\tau) = (1.44 \pm 0.23) \times 10^{-3}$ [3]

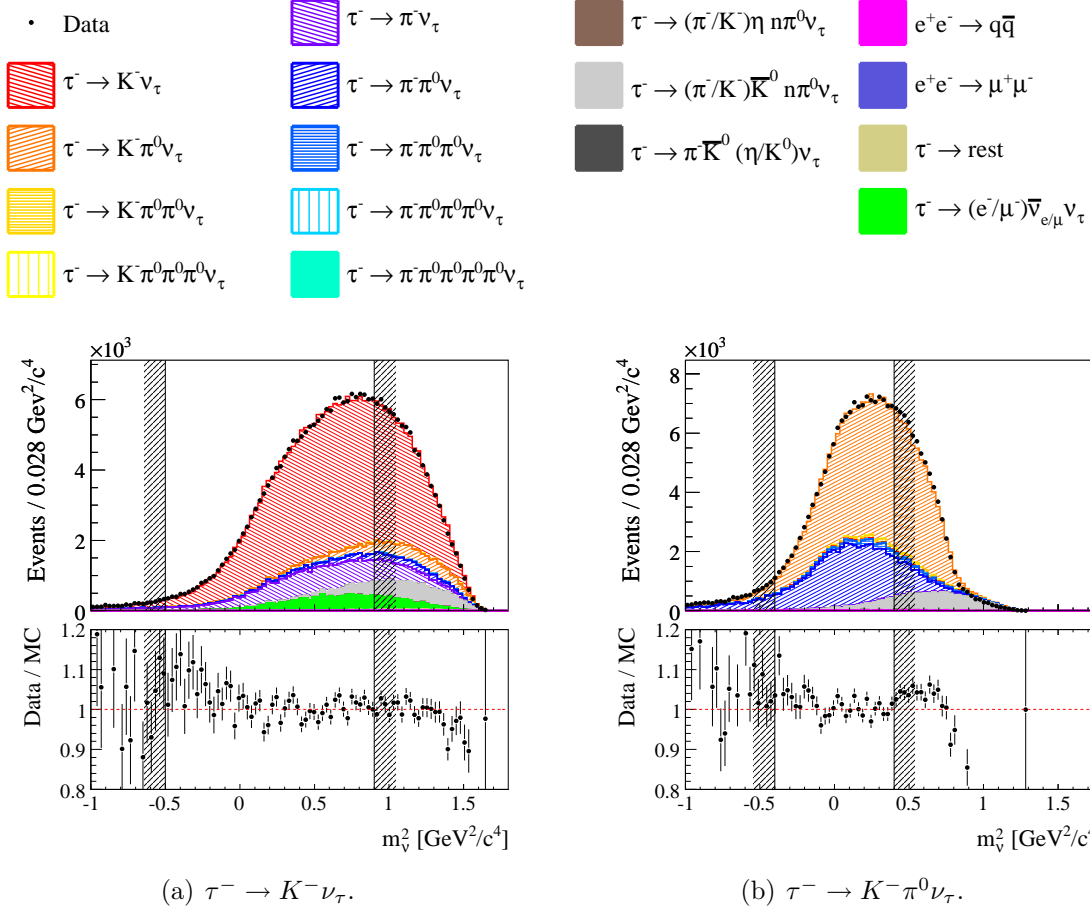**Figure 4.11:** Distributions of the squared invariant neutrino mass m_ν^2 for selected events of the type $\tau^- \to K^- \nu_\tau$ and $\tau^- \to K^- \pi^0 \nu_\tau$. Negative values occur because of the finite detector resolution and due to the rough estimate of the τ direction using the thrust direction. The selection criteria on this variable are indicated by the vertical lines.

In consequence, decays of the type $\tau^- \to K^- K^0 n\pi^0 \nu_\tau$ are suppressed by imposing the following selection criteria:

$$
\begin{aligned}
\tau^- \to K^- \nu_\tau & & -0.5 & < & m_\nu^2 & < & 0.9 \, \text{GeV}^2/c^4 \\
\tau^- \to K^- \pi^0 \nu_\tau & & -0.4 & < & m_\nu^2 & < & 0.4 \, \text{GeV}^2/c^4 \\
\tau^- \to K^- \pi^0 \pi^0 \nu_\tau & & -0.4 & < & m_\nu^2 & < & 0.2 \, \text{GeV}^2/c^4 \\
\tau^- \to K^- \pi^0 \pi^0 \pi^0 \nu_\tau & & -0.4 & < & m_\nu^2 & < & 0.1 \, \text{GeV}^2/c^4
\end{aligned}
\tag{4.26}
$$

In addition to events with missing K_L^0 mesons, these selection criteria also suppress reactions with additional π^0 mesons that escaped detection.

The selection criteria are chosen such that the uncertainties of the measured branching fractions that are induced by the uncertainties of the branching fractions of the subtracted backgrounds (Section 6.5.3) are of similar size as the total statistical uncertainties (Table 6.5). Thus, the imprecisely known backgrounds are suppressed as much as possible while assuring that the statistical uncertainties remain small.

All decay modes without net strangeness exhibit similar distributions of the squared neutrino mass. They are displayed in Figure A.11. Since the ratio of the branching fractions for the reactions $\tau^- \to \pi^- \overline{K}^0 n\pi^0 \nu_\tau$ and $\tau^- \to \pi^- n\pi^0 \nu_\tau$ is much smaller than for the corresponding decay channels with net strangeness (e. g., $\mathcal{B}(\tau^- \to \pi^- \pi^0 \nu_\tau)/\mathcal{B}(\tau^- \to \pi^- \overline{K}^0 \pi^0 \nu_\tau) \approx 70$ versus $\mathcal{B}(\tau^- \to K^- \pi^0 \nu_\tau)/\mathcal{B}(\tau^- \to K^- K^0 \pi^0 \nu_\tau) \approx 3$ [3]), the background contribution is strongly reduced in decay channels without net strangeness. In consequence, no selection criteria are applied for these modes.

After the rejection of all remaining backgrounds with different final states than those of the reconstructed decay channels, the selected event samples still contain background from resonant τ decays into the reconstructed final states, e. g., $\tau^- \to KK^0\nu_\tau$ ($K_S^0 \to \pi^0\pi^0$) and $\tau^- \to K^-\eta\nu_\tau$ ($\eta \to \pi^0\pi^0\pi^0$). Since resonant τ decays are not to be included into the measurements within this thesis, they are rejected by excluding the resonance regions in the invariant mass distributions of final state π^0 pairs and triplets.

Figure 4.12 shows the resonance regions of the invariant $\pi^0\pi^0$ masses for $\tau^- \to K^- n\pi^0\nu_\tau$ events with $n = 2, 3$ and the $\pi^0\pi^0\pi^0$ masses for $\tau^- \to K^-\pi^0\pi^0\pi^0\nu_\tau$ and $\tau^- \to \pi^-\pi^0\pi^0\pi^0\pi^0\nu_\tau$ reactions. All data distributions are reasonably well described by the Monte Carlo simulation. Given the masses of K^0 and η mesons, $m_{K^0} = (497.648 \pm 0.022)\,\mathrm{MeV}/c^2$ and $m_\eta = (547.41 \pm 0.18)\,\mathrm{MeV}/c^2$ [3], the resonances are rejected in the above decay modes by the following criteria:

$$
\begin{aligned}
K_S^0 \to \pi^0\pi^0 \quad &(\ m_{\pi^0\pi^0} \quad < \quad 0.44\,\mathrm{GeV}/c^2\ ) \quad \| \quad (\ m_{\pi^0\pi^0} \quad > \quad 0.52\,\mathrm{GeV}/c^2\ ) \\
\eta \to \pi^0\pi^0\pi^0 \quad &(\ m_{\pi^0\pi^0\pi^0} \quad < \quad 0.50\,\mathrm{GeV}/c^2\ ) \quad \| \quad (\ m_{\pi^0\pi^0\pi^0} \quad > \quad 0.60\,\mathrm{GeV}/c^2\ )
\end{aligned}
\tag{4.27}
$$

The remaining distributions for $\tau^- \to \pi^- n\pi^0\nu_\tau$ events are shown in Appendix A. Since $\tau^- \to \pi^-\eta\nu_\tau$ decays are forbidden in the limit of strong isospin and G-parity conservation [71], background from $\eta \to \pi^0\pi^0\pi^0$ decays in selected $\tau^- \to \pi^-\pi^0\pi^0\pi^0\nu_\tau$ reactions is restricted to the mode $\tau^- \to \pi^-\eta\pi^0\nu_\tau$ with an undetected π^0 meson and thus small. Because of the ratios of the relevant branching fractions [3], the background contribution from $K_S^0 \to \pi^0\pi^0$ decays is also relatively small in $\tau^- \to \pi^- n\pi^0\nu_\tau$ events. Since the $\pi^0\pi^0$ mass distributions are not well described by the Monte Carlo simulation, no selection criteria are applied for these modes.

4.8   Summary of the selection criteria

All criteria applied to select reactions of the type $e^+e^- \to \tau^+\tau^-$ and to reject cross feed between the different decay modes of the signal τ lepton are summarized in Table 4.2.

Table 4.3 summarizes the selection criteria that are applied to reject remaining background from QED processes and reactions of the type $e^+e^- \to q\bar{q}$ and $e^+e^- \to \tau^+\tau^-$.

Figures 4.13 and 4.14 display the momentum of the charged hadron in the signal hemisphere for all selected decay channels. No selection criterion is imposed on this quantity. The distributions of the modes $\tau^- \to \pi^-\pi^0\nu_\tau$, $\tau^- \to K^-\nu_\tau$ and $\tau^- \to K^-\pi^0\nu_\tau$ only display a small shift of the data towards smaller momenta—visible as the slope in the ratio of the data and Monte Carlo simulated distributions. In contrast, the distributions of the decay channels $\tau^- \to \pi^-\pi^0\pi^0\nu_\tau$, $\tau^- \to \pi^-\pi^0\pi^0\pi^0\nu_\tau$ and $\tau^- \to \pi^-\pi^0\pi^0\pi^0\pi^0\nu_\tau$ exhibit huge shifts of the data towards larger momenta. This is discussed for the most

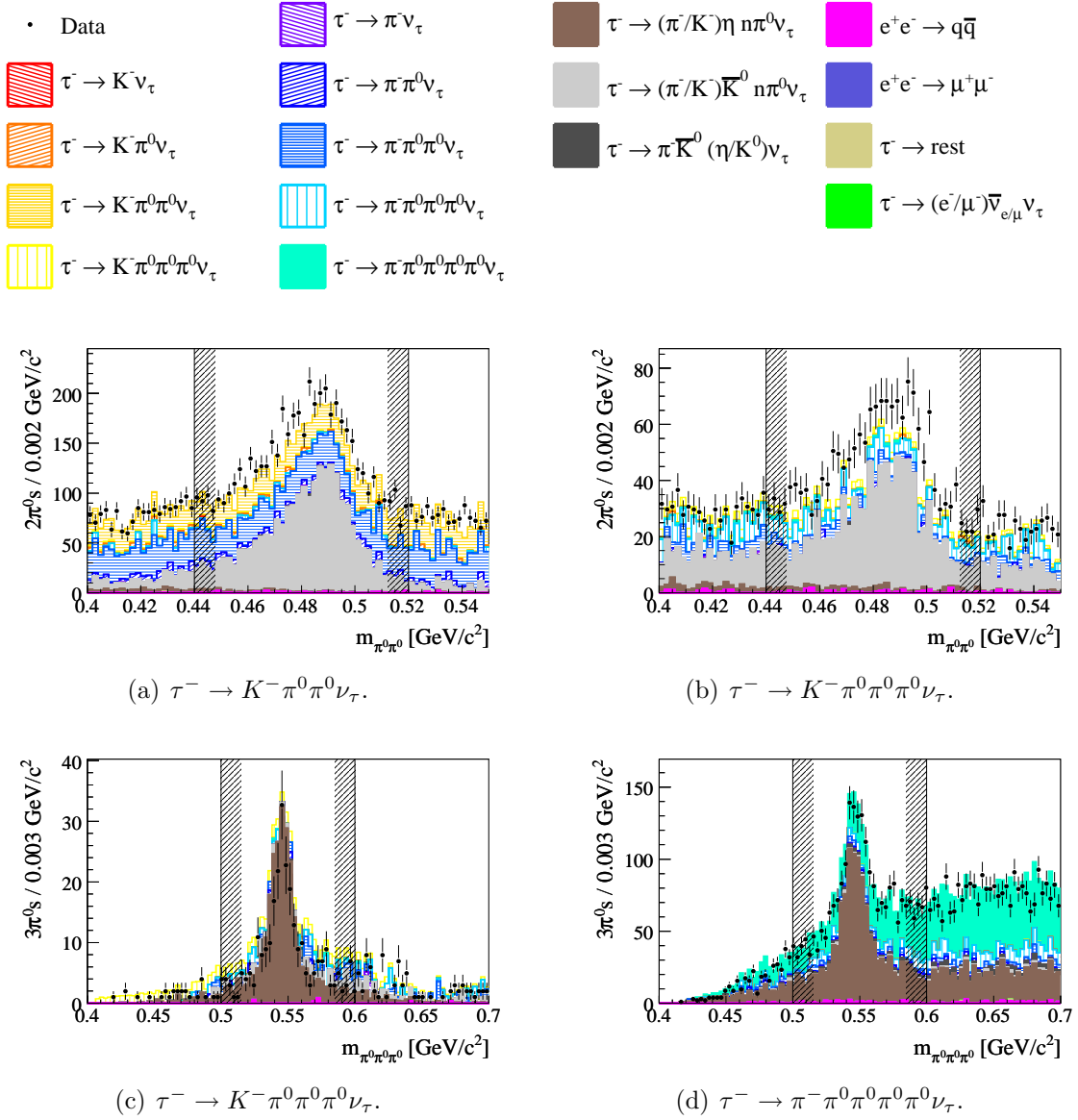**Figure 4.12:** Distributions of the invariant $\pi^0\pi^0$ masses $m_{\pi^0\pi^0}$ for $\tau^- \to K^- n\pi^0\nu_\tau$ events with $n = 2, 3$ **(a, b)** and the invariant $\pi^0\pi^0\pi^0$ masses $m_{\pi^0\pi^0\pi^0}$ for **(c)** $\tau^- \to K^-\pi^0\pi^0\pi^0\nu_\tau$ and **(d)** $\tau^- \to \pi^-\pi^0\pi^0\pi^0\pi^0\nu_\tau$ reactions in the relevant resonance regions (see text). The labels $2\pi^0 s$ and $3\pi^0 s$ refer to the combinations of π^0 pairs and triplets plotted in each histogram. Due to the ambiguity in combining the π^0 mesons, **(b)** contains three and **(d)** four entries per event. The selection criteria on these variables are indicated by the vertical lines.

significant case of selected events of the type $\tau^- \to \pi^-\pi^0\pi^0\nu_\tau$ in Section 5.5. The agreement for the modes $\tau^- \to K^-\pi^0\pi^0\nu_\tau$ and $\tau^- \to K^-\pi^0\pi^0\pi^0\nu_\tau$ is reasonable, albeit strongly statistically limited, especially in the latter case.

However, the agreement in the overall normalization is reasonably well described—also for the mode $\tau^- \to \pi^-\pi^0\pi^0\nu_\tau$, whose branching fraction is known with high precision, $\mathcal{B}(\tau^- \to \pi^-\pi^0\pi^0\nu_\tau) = (9.24 \pm 0.12)\%$ [3]. This is an important feature for

Table 4.2: Summary of the criteria applied to select reactions of the type $e^+e^- \to \tau^+\tau^-$ and to reject cross feed between the different decay modes of the signal τ lepton.

Quantity	Selection criteria		
Thrust		T	> 0.87
Event topology		1–1	
K_S^0 veto		$N_{K_S^0}$	$= 0$
Photon conversion veto		N_{conv}	$= 0$
Charge conservation		Q	$= 0$
Track fiducial volume	$0.45 <$	θ_{track}	$< 2.36\,\mathrm{rad}$
Lepton identification		N_ℓ	≥ 1
Electron veto		N_{sig}^e	$= 0$
Hadron-π^0 angle		$\alpha_{h\pi^0}^{\mathrm{cms}}$	$< 1.5\,\mathrm{rad}$
Unassociated neutral energy		E_{unass}	$< 0.1\,\mathrm{GeV}$

this analysis. In Section 5.4, any remaining deviations in the overall normalization are used to estimate the uncertainties of the branching fractions that result from the method of the π^0 efficiency correction as described in Sections 5.1 and 5.2. In addition, uncertainties due to deviations in the description of the selection variables by the Monte Carlo simulation are derived in Section 6.5.11.

Table 4.3: Summary of the selection criteria applied to reject remaining background from QED processes and reactions of the type $e^+e^- \to q\bar{q}$ and $e^+e^- \to \tau^+\tau^-$. The column *signal track* specifies if a criterion is applied to one or to both types of charged hadrons, π and K. The actual criteria for modes with the given number of π^0 mesons are listed in the columns $N_{\pi^0} = 0 - 4$. A "–" indicates that the given mode is not reconstructed, i. e., that the criterion is not applicable.

Quantity	Signal track				$N_{\pi^0} = 0$	$N_{\pi^0} = 1$	$N_{\pi^0} = 2$	$N_{\pi^0} = 3$	$N_{\pi^0} = 4$
Lepton momentum	π/K	p_ℓ^{cms}	[GeV/c]	$<$	5.0	5.0	5.0	5.0	5.0
Missing mass	π/K	m_{miss}	[GeV/c^2]	$>$	3.00	1.75	1.50	1.00	1.00
		m_{miss}	[GeV/c^2]	$<$	7.50	7.50	7.50	7.50	7.50
Hadron-lepton acoplanarity	π/K	$\Delta\phi_{h\ell}^{\mathrm{cms}}$	[rad]	$<$	2.95				
	π	T		$>$	–	0.87	0.87	0.87	0.92
	K	T		$>$	0.87	0.87	0.91	0.92	–
	K	m_ν^2	[GeV^2/c^4]	$>$	-0.5	-0.4	-0.4	-0.4	–
Signal side neutrino mass	K	m_ν^2	[GeV^2/c^4]	$<$	0.9	0.4	0.2	0.1	–
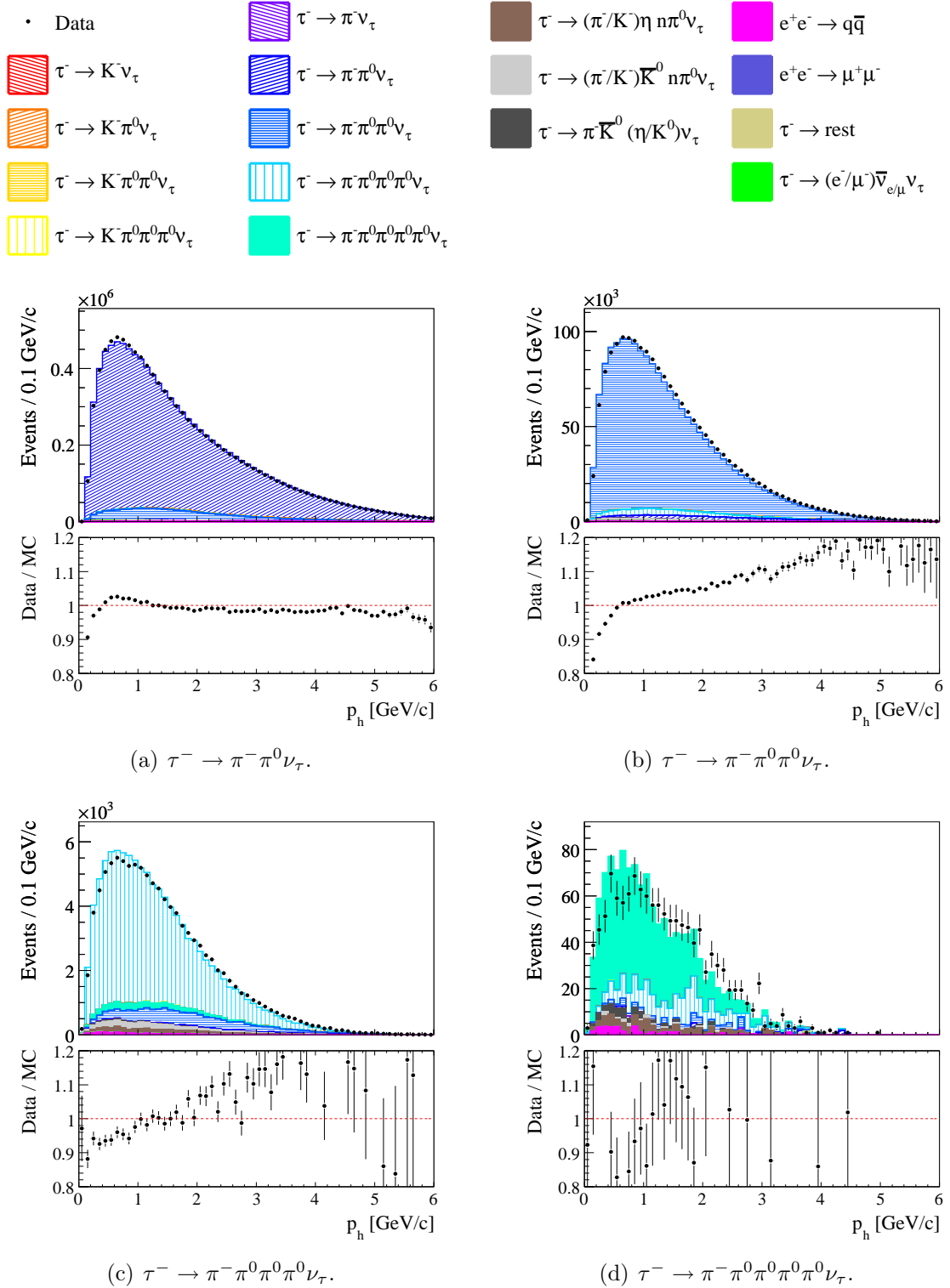
Figure 4.13: Distributions of the momentum p_h of the charged hadron for the different event categories without net strangeness, $\tau^- \to \pi^- n\pi^0 \nu_\tau$ with $n = 1, 2, 3, 4$. No selection criterion is imposed on this quantity.
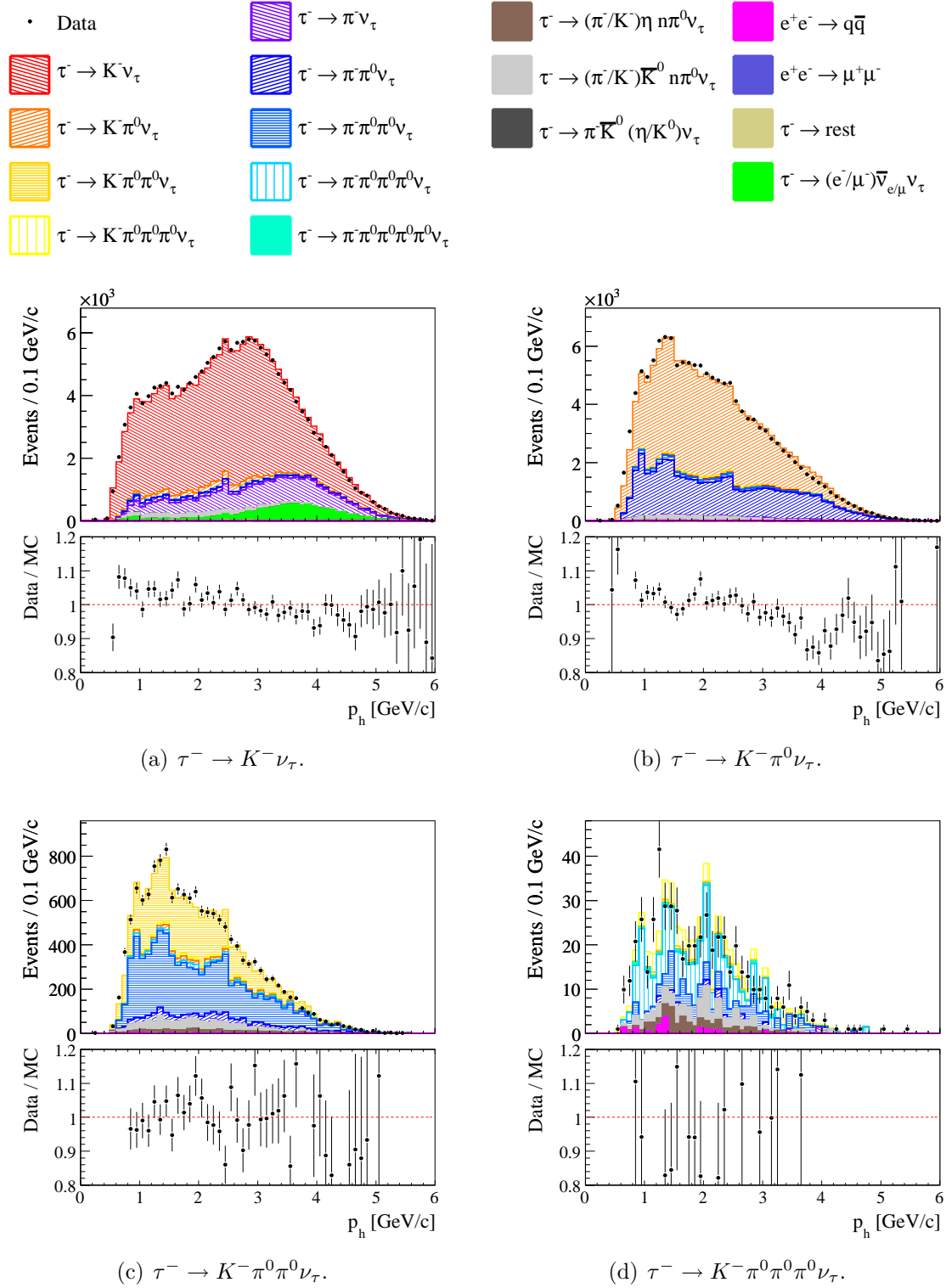
Figure 4.14: Distributions of the momentum p_h of the charged hadron for the different event categories with net strangeness, $\tau^- \to K^- n\pi^0 \nu_\tau$ with $n = 0, 1, 2, 3$. No selection criterion is imposed on this quantity.

Chapter 5

Systematics of the π^0 selection

Differences between the π^0 selection efficiency in data and Monte Carlo simulation are the dominant systematic uncertainty for branching fraction measurements of τ decays into final states containing π^0 mesons [26]. They are caused by deviations in the underlying photon quantities, e.g., the shower shape in the electromagnetic calorimeter (Figure 5.11). The standard treatment of these differences within the *BABAR* collaboration is an efficiency correction of $(-1.9 \pm 3.3)\,\%$ per π^0, which is applied to simulated events [72]. Two problems arise when using this correction within the presented analysis. Firstly, an uncertainty of $3.3\,\%$ per π^0 severely limits the possible precision of branching fraction measurements for final states containing multiple π^0 mesons. Secondly, at an early stage of this analysis, the standard π^0 efficiency correction was used to study the precisely measured decay modes $\tau^- \to \pi^- \pi^0 \nu_\tau$ and $\tau^- \to \pi^- \pi^0 \pi^0 \nu_\tau$ as selected in Chapter 4. The study showed that significant normalization differences between data and Monte Carlo simulation of 6 and $12\,\%$, respectively, still remain after the application of the standard π^0 efficiency correction.

One reason for the remaining deviations are differences in the selections of π^0 mesons for the determination of the standard correction and in the framework of this analysis. The standard π^0 efficiency correction is only determined using relatively loose π^0 selection criteria, which are not suited for the analysis of final states containing multiple π^0 mesons. As the deviations are caused by differences in the underlying photon quantities, which are used to select π^0 mesons, the discrepancies between data and Monte Carlo simulation are expected to depend on the selection criteria. In addition, the π^0 efficiencies in data and Monte Carlo simulation that are used to determine the standard efficiency correction are determined from the ratio of selected events of the type $\tau^- \to \pi^- \pi^0 \nu_\tau$ and $\tau^- \to \pi^- \nu_\tau$ [72]. A lepton tag is required, i.e., the second τ lepton in the event is reconstructed in its fully leptonic decay mode, $\tau^- \to \ell^- \overline{\nu}_\ell \nu_\tau$ with $\ell^- = e^-, \mu^-$ (Chapter 4). However, it was found within this work that decays of the type $\tau^- \to \pi^- \nu_\tau$ cannot be properly reconstructed in conjunction with a lepton tag due to the large amount of remaining QED backgrounds in the data, for which no appropriate Monte Carlo simulation exists (Sections 4.5, 2.3). In consequence, the correctness of the standard π^0 efficiency correction is questionable and it is not used within this analysis.

A possible solution to avoid both the large uncertainties in case of multiple π^0 mesons and the incorrectness of the standard π^0 efficiency correction would be a relative

measurement of each decay mode $\tau^- \to K^- n\pi^0 \nu_\tau$ with respect to the corresponding mode $\tau^- \to \pi^- n\pi^0 \nu_\tau$. In this case, most systematic effects and uncertainties related to the π^0 selection would cancel in first order. However, as many of the quantities needed for the event selection and the determination of the branching fractions are correlated between the different modes (Section 6.5) and as cross feed between modes with different numbers of π^0 mesons is not negligible (Section 4.4), the correlations between the measured branching fractions are expected to be significant and cannot be neglected. In consequence, separate relative measurements for each decay mode are not possible and a simultaneous determination of all branching fractions is needed to correctly account for all correlations.

To still profit from the benefits of a relative measurement, the π^0 efficiency correction is determined using the precisely measured decays of the type $\tau^- \to \pi^- \pi^0 \nu_\tau$ and applied for each π^0 in events containing (multiple) π^0 mesons. In this way, all π^0-related uncertainties cancel for the first π^0 in first order. The basic principle of this method is the fact that—apart from the π^0 selection efficiency—the Monte Carlo simulation of these decays is well understood and describes the data. It uses the precisely measured branching fraction $\mathcal{B}(\tau^- \to \pi^- \pi^0 \nu_\tau) = (25.46 \pm 0.12)\,\%$ [3] and all known deviations between data and Monte Carlo simulation, e.g., due to the charged particle reconstruction and identification, are corrected as described in Section 3.5. Thus, any remaining deviations are solely attributed to differences in the π^0 selection efficiency between data and simulated reactions.

This chapter presents the determination of the π^0 efficiency correction as needed for this analysis (Section 5.1) It also describes the application of this correction to simulated events containing (multiple) π^0 mesons (Section 5.2). Section 5.3 discusses systematic studies performed to validate and test the π^0 efficiency correction using the precisely measured decays of the type $\tau^- \to \pi^- \pi^0 \nu_\tau$ and $\tau^- \to \pi^- \pi^0 \pi^0 \nu_\tau$. In particular, reactions of the type $\tau^- \to \pi^- \pi^0 \pi^0 \nu_\tau$ are used to estimate a systematic uncertainty of the π^0 efficiency correction method (Section 5.4). A study of the kinematics in final states of the type $\pi^- \pi^0 \pi^0$ is summarized in Section 5.5. The chapter ends with a critical discussion of the presented methods and phenomena in Section 5.6.

5.1   Determination of the π^0 efficiency correction

The π^0 *selection efficiency* ε_{π^0} is defined as the probability to reconstruct a π^0 meson using the selection criteria summarized in Section 3.4. If a sample contains $N_{\pi^0}^{\mathrm{prod}}$ (produced) neutral pions of which $N_{\pi^0}^{\mathrm{sel}}$ are reconstructed (selected), the efficiency is

$$\varepsilon_{\pi^0} \equiv \frac{N_{\pi^0}^{\mathrm{sel}}}{N_{\pi^0}^{\mathrm{prod}}}\,. \tag{5.1}$$

It can be determined with the help of events of the (true) type $e^+ e^- \to \tau^+ (\to \ell^+ \nu_\ell \overline{\nu}_\tau) \tau^- (\to \pi^- \pi^0 \nu_\tau)$. They are selected as described in Chapter 4. Each of these events contains one π^0 meson. The number of events thus corresponds to the number of π^0 mesons in the event sample. The total efficiency to select an event of this type $\varepsilon_{\pi\pi^0}$ can be splitted into the efficiency to select a π^0 meson ε_{π^0} and the efficiency of the

remaining selection criteria $\varepsilon_{\pi\pi^0}^{\not\pi^0}$ (e. g., tracking and charged particle identification):

$$\varepsilon_{\pi\pi^0} \equiv \frac{N_{\pi\pi^0}^{\mathrm{sel}}}{N_{\pi\pi^0}^{\mathrm{prod}}} = \varepsilon_{\pi\pi^0}^{\not\pi^0} \cdot \varepsilon_{\pi^0} \ . \tag{5.2}$$

The symbols $N_{\pi\pi^0}^{\mathrm{sel}}$ and $N_{\pi\pi^0}^{\mathrm{prod}}$ denote the numbers of selected respectively produced events of the type $\tau^- \to \pi^- \pi^0 \nu_\tau$. Thus, the π^0 selection efficiency can be obtained from events of the type $\tau^- \to \pi^- \pi^0 \nu_\tau$ as

$$\varepsilon_{\pi^0} = \frac{N_{\pi\pi^0}^{\mathrm{sel}}}{\varepsilon_{\pi\pi^0}^{\not\pi^0} N_{\pi\pi^0}^{\mathrm{prod}}} \ . \tag{5.3}$$

Deviations between the π^0 selection efficiency in data and the one in the Monte Carlo simulation can occur due to differences in the underlying photon quantities. They can be corrected for by the application of a π^0 *efficiency correction factor* η_{π^0} to simulated events:

$$\eta_{\pi^0} \equiv \frac{\varepsilon_{\pi^0}^{\mathrm{data}}}{\varepsilon_{\pi^0}^{\mathrm{MC}}} = \frac{\dfrac{\left(N_{\pi\pi^0}^{\mathrm{sel}}\right)_{\mathrm{data}}}{\left(\varepsilon_{\pi\pi^0}^{\not\pi^0}\right)_{\mathrm{data}} \left(N_{\pi\pi^0}^{\mathrm{prod}}\right)_{\mathrm{data}}}}{\dfrac{\left(N_{\pi\pi^0}^{\mathrm{sel}}\right)_{\mathrm{MC}}}{\left(\varepsilon_{\pi\pi^0}^{\not\pi^0}\right)_{\mathrm{MC}} \left(N_{\pi\pi^0}^{\mathrm{prod}}\right)_{\mathrm{MC}}}} \ . \tag{5.4}$$

The $\varepsilon_{\pi^0}^{\mathrm{data}}$ and $\varepsilon_{\pi^0}^{\mathrm{MC}}$ are the above defined π^0 selection efficiencies, the $(\varepsilon_{\pi\pi^0}^{\not\pi^0})_{\mathrm{data/MC}}$ the efficiencies of the remaining selection criteria and the $(N_{\pi\pi^0}^{\mathrm{sel/prod}})_{\mathrm{data/MC}}$ the numbers of selected/produced events of the type $\tau^- \to \pi^- \pi^0 \nu_\tau$ in data and Monte Carlo simulation respectively. While the efficiency of the remaining selection criteria in the Monte Carlo simulation can be directly determined from the known number of selected events of (true) type $\tau^- \to \pi^- \pi^0 \nu_\tau$ at each stage of the event selection, the corresponding efficiency in data cannot be obtained directly. However, if the simulation describes all aspects of the real data apart from the π^0 efficiency, the efficiency is equal in data and Monte Carlo simulation and cancels in Equation 5.4. Thus, for the remainder of this chapter, all known deviations between data and Monte Carlo simulation other than those due to the π^0 selection, i. e., the ones due to the charged particle reconstruction and identification, are corrected as described in Section 3.5. In this case, any remaining deviation between data and Monte Carlo simulation results from differences in the π^0 selection efficiencies.

Similarly, if the Monte Carlo simulation uses the precisely measured branching fraction $\mathcal{B}(\tau^- \to \pi^- \pi^0 \nu_\tau) = (25.46 \pm 0.12)\,\%$ [3] and is scaled to the data luminosity as described in Section 6.1, the number of produced events of (true) type $\tau^- \to \pi^- \pi^0 \nu_\tau$ in the Monte Carlo simulation is equal to the a-priori unknown one in data. Thus, both numbers also cancel and Equation 5.4 simplifies to

$$\eta_{\pi^0} = \frac{\left(N_{\pi\pi^0}^{\mathrm{sel}}\right)_{\mathrm{data}}}{\left(N_{\pi\pi^0}^{\mathrm{sel}}\right)_{\mathrm{MC}}} \ . \tag{5.5}$$

The number of selected events of the (true) type $\tau^- \to \pi^- \pi^0 \nu_\tau$ is determined directly for the Monte Carlo simulation. However, the selected data sample is not free from

remaining background. Its amount $N_{\mathrm{BG}}^{\mathrm{sel}}$ is estimated using Monte Carlo simulation and subtracted from the number of selected events in data $N_{\mathrm{data}}^{\mathrm{sel}}$:

$$
\begin{aligned}
\left(N_{\pi\pi^0}^{\mathrm{sel}}\right)_{\mathrm{data}} &= N_{\mathrm{data}}^{\mathrm{sel}} - N_{\mathrm{MC,BG}}^{\mathrm{sel}} \\
&= N_{\mathrm{data}}^{\mathrm{sel}} - \sum_j N_{\mathrm{MC,BG}(j)}^{\mathrm{sel}} .
\end{aligned}
\tag{5.6}
$$

The symbol $N_{\mathrm{MC,BG}}^{\mathrm{sel}}$ denotes the number of selected background events in the Monte Carlo simulation. It is obtained as a sum of the selected events $N_{\mathrm{MC,BG}(j)}^{\mathrm{sel}}$ from all contributing background modes j. In this case, the sum over the background modes j contains all simulated modes other than $\tau^- \to \pi^- \pi^0 \nu_\tau$, including the decay channels measured in this analysis (Chapter 6). Combining Equations 5.5 and 5.6, the π^0 efficiency correction can be obtained from selected events of the type $\tau^- \to \pi^- \pi^0 \nu_\tau$ as

$$
\eta_{\pi^0} = \frac{\left(N_{\pi\pi^0}^{\mathrm{sel}}\right)_{\mathrm{data}}}{\left(N_{\pi\pi^0}^{\mathrm{sel}}\right)_{\mathrm{MC}}} = \frac{N_{\mathrm{data}}^{\mathrm{sel}} - N_{\mathrm{MC,BG}}^{\mathrm{sel}}}{\left(N_{\pi\pi^0}^{\mathrm{sel}}\right)_{\mathrm{MC}}} .
\tag{5.7}
$$

However, this method only works if the remaining background in the data sample is well described by the subtracted simulated background, i.e., if all deviations between data and Monte Carlo simulation—including those due to differences in the π^0 selection— are corrected for the simulated background events. In consequence, the π^0 efficiency correction is determined iteratively according to Equation 5.5. For each iteration, the π^0 efficiency correction from the previous one is used to correct the Monte Carlo simulated background as described in Section 5.2.

In principle, this iterative procedure would in turn have to be performed multiple times, as the subtracted backgrounds also contain the decay modes that are measured in this analysis. Their branching fractions are needed to correctly scale the subtracted backgrounds to the data luminosity (Section 6.1). But the background in selected events of the type $\tau^- \to \pi^- \pi^0 \nu_\tau$ is dominated by the precisely measured modes $\tau^- \to \pi^- \nu_\tau$ and $\tau^- \to \pi^- \pi^0 \pi^0 \nu_\tau$ (Figure 5.1, [3]). The background contribution from decay modes that are measured within this analysis is negligible. In consequence, the determination of the π^0 efficiency correction is performed using the world averages for all τ branching fractions [3].

Due to the correlation between the π^0 energy and the opening angle of the two daughter photons,[1] the deviations between data and Monte Carlo simulation are expected to depend on the π^0 energy. E.g., differences between the shower shapes in data and Monte Carlo simulation are expected to cause different effects at small photon-photon angles (i.e., at large π^0 energies) than at large angles (small energies). Because of the different π^0 energy spectra of the decay modes that are analyzed in this work (Figures B.1, B.2), an energy-dependent π^0 efficiency correction is thus necessary. This is achieved by considering Equation 5.5 as a function of the π^0 energy E_{π^0}:

$$
\eta_{\pi^0}(E_{\pi^0}) = \frac{N_{\mathrm{data}}^{\mathrm{sel}}(E_{\pi^0}) - N_{\mathrm{MC,BG}}^{\mathrm{sel}}(E_{\pi^0})}{\left(N_{\pi\pi^0}^{\mathrm{sel}}\right)_{\mathrm{MC}}(E_{\pi^0})} ,
\tag{5.8}
$$

---

[1]The invariant photon-photon mass is $m_{\gamma\gamma} = \sqrt{2 E_{\gamma_1} E_{\gamma_2} \left(1 + \cos \alpha_{\gamma_1 \gamma_2}\right)}$, where E_{γ_i} is the energy of photon i and $\alpha_{\gamma_1 \gamma_2}$ is the photon-photon opening angle. It is constrained to the π^0 mass and thus relates the opening angle and the π^0 energy $E_{\pi^0} = E_{\gamma_1} + E_{\gamma_2}$.

where $N^{\mathrm{sel}}_{\mathrm{data}}(E_{\pi^0})$ is the number of selected events of the type $\tau^- \to \pi^- \pi^0 \nu_\tau$ in data as a function of the π^0 energy. The symbol $N^{\mathrm{sel}}_{\mathrm{MC, BG}}(E_{\pi^0})$ denotes the number of selected simulated background events and $(N^{\mathrm{sel}}_{\pi\pi^0})_{\mathrm{MC}}(E_{\pi^0})$ the number of selected simulated events of the (true) type $\tau^- \to \pi^- \pi^0 \nu_\tau$.

5.1.1 Description of the data by the Monte Carlo simulation

An essential prerequisite for the above described determination of the π^0 efficiency correction is a good agreement between data and Monte Carlo simulation in all aspects that are not related to the π^0 reconstruction. This can be verified using the decay products of the leptonic τ decay. Due to kinematic correlations between the decay products of the signal τ lepton, the kinematics of the charged pion are influenced by the energy-dependent differences of the π^0 efficiency in data and Monte Carlo simulation. They cannot be used to verify the agreement prior to the application of the π^0 efficiency correction.

Figure 5.1 shows the lepton momentum and polar angle in the laboratory system for selected events of the type $\tau^- \to \pi^- \pi^0 \nu_\tau$. To remove the normalization difference

(a) Momentum. (b) Polar angle.
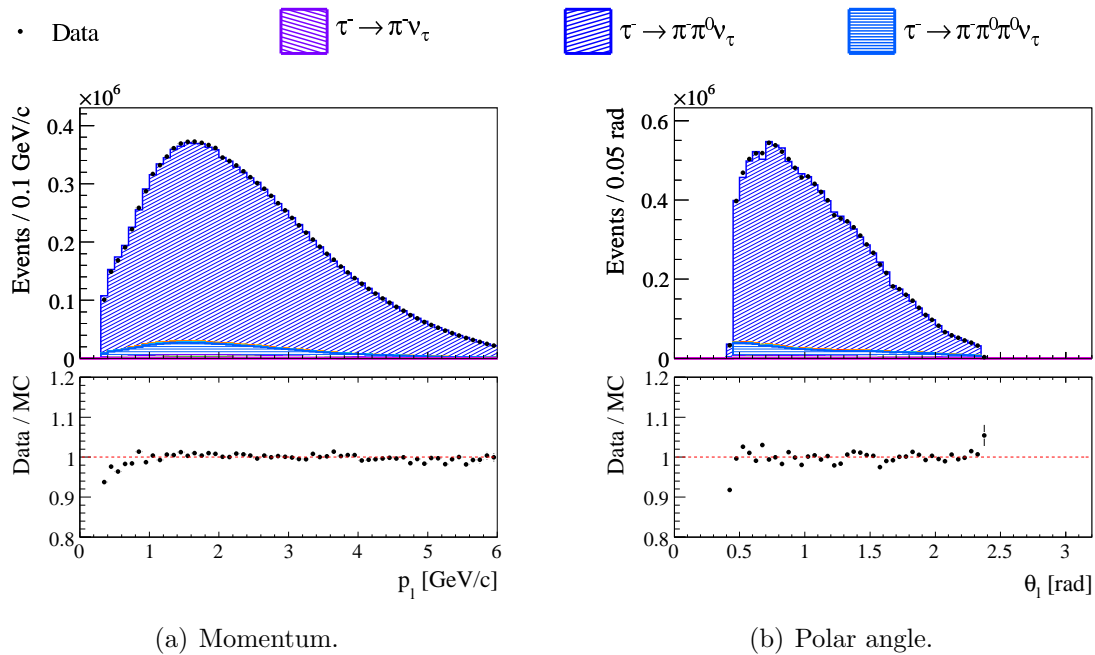
Figure 5.1: Distributions of the **(a)** lepton momentum p_ℓ and **(b)** polar angle θ_ℓ in the laboratory system for selected events of the type $\tau^- \to \pi^- \pi^0 \nu_\tau$. Data and Monte Carlo simulated distributions have been normalized to equal area. Only statistical uncertainties are included and all corrections except the π^0 efficiency correction are applied to the Monte Carlo simulated events as described in Section 3.5. The deviation at small momenta is caused by a known artifact of the track reconstruction [53, 73].

caused by differing π^0 efficiencies, data and Monte Carlo simulated distributions have been normalized to equal area. Both quantities exhibit a good description of the data by the Monte Carlo simulation except at very small momenta. This deviation is due to

a known artifact of the track reconstruction [53, 73]. Its influence on the overall event rate needed to extract the branching fractions is corrected for by the tracking efficiency correction. In consequence, selected events of the type $\tau^- \to \pi^- \pi^0 \nu_\tau$ can be used to extract an energy-dependent π^0 efficiency correction [53].

5.1.2   The π^0 efficiency correction

To determine the numbers of selected events in data and Monte Carlo simulation as needed in Equation 5.8, events that contain a decay of the type $\tau^- \to \pi^- \pi^0 \nu_\tau$ are selected. Since the rate of spurious π^0 mesons due to hadronic split-offs at small angles to the signal track is not described by the Monte Carlo simulation (Sections 3.2, 5.3.2), a minimal angular separation of the π^0 and the charged pion is required in addition to all selection criteria described in Chapter 4:

$$\alpha_{\pi\pi^0} > 0.25 \, \text{rad} \,, \tag{5.9}$$

where $\alpha_{\pi\pi^0}$ is the angle between the π^0 and the pion track in the laboratory system. A detailed study of split-offs and the implications for this analysis are presented in Section 5.3.2.

Figure 5.2(a) shows the π^0 energy distribution in selected events of the type $\tau^- \to \pi^- \pi^0 \nu_\tau$. For each bin, the energy-dependent π^0 efficiency correction η_{π^0} is calculated

(a) π^0 energy.

(b) π^0 efficiency correction.
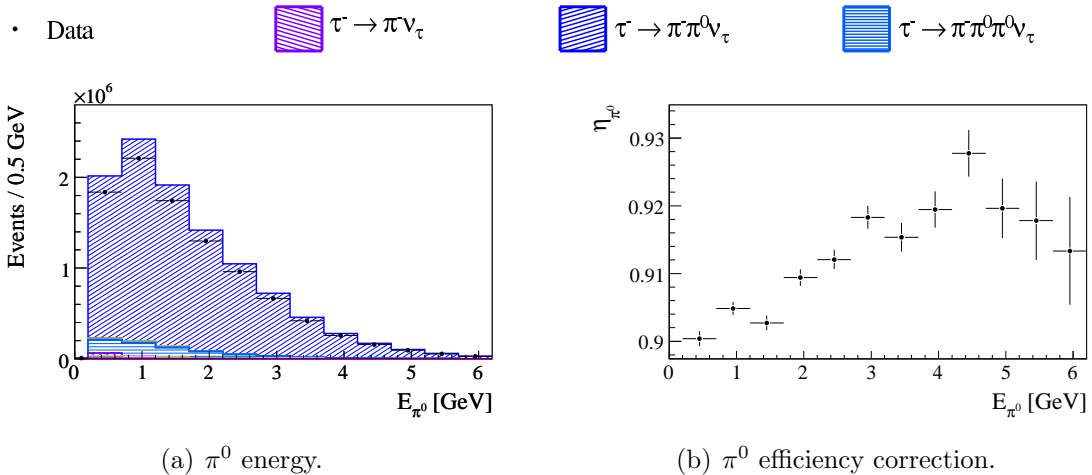
Figure 5.2: Neutral pion efficiency correction as a function of the π^0 energy E_{π^0} extracted from $\tau^- \to \pi^- \pi^0 \nu_\tau$ decays. The π^0 energy is shown in **(a)** for selected events of the type $\tau^- \to \pi^- \pi^0 \nu_\tau$. All corrections except the π^0 efficiency correction are applied to the Monte Carlo simulated events as described in Section 3.5 and only statistical uncertainties are included. **(b)** displays the π^0 efficiency correction η_{π^0} as obtained from the ratio $(N_{\text{data}} - N_{\text{MC, BG}})/N_{\text{MC, sig}}$ according to Equation 5.8.

according to Equation 5.8. To correctly treat the subtracted background, the iterative procedure is used as described above. The iteration is terminated if the correction factors in each bin as well as the energy-averaged overall correction factor do not change anymore within their statistical uncertainties. Figure 5.2(b) displays the resulting π^0

efficiency correction η_{π^0} after three iterations. To facilitate a smooth description and application of the π^0 efficiency correction, the actual correction for a given energy E_{π^0} is obtained as a linear interpolation of the neighboring energy bins.

5.2   Application of the π^0 efficiency correction

Analogous to the track efficiency correction and the efficiency correction for the charged particle identification (Section 3.5), the π^0 efficiency correction is applied in the form of event weights to each simulated event. A general event in this analysis contains n_{prod} produced π^0 mesons of which ($n_{\mathrm{reco}} \leq n_{\mathrm{prod}}$) are reconstructed. In addition to the event weights for all reconstructed π^0 mesons, weights also need to be applied for those π^0 mesons that escape detection, i.e., that are missed. This is necessary to correctly simulate the down-feed of events with n (true) π^0 mesons into the event sample with $(n-1)$ reconstructed π^0 mesons. Using the definition of the π^0 efficiency correction η_{π^0} from Equation 5.4, the correction weight $\eta_{\not\pi^0}$ for a missed π^0 is

$$\eta_{\not\pi^0} \equiv \frac{\varepsilon_{\not\pi^0}^{\mathrm{data}}}{\varepsilon_{\not\pi^0}^{\mathrm{MC}}} = \frac{1 - \varepsilon_{\pi^0}^{\mathrm{data}}}{1 - \varepsilon_{\pi^0}^{\mathrm{MC}}} = \frac{1 - \varepsilon_{\pi^0}^{\mathrm{MC}} \eta_{\pi^0}}{1 - \varepsilon_{\pi^0}^{\mathrm{MC}}} \ . \tag{5.10}$$

The $\varepsilon_{\pi^0}^{\mathrm{data}}$ and $\varepsilon_{\pi^0}^{\mathrm{MC}}$ are the π^0 efficiencies in data and Monte Carlo simulation and the $\varepsilon_{\not\pi^0} = 1 - \varepsilon_{\pi^0}$ are the corresponding inefficiencies. The total weight $\eta_{(n_{\mathrm{reco}}, n_{\mathrm{prod}})}$ for a general event with n_{prod} produced and n_{reco} reconstructed, i.e., $n_{\mathrm{miss}} = (n_{\mathrm{prod}} - n_{\mathrm{reco}})$ missed π^0 mesons is the product of the (energy-dependent) weights for all π^0 mesons:

$$
\begin{aligned}
\eta_{(n_{\mathrm{reco}}, n_{\mathrm{prod}})}(\{E_i\}) &= \prod_j^{n_{\mathrm{reco}}} \eta_{\pi^0}(E_j) \prod_k^{(n_{\mathrm{prod}} - n_{\mathrm{reco}})} \eta_{\not\pi^0}(E_k) \\
&= \prod_j^{n_{\mathrm{reco}}} \eta_{\pi^0}(E_j) \prod_k^{(n_{\mathrm{prod}} - n_{\mathrm{reco}})} \frac{1 - \varepsilon_{\pi^0}^{\mathrm{MC}} \eta_{\pi^0}}{1 - \varepsilon_{\pi^0}^{\mathrm{MC}}}(E_k) \ ,
\end{aligned}
\tag{5.11}
$$

where the E_i are the energies of all produced π^0 mesons.

Equation 5.11 shows that, in addition to the π^0 efficiency correction, the energy-dependent absolute π^0 efficiency in the Monte Carlo simulation is needed to calculate the full correction factor. It is determined from simulated events of the type $\tau^- \to \pi^- \pi^0 \nu_\tau$ and displayed in Figure 5.3. The decrease at small energies is caused by the requirement of a minimal photon energy of $0.075\,\mathrm{GeV}$ (Section 3.4). In contrast, the decrease at large energies is due to an increasing fraction of merged π^0 mesons. The constraint of the invariant photon-photon mass to the π^0 mass causes an anti-correlation of the π^0 energy and the photon-photon angle (Section 5.1). I.e., the photon daughters of high-energetic π^0 mesons are closer together, which increases the relative fraction of merged π^0 mesons. As these are not reconstructed in this analysis, they cause a decrease of the selection efficiency. A more detailed study of the relative fractions of merged and composite π^0 mesons for the specific π^0 energy spectra in this analysis is presented in Section 5.3.3.

To obtain a smooth description of the π^0 efficiency, the individual bins in Figure 5.3 are interpolated with a linear function when extracting the π^0 efficiency for a given π^0 energy E_{π^0}.
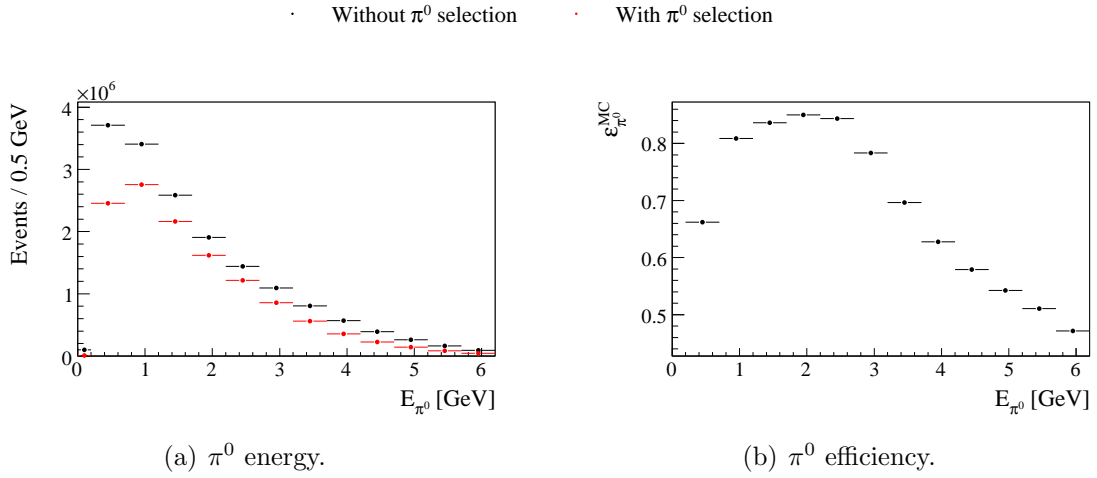
· Without π^0 selection   · With π^0 selection

(a) π^0 energy.

(b) π^0 efficiency.

Figure 5.3: The π^0 efficiency as a function of the π^0 energy E_{π^0} extracted from simulated decays of the type $\tau^- \to \pi^- \pi^0 \nu_\tau$. The numbers of events with (N^{sel}, red dots) and without (N^{prod}, black dots) π^0 selection are shown in **(a)** as a function of the π^0 energy. **(b)** displays the efficiency of the π^0 selection, $\varepsilon^{\mathrm{MC}} \equiv (N^{\mathrm{sel}}/N^{\mathrm{prod}})_{\mathrm{MC}}$. Only statistical uncertainties are included.

5.2.1 Combinatorial photon pairs

When applying the π^0 efficiency correction, which is determined from single-π^0 events, to final states that contain multiple π^0 mesons, a fundamental difference between these two types of events needs to be considered: *combinatorial* background from randomly combined photons. Each one-π^0 event ideally contains exactly two real photons and hence one unique π^0 candidate (modulo initial and final state radiation). In contrast, final states with n π^0 mesons contain at least $2n$ real photons and thus

$$n_{\gamma\gamma} = \binom{2n}{2} \tag{5.12}$$

two-photon combinations, i.e., π^0 candidates. For events with two π^0 mesons, $n_{\gamma\gamma} = 6$, in case of three π^0 mesons, $n_{\gamma\gamma} = 15$.

As described in Section 3.4.2, spurious π^0 mesons caused by randomly combined photons are rejected by requiring that each photon be only used once to reconstruct a π^0 meson. The necessity of this criterion is illustrated by Figure 5.4. Figure 5.4(a) shows the π^0 energies for selected events of the type $\tau^- \to \pi^- \pi^0 \pi^0 \pi^0 \nu_\tau$, where a π^0 is defined as a photon-photon combination that fulfills the criteria specified in Table 3.1. I. e., spurious π^0 mesons due to random $\gamma\gamma$ combinations are not removed once they pass the listed selection criteria. The measured branching fractions in the Monte Carlo simulation—including the one of the mode $\tau^- \to \pi^- \pi^0 \pi^0 \pi^0 \nu_\tau$—are reweighted to the results obtained in Chapter 6 and the mode $\tau^- \to \pi^- \pi^0 \pi^0 \nu_\tau$ uses the precisely measured world average $\mathcal{B}(\tau^- \to \pi^- \pi^0 \pi^0 \nu_\tau) = (9.24 \pm 0.12)\,\%$ [3]. All corrections summarized in Section 3.5 including the π^0 efficiency correction described above are applied to the Monte Carlo simulated events.
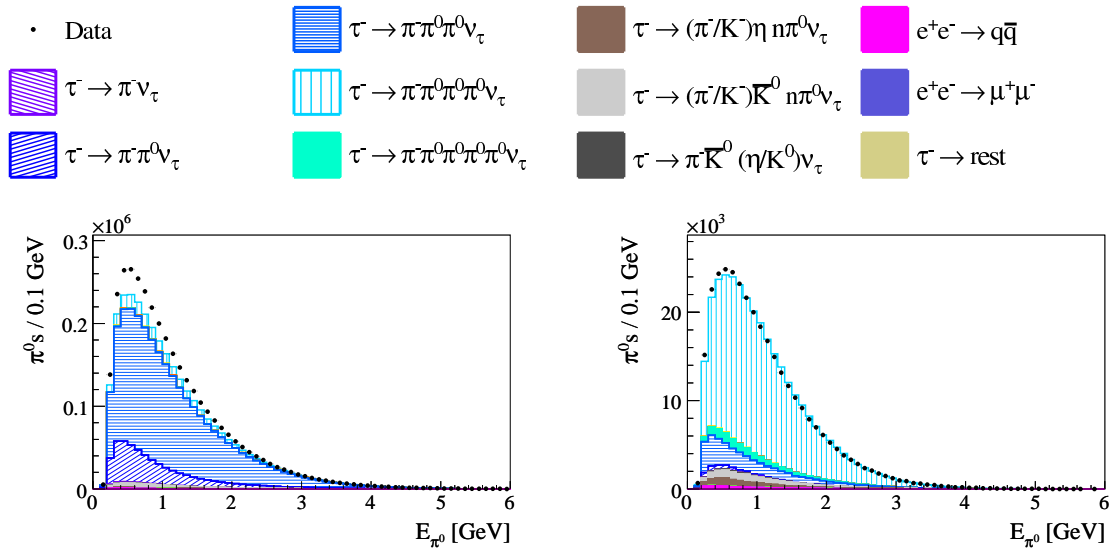
(a) No removal of combinatorial background.   (b) Removed combinatorial background.

Figure 5.4: Distributions of the π^0 energies E_{π^0} for selected reactions of the type $\tau^- \to \pi^- \pi^0 \pi^0 \pi^0 \nu_\tau$. The histogram in **(a)** contains events in which spurious π^0 mesons due to combinatorial photon pairs have not been eliminated, **(b)** displays reactions in which combinatorial photon pairs have been removed as described in Section 3.4.2. In both cases, the measured branching fractions are reweighted to the results obtained in Chapter 6 and the mode $\tau^- \to \pi^- \pi^0 \pi^0 \nu_\tau$ uses the precisely measured world average $\mathcal{B}(\tau^- \to \pi^- \pi^0 \pi^0 \nu_\tau) = (9.24 \pm 0.12)\,\%$ [3]. All corrections described in Section 3.5 including the π^0 efficiency correction from Section 5.1 are applied to the Monte Carlo simulated events.

Two important features are observed in Figure 5.4(a). Firstly, the sample of events that contain three reconstructed π^0 mesons is dominated by events of the (true) type $\tau^- \to \pi^- \pi^0 \pi^0 \nu_\tau$. This is caused by the above described combinatorial photon pairs in conjunction with the ratio of the branching fractions, $\mathcal{B}(\tau^- \to \pi^- \pi^0 \pi^0 \nu_\tau)/\mathcal{B}(\tau^- \to \pi^- \pi^0 \pi^0 \pi^0 \nu_\tau) \approx 10$ [3]. Secondly, the data is not described by the Monte Carlo simulation. An overall excess of 10 % is observed in the data with respect to the simulated event sample. Since the simulated decays of the type $\tau^- \to \pi^- \pi^0 \pi^0 \nu_\tau$ use the precisely measured branching fraction $\mathcal{B}(\tau^- \to \pi^- \pi^0 \pi^0 \nu_\tau) = (9.24 \pm 0.12)\,\%$ [3], they cannot be the reason for the deviation. However, the observed deviation is of similar size as the total amount of selected events of the type $\tau^- \to \pi^- \pi^0 \pi^0 \pi^0 \nu_\tau$. If these reactions were responsible for the deviation, their branching fraction as measured in Section 6.3 would have to be too small by a factor of two. This corresponds to a deviation of more than ten standard deviations from the current world average of $\mathcal{B}(\tau^- \to \pi^- \pi^0 \pi^0 \pi^0 \nu_\tau) = (0.98 \pm 0.09)\,\%$ [3]. In consequence, events of the type $\tau^- \to \pi^- \pi^0 \pi^0 \pi^0 \nu_\tau$ are not responsible for the observed deviation either. It is caused by an excess of approximately 10 % of background due to combinatorial photon pairs in data with respect to the Monte Carlo simulation. As no combinatorial background exists in single-π^0 reactions, it cannot be corrected for by the π^0 efficiency correction, which is determined using

decays of the type $\tau^- \to \pi^- \pi^0 \nu_\tau$ (Section 5.1).

Figure 5.4(b) shows the π^0 energies for selected events of the type $\tau^- \to \pi^- \pi^0 \pi^0 \pi^0 \nu_\tau$ as described in Section 3.4.2, including the rejection of combinatorial π^0 candidates. In this case, at most n π^0 mesons can be reconstructed from $2n$ photons. This is similar to the situation in single-π^0 events. Hence, the π^0 efficiency correction can be applied to multi-π^0 final states whose combinatorial background has been rejected. The reasonable agreement of data and Monte Carlo simulation in Figure 5.4(b) shows that the π^0 efficiency correction works well for final states containing multiple π^0 mesons. Moreover, the background from events of the type $\tau^- \to \pi^- \pi^0 \pi^0 \nu_\tau$ is negligible.

5.3   Systematic studies

This section describes studies that are performed to validate the method of the π^0 efficiency correction. To this end, the description of important π^0 and photon quantities in selected events of the type $\tau^- \to \pi^- \pi^0 \nu_\tau$ is examined after the application of the π^0 efficiency correction. Thus, for the remainder of this chapter, all corrections including the π^0 efficiency correction are applied to all simulated event numbers and distributions.

5.3.1   Precision of the π^0 efficiency correction

Figure 5.5 shows the π^0 energy and the energies of the two daughter photons in the laboratory system for selected events of the type $\tau^- \to \pi^- \pi^0 \nu_\tau$. The agreement between data and Monte Carlo simulation at the 1% level over the entire π^0 energy range in Figure 5.5(a) indicates the precision of the correction procedure. In addition, Figure 5.5(b) displays an agreement between data and simulated events at the sub-per cent level for all but the smallest photon energies and a discontinuity around $1\,\text{GeV}$. The discontinuity is caused by an additional energy correction for high-energy photons that is switched on at an energy of $1\,\text{GeV}$ [74]. The difference at small photon energies is due to a known deviation in the photon reconstruction efficiency [72]. However, the agreement in Figure 5.5(a) shows that the effect is accounted for by the π^0 efficiency correction. In consequence, a correction of the π^0 efficiency as a function of the π^0 energy is sufficient within this analysis. A two-dimensional correction as a function of the photon energies is not necessary.

5.3.2   Split-offs

Figure 5.6 displays the π^--π^0 angle $\alpha_{\pi\pi^0}$ in the laboratory system and the distance $\Delta_{\pi\gamma}^{\text{EMC}}$ between the track extrapolation and the closest of the two daughter photons in the calorimeter front face (cf. Figure 5.7). A significant excess of data events is observed at both small angles, $\alpha_{\pi\pi^0} < 0.25\,\text{rad}$, and small distances, $\Delta_{\pi\gamma}^{\text{EMC}} < 30\,\text{cm}$. For all other angles and distances, the data is described by the Monte Carlo simulation at the 1 and 0.5% level, respectively.

These deviations could be due to hadronic split-offs as described in Section 3.2. Split-offs produce spurious photons and are not described by the Monte Carlo simulation as the used models are not adequate to simulate hadronic showers in this detail. If the
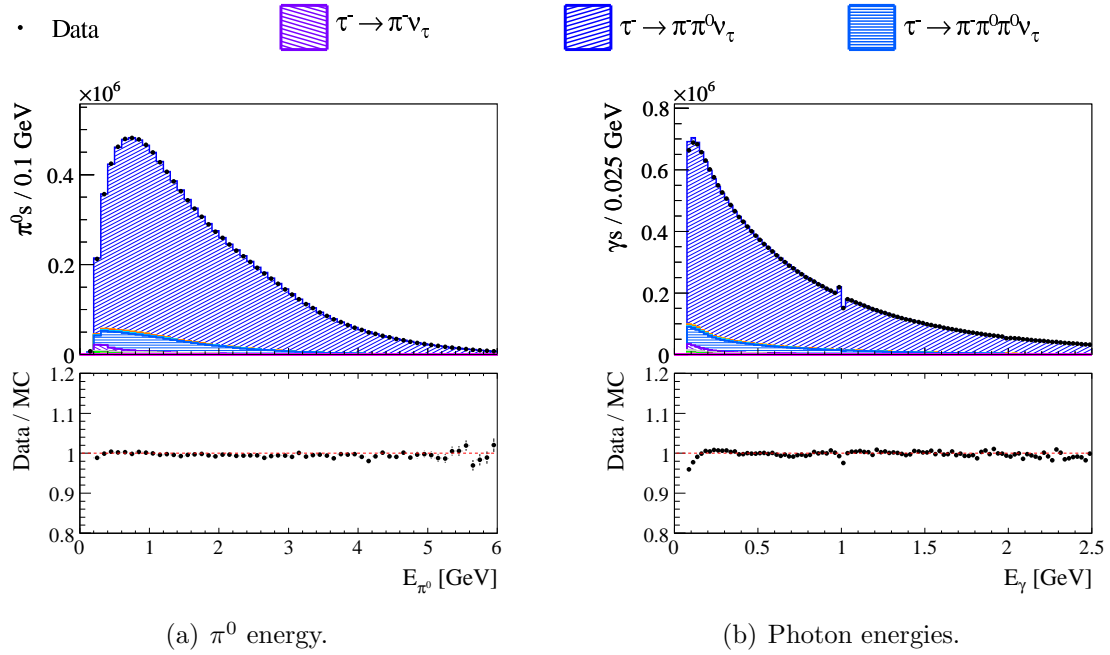
(a) π^0 energy.   (b) Photon energies.

Figure 5.5: Distributions of the **(a)** π^0 and **(b)** π^0 daughter photon energies, E_{π^0}, E_γ, in the laboratory system for events of the type $\tau^- \to \pi^- \pi^0 \nu_\tau$. All corrections including the π^0 efficiency correction are applied to the Monte Carlo simulation. The difference at small photon energies is due to a known deviation in the photon reconstruction efficiency [72]. The discontinuity in the photon energy distribution around 1 GeV is caused by an additional energy correction for high-energy photons that is switched on at an energy of 1 GeV [74].

split-offs produced more spurious photons in data than in the Monte Carlo simulation, an excess of data events at small track-photon distances could be caused by random combinations of the split-offs with real photons.

This hypothesis is investigated by the examination of two types of events:

1. Events with *split-off enhanced* photon candidates. To enrich split-offs, events are considered in which the π^0 daughter photon with the smallest distance to the pion track originates from the same multi-bump calorimeter cluster to which the pion track is matched. In this way, $603,256$ events are selected.

2. Events with *split-off suppressed* photon candidates. To suppress split-offs, only those events are selected in which the π^0 daughter photon with the smallest distance to the pion track originates from a single-bump cluster. This event sample contains $9,819,847$ events and is thus approximately 16 times bigger than the split-off enhanced event sample.

Figure 5.7 illustrates the definition of the two event categories. It displays a schematic view of the energy deposits of the charged pion and the closest π^0 daughter photon for a split-off (Figure 5.7(a)) and a well separated, real photon (Figure 5.7(b)).

The distance $\Delta_{\pi\gamma}^{\mathrm{EMC}}$ is shown in Figure 5.8 for the two event categories. Split-off

(a) π^--π^0 angle. (b) Minimal pion-photon distance.
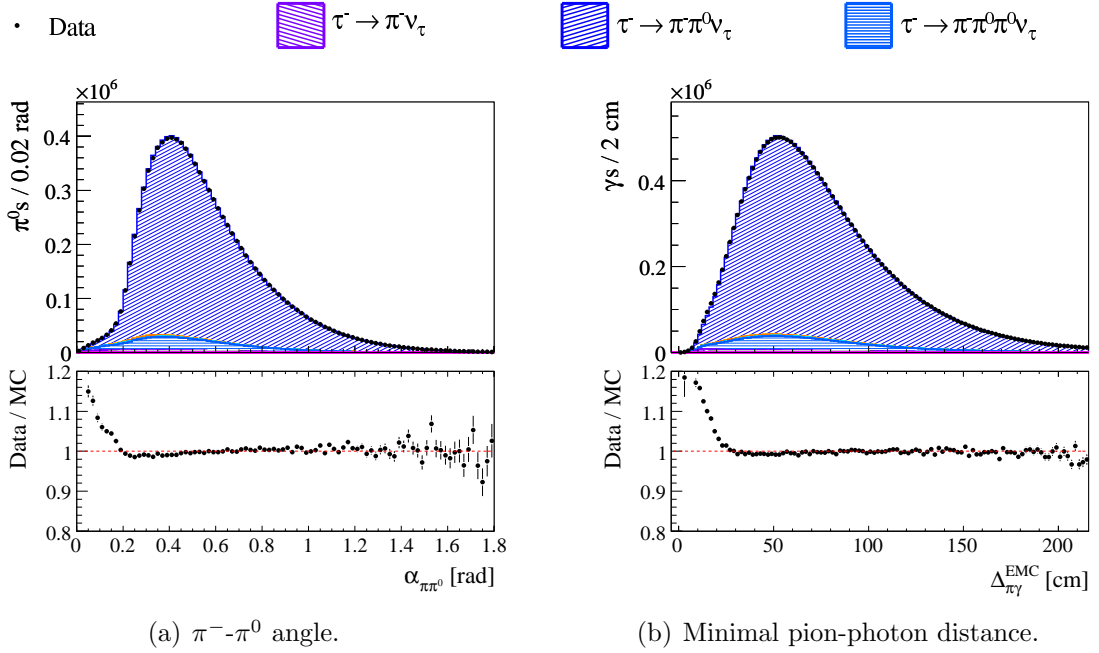
Figure 5.6: Distributions of the **(a)** π^--π^0 angle in the laboratory system $\alpha_{\pi\pi^0}$ and the **(b)*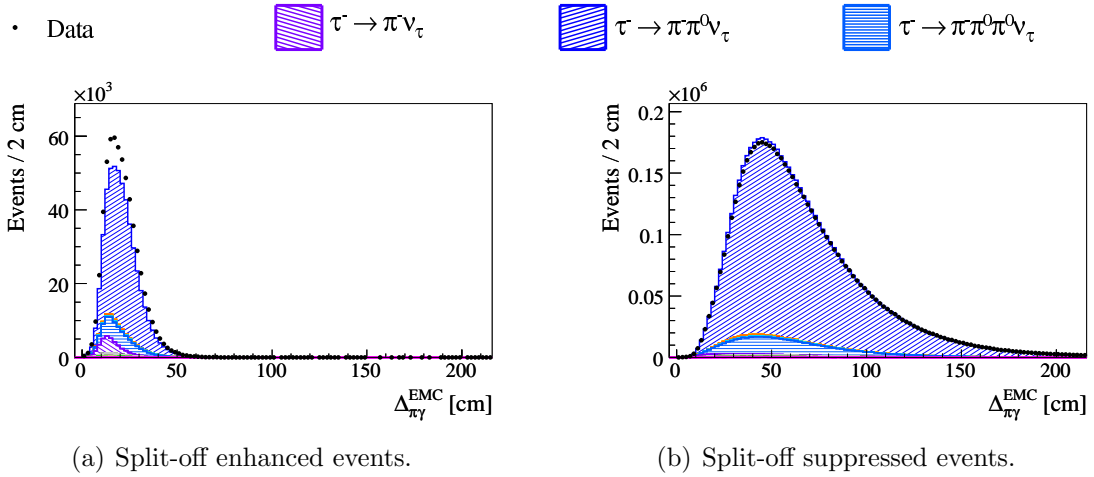* distance in the calorimeter front face between the track extrapolation and the closest of the two daughter photons $\Delta_{\pi\gamma}^{\mathrm{EMC}}$ for events of the type $\tau^- \to \pi^-\pi^0\nu_\tau$.

candidates are located at small distances and exhibit a large excess of data events (Figure 5.8(a)). Moreover, most background reactions of the type $\tau^- \to \pi^-\nu_\tau$ are contained in the split-off enhanced event sample at very small track-photon distances. Since these reactions are only reconstructed as $\tau^- \to \pi^-\pi^0\nu_\tau$ events if a spurious π^0 exists, this is a strong indication that the data excess in the split-off enhanced event sample is indeed caused primarily by split-offs. In contrast, split-off suppressed events are described reasonably well by the Monte Carlo simulation (Figure 5.8(b)). Their photons are distributed over a wide range of distances but only few entries exist at small values. Thus, the excess of data events at small angles and distances in Figure 5.6 is correlated with the excess of split-off candidates in Figure 5.8(a).

To further examine the nature of these reactions, Figures 5.9(a) and 5.9(b) show the ratio of the calorimeter energy associated with the track and the track momentum $E_\pi^{\mathrm{calo}}/p_\pi$ for the above defined split-off enhanced and suppressed events. While tracks that created a split-off are expected to produce extended hadronic showers, a large fraction of the remaining tracks is expected not to shower. I. e., their energy deposit in the calorimeter should be similar to the one of minimum ionizing particles, ($E_\pi^{\mathrm{calo}}/p_\pi \sim 0.1$ [33]).

Indeed, most tracks in split-off enhanced events deposit a significant part of their energy in the calorimeter ($E_\pi^{\mathrm{calo}}/p_\pi \approx 0.5$ for data events, Figure 5.9(a)), i. e., they produce extended hadronic showers. In contrast, a large fraction of the charged particles in split-off suppressed events do not produce hadronic showers, i. e., they are minimum ionizing particles ($E_\pi^{\mathrm{calo}}/p_\pi \lesssim 0.2$, Figure 5.9(b)). However, as visible from the numbers of events at large $E_\pi^{\mathrm{calo}}/p_\pi \approx 0.5$, the split-off suppressed event sample also contains a

(a) Split-off.

(b) Well separated, real photon.
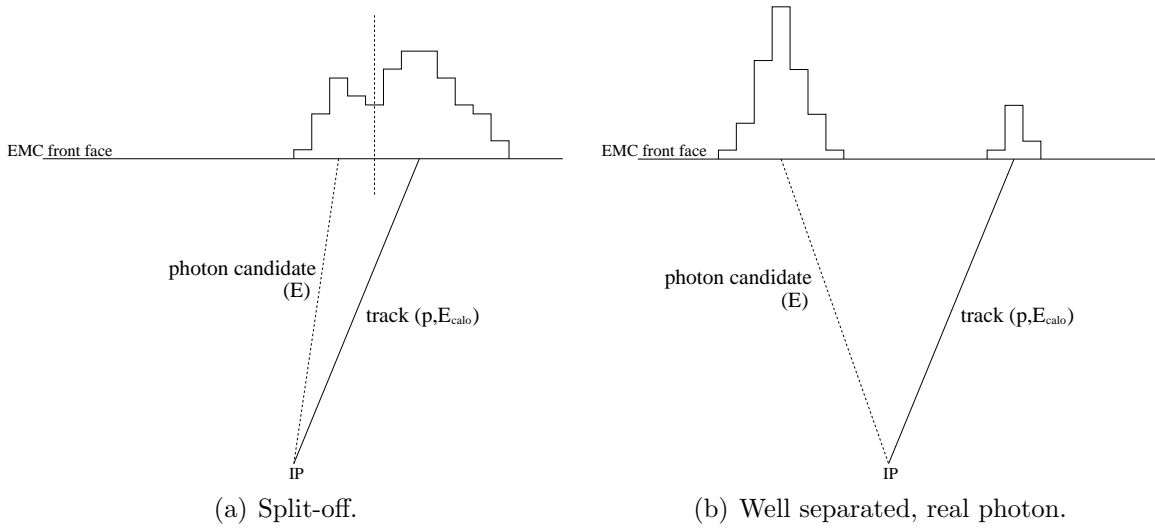
Figure 5.7: Illustration of split-offs. The drawings show a schematic view of an **(a)** split-off and a **(b)** well separated, real photon. The interaction point is denoted as IP and the horizontal line symbolizes the calorimeter front face. The histograms show the energy deposit in the electromagnetic calorimeter, where each bin corresponds to one crystal and the bin content is proportional to the deposited energy. Each subfigure contains a reconstructed track (solid line) with energy E_π^{calo} and momentum p_π and a reconstructed photon candidate (dashed line) with energy E_γ. In **(a)**, the photon candidate is a local maximum in a multi-bump cluster. The cluster originates from the extended hadronic shower of the charged particle and the local maximum is spuriously split off as indicated by the dashed line. In **(b)**, the charged pion is a minimum ionizing particle and only deposits a small amount of energy in the calorimeter. The photon candidate is an electromagnetic shower that creates a single-bump cluster and is well separated from the track.

significant fraction of tracks that produce an extended hadronic shower. These showers are not described by the Monte Carlo simulation either. But in contrast to the split-off enhanced sample, they do not produce split-offs and thus do not induce a deviation between the number of selected events in data and in the Monte Carlo simulation. In addition, both figures show that, on average, hadronic particles that have started to shower deposit more energy in the calorimeter in data than in the Monte Carlo simulation.

The ratio of the photon energy and the track's calorimeter energy $E_\gamma/E_\pi^{\mathrm{calo}}$ is displayed for both event classes in Figures 5.9(c) and 5.9(d). In case of split-off suppressed events, i.e., without multi-bump clusters, the photon with the smallest distance to the pion track is chosen to calculate the ratio. For split-offs, only a small part of the hadronic shower is expected to be splitted. Thus, split-offs are expected to have only a small fraction of the energy that the track deposited in the calorimeter. In contrast, real photons deposit—on average—more energy in the electromagnetic calorimeter with respect to the corresponding track as a large fraction of the latter do not shower.

Indeed, the ratio of the energy of the photon candidate to the track calorimeter

(a) Split-off enhanced events.
(b) Split-off suppressed events.

Figure 5.8: Distributions of the distance in the calorimeter front face between the track extrapolation and the closest of the two daughter photons $\Delta_{\pi\gamma}^{\mathrm{EMC}}$ for **(a)** split-off enhanced events and **(b)** split-off suppressed events using reactions of the type $\tau^- \to \pi^-\pi^0\nu_\tau$.

energy peaks at small values for split-off candidates, $E_\gamma/E_\pi^{\mathrm{calo}} \approx 0.2$ (Figure 5.9(c)). In addition, most of the data excess in the split-off candidates is concentrated at small values, $E_\gamma/E_\pi^{\mathrm{calo}} \approx 0.2$. These "photons" only carry a small fraction of the hadron's energy, as expected for split-offs in hadronic showers. The interpretation is supported by the fact that most reactions of the type $\tau^- \to \pi^-\nu_\tau$ that are selected as $\tau^- \to \pi^-\pi^0\nu_\tau$ decays are located in this region of the distribution. Such events can only be reconstructed as $\tau^- \to \pi^-\pi^0\nu_\tau$ reactions if a spurious π^0, e.g., in conjunction with a hadronic split-off, is accepted. In contrast, the distribution for split-off suppressed events is much broader and shifted to larger values (Figure 5.9(d)). As expected, "real" photons from these events are on average more energetic compared to the charged hadron's energy deposit in the calorimeter. The data excess at small $E_\gamma/E_\pi^{\mathrm{calo}}$ for split-off suppressed events as defined above indicates that these still contain a small fraction of possible split-offs in data.

All findings thus support the hypothesis that the excess of data events at small track-photon distances could be caused by hadronic split-offs. Due to inaccurate hadronic shower models, they cannot be described by the Monte Carlo simulation.

Due to their origin, split-offs are concentrated at small photon energies. They would thus distort the energy dependence of the π^0 efficiency correction. In addition, the mean π^0 efficiency correction would be falsified by the excess of data events. Since these excess events are caused by a track-related phenomenon, they only occur per track. The π^0 efficiency correction is however applied per π^0, i.e., multiple times in multi-π^0 events. Thus, the data excess due to split-offs would be over-corrected in τ decays into final states containing more than one π^0 meson. In conjunction with the smaller mean π^0 energies in events containing multiple π^0 mesons, this could produce a sizeable deviation between data and Monte Carlo simulation although the absolute data excess due to split-offs in events of the type $\tau^- \to \pi^-\pi^0\nu_\tau$ is small (see below).

(a) $E_\pi^{\text{calo}}/p_\pi$ for split-off enhanced events.

(b) $E_\pi^{\text{calo}}/p_\pi$ for split-off suppressed events.

(c) $E_\gamma/E_\pi^{\text{calo}}$ for split-off enhanced events.

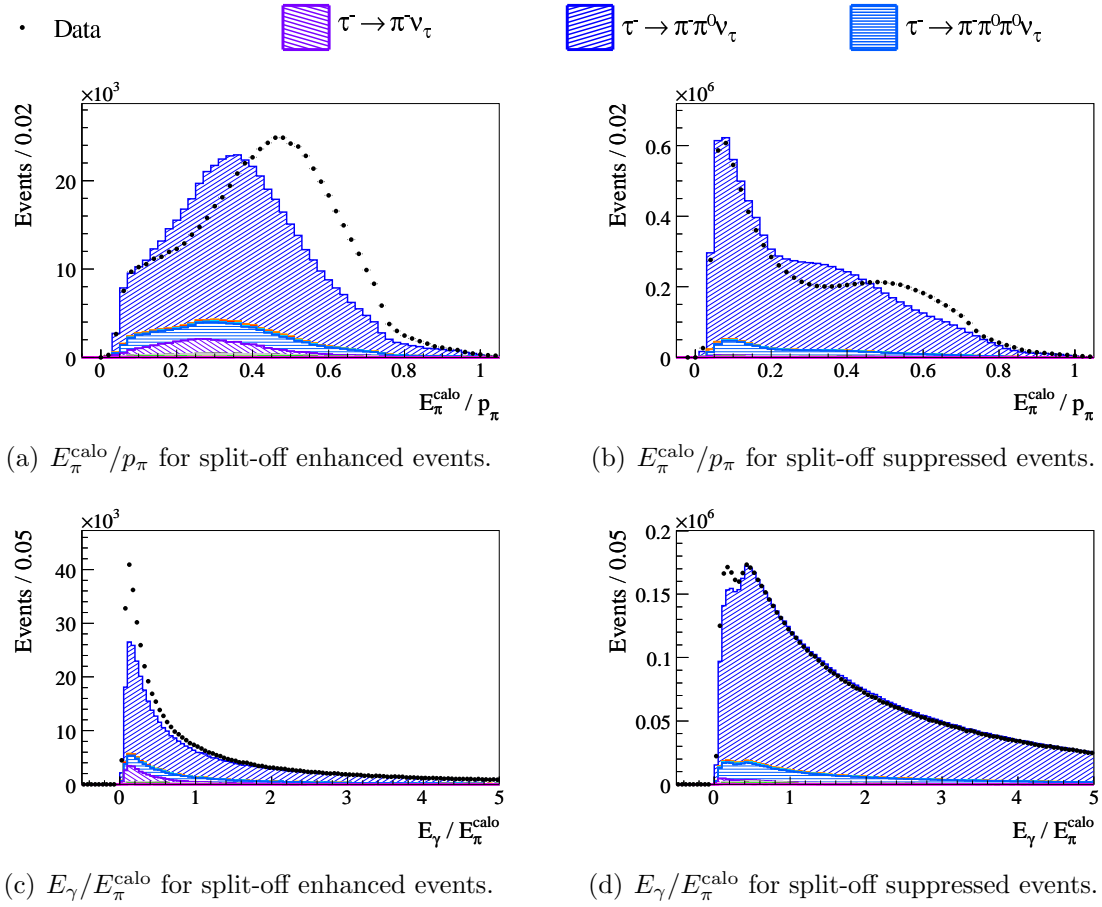(d) $E_\gamma/E_\pi^{\text{calo}}$ for split-off suppressed events.

Figure 5.9: Distributions of the ratio of the calorimeter energy associated with the track and the track momentum $E_\pi^{\text{calo}}/p_\pi$ **(a, b)** and of the ratio of the photon energy and the track calorimeter energy $E_\gamma/E_\pi^{\text{calo}}$ **(c, d)** for **(a, c)** split-off enhanced and **(b, d)** split-off suppressed events using reactions of the type $\tau^- \to \pi^- \pi^0 \nu_\tau$. The different quantities are illustrated in Figure 5.7.

In consequence, the data excess at small π^--π^0 angles, which is caused by split-offs, is excluded from the determination of the π^0 efficiency correction by requiring a minimal π^--π^0 angle (Section 5.1),

$$\alpha_{\pi\pi^0} > 0.25\,\text{rad}\,. \tag{5.13}$$

To estimate the effect of such a selection criterion on decay modes with multiple π^0 mesons, Figure 5.10 shows the minimal K^-/π^--π^0 angle for events of the type $\tau^- \to K^- \pi^0 \pi^0 \nu_\tau$ and $\tau^- \to \pi^- \pi^0 \pi^0 \pi^0 \nu_\tau$. They exemplify that kinematic conservation laws force the π^0 mesons to be closer to the hadron track the more π^0 mesons an event contains and the heavier the charged particle is. A requirement on the minimal distance of the π^0 daughter photons to the hadron track would thus reject a large fraction of the already rare τ decays into final states with net strangeness and multiple π^0 mesons. As the π^0 efficiency correction is not expected to depend on the K^-/π^--π^0 angle [72], no criterion is applied when selecting the final states for the branching
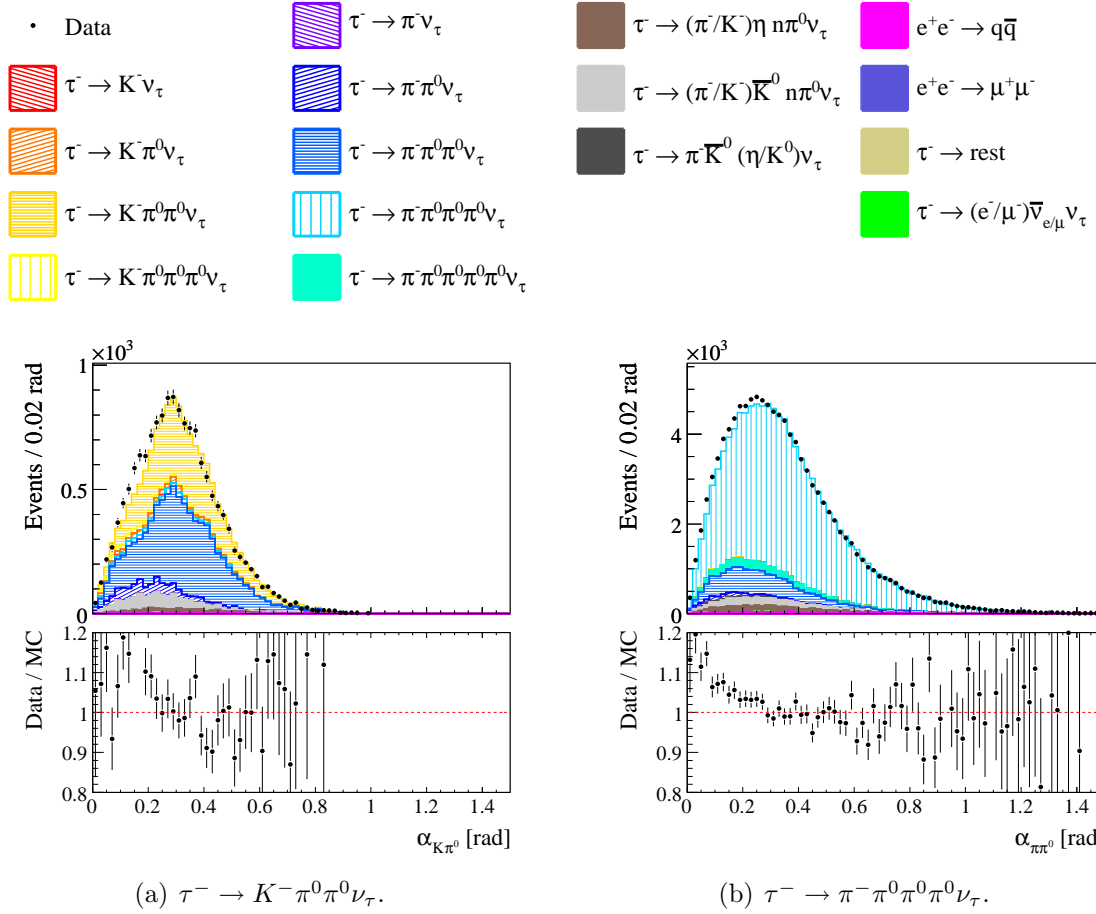
Figure 5.10: Distributions of the minimal K^-/π^--π^0 angle $\alpha_{\pi/K\pi^0}$ for events of the type **(a)** $\tau^- \to K^-\pi^0\pi^0\nu_\tau$ and **(b)** $\tau^- \to \pi^-\pi^0\pi^0\pi^0\nu_\tau$. The data excess at small angles is caused by spurious π^0 mesons due to split-offs.

fraction measurements. The π^0 efficiency correction is extrapolated from the region $\alpha_{\pi\pi^0} > 0.25$ rad to smaller K^-/π^--π^0 angles.

Thus, the selected data event samples that are used for the extraction of the branching fractions still contain an excess of background events due to split-offs with respect to the Monte Carlo simulation (cf. Figure 5.10). The amount of excessive background is estimated for each of the analyzed decay modes and subtracted from the number of selected data events. This estimate is performed in two steps. Firstly, a general relation is developed that quantifies the excess of split-off events in the selected data relative to the total number of selected events in the considered mode. Secondly, the relation is evaluated for each decay mode using the excess of data events in selected reactions of the type $\tau^- \to \pi^-\pi^0\nu_\tau$.

Let $f_{\text{excess}}^{\text{track}}$ be the fractional excess of data events with respect to the Monte Carlo simulation that are reconstructed with an additional π^0 meson due to split-offs. As split-offs are a track related occurrence, $f_{\text{excess}}^{\text{track}}$ is in first order constant for τ decays into final states containing one charged hadron. The main background that enters an event

sample with n π^0 mesons due to hadronic split-offs originates from the corresponding event category with one π^0 less, e.g., $\tau^- \to K\pi^0\nu_\tau$ reactions as background in selected $\tau^- \to K\pi^0\pi^0\nu_\tau$ events. Thus, the fractional data excess in events with n reconstructed π^0 mesons $f_{\text{excess}}^{n\pi^0}$ can be estimated in first order by the product of the fractional excess per charged hadron $f_{\text{excess}}^{\text{track}}$ and the ratio $R_{(n-1)\pi^0,n\pi^0}$ of the branching fractions of the decay modes containing $(n-1)$ and n π^0 mesons:

$$f_{\text{excess}}^{n\pi^0} = f_{\text{excess}}^{\text{track}} \, R_{(n-1)\pi^0,n\pi^0} \tag{5.14}$$

with

$$R_{(n-1)\pi^0,n\pi^0} = \frac{\mathcal{B}(\tau^- \to \pi^-/K^-(n-1)\pi^0\nu_\tau)}{\mathcal{B}(\tau^- \to \pi^-/K^- n\pi^0\nu_\tau)} \,. \tag{5.15}$$

Split-off events with different identities π/K of the charged particles are additionally suppressed by the kaon/pion selection. Hence, only the branching fractions of modes with charged hadrons of the same type, i.e., $\mathcal{B}(\tau^- \to \pi^- n\pi^0\nu_\tau)$ and $\mathcal{B}(\tau^- \to \pi^-(n-1)\pi^0\nu_\tau)$, and $\mathcal{B}(\tau^- \to K^- n\pi^0\nu_\tau)$ and $\mathcal{B}(\tau^- \to K^-(n-1)\pi^0\nu_\tau)$, are considered for this estimate.

The fractional excess of background due to split-offs in selected data events of the type $\tau^- \to \pi^-\pi^0\nu_\tau$ $f_{\text{excess}}^{\pi\pi^0}$ can be directly estimated by the excess of data events at small π^--π^0 angles relative to the number of all selected events (Figure 5.6(a)):

$$f_{\text{excess}}^{\pi\pi^0} = \frac{N_{\text{data}}^{<0.25\,\text{rad}} - N_{\text{MC}}^{<0.25\,\text{rad}}}{N_{\text{data}}} = 0.11\,\% \,, \tag{5.16}$$

where N_{data} is the number of all selected data events. The symbols $N_{\text{data}}^{<0.25\,\text{rad}}$ and $N_{\text{MC}}^{<0.25\,\text{rad}}$ denote the numbers of selected events in data and Monte Carlo simulation that contain π^0 mesons at less than $0.25\,\text{rad}$ from the hadron track.

In conjunction with Equation 5.14, this fraction can be used to calculate the fractional data excess due to split-offs for all remaining decay modes:

$$f_{\text{excess}}^{n\pi^0} = f_{\text{excess}}^{\pi\pi^0} \, \frac{R_{(n-1)\pi^0,n\pi^0}}{R_{\pi,\pi\pi^0}} \,. \tag{5.17}$$

Table 5.1 lists the ratio $R_{(n-1)\pi^0,n\pi^0}$, the double ratio $R_{(n-1)\pi^0,n\pi^0}/R_{\pi,\pi\pi^0}$ and the resulting fractional excess of remaining background in the data with respect to the Monte Carlo simulation due to split-offs $f_{\text{excess}}^{\pi\pi^0}$ for all decay modes included into this analysis.

As described above, the number of selected events of the type $\tau^- \to \pi^-/K^- n\pi^0\nu_\tau$ with $n > 0$ is increased in data by the additional background from events of the type $\tau^- \to \pi^-/K^-(n-1)\pi^0\nu_\tau$ in conjunction with split-offs. In contrast, data events of the type $\tau^- \to K^-\nu_\tau$ are more often reconstructed as events of the type $\tau^- \to K^-\pi^0\nu_\tau$ due to split-offs than the corresponding Monte Carlo simulated reactions. Thus, the fractional difference in the number of selected events due to split-offs is estimated and added to the number of reconstructed data events in the case of reactions of the type $\tau^- \to K^-\nu_\tau$. The fractional excess of events that are falsely reconstructed in the decay mode $\tau^- \to K^-\pi^0\nu_\tau$ in data with respect to simulated events is given by the fractional excess per track:

$$f_{\text{excess}}^{K} = -f_{\text{excess}}^{\text{track}} \,. \tag{5.18}$$

Table 5.1: Estimate of the excess of remaining background in the data due to split-offs for all selected event samples. The table specifies the selected event sample with n π^0 mesons, the ratio of its branching fraction $R_{(n-1)\pi^0,n\pi^0}$ with respect to the main background sample with $(n-1)$ π^0 mesons (Equation 5.15), the double ratio with respect to selected $\tau^- \to \pi^-\pi^0\nu_\tau$ reactions $R_{(n-1)\pi^0,n\pi^0}/R_{\pi,\pi\pi^0}$ and the estimated fractional excess of the remaining background $f_{\text{excess}}^{n\pi^0}$ in the data with respect to the Monte Carlo simulation according to Equations 5.17 and 5.19. A systematic uncertainty of 50 % is assigned to all corrections.

Selected sample	n_{π^0}	$R_{(n-1)\pi^0,n\pi^0}$	$\dfrac{R_{(n-1)\pi^0,n\pi^0}}{R_{\pi,\pi\pi^0}}$	$f_{\text{excess}}^{n\pi^0}$ [%]
$\tau^- \to \pi^-\pi^0\nu_\tau$	$n=1$	0.4	1	0.11 ± 0.05
$\tau^- \to \pi^-\pi^0\pi^0\nu_\tau$	$n=2$	2.8	6.5	0.70 ± 0.35
$\tau^- \to \pi^-\pi^0\pi^0\pi^0\nu_\tau$	$n=3$	7.3	17	1.8 ± 0.9
$\tau^- \to \pi^-\pi^0\pi^0\pi^0\pi^0\nu_\tau$	$n=4$	13	31	3.3 ± 1.6
$\tau^- \to K^-\nu_\tau$	$n=0$	–	–	-0.26 ± 0.13
$\tau^- \to K^-\pi^0\nu_\tau$	$n=1$	1.4	3.4	0.36 ± 0.18
$\tau^- \to K^-\pi^0\pi^0\nu_\tau$	$n=2$	9.1	21	2.2 ± 1.1
$\tau^- \to K^-\pi^0\pi^0\pi^0\nu_\tau$	$n=3$	3.9	9.1	1.0 ± 0.5

Using Equation 5.14, this fraction can be calculated from the measured fractional excess in events of the type $\tau^- \to \pi^-\pi^0\nu_\tau$ as follows:

$$f_{\text{excess}}^K = -\frac{f_{\text{excess}}^{\pi\pi^0}}{R_{\pi,\pi\pi^0}} \ . \tag{5.19}$$

The resulting fraction is also listed in Table 5.1.

When calculating the branching fractions (Section 6.3), the fractional excess of data with respect to the Monte Carlo simulation is subtracted from the number of the selected data events. I. e., in the case of events of the type $\tau^- \to K^-\nu_\tau$, the number of selected data events is increased by the corresponding fraction. Due to the rough estimate, a 50 % uncertainty is assigned to all fractions and subtracted or added event numbers.

5.3.3   Merged π^0 mesons

Figure 5.11(a) displays the lateral moment of the two π^0 daughter photons for single-π^0 events of the type $\tau^- \to \pi^-\pi^0\nu_\tau$. The shift of the data to larger values with respect to the Monte Carlo simulation illustrates that photon showers are on average wider in data than in the simulation. Two π^0 daughter photons with broader showers in data may produce a single merged cluster at larger distances than corresponding photons in the Monte Carlo simulation. Two photons in the data may hence no longer be separable at
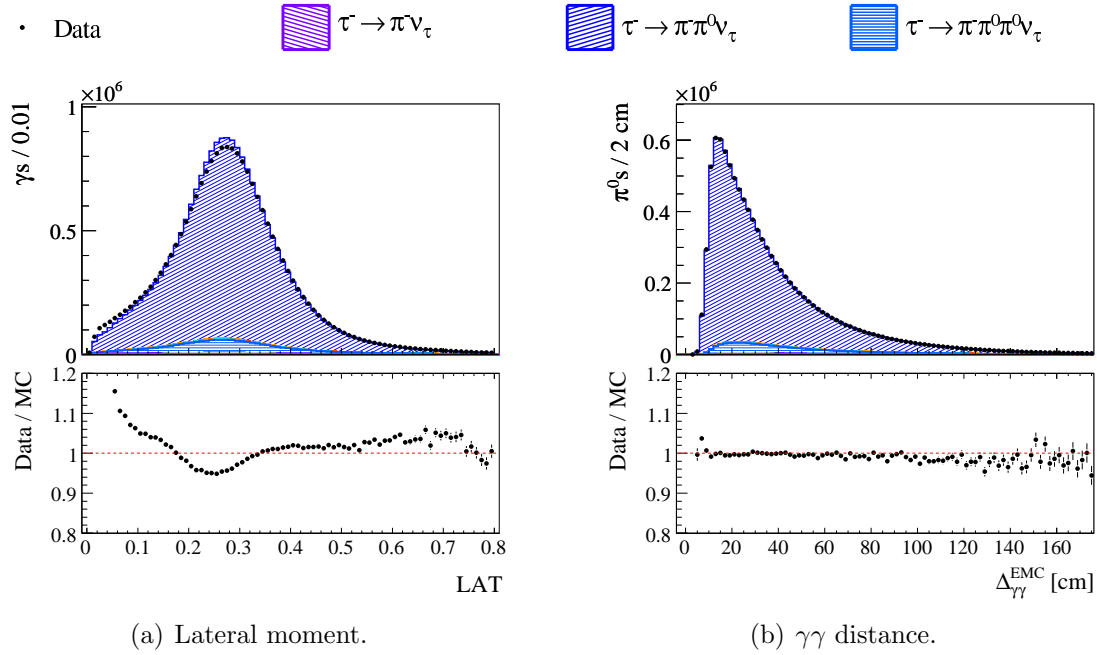
(a) Lateral moment.

(b) $\gamma\gamma$ distance.

Figure 5.11: Distributions of the **(a)** lateral moment LAT and the **(b)** distance $\Delta_{\gamma\gamma}^{\mathrm{EMC}}$ in the calorimeter front face of the π^0 daughters for selected events of the type $\tau^- \to \pi^-\pi^0\nu_\tau$.

a given photon-photon distance, while the corresponding simulated photons can still be splitted into two bumps. This is illustrated by Figure 5.12. Figure 5.12(a) displays a calorimeter cluster that consists of two merged electromagnetic showers. Due to the two distinct local maxima, the cluster can be splitted into two bumps and be used in the reconstruction of composite π^0 mesons (Section 3.4). In contrast, Figure 5.12(b) shows a calorimeter cluster that can no longer be splitted into its components. The photons are too close together and no local maxima can be distinguished anymore.

The sketches illustrate that larger showers may no longer be separable, while narrower ones still can be splitted. Due to the different size of the electromagnetic showers in data and in the Monte Carlo simulation (Figure 5.11(a)), this may lead to a larger fraction of non-separable merged π^0 mesons in data than in simulated events. Since only composite π^0 mesons are considered in this analysis (Section 3.4), this could result in a deviation between data and Monte Carlo simulation with respect to the fraction of π^0 mesons of a given energy that are reconstructed as composite π^0 mesons. While these effects are in principle covered by the π^0 efficiency correction, the dependence of the photon-photon distance on the π^0 energy and on the position in the detector would bias the π^0 efficiency correction.

To investigate any deviations between data and Monte Carlo simulation due to merged π^0 mesons, Figure 5.11(b) shows the distance of the two π^0 daughter photons in the calorimeter front face (Figure 5.12) for selected events of the type $\tau^- \to \pi^-\pi^0\nu_\tau$ after the application of the π^0 efficiency correction. If different fractions of π^0 mesons were inseparably merged in data and Monte Carlo simulation, this should be visible as a deviation between data and simulated events at small photon-photon distances. E. g., if a larger fraction of π^0 mesons were inseparably merged in data due to the larger shower

(a) Separable photons.   (b) Inseparable photons.
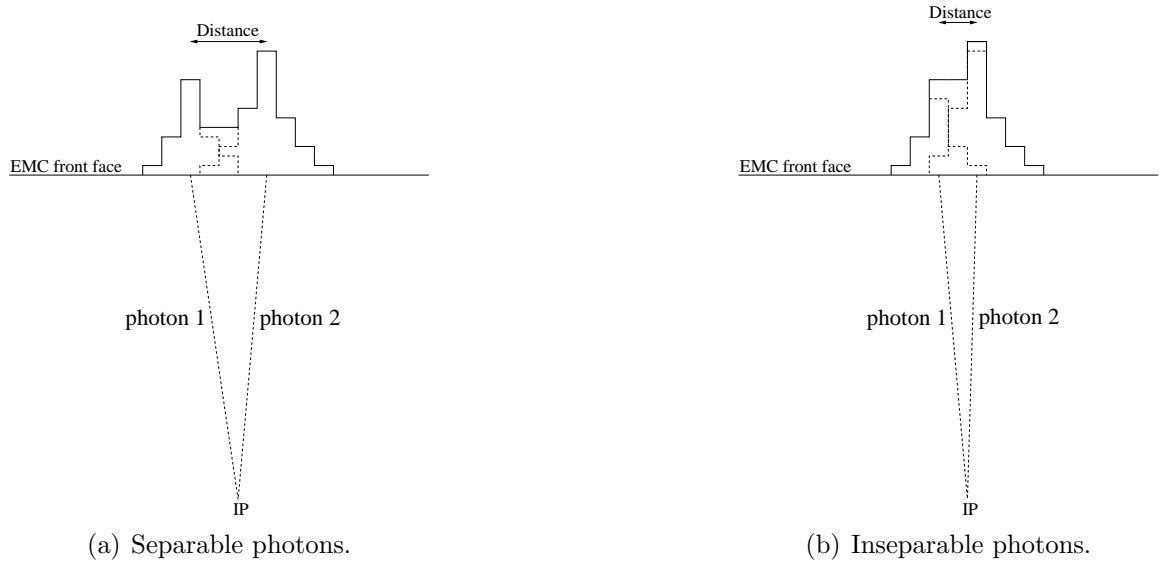
Figure 5.12: Illustration of **(a)** separable and **(b)** inseparable photons. The drawings show a schematic view of the energy deposits of the photons in the electromagnetic calorimeter. The interaction point is denoted as IP and the horizontal line symbolizes the calorimeter front face. The histograms show the energy deposit in the electromagnetic calorimeter, where each bin corresponds to one crystal and the bin content is proportional to the deposited energy. Each subfigure contains two photons whose energy deposits are merged into a single cluster. The measured clusters are symbolized by the solid lines, while the individual photon energies are indicated by the dashed ones. In **(a)**, the cluster contains two local maxima and can be splitted into the bumps from the two photons. In **(b)**, the cluster does not exhibit any local maxima. The photons are too close together and can no longer be separated. The minimal separable distance depends on the transverse size of the showers and may be different for data and Monte Carlo simulation.

size, data events should be depleted at small distances, as only composite π^0 mesons are included in Figure 5.11. The reasonable agreement at small distances indicates that the fractions and rates of merged π^0 mesons pose no problem within this analysis. Due to the decrease of the average energy of the π^0 mesons in samples with kaons and multiple π^0 mesons (Figures B.1, B.2), i. e., the increase of the average angular separation of the daughter photons, the problem is less important in these modes.

5.4 Systematic uncertainty of the π^0 efficiency correction

This section discusses the description of events of the type $\tau^- \to \pi^- \pi^0 \pi^0 \nu_\tau$ by the Monte Carlo simulation after the application of the π^0 efficiency correction. A systematic uncertainty of the π^0 efficiency correction method is derived from any remaining deviations. Within this section, the Monte Carlo simulation uses the precisely measured branching fraction $\mathcal{B}(\tau^- \to \pi^- \pi^0 \pi^0 \nu_\tau) = (9.24 \pm 0.12)\,\%$ [3] and all measured branching

fractions are scaled to the values obtained in Chapter 6. All corrections are applied as described in Sections 3.5 and 5.2.

Figure 5.13 displays the lepton momentum p_ℓ for selected events of the type $e^+e^- \to \tau^+(\to \ell^+\nu_\ell\overline{\nu}_\tau)\tau^-(\to \pi^-\pi^0\pi^0\nu_\tau)$ with $\ell = e,\mu$. The overall scale agrees between data
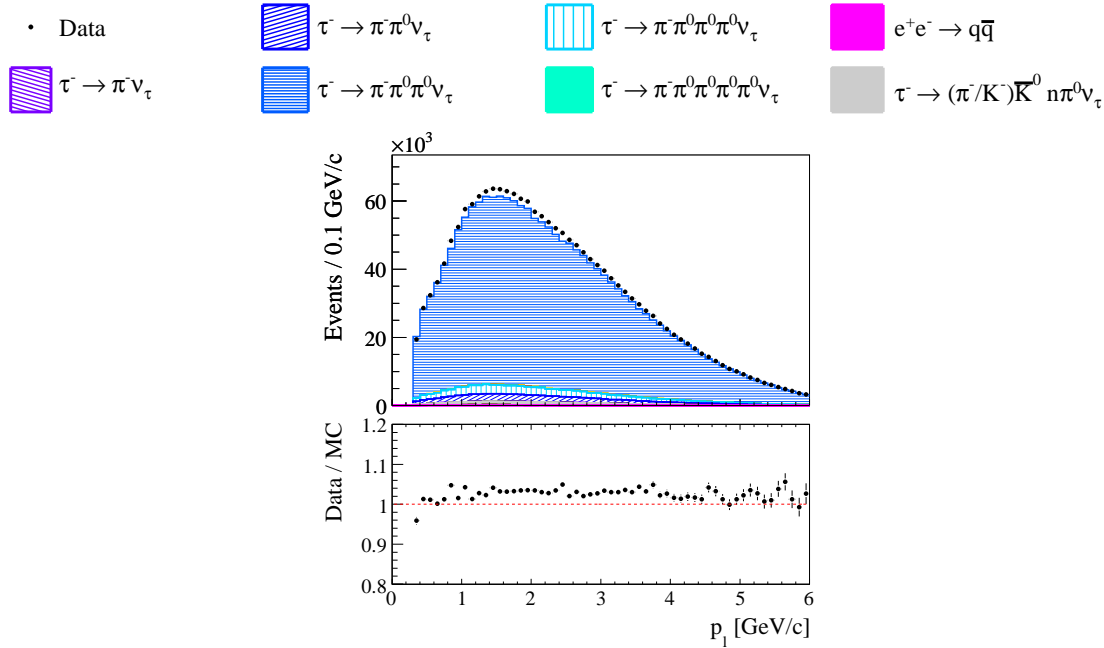
Figure 5.13: Distribution of the lepton momentum p_ℓ for selected events of the type $\tau^- \to \pi^-\pi^0\pi^0\nu_\tau$.

and Monte Carlo simulation at the $3\,\%$ level. In addition, a similar level of agreement is observed with respect to the kinematics of the leptonic τ decay. The observed difference is fully attributed to the π^0 efficiency correction. It is considered as the systematic uncertainty of the determination of the π^0 efficiency correction from events of the type $\tau^- \to \pi^-\pi^0\nu_\tau$ and its application to reactions containing multiple π^0 mesons. As there are two π^0 mesons per event, the uncertainty is

$$\Delta\eta_{\pi^0} = 1.5\,\% \tag{5.20}$$

for each selected π^0 meson. It is considered when calculating the uncertainties of the branching fractions in Section 6.5.

As the selection criterion on the unassociated energy mainly determines the amount of background from events with additional π^0 mesons (Section 4.4), it strongly influences the agreement between data and Monte Carlo simulation in Figure 5.13. The criterion from Equation 4.14 is chosen such that the uncertainty from Equation 5.20 is minimized. The disagreement between data and Monte Carlo simulation with respect to the unassociated energy is thus closely related to the observed deviation in Figure 5.13 and covered by the corresponding uncertainty.

5.5   Kinematics of $\tau^- \rightarrow \pi^- \pi^0 \pi^0 \nu_\tau$ decays

In addition to the overall scale from Section 5.4, the kinematic description of hadronic τ decays into the final states $\pi^- \pi^0 \pi^0 \nu$ is briefly discussed in this section. Within the scope of this analysis, i. e., for the measurement of the branching fractions, a good description of these kinematics is not needed as long as all selection variables agree reasonably well between data and Monte Carlo simulation. However, the study provides a first glimpse at the feasibility of a measurement of the hadronic spectral functions in τ decays using the BABAR experiment (see Chapter 1). While the most precise measurements of $|V_{us}|$ from τ decays are obtained using the branching fractions of the τ lepton into final states with net strangeness [4, 5, 75–78]—as performed in this work, the determination of the spectral functions provides additional insight into the physics of hadronic τ decays [10]. It also allows a simultaneous determination of $|V_{us}|$ and m_s—although with limited precision and strong theoretical limitations [4, 5, 75–78]. As the spectral functions are obtained from the invariant mass spectra of the hadronic final states (Section 1.2.4), a good description of their kinematics is a prerequisite for this measurement.

To investigate the description of the kinematics of the hadronic τ decay, Figure 5.14 displays the π^- momentum p_π and the π^0 energies E_{π^0} for selected events of the type $\tau^- \rightarrow \pi^- \pi^0 \pi^0 \nu_\tau$. The π^- momentum is shifted to significantly lower momenta in the

(a) π^- momentum.   (b) π^0 energies.
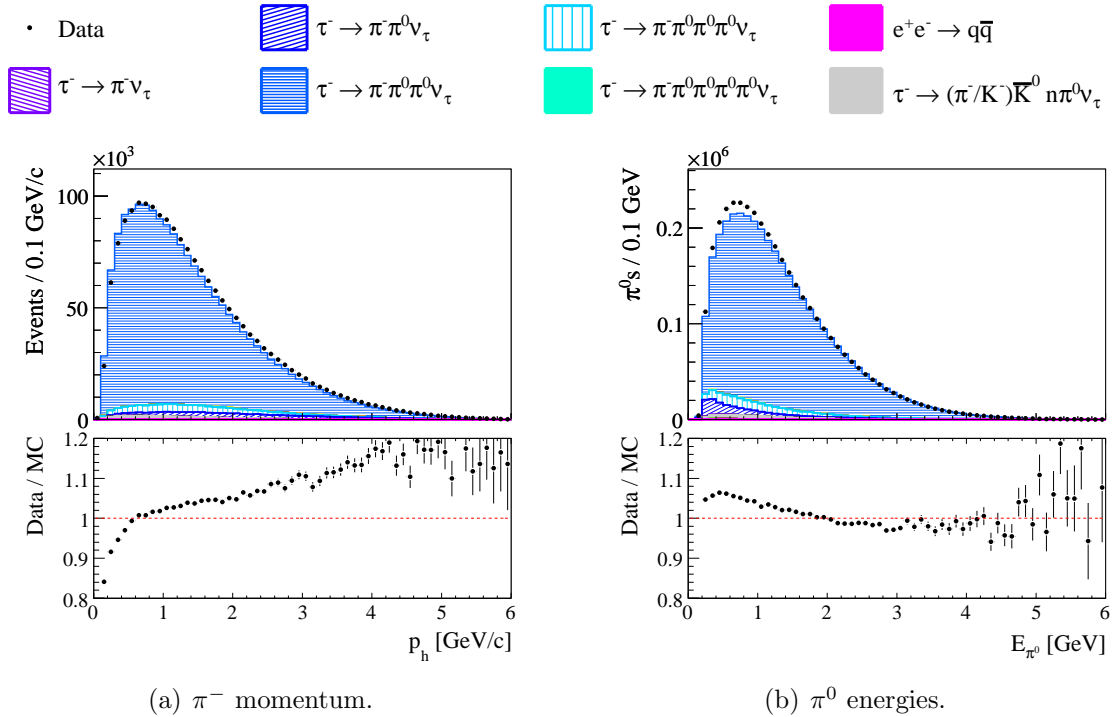
Figure 5.14: Distributions of the **(a)** π^- momentum p_π and the **(b)** π^0 energies E_{π^0} for selected events of the type $\tau^- \rightarrow \pi^- \pi^0 \pi^0 \nu_\tau$.

Monte Carlo simulation—as demonstrated by the positive slope of the ratio of data and simulated event numbers. In contrast, the π^0 energy is significantly larger in the Monte Carlo simulation than in real data.

In the simulated events used within this analysis, the final state $\pi^-\pi^0\pi^0$ is produced exclusively via the a_1 resonance. The a_1 in turn decays exclusively via the lowest-dimensional (mainly s-wave) $(\rho\pi)^-$ Born amplitude [79–81]:

$$
\begin{aligned}
\tau^- &\rightarrow a_1^- \; \nu_\tau \\
&\hookrightarrow \; \rho^- \; \pi^0 \\
&\qquad \hookrightarrow \; \pi^- \; \pi^0 \, .
\end{aligned}
\tag{5.21}
$$

However, analysis of the hadronic structure of the decay $\tau^- \rightarrow \pi^-\pi^0\pi^0\nu_\tau$ by the CLEO collaboration [81] showed that significant contributions from amplitudes of further a_1 decays $a_1 \rightarrow \sigma\pi$, $a_1 \rightarrow f_0(1370)\pi$ and $a_1 \rightarrow f_2(1270)\pi^0$ as well as higher-dimensional $a_1 \rightarrow \rho\pi$ and $a_1 \rightarrow \rho'\pi$ amplitudes exist. Notably, the $\sigma\pi$ amplitude accounts for approximately 15 % of the total $\tau^- \rightarrow \pi^-\pi^0\pi^0\nu_\tau$ decay rate. As the angular distribution of the $\pi^-\pi^0\pi^0$ final state particles depends strongly on the nature of the intermediate resonances, the oversimplified decay model used by the Monte Carlo simulation cannot be expected to correctly describe the data.

Thus, while the agreement between data and Monte Carlo simulation is sufficient for the purpose of this analysis—the precise measurement of the branching fractions—an improved Monte Carlo simulation would be beneficial to measure the invariant final state masses for a determination of the spectral functions. As the π^0 efficiency correction is determined using single-π^0 events of the type $\tau^- \rightarrow \pi^-\pi^0\nu_\tau$, it cannot be expected to correct for specific problems in the description of the kinematics of final states that contain two neutral pions. However, as the description of the higher moments in the spectral function of final states with net strangeness still suffers from theoretical problems (Section 1.4.2, [10]), a simultaneous determination of $|V_{us}|$ and m_s from hadronic τ decays is not feasible until further improvement of the theoretical calculations is achieved. The best determination of $|V_{us}|$ is provided by the branching fractions and the hadronic decay rate of the τ lepton as performed in this analysis (Sections 1.4.2, 7.2).

5.6   Critical discussion

The method of the π^0 efficiency correction as derived in Section 5.1 relies on the accurate description of all effects that are not related to the π^0 selection by the Monte Carlo simulation. The best possible agreement between data and simulated events is achieved by correcting for known deviations, e. g., due to the charged particle reconstruction and identification. The level of agreement is illustrated by Figure 5.1.

The determination of the π^0 efficiency correction from selected events of the type $\tau^- \rightarrow \pi^-\pi^0\nu_\tau$ and its application to the decay mode $\tau^- \rightarrow K^-\pi^0\nu_\tau$ is similar to a relative measurement. Many of the uncertainties that are not related to the π^0 selection cancel for this decay mode in first order, i. e., neglecting dependencies on the π^0 energy spectra and the background contributions. Moreover, many of the uncertainties that are related to the π^0 reconstruction cancel for the first π^0 in all other decay modes in first order due to the same argument. The remaining uncertainty inherent to the presented method has been estimated by the deviation of the rate of observed reactions of the

type $\tau^- \to \pi^- \pi^0 \pi^0 \nu_\tau$ from the prediction using the world average of the branching fraction $\mathcal{B}(\tau^- \to \pi^- \pi^0 \pi^0 \nu_\tau) = (9.24 \pm 0.12)\,\%$ [3].

A set of systematic studies of the π^0 selection and the description of the data by the Monte Carlo simulation has been presented in Section 5.3. The studies have been used to estimate additional systematic uncertainties from deviations between data and simulated events. The displayed distributions, which sometimes exhibit large deviations between data and Monte Carlo simulation, have been chosen to best illustrate the investigated phenomena (Figures 5.6, 5.8–5.11) and to estimate their influence on the measured branching fractions. However, none of the shown quantities are used for the event selection or for any other purpose than the estimate of additional uncertainties. All selection variables are displayed in Chapter 4 and Appendix A. They generally show a good agreement of data and Monte Carlo simulation. Uncertainties due to deviations between the distributions of the selection variables in data and Monte Carlo simulation are estimated in Section 6.5.11.

Finally, Section 5.5 presents the disagreement between data and simulated events in the description of the kinematics of $\tau^- \to \pi^- \pi^0 \pi^0 \nu_\tau$ decays. The explanation for the observed differences is provided. However, the remedy for the deviations is beyond the scope of this thesis as it is not necessary for the presented measurements. Any systematic effects on the overall event numbers needed for the extraction of the branching fractions are estimated by the uncertainty derived in Section 5.4.

In consequence, although significant deviations between data and Monte Carlo simulation have been presented in some cases in this chapter, their influence on the presented measurements has in each case been carefully estimated, corrected for and included into the systematic uncertainties of the measured branching fractions.

Chapter 6

Extraction of the branching fractions

Chapter 4 describes the selection of events that contain a τ decay into one charged hadron and additional neutral pions from the BABAR data set. In detail, the selected τ decays are

$$
\begin{aligned}
\tau^- &\to \pi^- \pi^0 \nu_\tau \,, \\
\tau^- &\to \pi^- \pi^0 \pi^0 \nu_\tau \,, \\
\tau^- &\to \pi^- \pi^0 \pi^0 \pi^0 \nu_\tau \,, \\
\tau^- &\to \pi^- \pi^0 \pi^0 \pi^0 \pi^0 \nu_\tau \,, \\
\tau^- &\to K^- \nu_\tau \,, \\
\tau^- &\to K^- \pi^0 \nu_\tau \,, \\
\tau^- &\to K^- \pi^0 \pi^0 \nu_\tau \,, \\
\tau^- &\to K^- \pi^0 \pi^0 \pi^0 \nu_\tau \,.
\end{aligned}
\tag{6.1}
$$

The decay mode $\tau^- \to \pi^- \nu_\tau$ is not selected due to large irreducible QED backgrounds. Reactions of the type $\tau^- \to \pi^- \pi^0 \nu_\tau$ are used to determine the π^0 efficiency correction. Its validity and its applicability to multi-π^0 final states are assured and verified with the help of events of the type $\tau^- \to \pi^- \pi^0 \pi^0 \nu_\tau$ (Chapter 5). This chapter describes the simultaneous extraction of the branching fractions for the remaining six decay modes (Sections 6.1–6.3). In addition, the statistical and systematic uncertainties of the measured branching fractions are estimated as well as their correlations between the different decay channels (Sections 6.4, 6.5).

The method to simultaneously extract the branching fractions and the basic recipe of estimating their uncertainties were developed in cooperation with a diploma student [82]. All analyses and studies concerned with π^0 mesons are unique to this work. On the basis of two earlier diploma theses that developed the selection of τ decays into final states containing three charged particles [83, 84], the cooperation resulted in the simultaneous measurement of the decay modes $\tau^- \to h^- h^+ h^- \nu_\tau$ with $h = \pi, K$ [82].

6.1   Calculation of branching fractions

The branching fraction $\mathcal{B}$ of the decay $\tau \to$ signal is defined as the ratio of its decay width $\Gamma(\tau \to$ signal$)$ to the total decay width of the τ lepton $\Gamma_\tau \equiv \Gamma(\tau \to$ anything$)$ [3]. It is measured using the number of τ leptons decaying into the signal mode $N(\tau \to$ signal$)$ and the total number of τ leptons $N_\tau \equiv N(\tau \to$ anything$)$:

$$\mathcal{B}(\tau \to \text{signal}) \equiv \frac{\Gamma(\tau \to \text{signal})}{\Gamma_\tau} \equiv \frac{N(\tau \to \text{signal})}{N_\tau} \, . \tag{6.2}$$

The τ leptons are produced in $\tau^+\tau^-$ pairs via the reaction $e^+e^- \to \tau^+\tau^-$. The event selection in Chapter 4 describes the selection of specific $\tau^+\tau^-$ events. Per event, only one signal decay is reconstructed, although events with two signal τ decays occur. Thus, only events and not single τ decays can be counted. This necessitates a consistent definition of a *signal event* that provides a well-defined relation between the number of signal *events* and the number of signal τ *decays*. In principle, two definitions seem sensible. An event may be called a signal event if

1. one τ lepton decays into the signal mode and the second one leptonically: $(\tau_1 \to$ signal, $\tau_2 \to \ell\nu\bar{\nu})$ with $\ell = e, \mu$,

2. at least one τ lepton decays into the signal mode. The second one decays into any final state, which may also be the signal mode: $(\tau_1 \to$ signal, $\tau_2 \to$ anything$)$.

These definitions of signal events are based on the "true nature" of an event and are independent of any selection criteria.

If a signal event is defined according to method 1, the branching fraction of the signal mode is obtained from

$$\mathcal{B}(\tau \to \text{signal}) = \frac{N(\tau_1 \to \text{signal}, \ \tau_2 \to \ell\nu\bar{\nu})}{2\mathcal{B}(\tau \to \ell\nu\bar{\nu})N_{\tau\tau}} \, . \tag{6.3}$$

The symbol $N(\tau_1 \to$ signal, $\tau_2 \to \ell\nu\bar{\nu})$ denotes the number of signal events according to definition 1 that are produced in e^+e^- collisions at the $B\!A\!B\!A\!R$ experiment. The branching fraction of τ decays into leptons is symbolized by $\mathcal{B}(\tau \to \ell\nu\bar{\nu})$ and $N_{\tau\tau}$ is the total number of produced $\tau^+\tau^-$ pairs. This method has a significant disadvantage. Events that contain two signal decays are per definition background. They enter the sample of selected events if one of the signal decays is misidentified as a leptonic (tag) τ decay (Section 4.1). Like any other background (see below), their number has to be subtracted from the number of selected events in order to determine the number of signal events $N(\tau_1 \to$ signal, $\tau_2 \to \ell\nu\bar{\nu})$. This number of *double signal* events depends on the branching fraction to be measured—and thus so does the number of subtracted background reactions.

This problem does not occur if the branching fraction is calculated using the definition of a signal event according to method 2. But instead of Equation 6.3, method 2 results in a non-linear relation between the numbers of events and the branching fraction. This is caused by the inclusion of double signal events, in which both the negative and the positive τ lepton decay in the signal channel, $\tau^- \to$ sig and $\tau^+ \to$ sig. In addition, a

signal event is obtained if either the negative or the positive τ lepton decays in the signal mode while the second one decays in another (non-signal) channel, $\tau^{\pm} \to$ sig and $\tau^{\mp} \not\to$ sig. Thus, if $\mathcal{B}_{\text{sig}} \equiv \mathcal{B}(\tau \to \text{signal})$ is the branching fraction of the signal mode, the number of signal events according to definition 2 that are produced at the $B\text{A}B\text{AR}$ experiment is

$$N(\tau_1 \to \text{signal}, \ \tau_2 \to \text{anything})$$

$$= \left\{ \underbrace{\mathcal{B}_{\text{sig}}}_{\tau^- \to \text{sig}} \cdot \underbrace{(1 - \mathcal{B}_{\text{sig}})}_{\tau^+ \not\to \text{sig}} + \underbrace{(1 - \mathcal{B}_{\text{sig}})}_{\tau^- \not\to \text{sig}} \cdot \underbrace{\mathcal{B}_{\text{sig}}}_{\tau^+ \to \text{sig}} + \underbrace{\mathcal{B}_{\text{sig}}}_{\tau^- \to \text{sig}} \cdot \underbrace{\mathcal{B}_{\text{sig}}}_{\tau^+ \to \text{sig}} \right\} \times N_{\tau\tau}$$

$$= \left\{ 2\mathcal{B}_{\text{sig}} - (\mathcal{B}_{\text{sig}})^2 \right\} \times N_{\tau\tau} . \tag{6.4}$$

The branching fraction is then calculated according to

$$\mathcal{B}(\tau \to \text{signal}) = 1 - \sqrt{1 - \frac{N(\tau_1 \to \text{signal}, \ \tau_2 \to \text{anything})}{N_{\tau\tau}}} . \tag{6.5}$$

The second solution of the quadratic Equation 6.4 is unphysical and hence discarded. If $\mathcal{B}(\tau \to \text{signal}) \ll 1$, i.e., $N(\tau_1 \to \text{signal}, \ \tau_2 \to \text{anything}) \ll N_{\tau\tau}$, Equation 6.5 results in

$$\mathcal{B}(\tau \to \text{signal}) \approx \frac{N(\tau_1 \to \text{signal}, \ \tau_2 \to \text{anything})}{2N_{\tau\tau}} . \tag{6.6}$$

In contrast to Equation 6.3, this is independent of the branching fraction to be measured. Thus, method 2 is used for the following measurements. It is however noted that—due to the lepton tag selection (Section 4.1)—Equation 6.6 still contains a dependence on the leptonic branching fraction $\mathcal{B}(\tau^- \to \ell^- \overline{\nu}_\ell \nu_\tau)$. The dependence does not appear explicitly as for definition 1 but has been absorbed into the signal efficiency (see below).

The number of $\tau^+\tau^-$ pairs produced at the $B\text{A}B\text{AR}$ experiment is obtained from the integrated luminosity of the data sample used in this analysis, $\mathcal{L} = (464.4 \pm 3.0) \, \text{fb}^{-1}$, and the cross section for the reaction $e^+e^- \to \tau^+\tau^-$, $\sigma_{\tau\tau} = (0.919 \pm 0.003) \, \text{nb}$ (Tables 2.1, 2.2):

$$N_{\tau\tau} = \mathcal{L} \cdot \sigma_{\tau\tau} = (426.8 \pm 3.1) \times 10^6 . \tag{6.7}$$

Due to the different center-of-mass energies of the On-Peak and Off-Peak data samples (Section 2.3.1), a luminosity-averaged cross section is used for all calculations within this thesis.

To obtain the number of produced signal events $N(\tau_1 \to \text{signal}, \ \tau_2 \to \text{anything})$ from the number of selected events in data, two steps are necessary. Despite the careful selection, the sample of selected events is not free from remaining background (cf. Figures 4.13, 4.14). Its amount is estimated using the Monte Carlo simulation and subtracted from the number of selected events in data. In addition, only a fraction of all signal events passes the selection criteria as described in Chapter 4. This fraction is called the *signal efficiency* ε_{sig}. For data, it is estimated by the signal efficiency in the

Monte Carlo simulation:

$$\varepsilon_{\mathrm{sig}} \equiv \varepsilon_{\mathrm{sig}}^{\mathrm{data}} \approx \varepsilon_{\mathrm{sig}}^{\mathrm{MC}} \equiv \frac{N_{\mathrm{MC,\,sig}}^{\mathrm{sel}}}{N_{\mathrm{MC,\,sig}}^{\mathrm{gen}}} , \qquad (6.8)$$

where $N_{\mathrm{MC,\,sig}}^{\mathrm{sel}}$ is the number of signal events in the Monte Carlo simulated selected event sample. The efficiency corrections described in Sections 3.5 and 5.2 are applied to each selected simulated event. The symbol $N_{\mathrm{MC,\,sig}}^{\mathrm{gen}}$ denotes the number of generated signal events before any reconstruction or event selection is applied. It corresponds to the (unknown) number of signal events in data, which are produced via e^+e^- collisions at the $B\!A\!B\!A\!R$ experiment.

With these approximations of the remaining background and the signal efficiency, the number of produced signal events in data can be calculated:

$$N(\tau_1 \to \text{signal}, \ \tau_2 \to \text{anything})$$

$$= \frac{N_{\mathrm{sig}}^{\mathrm{sel}}}{\varepsilon_{\mathrm{sig}}} \qquad (6.9)$$

$$= \frac{N^{\mathrm{sel}} - \displaystyle\sum_{i \in \mathrm{BG}} w_i \, N_{\mathrm{MC,\,BG}(i)}^{\mathrm{sel}}}{\varepsilon_{\mathrm{sig}}^{\mathrm{MC}}} ,$$

where $N_{\mathrm{sig}}^{\mathrm{sel}}$ is the number of selected signal events and N^{sel} the number of all selected events in data. The symbol $N_{\mathrm{MC,\,BG}(i)}^{\mathrm{sel}}$ denotes the number of simulated events of background type i that are selected as signal. The sum comprises all background modes included into the Monte Carlo simulation. All efficiency corrections are applied to these selected background events. The w_i are weights to scale the numbers of simulated events to the integrated luminosity $\mathcal{L}$ of the data:

$$w_i = \frac{\mathcal{L} \cdot \sigma_i}{N_{\mathrm{MC,\,BG}(i)}^{\mathrm{gen}}} , \qquad (6.10)$$

where σ_i is the cross section for the reaction $e^+e^- \to \mathrm{BG}(i)$ and $N_{\mathrm{MC,\,BG}(i)}^{\mathrm{gen}}$ is the number of generated events of background type i. Using Equation 6.9, the branching fraction can be calculated according to Equation 6.5.

6.2   Determination of the event migration

Within this work, the branching fractions of six τ decay modes are determined. Since their final states are very similar, they are also mutual backgrounds (Figures 4.13, 4.14). E. g., 6 % of all $\tau^- \to \pi^- \pi^0 \pi^0 \pi^0 \nu_\tau$ candidates are expected to be decays of the type $\tau^- \to \pi^- \pi^0 \pi^0 \pi^0 \pi^0 \nu_\tau$ where one π^0 meson has not been reconstructed.

According to Equation 6.9, the remaining background needs to be subtracted from the number of selected data events in order to calculate the branching fraction. For a background contribution from a τ decay $\tau \to i_\tau$, the effective production cross section σ_{i_τ} for this analysis (Equation 6.10) is the product of the $\tau\tau$ production cross section $\sigma_{\tau\tau}$ and the probability that a $\tau\tau$ event is an event of the type i_τ according to definition 2. If

$\mathcal{B}_{i_\tau}$ is the corresponding branching fraction, this probability is $N_{i_\tau}/N_{\tau\tau} = \{2\mathcal{B}_{i_\tau} - (\mathcal{B}_{i_\tau})^2\}$ (Equation 6.4), where N_{i_τ} is the number of events that contain a decay of the type $\tau \to i_\tau$. Thus, the effective production cross section σ_{i_τ} is obtained as

$$\sigma_{i_\tau} = \left\{ 2\mathcal{B}_{i_\tau} - (\mathcal{B}_{i_\tau})^2 \right\} \sigma_{\tau\tau} . \tag{6.11}$$

The weight w_{i_τ} and hence the branching fraction to be measured depend on the branching fraction of the τ decay channel i_τ. In the case of a measurement of several decay modes that are mutual backgrounds, this results in a system of coupled equations. It can, e. g., be solved iteratively.

In this analysis, a different ansatz is used. Let $N^{\mathrm{prod}(j)}$ be the number of signal events of the ("true") type j produced in e^+e^- collisions at the $B_A B_{AR}$ experiment. The corresponding vector for all n decay channels to be measured simultaneously is

$$\mathbf{N}^{\mathrm{prod}} = \left(N^{\mathrm{prod}(1)}, \ldots, N^{\mathrm{prod}(n)} \right) . \tag{6.12}$$

The number of selected events of (reconstructed) type i is called $N^{\mathrm{sel}(i)}$. Subtracting the number of selected background events $N_{\mathrm{BG}}^{\mathrm{sel}(i)}$, the number of signal events selected in decay mode i, $N_{\mathrm{sig}}^{\mathrm{sel}(i)}$, is obtained:

$$\begin{aligned} N_{\mathrm{sig}}^{\mathrm{sel}(i)} &= N^{\mathrm{sel}(i)} - N_{\mathrm{BG}}^{\mathrm{sel}(i)} \\ &= N^{\mathrm{sel}(i)} - \sum_{j \in \mathrm{BG}} w_j N_{\mathrm{MC,BG}(j)}^{\mathrm{sel}(i)} . \end{aligned} \tag{6.13}$$

The $N_{\mathrm{MC,BG}(j)}^{\mathrm{sel}(i)}$ are the numbers of simulated events of background type j that are selected in decay mode i. They are scaled to the data luminosity using the weights w_j as defined in Equation 6.10. In the above sum and in the remainder of this chapter, the *background* modes $j \in \mathrm{BG}$ do not comprise the *migrated* events of (true) type $j \neq i$ of the n decay channels to be measured simultaneously. They are contained in the signal events $N_{\mathrm{sig}}^{\mathrm{sel}(i)}$ selected in decay channel i and are referred to as *cross feed*. The vector for all analyzed decay modes is called $\mathbf{N}_{\mathrm{sig}}^{\mathrm{sel}}$.

If M_{ij} is the probability of reconstructing an event of produced type j as selected type i, the relation between the produced and selected event numbers is given by

$$N_{\mathrm{sig}}^{\mathrm{sel}(i)} = \sum_{j=1}^{n} M_{ij} N^{\mathrm{prod}(j)} . \tag{6.14}$$

For selected events of type $\tau^- \to K^- \nu_\tau$, the resulting equation is

$$\begin{aligned} N_{\mathrm{sig}}^{\mathrm{sel}(K)} = \quad & M_{K,\pi 3\pi^0} && N^{\mathrm{prod}(\pi 3\pi^0)} \\ + \;\; & M_{K,\pi 4\pi^0} && N^{\mathrm{prod}(\pi 4\pi^0)} \\ + \;\; & M_{K,K} && N^{\mathrm{prod}(K)} \\ + \;\; & M_{K,K\pi^0} && N^{\mathrm{prod}(K\pi^0)} \\ + \;\; & M_{K,K2\pi^0} && N^{\mathrm{prod}(K2\pi^0)} \\ + \;\; & M_{K,K3\pi^0} && N^{\mathrm{prod}(K3\pi^0)} . \end{aligned} \tag{6.15}$$

The linear equation system of Equation 6.14 can be written in matrix form as

$$\mathbf{N}_{\text{sig}}^{\text{sel}} = \mathbf{M} \cdot \mathbf{N}^{\text{prod}} . \tag{6.16}$$

The matrix $\mathbf{M}$ is called *migration matrix*. Its elements M_{ij} are specified by Equation 6.14. For a decay mode i, the diagonal element M_{ii} corresponds to the signal efficiency from Equation 6.8, $M_{ii} \equiv \varepsilon_{\text{sig}(i)}$. The off-diagonal elements are the misidentification probabilities to select an event of decay channel $j \neq i$ in decay channel i. Analogous to the signal efficiencies, the matrix elements are estimated using the Monte Carlo simulation:

$$M_{ij} \equiv \frac{N_{\text{data}}^{\text{sel}(i),\text{prod}(j)}}{N_{\text{data}}^{\text{prod}(j)}} \approx \frac{N_{\text{MC}}^{\text{sel}(i),\text{gen}(j)}}{N_{\text{MC}}^{\text{gen}(j)}} . \tag{6.17}$$

The $N_{\text{data}}^{\text{sel}(i),\text{prod}(j)}$ ($N_{\text{MC}}^{\text{sel}(i),\text{gen}(j)}$) denote the numbers of events of produced (generated) type j selected as type i in data (Monte Carlo simulation). All efficiency corrections are applied to each selected simulated event as described in Sections 3.5 and 5.2.

The inverse migration matrix $\mathbf{M}^{-1}$ can be used to extract the numbers of initially produced events in data from the numbers of selected events simultaneously for all decay modes:

$$\mathbf{N}^{\text{prod}} = \mathbf{M}^{-1} \cdot \mathbf{N}_{\text{sig}}^{\text{sel}} . \tag{6.18}$$

According to Equation 6.5, the branching fractions $\mathcal{B}_i$ are then calculated by

$$\mathcal{B}_i = 1 - \sqrt{1 - \frac{N^{\text{prod}(i)}}{N_{\tau\tau}}} . \tag{6.19}$$

6.3   Measurement of the branching fractions

In this analysis, the migration matrix method is used to determine the branching fractions of the six decay modes $\tau^- \to \pi^- n\pi^0 \nu_\tau$ with $n = 3, 4$ and $\tau^- \to K^- n\pi^0 \nu_\tau$ with $n = 0, 1, 2, 3$. The extended form of the migration matrix $\mathbf{M} = (M_{\text{sel,prod}})$ is

$$\mathbf{M} = \begin{pmatrix} M_{\pi 3\pi^0, \pi 3\pi^0} & M_{\pi 3\pi^0, \pi 4\pi^0} & M_{\pi 3\pi^0, K} & M_{\pi 3\pi^0, K\pi^0} & M_{\pi 3\pi^0, K2\pi^0} & M_{\pi 3\pi^0, K3\pi^0} \\ M_{\pi 4\pi^0, \pi 3\pi^0} & M_{\pi 4\pi^0, \pi 4\pi^0} & M_{\pi 4\pi^0, K} & M_{\pi 4\pi^0, K\pi^0} & M_{\pi 4\pi^0, K2\pi^0} & M_{\pi 4\pi^0, K3\pi^0} \\ M_{K, \pi 3\pi^0} & M_{K, \pi 4\pi^0} & M_{K, K} & M_{K, K\pi^0} & M_{K, K2\pi^0} & M_{K, K3\pi^0} \\ M_{K\pi^0, \pi 3\pi^0} & M_{K\pi^0, \pi 4\pi^0} & M_{K\pi^0, K} & M_{K\pi^0, K\pi^0} & M_{K\pi^0, K2\pi^0} & M_{K\pi^0, K3\pi^0} \\ M_{K2\pi^0, \pi 3\pi^0} & M_{K2\pi^0, \pi 4\pi^0} & M_{K2\pi^0, K} & M_{K2\pi^0, K\pi^0} & M_{K2\pi^0, K2\pi^0} & M_{K2\pi^0, K3\pi^0} \\ M_{K3\pi^0, \pi 3\pi^0} & M_{K3\pi^0, \pi 4\pi^0} & M_{K3\pi^0, K} & M_{K3\pi^0, K\pi^0} & M_{K3\pi^0, K2\pi^0} & M_{K3\pi^0, K3\pi^0} \end{pmatrix} .$$

The first index denotes the reconstructed (selected) decay mode, while the second one indicates the (true) produced decay channel.

The numbers of selected events needed to calculate the migration matrix elements (Equation 6.17) are provided by the event selection (Chapter 4). Tables 2.2 and 2.3 specify the numbers of generated events. In case of a signal decay mode i_{sig} that is

contained in the simulated $\tau\tau$ event sample, the number of generated events $N^{\text{gen}(i_{\text{sig}})}$ is calculated according to Equation 6.4:

$$N^{\text{gen}(i_{\text{sig}})} = \left\{ 2\mathcal{B}_{i_{\text{sig}}} - \left(\mathcal{B}_{i_{\text{sig}}}\right)^2 \right\} \times N^{\text{gen}(\tau\tau)} . \tag{6.20}$$

The symbol $N^{\text{gen}(\tau\tau)}$ denotes the number of generated $\tau^+\tau^-$ events and $\mathcal{B}_{i_{\text{sig}}}$ is the branching fraction of the decay mode i_{sig} that is used to simulate the decay of the generated τ leptons.

An event in which both τ leptons decay into a signal mode, e. g., $\tau^- \to K^-\pi^0\pi^0\nu_\tau$ and $\tau^+ \to K^+\bar{\nu}_\tau$, is counted as generated event in both channels. However, if selected, i. e., if one of the decays is misidentified as a leptonic τ decay, it is only counted once as selected event in the decay channel that is reconstructed in the signal hemisphere (Section 4.2). If these *double signal* events constitute a significant fraction of the *selected* event sample, each measured branching fraction depends on the branching fractions of the remaining signal modes. Due to the stringent selection criteria, double signal events only represent a minor contribution of less than $0.08\,\%$ of all selected events. The dependence is thus negligible.

The migration matrix that results from the numbers of selected and generated event numbers according to Equation 6.17 is

$$\mathbf{M} = \begin{pmatrix} 7.83 \cdot 10^{-3} & 5.19 \cdot 10^{-3} & 5.82 \cdot 10^{-7} & 5.61 \cdot 10^{-6} & 8.96 \cdot 10^{-5} & 9.64 \cdot 10^{-4} \\ 2.24 \cdot 10^{-5} & 9.97 \cdot 10^{-4} & 0.00 & 0.00 & 1.04 \cdot 10^{-6} & 5.85 \cdot 10^{-6} \\ 1.41 \cdot 10^{-6} & 3.29 \cdot 10^{-7} & 2.20 \cdot 10^{-2} & 1.20 \cdot 10^{-3} & 2.52 \cdot 10^{-4} & 2.13 \cdot 10^{-5} \\ 8.48 \cdot 10^{-6} & 3.67 \cdot 10^{-6} & 1.18 \cdot 10^{-4} & 2.22 \cdot 10^{-2} & 3.81 \cdot 10^{-3} & 3.93 \cdot 10^{-4} \\ 3.12 \cdot 10^{-5} & 9.81 \cdot 10^{-6} & 1.40 \cdot 10^{-6} & 8.87 \cdot 10^{-5} & 1.24 \cdot 10^{-2} & 2.14 \cdot 10^{-3} \\ 1.92 \cdot 10^{-5} & 1.10 \cdot 10^{-5} & 0.00 & 0.00 & 2.90 \cdot 10^{-5} & 8.25 \cdot 10^{-4} \end{pmatrix} .$$

Its diagonal elements are the signal efficiencies for the selected decay channels,

$$\boldsymbol{\varepsilon}_{\text{sig}} = \begin{pmatrix} \varepsilon_{\text{sig}}^{\pi 3\pi^0} \\ \varepsilon_{\text{sig}}^{\pi 4\pi^0} \\ \varepsilon_{\text{sig}}^{K} \\ \varepsilon_{\text{sig}}^{K\pi^0} \\ \varepsilon_{\text{sig}}^{K 2\pi^0} \\ \varepsilon_{\text{sig}}^{K 3\pi^0} \end{pmatrix} = \begin{pmatrix} 0.78 \ \% \\ 0.10 \ \% \\ 2.20 \ \% \\ 2.22 \ \% \\ 1.24 \ \% \\ 0.08 \ \% \end{pmatrix} . \tag{6.21}$$

The general decrease of the signal efficiency with increasing number of π^0 mesons is due to the finite π^0 selection efficiency (Section 5.2). In contrast, the relatively low efficiency for the decay mode $\tau^- \to K^-\nu_\tau$ is due to the stringent criteria applied to reject remaining QED background (Section 4.5). The low level of the selection efficiencies is partly caused by the boost of the e^+e^- center-of-mass system (Section 2.1). Due to this boost, a significant fraction of the τ decay products escapes detection outside the fiducial volume of the *BABAR* detector. Additionally, the branching fractions of the leptonic tag decays are absorbed into the selection efficiencies (Section 6.1), which reduces the efficiencies by a factor of three [3].

Because of the finite size of the generated event samples, the calculated signal
efficiencies and migration matrix elements are subject to statistical fluctuations. Since
the numbers of selected events are subsets of the numbers of generated events, the
resulting uncertainties are estimated using binomial statistics:

$$\Delta M_{ij}^{(\text{stat})} = \sqrt{\frac{N^{\text{sel}(i),\text{gen}(j)}\left[N^{\text{gen}(j)} - N^{\text{sel}(i),\text{gen}(j)}\right]}{\left[N^{\text{gen}(j)}\right]^3}}. \tag{6.22}$$

The *relative* statistical uncertainties of the above migration matrix $\Delta M_{ij}/M_{ij}$ are

$$\frac{\Delta \mathbf{M}}{\mathbf{M}} = \begin{pmatrix}
3.91 \cdot 10^{-3} & 1.42 \cdot 10^{-2} & 5.43 \cdot 10^{-1} & 2.15 \cdot 10^{-1} & 1.50 \cdot 10^{-1} & 5.73 \cdot 10^{-2} \\
7.34 \cdot 10^{-2} & 3.24 \cdot 10^{-2} & - & - & 1.39 & 7.36 \cdot 10^{-1} \\
2.92 \cdot 10^{-1} & 1.78 & 2.76 \cdot 10^{-3} & 1.47 \cdot 10^{-2} & 8.95 \cdot 10^{-2} & 3.85 \cdot 10^{-1} \\
1.19 \cdot 10^{-1} & 5.34 \cdot 10^{-1} & 3.81 \cdot 10^{-2} & 3.37 \cdot 10^{-3} & 2.30 \cdot 10^{-2} & 8.98 \cdot 10^{-2} \\
6.21 \cdot 10^{-2} & 3.26 \cdot 10^{-1} & 3.50 \cdot 10^{-1} & 5.40 \cdot 10^{-2} & 1.27 \cdot 10^{-2} & 3.84 \cdot 10^{-2} \\
7.93 \cdot 10^{-2} & 3.09 \cdot 10^{-1} & - & - & 2.64 \cdot 10^{-1} & 6.19 \cdot 10^{-2}
\end{pmatrix}.$$

A "$-$" indicates that no uncertainty can be calculated since no events of type j are
selected as type i.[1] The resulting uncertainties of the measured branching fractions are
derived in Section 6.5.6.

The numbers of events in data that pass the selection criteria as described in
Chapter 4 are

$$\mathbf{N}^{\text{sel}} = \begin{pmatrix}
N^{\text{sel}(\pi 3\pi^0)} \\
N^{\text{sel}(\pi 4\pi^0)} \\
N^{\text{sel}(K)} \\
N^{\text{sel}(K\pi^0)} \\
N^{\text{sel}(K2\pi^0)} \\
N^{\text{sel}(K3\pi^0)}
\end{pmatrix} = \begin{pmatrix}
(1.0897 \pm 0.0033) \cdot 10^5 \\
(1.287 \pm 0.035) \cdot 10^3 \\
(1.7013 \pm 0.0041) \cdot 10^5 \\
(1.4119 \pm 0.0038) \cdot 10^5 \\
(1.504 \pm 0.012) \cdot 10^4 \\
(5.48 \pm 0.23) \cdot 10^2
\end{pmatrix}. \tag{6.23}$$

The given uncertainties are statistical only and assume a Poisson distribution of the
numbers of selected events, i.e., the uncertainty is $\Delta N^{\text{sel}(i)} = \sqrt{N^{\text{sel}(i)}}$. The resulting
numbers of background subtracted events in data (Equation 6.13) are

$$\mathbf{N}^{\text{sel}}_{\text{sig}} = \begin{pmatrix}
N^{\text{sel}(\pi 3\pi^0)}_{\text{sig}} \\
N^{\text{sel}(\pi 4\pi^0)}_{\text{sig}} \\
N^{\text{sel}(K)}_{\text{sig}} \\
N^{\text{sel}(K\pi^0)}_{\text{sig}} \\
N^{\text{sel}(K2\pi^0)}_{\text{sig}} \\
N^{\text{sel}(K3\pi^0)}_{\text{sig}}
\end{pmatrix} = \begin{pmatrix}
8.83 \cdot 10^4 \\
1.06 \cdot 10^3 \\
1.28 \cdot 10^5 \\
8.96 \cdot 10^4 \\
6.30 \cdot 10^3 \\
3.19 \cdot 10^2
\end{pmatrix}. \tag{6.24}$$

---

[1] It makes no sense to derive upper limits on individual migration matrix elements as their uncertainties are correlated.

In addition to the background as estimated from the Monte Carlo simulation (Equation 6.13), the excess of selected data events due to hadronic split-offs has also been subtracted (Section 5.3.2). The fractional excess with respect to the total selected data samples is summarized for the analyzed decay modes in Table 5.1. Since the subtracted background event numbers are not independent for the different decay modes, no uncertainties are given for the background subtracted event numbers in data. The uncertainties of the branching fractions due to the background subtraction are determined in Sections 6.5.7 and 6.5.9.

Using Equation 6.18 and the inverse of the migration matrix, the numbers of signal events that are produced in e^+e^- collisions at the $B\textsc{a}B\textsc{ar}$ experiment are obtained:

$$\mathbf{N}^{\mathrm{prod}} = \begin{pmatrix} N^{\mathrm{prod}(\pi 3\pi^0)} \\ N^{\mathrm{prod}(\pi 4\pi^0)} \\ N^{\mathrm{prod}(K)} \\ N^{\mathrm{prod}(K\pi^0)} \\ N^{\mathrm{prod}(K2\pi^0)} \\ N^{\mathrm{prod}(K3\pi^0)} \end{pmatrix} = \begin{pmatrix} 1.07 \cdot 10^7 \\ 8.22 \cdot 10^5 \\ 5.59 \cdot 10^6 \\ 3.92 \cdot 10^6 \\ 4.31 \cdot 10^5 \\ 1.12 \cdot 10^5 \end{pmatrix}. \tag{6.25}$$

Inserting these event numbers and the number of $\tau^+\tau^-$ pairs from Equation 6.7 into Equation 6.19 results in the measured branching fractions of

$$\begin{aligned} \mathcal{B}(\tau^- \to \pi^-\pi^0\pi^0\pi^0\nu_\tau) &= 1.263 \times 10^{-2} \ , \\ \mathcal{B}(\tau^- \to \pi^-\pi^0\pi^0\pi^0\pi^0\nu_\tau) &= 9.63 \ \times 10^{-4} \ , \\ \mathcal{B}(\tau^- \to K^-\nu_\tau) &= 6.574 \times 10^{-3} \ , \\ \mathcal{B}(\tau^- \to K^-\pi^0\nu_\tau) &= 4.607 \times 10^{-3} \ , \\ \mathcal{B}(\tau^- \to K^-\pi^0\pi^0\nu_\tau) &= 5.05 \ \times 10^{-4} \ , \\ \mathcal{B}(\tau^- \to K^-\pi^0\pi^0\pi^0\nu_\tau) &= 1.31 \ \times 10^{-4} \ . \end{aligned} \tag{6.26}$$

6.4 Statistical uncertainties and their correlations

Due to the simultaneous extraction and the similar selection procedure, the numbers of selected events and the measured branching fractions are correlated between the different analyzed decay modes. The determination of the correlations necessitates a treatment of the uncertainties in form of covariance and correlation matrices. Statistical uncertainties resulting from the statistical fluctuations of the numbers of selected data events are determined in this section. The uncertainties due to the limited numbers of available simulated events are studied and estimated in the next section together with the systematic uncertainties inherent to this measurement.

To be able to calculate the statistical uncertainties, the error propagation is summarized for a general function $\mathbf{f}$ with

$$
\mathbf{f}(\mathbf{x}) \equiv \begin{pmatrix} f_1(x_1,\, x_2,\, \ldots,\, x_n) \\ f_2(x_1,\, x_2,\, \ldots,\, x_n) \\ \vdots \\ f_m(x_1,\, x_2,\, \ldots,\, x_n) \end{pmatrix} . \tag{6.27}
$$

The $\mathbf{f} = (f_1,\, f_2,\, \ldots,\, f_m)$ symbolize the quantities of interest that are calculated from the measured quantities $\mathbf{x} = (x_1,\, x_2,\, \ldots,\, x_n)$. Let $\mathbf{V_x}$ be the covariance matrix of the measured quantities $\mathbf{x} = (x_1,\, x_2,\, \ldots,\, x_n)$,

$$
\mathbf{V_x} \equiv \begin{pmatrix} V_{11} & V_{12} & \ldots & V_{1n} \\ \vdots & \vdots & \ddots & \vdots \\ V_{n1} & V_{n2} & \ldots & V_{nn} \end{pmatrix} , \tag{6.28}
$$

with elements

$$
V_{ij} \equiv \mathrm{cov}(x_i, x_j) . \tag{6.29}
$$

The covariance matrix $\mathbf{V_f}$ of $\mathbf{f}$ is then obtained according to

$$
\mathbf{V_f} = \mathbf{J} \cdot \mathbf{V_x} \cdot \mathbf{J}^\mathsf{T} , \tag{6.30}
$$

where $\mathbf{J}$ is the Jacobian matrix of $\mathbf{f}$ and $\mathbf{J}^\mathsf{T}$ its transpose:

$$
\mathbf{J} \equiv \frac{\partial \mathbf{f}}{\partial \mathbf{x}} \equiv \begin{pmatrix} \frac{\partial f_1}{\partial x_1} & \frac{\partial f_1}{\partial x_2} & \cdots & \frac{\partial f_1}{\partial x_n} \\ \vdots & \vdots & \ddots & \vdots \\ \frac{\partial f_m}{\partial x_1} & \frac{\partial f_m}{\partial x_2} & \cdots & \frac{\partial f_m}{\partial x_n} \end{pmatrix} . \tag{6.31}
$$

A detailed derivation of the presented formulae may be found in Reference [85].

For the determination of the branching fractions, the numbers of produced events in data $\mathbf{N}^\mathrm{prod}$ are calculated from the measured numbers of selected events in data $\mathbf{N}^\mathrm{sel}$ using Equations 6.13 and 6.18:

$$
\begin{aligned}
\mathbf{N}^\mathrm{prod} &= \mathbf{M}^{-1} \cdot \mathbf{N}^\mathrm{sel}_\mathrm{sig} \\
&= \mathbf{M}^{-1} \cdot \left(\mathbf{N}^\mathrm{sel} - \mathbf{N}^\mathrm{sel}_\mathrm{BG} \right) .
\end{aligned} \tag{6.32}
$$

The symbol $\mathbf{M}^{-1}$ denotes the inverse migration matrix and $\mathbf{N}^\mathrm{sel}_\mathrm{BG}$ are the numbers of selected background events in the Monte Carlo simulation. They do not include the cross feed events from the measured decay channels (Equation 6.13).

In this section, only the statistical uncertainties from statistical variations of the selected event numbers in data $\mathbf{N}^\mathrm{sel}$ are calculated. The subtracted background events $\mathbf{N}^\mathrm{sel}_\mathrm{BG}$ are also subject to statistical fluctuations due to the finite size of the simulated event samples. They are considered in the context of systematic uncertainties in Section 6.5.7.

If $\mathbf{V}^{\text{sel}}$ is the covariance matrix of the selected event numbers in data $\mathbf{N}^{\text{sel}}$, the one of the produced event numbers $\mathbf{N}^{\text{prod}}$, $\mathbf{V}^{\text{prod}}$, is calculated from Equation 6.32 according to Equation 6.30:

$$\mathbf{V}^{\text{prod}} = \mathbf{M}^{-1} \cdot \mathbf{V}^{\text{sel}} \cdot \left(\mathbf{M}^{-1}\right)^{\mathsf{T}}, \tag{6.33}$$

where $\mathbf{J}^{\text{prod}} = \mathbf{M}^{-1}$. Equation 6.19 specifies the relations between the branching fractions $\mathcal{B}_i$ and the produced event numbers. Their Jacobian matrix $\mathbf{J}^{\mathcal{B}}$ is diagonal:

$$J^{\mathcal{B}}_{ij} = \frac{\partial \mathcal{B}_i}{\partial N^{\text{prod}(j)}} = \delta_{ij} \frac{1}{2\mathcal{L}\sigma_{\tau\tau}} \sqrt{1 - \frac{N^{\text{prod}(j)}}{\mathcal{L}\sigma_{\tau\tau}}} \quad \text{with} \quad \delta_{ij} = \left\{ \begin{array}{ll} 1: & i = j \\ 0: & i \neq j \end{array} \right. . \tag{6.34}$$

The resulting covariance matrix $\mathbf{V}^{\mathcal{B}}$ of the measured branching fractions is

$$\begin{aligned} \mathbf{V}^{\mathcal{B}} &= \mathbf{J}^{\mathcal{B}} \cdot \mathbf{V}^{\text{prod}} \cdot \left(\mathbf{J}^{\mathcal{B}}\right)^{\mathsf{T}} \\ &= \mathbf{J}^{\mathcal{B}} \cdot \mathbf{M}^{-1} \cdot \mathbf{V}^{\text{sel}} \cdot \left(\mathbf{M}^{-1}\right)^{\mathsf{T}} \cdot \left(\mathbf{J}^{\mathcal{B}}\right)^{\mathsf{T}} \\ &= \mathbf{J}^{\mathcal{B}} \cdot \mathbf{M}^{-1} \cdot \mathbf{V}^{\text{sel}} \cdot \left(\mathbf{J}^{\mathcal{B}} \cdot \mathbf{M}^{-1}\right)^{\mathsf{T}} . \end{aligned} \tag{6.35}$$

All numbers of selected events in data $N^{\text{sel}(i)}$ from Equation 6.23 are assumed to be statistically independent, i. e., their statistical covariance matrix is diagonal. Here, the statistical independence needs to be distinguished from correlations due to the event selection. The latter are considered as systematic uncertainties in Section 6.5. The $N^{\text{sel}(i)}$ are assumed to be Poisson distributed, i. e., their variances V_{ij} are $V_{ij} = \delta_{ij} N^{\text{sel}(i)}$ and the full covariance matrix takes the form

$$\mathbf{V}^{\text{sel}} = \begin{pmatrix} N^{\text{sel}(1)} & 0 & \dots & 0 \\ 0 & N^{\text{sel}(2)} & 0 & \vdots \\ \vdots & 0 & \ddots & 0 \\ 0 & \dots & 0 & N^{\text{sel}(n)} \end{pmatrix} . \tag{6.36}$$

The matrix $\mathbf{V}^{\mathcal{B}}$ is calculated from $\mathbf{V}^{\text{sel}}$ as described by Equation 6.35. Instead of giving the covariance matrix, the *standard deviations* $\sigma_{\mathcal{B}_i}$ of the branching fractions and the corresponding *correlation matrix* $\boldsymbol{\rho}_{\mathcal{B}}$ are specified for each estimated uncertainty. The standard deviations are defined as

$$\sigma_{\mathcal{B}_i} \equiv \sqrt{V^{\mathcal{B}}_{ii}} \tag{6.37}$$

and the elements of the correlation matrix are

$$\rho^{\mathcal{B}}_{ij} \equiv \frac{V^{\mathcal{B}}_{ij}}{\sigma_{\mathcal{B}_i}\sigma_{\mathcal{B}_j}} \in [-1, +1] . \tag{6.38}$$

Per definition, $\rho^{\mathcal{B}}_{ii} = 1$. The standard deviation $\sigma_{\mathcal{B}_i}$ is used to specify the uncertainty of the single branching fraction $\mathcal{B}_i$, while the correlation matrix illustrates the correlations between the different decay channels more intuitively than the covariance matrix.

The resulting statistical uncertainties, i. e., standard deviations, for the measured branching fractions are

$$
\begin{aligned}
\mathcal{B}(\tau^- \to \pi^- \pi^0 \pi^0 \pi^0 \nu_\tau) &= (\, 1.263 \pm 0.006_{\text{(stat)}} \,) \times 10^{-2} \,, \\
\mathcal{B}(\tau^- \to \pi^- \pi^0 \pi^0 \pi^0 \pi^0 \nu_\tau) &= (\, 9.63 \pm 0.43_{\text{(stat)}} \,) \times 10^{-4} \,, \\
\mathcal{B}(\tau^- \to K^- \nu_\tau) &= (\, 6.574 \pm 0.022_{\text{(stat)}} \,) \times 10^{-3} \,, \\
\mathcal{B}(\tau^- \to K^- \pi^0 \nu_\tau) &= (\, 4.607 \pm 0.020_{\text{(stat)}} \,) \times 10^{-3} \,, \\
\mathcal{B}(\tau^- \to K^- \pi^0 \pi^0 \nu_\tau) &= (\, 5.05 \pm 0.13_{\text{(stat)}} \,) \times 10^{-4} \,, \\
\mathcal{B}(\tau^- \to K^- \pi^0 \pi^0 \pi^0 \nu_\tau) &= (\, 1.31 \pm 0.34_{\text{(stat)}} \,) \times 10^{-4} \,.
\end{aligned}
\tag{6.39}
$$

Their correlations are given by the following statistical correlation matrix

$$
\rho^{\mathcal{B}}_{\text{(stat)}} =
\begin{array}{c}
\begin{array}{cccccc}
\pi 3\pi^0 & \pi 4\pi^0 & K & K\pi^0 & K2\pi^0 & K3\pi^0
\end{array} \\
\left(
\begin{array}{cccccc}
1.000 & -0.513 & -0.000 & -0.002 & 0.034 & -0.100 \\
-0.513 & 1.000 & 0.000 & -0.000 & 0.002 & 0.001 \\
-0.000 & 0.000 & 1.000 & -0.055 & -0.001 & 0.001 \\
-0.002 & -0.000 & -0.055 & 1.000 & -0.109 & 0.021 \\
0.034 & 0.002 & -0.001 & -0.109 & 1.000 & -0.455 \\
-0.100 & 0.001 & 0.001 & 0.021 & -0.455 & 1.000
\end{array}
\right)
\begin{array}{l}
\pi 3\pi^0 \\
\pi 4\pi^0 \\
K \\
K\pi^0 \\
K2\pi^0 \\
K3\pi^0
\end{array}
\end{array}
\tag{6.40}
$$

The branching fractions of decay channels that differ by one π^0, e. g., $\tau^- \to K^- \pi^0 \pi^0 \nu_\tau$ with respect to $\tau^- \to K^- \pi^0 \nu_\tau$ and $\tau^- \to K^- \pi^0 \pi^0 \pi^0 \nu_\tau$, are anti-correlated. If a true decay of the type $\tau^- \to K^- \pi^0 \pi^0 \nu_\tau$ is reconstructed as a $\tau^- \to K^- \pi^0 \nu_\tau$ reaction, the number of selected events of the type $\tau^- \to K^- \pi^0 \nu_\tau$ increases by one while the number of $\tau^- \to K^- \pi^0 \pi^0 \nu_\tau$ reactions decreases. The same argument holds for the case that a $\tau^- \to K^- \pi^0 \pi^0 \nu_\tau$ decay is selected as a reaction of the type $\tau^- \to K^- \pi^0 \pi^0 \pi^0 \nu_\tau$. Similarly, due to the identification of charged pions as "not being kaons" (Section 3.3.2), the branching fractions of $\tau^- \to \pi^- \pi^0 \pi^0 \pi^0 \nu_\tau$ and $\tau^- \to K^- \pi^0 \pi^0 \pi^0 \nu_\tau$ decays are also anti-correlated. If an event of true type $\tau^- \to \pi^- \pi^0 \pi^0 \pi^0 \nu_\tau$ is spuriously identified as an event of the type $\tau^- \to K^- \pi^0 \pi^0 \pi^0 \nu_\tau$, the event is not counted in the decay mode $\tau^- \to \pi^- \pi^0 \pi^0 \pi^0 \nu_\tau$ while the number of reconstructed $\tau^- \to K^- \pi^0 \pi^0 \pi^0 \nu_\tau$ events increases. Thus, the two modes are anti-correlated.

6.5 Systematic uncertainties

This section describes the investigation of systematic effects and the estimate of the corresponding uncertainties of the branching fractions. Most of the systematic uncertainties are determined numerically using a *variation method*. It facilitates the calculation of the full covariance matrices for the branching fractions. As for the statistical uncertainties, the standard deviations are quoted as the uncertainties and the correlation matrices are specified instead of the covariances (Equations 6.37, 6.38).

If a quantity X, e. g., the $\tau^+ \tau^-$ production cross section in $e^+ e^-$ collisions, enters into the calculation of the branching fractions, the corresponding systematic uncertainty

is estimated by varying X within its uncertainty ΔX. This is achieved by generating a random number r according to a Gaussian distribution with mean zero and standard deviation one. The varied quantity X_{var} is calculated as

$$X_{\text{var}} = X + r \cdot \Delta X \,. \tag{6.41}$$

The full extraction of the branching fractions is then performed using the varied quantity X_{var}. Since most quantities enter both the determination of the π^0 efficiency correction and the calculation of the branching fractions (Sections 5.1, 6.1), this implies two steps:

1. The determination of the π^0 efficiency correction according to Section 5.1 and

2. the measurement of the branching fractions according to Section 6.3, using the varied π^0 efficiency correction from step 1.

The variation procedure is repeated $N = 1000$ times, each time generating a new random number r. The covariance matrix of the branching fractions $\mathbf{V}^{\mathcal{B}}$ resulting from the uncertainty of X is calculated from the N varied branching fractions $\mathcal{B}_i^{(k)}$ according to its definition [85]

$$V_{ij}^{\mathcal{B}} \equiv \text{cov}(\mathcal{B}_i, \mathcal{B}_j) \equiv \frac{1}{N} \sum_{k=1}^{N} \left(\mathcal{B}_i^{(k)} - \overline{\mathcal{B}_i} \right) \left(\mathcal{B}_j^{(k)} - \overline{\mathcal{B}_j} \right) \,. \tag{6.42}$$

The sum comprises all variations and the $\overline{\mathcal{B}_i}$ are the mean values of the varied branching fractions:

$$\overline{\mathcal{B}_i} \equiv \frac{1}{N} \sum_{k=1}^{N} \mathcal{B}_i^{(k)} \,. \tag{6.43}$$

They should agree with the measured values of the $\mathcal{B}_i$ in Equation 6.26. The systematic uncertainties for the different decay channels are estimated by the standard deviations as defined in Equation 6.37 and their correlations are specified in form of the correlation matrix (Equation 6.38). For each of the following uncertainties, the standard deviations of all measured branching fractions are listed in Table 6.5. For the sake of legibility, the corresponding individual correlation matrices are not listed in this chapter but included in Appendix C. The total statistical and systematic correlation matrices are specified in Section 6.6.

6.5.1 $\tau\tau$ production cross section $\sigma(e^+e^- \to \tau^+\tau^-)$

The $\tau^+\tau^-$ production cross section in e^+e^- collisions $\sigma_{\tau\tau} \equiv \sigma(e^+e^- \to \tau^+\tau^-)$ enters into the number of $\tau^+\tau^-$ pairs produced at the BABAR experiment (Equation 6.7). It is needed to normalize the τ backgrounds to the data luminosity when calculating the π^0 efficiency correction (Section 5.1) and when extracting the branching fractions (Equations 6.10, 6.11). Its relative uncertainty for the data set used in this analysis is calculated using Monte Carlo simulation methods [9]:

$$\frac{\Delta\sigma_{\tau\tau}}{\sigma_{\tau\tau}} = 0.31\,\% \,. \tag{6.44}$$

The resulting uncertainties of the branching fractions are determined using the variation method according to Equation 6.41. As expected, the uncertainty of the mode $\tau^- \to K^-\pi^0\nu_\tau$ is very small (Table 6.5). The method of the π^0 efficiency correction results in a way in a relative measurement of the mode $\tau^- \to K^-\pi^0\nu_\tau$ with respect to the channel $\tau^- \to \pi^-\pi^0\nu_\tau$ (Section 5.1). In consequence, many uncertainties cancel in first order. It is also observed that the uncertainties increase with increasing number of π^0 mesons. This is due to the fact that the $\tau\tau$ production cross section enters the calculation of the π^0 efficiency correction, which is applied for each reconstructed π^0 meson. The same arguments hold for the integrated luminosity and the tracking efficiency, which enter the calculation of the branching fractions in the same way as the $\tau\tau$ production cross section (Sections 6.5.2, 6.5.4).

6.5.2   Luminosity

The integrated luminosity $\mathcal{L}$ is measured using Bhabha, di-muon and two-photon processes. According to References [41–43], its uncertainty depends on the run periods of BABAR data taking (Section 2.3) and consists of two contributions:

1. The uncertainty from the reconstruction, selection and analysis of the Bhabha, di-muon and two-photon events. This part is correlated for the data taking periods

   (a) run I–III with a relative uncertainty of 0.8 % and

   (b) run IV–VI with a relative uncertainty of 0.49 %.

   Both contributions in (a) and (b) are uncorrelated between the two periods.

2. The uncertainty due to the dominant Bhabha cross section with a relative size of 0.5 %. It is fully correlated for all run periods but uncorrelated with either contribution from 1.

The variation of Equation 6.41 is extended to accommodate all three contributions of the uncertainty. For each run period $i = \mathrm{I}, \ldots, \mathrm{VI}$ (Table 2.1), the varied luminosity $\mathcal{L}_i^{\mathrm{var}}$ is calculated as

$$\mathcal{L}_i^{\mathrm{var}} = \mathcal{L}_i \cdot \left[1 + r_{1(\mathrm{a/b})} \left(\frac{\Delta\mathcal{L}_i}{\mathcal{L}_i} \right)_{1(\mathrm{a/b})} + r_2 \left(\frac{\Delta\mathcal{L}_i}{\mathcal{L}_i} \right)_2 \right] . \tag{6.45}$$

The $(\Delta\mathcal{L}_i/\mathcal{L}_i)_j$ are the above contributions to the luminosity uncertainty and the r_j are the corresponding random numbers. For each run period either the contribution 1a or 1b and the contribution 2 are used to calculate the varied luminosity. I.e., for $i = \mathrm{I}, \ldots, \mathrm{III}$, $(\Delta\mathcal{L}_i/\mathcal{L}_i)_{1a} = 0.8\,\%$ is used, for $i = \mathrm{IV}, \ldots, \mathrm{VI}$, $(\Delta\mathcal{L}_i/\mathcal{L}_i)_{1b} = 0.49\,\%$ is applied. The uncertainty $(\Delta\mathcal{L}_i/\mathcal{L}_i)_2 = 0.5\,\%$ is used for all run periods. To account for the correlations of the uncertainties 1a and 1b for the run periods I–III and IV–VI, respectively, and 2 for all run periods, only three random numbers r_j are generated per variation. They are used for all run periods.

6.5.3 Background normalization

Background from non-migrating τ decays

According to Equations 6.10 and 6.11, the branching fraction $\mathcal{B}_{i_\tau}$ of a τ background $\tau \to \mathrm{BG}(i)$ is needed in addition to the $\tau\tau$ cross section in order to normalize the Monte Carlo simulated events to the data luminosity. Since all background branching fractions are known with finite precision only, this introduces an additional uncertainty of the measured branching fractions. Within this analysis, the branching fractions of all major τ decays into final states containing one charged particle are varied within their uncertainties as specified in Reference [3]. However, no Monte Carlo simulation and no branching fraction measurements exist for the decay channels $\tau^- \to \pi^- \pi^0 \pi^0 \pi^0 \pi^0 \pi^0 \nu_\tau$ and $\tau^- \to K^- \pi^0 \pi^0 \pi^0 \pi^0 \nu_\tau$. The uncertainty resulting from these two modes is estimated in Section 6.5.10.

In addition to being background for the signal decay modes, the modes $\tau^- \to \ell^- \overline{\nu}_\ell \nu_\tau$ with $\ell = e, \mu$ are used to tag the selected $\tau\tau$ events (Section 4.1). Their branching fractions also enter into the measured selection efficiency as they are used to generate the decay of the tag τ lepton. The variation of the branching fractions includes the decay of the tag τ lepton and thus covers the additional uncertainty.

Table 6.1 lists the branching fractions and their relative uncertainties for all decay modes included into the variation [3]. For each mode, the branching fraction is varied according to Equation 6.41. Since the measurements from Reference [3] are assumed to be uncorrelated, a different random number r is used for each branching fraction.

Non-τ background

Backgrounds from reactions other than $e^+ e^- \to \tau^+ \tau^-$ are negligible within this analysis (Figures 4.13, 4.14). So is the uncertainty due to their production cross sections.

6.5.4 Tracking efficiency

Section 3.5.1 briefly summarizes the determination of the tracking efficiency from $\tau\tau$ reactions. In principle, this efficiency $\varepsilon_{\mathrm{track}}$ can be different in data and Monte Carlo simulated events. In this case, a correction factor of

$$\eta_{\mathrm{track}} \equiv \frac{\varepsilon_{\mathrm{track}}^{\mathrm{data}}}{\varepsilon_{\mathrm{track}}^{\mathrm{MC}}} \tag{6.46}$$

has to be applied for each reconstructed track in the Monte Carlo simulation. According to Reference [53], the tracking efficiency correction at the *BaBar* experiment is consistent with one but has a non-zero uncertainty:

$$\eta_{\mathrm{track}} = (1.0000 \pm 0.0021) \,. \tag{6.47}$$

Since the correction factor is estimated from τ decays, uncertainties due to residual dependencies of the track efficiency on the position in the detector need not be considered in this analysis. The mean position of the tracks mainly depends on the direction of the original τ lepton and is very similar for all τ decays. The dependencies thus cancel for all analyses of τ final states [53]. They are not included in the above value.

Table 6.1: Decay modes of the τ lepton whose normalization to the data luminosity is varied according to the uncertainties of their branching fractions. The table specifies the branching fractions and their relative uncertainties in [%] as summarized in Reference [3].

	$\mathcal{B}$	$\frac{\Delta\mathcal{B}}{\mathcal{B}}$ [%]
$\tau^- \to \pi^- \nu_\tau$	10.83 %	1.0
$\tau^- \to \pi^- \pi^0 \nu_\tau$	25.46 %	0.47
$\tau^- \to \pi^- \pi^0 \pi^0 \nu_\tau$	9.24 %	1.3
$\tau^- \to \pi^- \eta \pi^0 \nu_\tau$	1.73×10^{-3}	14
$\tau^- \to \pi^- \eta \pi^0 \pi^0 \nu_\tau$	1.5×10^{-4}	33
$\tau^- \to K^- \eta \nu_\tau$	2.7×10^{-4}	22
$\tau^- \to K^- \eta \pi^0 \nu_\tau$	1.8×10^{-4}	50
$\tau^- \to \pi^- \overline{K}^0 \nu_\tau$	8.8×10^{-3}	5.7
$\tau^- \to \pi^- \overline{K}^0 \pi^0 \nu_\tau$	3.6×10^{-3}	11
$\tau^- \to K^- K^0 \nu_\tau$	1.58×10^{-3}	11
$\tau^- \to K^- K^0 \pi^0 \nu_\tau$	1.44×10^{-3}	16
$\tau^- \to \pi^- \overline{K}^0 \eta \nu_\tau$	2.2×10^{-4}	32
$\tau^- \to \pi^- \overline{K}^0 K^0 \nu_\tau$	1.53×10^{-3}	22
$\tau^- \to e^- \overline{\nu}_e \nu_\tau$	17.82 %	0.28
$\tau^- \to \mu^- \overline{\nu}_\mu \nu_\tau$	17.33 %	0.29

As each event contains two tracks whose reconstruction efficiencies are fully correlated, the total varied tracking efficiency correction is calculated as

$$\eta_{\text{track}}^{\text{var}} = \eta_{\text{track}} + 2r \cdot \Delta\eta_{\text{track}} \,, \tag{6.48}$$

where r is a random number.

Since the down feed of events with more than two tracks into the selected event sample is small ($\mathcal{O}(0.4\,\%)$, Section 4.1), the uncertainty due to deviations between data and Monte Carlo simulation with respect to this down feed is neglected.

6.5.5 Charged particle identification efficiency

As described in Sections 3.3.2 and 3.5.2, the charged particle identification efficiencies and misidentification probabilities in the Monte Carlo simulation have to be corrected to describe the data. Correction factors are applied for each identified or vetoed particle in the Monte Carlo simulation. In this analysis, the track in the lepton hemisphere

(Figure 4.1) is required to originate from an electron or muon and the signal track must either pass the kaon or the pion selection criteria. In addition, the signal track has to fail the electron selection criteria used as electron veto (Section 3.3.2). Thus, three correction factors are applied to each Monte Carlo simulated event in the form of event weights.

The correction factors are provided for each particle hypothesis by the Charged Particles Identification Working Group of the BABAR collaboration [63] in the form of look-up tables. They depend on the run period, the particle's momentum p and its position in the detector (θ, ϕ). Along with the corrections, the tables also provide uncertainties for each correction factor. These include uncertainties due to the limited statistics of the control samples as well as those that are inherent to the method of determining the weights [41]. All uncertainties are independent for the different run periods and each bin in (p, θ, ϕ). In the case of a reconstructed charged particle in a phase space region for which the control samples provide no information, the average of all remaining weights for this selection algorithm is used as correction factor (Section 3.5). The assigned uncertainty is estimated from the standard deviation of the weights that are used to calculate the average.

To estimate the resulting uncertainties of the branching fractions, a random number is generated for each particle hypothesis and run period and for each of the phase space bins in the corresponding table.

6.5.6   Signal selection efficiencies

Due to the finite number of Monte Carlo simulated events used for the determination of the migration matrix (Tables 2.2, 2.3), its elements M_{ij} are subject to statistical fluctuations (Section 6.3). Unlike the remaining uncertainties discussed in Section 6.5—apart from the background misidentification probabilities—these are of inherent statistical nature and thus, e. g., independent between the different run periods. To determine the uncertainties of the branching fractions caused by these fluctuations, the M_{ij} are varied within their uncertainties.

However, care needs to be taken since the migration matrix elements are partly correlated. The reason is similar to the one for the statistical correlations in Section 6.4. If an event of true type $\tau^- \to K^- \pi^0 \nu_\tau$ passes the selection criteria for any of the reconstructed modes $\tau^- \to h^- n\pi^0 \nu_\tau$ with $n = 3, 4$ for $h^- = \pi^-$ and $n = 0, 1, 2, 3$ for $h^- = K^-$, it is sorted into one of these decay channels. One of the migration matrix elements $M_{i,K\pi^0}$ is increased. If the event is correctly identified, it is counted for $M_{K\pi^0,K\pi^0}$. In contrast, if the event is misidentified, e. g., as a $\tau^- \to K^- \nu_\tau$ reaction, $M_{K,K\pi^0}$ is increased and the event is not counted for $M_{K\pi^0,K\pi^0}$. Thus, $M_{K\pi^0,K\pi^0}$ and $M_{K,K\pi^0}$ are partly anti-correlated.

In consequence, all matrix elements belonging to a true decay mode j_{gen} are correlated, where j_{gen} symbolizes any of the six measured decay modes $\tau^- \to h^- n\pi^0 \nu_\tau$ with $n = 3, 4$ for $h^- = \pi^-$ and $n = 0, 1, 2, 3$ for $h^- = K^-$. That is to say, all elements $M_{i,j_{\mathrm{gen}}}$ of one column of the migration matrix (cf. Section 6.3) are correlated, whereas they are independent with respect to different true decay modes j_{gen}. The elements $M_{i,j_{\mathrm{gen}}}$ can thus not be varied independently, but they are not fully correlated either.

A method to determine the correlations is the division of the event selection into

several steps. First, all signal events of the type $\tau^- \to h^- n\pi^0\nu_\tau$ with $n = 3, 4$ for $h^- = \pi^-$ and $n = 0, 1, 2, 3$ for $h^- = K^-$ are selected. In each of the following steps, the remaining event sample is separated into those events that are selected as one of the measured decay channels, e. g., $\tau^- \to \pi^-\pi^0\pi^0\pi^0\nu_\tau$, and those that are not selected in this mode. If $\varepsilon \equiv N^{\mathrm{sel}}/N^{\mathrm{gen}}$ is the efficiency to select an event of the type $\tau^- \to \pi^-\pi^0\pi^0\pi^0\nu_\tau$ from all $\tau^- \to h^- n\pi^0\nu_\tau$ reactions, the efficiency to obtain an event that is not selected as a $\tau^- \to \pi^-\pi^0\pi^0\pi^0\nu_\tau$ decay is $(1 - \varepsilon)$. Both efficiencies are fully anti-correlated. The corresponding uncertainty $\Delta\varepsilon$ is calculated using binomial statistics (Equation 6.22):

$$\Delta\varepsilon = \sqrt{\frac{N^{\mathrm{sel}}\left[N^{\mathrm{sel}} - N^{\mathrm{gen}}\right]}{\left[N^{\mathrm{gen}}\right]^3}} \, . \tag{6.49}$$

Figure 6.1 illustrates the division of the selection procedure into such steps for all selected events of a true decay mode j_{gen}.
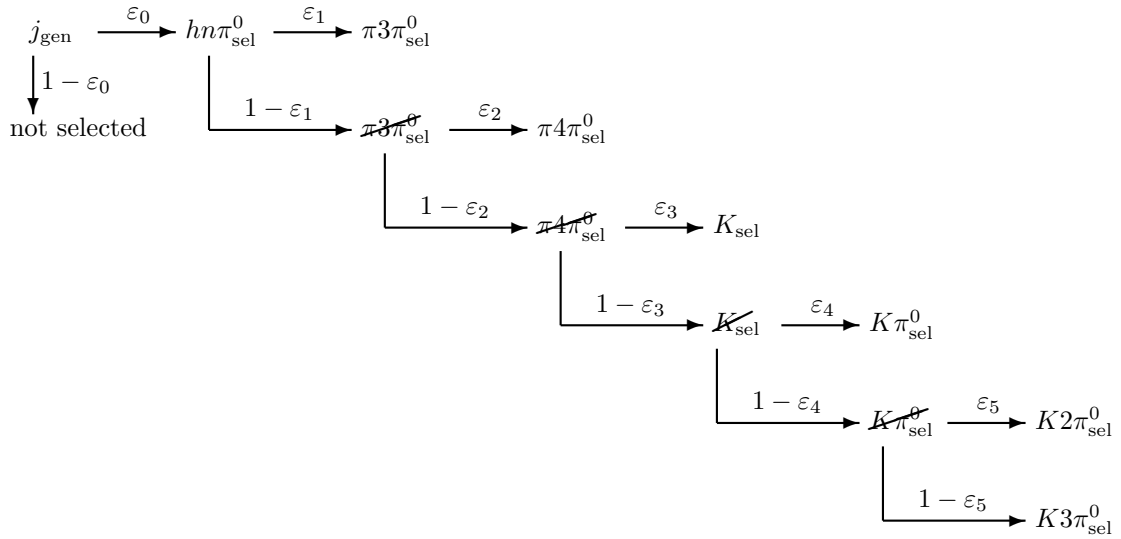
Figure 6.1: Division of the selection procedure into several steps in order to determine the statistical correlations of the migration matrix elements. The abbreviation j_{gen} symbolizes the generated events of any of the measured signal modes $\tau^- \to h^- n\pi^0\nu_\tau$. The superscript *sel* symbolizes events that are selected as the given decay mode, while a symbol that is crossed out indicates events that are selected as not being of the given type. For each selection step, the corresponding efficiencies ε_i and $(1 - \varepsilon_i)$ are fully anti-correlated, whereas all ε_i are uncorrelated for different selection steps i. The migration matrix elements are obtained as products of these single-step efficiencies. Per construction, the correlations of the matrix elements are considered.

The migration matrix elements are obtained as products of the single-step efficiencies:

$$
\begin{aligned}
M_{\pi 3\pi^0, j_{\mathrm{gen}}} &= \varepsilon_0 \cdot \varepsilon_1 \,, \\
M_{\pi 4\pi^0, j_{\mathrm{gen}}} &= \varepsilon_0 \cdot (1 - \varepsilon_1) \cdot \varepsilon_2 \,, \\
M_{K, j_{\mathrm{gen}}} &= \varepsilon_0 \cdot (1 - \varepsilon_1) \cdot (1 - \varepsilon_2) \cdot \varepsilon_3 \,, \\
M_{K\pi^0, j_{\mathrm{gen}}} &= \varepsilon_0 \cdot (1 - \varepsilon_1) \cdot (1 - \varepsilon_2) \cdot (1 - \varepsilon_3) \cdot \varepsilon_4 \,, \\
M_{K 2\pi^0, j_{\mathrm{gen}}} &= \varepsilon_0 \cdot (1 - \varepsilon_1) \cdot (1 - \varepsilon_2) \cdot (1 - \varepsilon_3) \cdot (1 - \varepsilon_4) \cdot \varepsilon_5 \,, \\
M_{K 3\pi^0, j_{\mathrm{gen}}} &= \varepsilon_0 \cdot (1 - \varepsilon_1) \cdot (1 - \varepsilon_2) \cdot (1 - \varepsilon_3) \cdot (1 - \varepsilon_4) \cdot (1 - \varepsilon_5) \,.
\end{aligned}
\tag{6.50}
$$

Their numerical values do not depend on the specific division of the selection procedure as illustrated in Figure 6.1. Any permutation of the selected final states yields identical results for the matrix elements. Since the efficiencies ε_i are uncorrelated for the different selection steps i, the correlations of the matrix elements are automatically considered. Equation 6.50 results in 36 equations for the 36 migration matrix elements, of which the six equations belonging to one generated decay mode j_{gen} are correlated.

Each of the 36 independent ε_i is varied according to Equation 6.41 using 36 random numbers r_i and the varied migration matrix elements are calculated:

$$
\begin{aligned}
M^{\mathrm{var}}_{\pi 3\pi^0, j_{\mathrm{gen}}} &= \quad (\varepsilon_0 + r_0 \Delta\varepsilon_0) \cdot \quad (\varepsilon_1 + r_1 \Delta\varepsilon_1) \,, \\[4pt]
M^{\mathrm{var}}_{\pi 4\pi^0, j_{\mathrm{gen}}} &= \quad (\varepsilon_0 + r_0 \Delta\varepsilon_0) \cdot (1 - \varepsilon_1 - r_1 \Delta\varepsilon_1) \cdot \quad (\varepsilon_2 + r_2 \Delta\varepsilon_2) \,, \\[4pt]
M^{\mathrm{var}}_{K, j_{\mathrm{gen}}} &= \quad (\varepsilon_0 + r_0 \Delta\varepsilon_0) \cdot (1 - \varepsilon_1 - r_1 \Delta\varepsilon_1) \cdot (1 - \varepsilon_2 - r_2 \Delta\varepsilon_2) \cdot \\
& \quad (\varepsilon_3 + r_3 \Delta\varepsilon_3) \,, \\[4pt]
M^{\mathrm{var}}_{K\pi^0, j_{\mathrm{gen}}} &= \quad (\varepsilon_0 + r_0 \Delta\varepsilon_0) \cdot (1 - \varepsilon_1 - r_1 \Delta\varepsilon_1) \cdot (1 - \varepsilon_2 - r_2 \Delta\varepsilon_2) \cdot \\
& \quad (1 - \varepsilon_3 - r_3 \Delta\varepsilon_3) \cdot \quad (\varepsilon_4 + r_4 \Delta\varepsilon_4) \,, \\[4pt]
M^{\mathrm{var}}_{K 2\pi^0, j_{\mathrm{gen}}} &= \quad (\varepsilon_0 + r_0 \Delta\varepsilon_0) \cdot (1 - \varepsilon_1 - r_1 \Delta\varepsilon_1) \cdot (1 - \varepsilon_2 - r_2 \Delta\varepsilon_2) \cdot \\
& \quad (1 - \varepsilon_3 - r_3 \Delta\varepsilon_3) \cdot (1 - \varepsilon_4 - r_4 \Delta\varepsilon_4) \cdot \quad (\varepsilon_5 + r_5 \Delta\varepsilon_5) \,, \\[4pt]
M^{\mathrm{var}}_{K 3\pi^0, j_{\mathrm{gen}}} &= \quad (\varepsilon_0 + r_0 \Delta\varepsilon_0) \cdot (1 - \varepsilon_1 - r_1 \Delta\varepsilon_1) \cdot (1 - \varepsilon_2 - r_2 \Delta\varepsilon_2) \cdot \\
& \quad (1 - \varepsilon_3 - r_3 \Delta\varepsilon_3) \cdot (1 - \varepsilon_4 - r_4 \Delta\varepsilon_4) \cdot (1 - \varepsilon_5 - r_5 \Delta\varepsilon_5) \,.
\end{aligned}
\tag{6.51}
$$

As the statistical uncertainties of the migration matrix elements have no effect on the determination of the π^0 efficiency correction, only the branching fractions are re-calculated for each varied migration matrix. This strongly limits the amount of computing time needed to perform a variation. Hence, $N = 10000$ variations are performed to determine the resulting uncertainties of the branching fractions.

6.5.7 Background misidentification probabilities

The remaining background in the selected data samples is estimated using Monte Carlo simulated reactions and subtracted from the data according to Equations 6.9 and 6.10. As for the determination of the signal efficiencies, only a finite set of Monte Carlo simulated events is available. Thus, the numbers of selected events $N^{\mathrm{sel}}_{\mathrm{MC, BG}(j)}$ of

background type $\mathrm{BG}(j)$ are subject to statistical fluctuations. The ratio

$$\varepsilon_j \equiv \frac{N_{\mathrm{MC,\,BG}(j)}^{\mathrm{sel}}}{N_{\mathrm{MC,\,BG}(j)}^{\mathrm{gen}}} \tag{6.52}$$

from Equations 6.9 and 6.10 is the probability to misidentify (i. e., select) an event of background type $\mathrm{BG}(j)$ as signal, where $N_{\mathrm{MC,\,BG}(j)}^{\mathrm{gen}}$ is the number of generated background reactions. It has the functional form of an efficiency and its uncertainty is calculated according to Equation 6.49.

In case of the migration matrix method (Section 6.2), the probability to misidentify an event of background type $\mathrm{BG}(j)$ as a signal event of type i is

$$\varepsilon_{ij}^{\mathrm{BG}} \equiv \frac{N_{\mathrm{MC,\,BG}}^{\mathrm{sel}(i),\mathrm{gen}(j)}}{N_{\mathrm{MC,\,BG}}^{\mathrm{gen}(j)}} \tag{6.53}$$

in full analogy to the migration matrix elements in Equation 6.17. The $N_{\mathrm{MC,\,BG}}^{\mathrm{gen}(j)}$ denote the number of generated events of background $\mathrm{BG}(j)$ and $N_{\mathrm{MC,\,BG}}^{\mathrm{sel}(i),\mathrm{gen}(j)}$ the subset of these that is selected as signal type i. Only the non-migrating backgrounds, i. e., those that do not originate from any of the measured decay modes, are considered.

As in the case of the migration matrix, the six $\varepsilon_{i,j_{\mathrm{BG}}}$ that belong to a specific background type $\mathrm{BG}(j)$ are not independent. They are correlated in the same way as the migration matrix elements $M_{i,j_{\mathrm{gen}}}$ in Figure 6.1 and Equation 6.50. Similarly, the misidentification probabilities are independent for different background types $\mathrm{BG}(j)$. In consequence, the $\varepsilon_{i,j_{\mathrm{BG}}}$ are varied like the migration matrix elements according to Equation 6.51 in order to obtain the resulting uncertainties of the branching fractions.

All background modes from Table 6.1 are included into the variations and 10000 iterations are performed. Due to the relatively small number of selected $\tau^- \to \pi^- \pi^0 \nu_\tau$ events in the measured signal modes and the huge number of generated $\tau^- \to \pi^- \pi^0 \nu_\tau$ reactions, correlations with the uncertainty of the π^0 efficiency correction are neglected. This uncertainty is considered in Section 6.5.8.

6.5.8 π^0 efficiency correction

The π^0 efficiency correction is discussed in Chapter 5. Section 5.4 describes the derivation of a systematic uncertainty of the correction method by considering the decay mode $\tau^- \to \pi^- \pi^0 \pi^0 \nu_\tau$. An uncertainty of $\Delta\eta_{\pi^0} = 1.5\,\%$ per reconstructed π^0 meson is assigned to account for the remaining differences between data and Monte Carlo simulation. Due to the derivation from the overall difference between data and Monte Carlo simulation, the uncertainty of the correction factor is assumed to be fully correlated for all π^0 energies.

The resulting uncertainties of the branching fractions are obtained by varying the π^0 efficiency correction factor for each selected event and π^0 meson within the uncertainty of $1.5\,\%$ according to Equation 6.41. To account for the correlations, only one random number r is generated per variation and used for all π^0 energies.

6.5.9 Split-offs

The uncertainties of the selected event numbers N in data due to spurious π^0 mesons that are created by hadronic split-offs are discussed in Section 5.3.2. They are summarized for the measured decay channels in Table 5.1. Since split-offs are a track-related phenomenon, the uncertainties of the selected data event numbers are assumed to be fully correlated between the different decay modes. I.e., all elements of the correlation matrix of these event numbers are set to one, $\rho_{ij}^N = +1$.

The resulting uncertainties of the branching fractions are obtained by varying the numbers of selected data events within the uncertainties from Table 5.1 according to Equation 6.41. To account for the correlations, only one random number r is generated per variation and used for all decay modes. As split-offs are rejected for the determination of the π^0 efficiency correction (Section 5.1), only the branching fractions need to be re-calculated for each variation. Thus, 10000 iterations are performed.

6.5.10 Background with additional π^0 mesons

Figures 4.13 and 4.14 show that the *down feed* of events that contain an additional π^0 meson contributes a significant amount of background to the selected data samples. For example, 6 % of all selected events of the type $\tau^- \to \pi^- 3\pi^0 \nu_\tau$ originate from (true) $\tau^- \to \pi^- 4\pi^0 \nu_\tau$ decays. This is accounted for by the Monte Carlo simulation in case of selected events of the type $\tau^- \to \pi^- n\pi^0 \nu_\tau$ with $n \le 3$ and $\tau^- \to K^- n\pi^0 \nu_\tau$ with $n \le 2$. However, no Monte Carlo simulation exists to estimate the down feed of $\tau^- \to \pi^- 5\pi^0 \nu_\tau$ decays into selected events of the type $\tau^- \to \pi^- 4\pi^0 \nu_\tau$ or of $\tau^- \to K^- 4\pi^0 \nu_\tau$ reactions into the sample of $\tau^- \to K^- 3\pi^0 \nu_\tau$ events. These backgrounds cannot be subtracted from the number of selected data events when calculating the branching fractions (Equation 6.9).

Instead, the resulting uncertainty of the measured branching fractions is estimated by an upper limit on the number of events of the true type $\tau^- \to \pi^- 5\pi^0 \nu_\tau$ ($\tau^- \to K^- 4\pi^0 \nu_\tau$) that are reconstructed as $\tau^- \to \pi^- 4\pi^0 \nu_\tau$ ($\tau^- \to K^- 3\pi^0 \nu_\tau$) decays in data. In the following discussion, events of the type $\tau^- \to \pi^- 5\pi^0 \nu_\tau$ and $\tau^- \to K^- 4\pi^0 \nu_\tau$ are generically named events with $(n+1)\ \pi^0$ mesons. Similarly, the corresponding $\tau^- \to \pi^- 4\pi^0 \nu_\tau$ and $\tau^- \to K^- 3\pi^0 \nu_\tau$ reactions are denoted as $n\ \pi^0$ reactions. The entire procedure is applied to both events of the type $\tau^- \to \pi^- 5\pi^0 \nu_\tau$ as background in selected $\tau^- \to \pi^- 4\pi^0 \nu_\tau$ reactions and to decays of the type $\tau^- \to K^- 4\pi^0 \nu_\tau$ as background in the sample of selected $\tau^- \to K^- 3\pi^0 \nu_\tau$ events.

The upper limit is obtained in two steps. First, events that contain $(n+1)\ \pi^0$ mesons are explicitly selected in data and Monte Carlo simulation. As there is no signal Monte Carlo simulation for these events, the selected simulated events are all background reactions that have been misidentified. In contrast, the selected data contains both potential signal and background events. The applied selection criteria are—apart from the number of reconstructed π^0 mesons—identical to those used to reconstruct the corresponding mode with $n\ \pi^0$ mesons. An upper limit on the number of selected data events that truly contain $(n+1)\ \pi^0$ mesons is calculated from the numbers of selected events in data and Monte Carlo simulation. In a second step, the ratio of the number of $(n+1)\ \pi^0$ background events in the $n\ \pi^0$ sample to the number of correctly selected

$(n+1)$ π^0 events is estimated. The product of this ratio and the derived upper limit on the number of correctly reconstructed $(n+1)$ π^0 events yields an upper limit on the number of $(n+1)$ π^0 background events in the selected n π^0 sample.

Table 6.2 summarizes the numbers of explicitly selected events of the type $\tau^- \rightarrow \pi^- 5\pi^0 \nu_\tau$ and $\tau^- \rightarrow K^- 4\pi^0 \nu_\tau$ for data and Monte Carlo simulation, respectively. The

Table 6.2: Upper limits on the numbers of explicitly selected data events of the type $\tau^- \rightarrow \pi^- 5\pi^0 \nu_\tau$ and $\tau^- \rightarrow K^- 4\pi^0 \nu_\tau$. The table lists the numbers of selected events in data and Monte Carlo simulation $N_{\text{data}}^{\text{sel}}$ and $N_{\text{MC}}^{\text{sel}}$ and the derived upper limits on the number of true signal events in the data $\mu_{\text{sig}}^{\text{CL}}$ at $CL = 68, 90, 95\,\%$ confidence level.

	$\tau^- \rightarrow \pi^- 5\pi^0 \nu_\tau$	$\tau^- \rightarrow K^- 4\pi^0 \nu_\tau$
$N_{\text{data}}^{\text{sel}}$	60	80
$N_{\text{MC}}^{\text{sel}}$	25.3	93.7
μ_{sig}^{68}	39.0	8.4
μ_{sig}^{90}	46.8	15.0
μ_{sig}^{95}	50.3	18.6

calculation of the upper limit—as described in the next paragraphs—follows the procedure outlined in Reference [3]. Let μ_{BG} and μ_{sig} be the true numbers of background and signal events, respectively. Assuming that the selected event numbers are Poisson distributed [3], the probabilities to observe N_{BG} background and $N_{\text{sig+BG}}$ signal and background events, $P_{\mu_{\text{BG}}}(N_{\text{BG}})$ and $P_{\mu_{\text{sig}}+\mu_{\text{BG}}}(N_{\text{sig+BG}}; \mu_{\text{BG}})$, are

$$P_{\mu_{\text{BG}}}(N_{\text{BG}}) = \frac{(\mu_{\text{BG}})^{N_{\text{BG}}}}{(N_{\text{BG}})!} e^{-\mu_{\text{BG}}},$$

$$P_{\mu_{\text{sig}}+\mu_{\text{BG}}}(N_{\text{sig+BG}}; \mu_{\text{BG}}) = \frac{(\mu_{\text{sig}} + \mu_{\text{BG}})^{N_{\text{sig+BG}}}}{(N_{\text{sig+BG}})!} e^{-(\mu_{\text{sig}}+\mu_{\text{BG}})}. \tag{6.54}$$

In this study, the number of background events is given by the number of selected simulated events, $N_{\text{BG}} \equiv N_{\text{MC}}^{\text{sel}}$. The number of selected data events corresponds to the number of signal and background events, $N_{\text{sig+BG}} \equiv N_{\text{data}}^{\text{sel}}$. The combined probability for μ_{sig} true signal events is

$$P_{\mu_{\text{sig}}}(N_{\text{sig+BG}}, N_{\text{BG}}) = \int_0^\infty d\mu_{\text{BG}}\, P_{\mu_{\text{BG}}}(N_{\text{BG}})\, P_{\mu_{\text{sig}}+\mu_{\text{BG}}}(N_{\text{sig+BG}}; \mu_{\text{BG}}) \tag{6.55}$$

$$= \int_0^\infty d\mu_{\text{BG}} \frac{(\mu_{\text{BG}})^{N_{\text{BG}}}}{(N_{\text{BG}})!} e^{-\mu_{\text{BG}}} \frac{(\mu_{\text{sig}} + \mu_{\text{BG}})^{N_{\text{sig+BG}}}}{(N_{\text{sig+BG}})!} e^{-(\mu_{\text{sig}}+\mu_{\text{BG}})}.$$

The upper limit on the number of selected events $\mu_{\text{sig}}^{\text{CL}}$ that truly contain $(n+1)$ π^0

mesons is obtained at the *confidence level CL* by the requirement

$$CL \overset{!}{=} \frac{\int\limits_0^{\mu_{\text{sig}}^{\text{CL}}} d\mu_{\text{sig}} \, P_{\mu_{\text{sig}}}(N_{\text{sig+BG}}, N_{\text{BG}})}{\int\limits_0^{\infty} d\mu_{\text{sig}} \, P_{\mu_{\text{sig}}}(N_{\text{sig+BG}}, N_{\text{BG}})} \,. \tag{6.56}$$

The resulting values for the decay modes $\tau^- \to \pi^- 5\pi^0 \nu_\tau$ and $\tau^- \to K^- 4\pi^0 \nu_\tau$ are summarized in Table 6.2 at 68 % CL (one *standard deviation*) as well as at 90 % and 95 % CL.

All selection criteria—apart from the number of reconstructed π^0 mesons—are identical for the selection of events containing n and $(n+1)$ π^0 mesons. The efficiency of these non-π^0 related selection criteria is assumed to be similar for the selected n and $(n+1)$ π^0 events. This is sufficient for the estimate of an uncertainty. Thus, the only factor that determines into which sample an event is selected is the π^0 reconstruction. Given the π^0 selection efficiency ε_{π^0}, the probability to reconstruct an event that contains $(n+1)$ π^0 mesons as such $\varepsilon_{(n+1)\to(n+1)}$ is

$$\varepsilon_{(n+1)\to(n+1)} \propto \left(\varepsilon_{\pi^0}\right)^{(n+1)} \,. \tag{6.57}$$

In contrast, the probability to misidentify the event as an n π^0 reaction $\varepsilon_{(n+1)\to n}$ is

$$\varepsilon_{(n+1)\to n} \propto (n+1)\left(1 - \varepsilon_{\pi^0}\right)\left(\varepsilon_{\pi^0}\right)^n \,, \tag{6.58}$$

where $(1 - \varepsilon_{\pi^0})$ is the probability to miss a π^0. The factor $(n+1)$ is due to the fact that each of the $(n+1)$ π^0 mesons may be missed. The ratio $r_{n,(n+1)}$ of the number of $(n+1)$ π^0 background events in the n π^0 sample to the number of correctly selected $(n+1)$ π^0 events is given by the ratio of the π^0 efficiency terms from Equations 6.58 and 6.57:

$$r_{n,(n+1)} = \frac{\varepsilon_{(n+1)\to n}}{\varepsilon_{(n+1)\to(n+1)}} \approx \frac{(n+1)\left(1 - \varepsilon_{\pi^0}\right)}{\varepsilon_{\pi^0}} \,. \tag{6.59}$$

The remaining number of $(n+1)$ π^0 background events $N_{\text{BG}}^{\text{CL}}$ in the selected n π^0 sample can thus be estimated at confidence level *CL* as

$$N_{\text{BG}}^{\text{CL}} = r_{n,(n+1)} \cdot \mu_{(n+1)}^{\text{CL}} = \frac{(n+1)\left(1 - \varepsilon_{\pi^0}\right)}{\varepsilon_{\pi^0}} \cdot \mu_{(n+1)}^{\text{CL}} \,. \tag{6.60}$$

To calculate these numbers, the average efficiency to select a π^0 meson in correctly reconstructed n π^0 events is used. These events most closely match the event environment of real $(n+1)$ π^0 reactions that are reconstructed as n π^0 events. In the case of reactions of the type $\tau^- \to \pi^- 4\pi^0 \nu_\tau$ and $\tau^- \to K^- 3\pi^0 \nu_\tau$, the average π^0 selection efficiencies are

$$\begin{aligned} \langle \varepsilon_{\pi^0}^{\pi 4\pi^0} \rangle &= 76.3\,\% \,, \\ \langle \varepsilon_{\pi^0}^{K 3\pi^0} \rangle &= 74.5\,\% \,. \end{aligned} \tag{6.61}$$

The resulting upper limits on the remaining background are summarized in Table 6.3 for $(n+1)$ π^0 events of the type $\tau^- \to \pi^- 5\pi^0 \nu_\tau$ ($\tau^- \to K^- 4\pi^0 \nu_\tau$) that feed down into selected n π^0 reactions of the type $\tau^- \to \pi^- 4\pi^0 \nu_\tau$ ($\tau^- \to K^- 3\pi^0 \nu_\tau$).

Table 6.3: Upper limits on the numbers of background events of the type $\tau^- \to \pi^- 5\pi^0 \nu_\tau$ and $\tau^- \to K^- 4\pi^0 \nu_\tau$ in selected $\tau^- \to \pi^- 4\pi^0 \nu_\tau$ and $\tau^- \to K^- 3\pi^0 \nu_\tau$ reactions, respectively. The symbols $N_{\mathrm{BG}}^{\mathrm{CL}}$ denote the upper limits at $CL = 68, 90, 95\,\%$ confidence level. The table also lists the total numbers of selected events N^{sel} for the two event samples.

	$\tau^- \to \pi^- 4\pi^0 \nu_\tau$	$\tau^- \to K^- 3\pi^0 \nu_\tau$
N_{BG}^{68}	60.6	11.4
N_{BG}^{90}	72.6	20.5
N_{BG}^{95}	78.0	25.4
N^{sel}	1287	548

The uncertainties of the numbers of selected events of the type $\tau^- \to \pi^- 4\pi^0 \nu_\tau$ $(\tau^- \to K^- 3\pi^0 \nu_\tau)$ in data are estimated by the full upper limit on the background contribution from $\tau^- \to \pi^- 5\pi^0 \nu_\tau$ $(\tau^- \to K^- 4\pi^0 \nu_\tau)$ reactions at $68\,\%$ CL, i.e., at one standard deviation:

$$
\begin{aligned}
\Delta N_{\pi 4\pi^0}^{\mathrm{data}} &= 60.6\,, \\
\Delta N_{K 3\pi^0}^{\mathrm{data}} &= 11.4\,.
\end{aligned}
\tag{6.62}
$$

The resulting uncertainties of the measured branching fractions are obtained by varying the numbers of selected data events of the type $\tau^- \to \pi^- 4\pi^0 \nu_\tau$ and $\tau^- \to K^- 3\pi^0 \nu_\tau$ within the above uncertainties according to Equation 6.41. Since the branching fractions of the modes $\tau^- \to \pi^- 5\pi^0 \nu_\tau$ and $\tau^- \to K^- 4\pi^0 \nu_\tau$ are uncorrelated, two random numbers $r_{1,2}$ are used per variation. As the down feed is most significant in the channel with one π^0 meson less and the same identity of the charged hadron, only the down feed into selected events of the type $\tau^- \to \pi^- 4\pi^0 \nu_\tau$ and $\tau^- \to K^- 3\pi^0 \nu_\tau$ is considered. However, due to the changes in the calculated branching fractions of these two modes, the backgrounds also induce small uncertainties of the modes with two π^0 mesons difference. This is correctly accounted for by the variation method. As only the numbers of selected data events of the type $\tau^- \to \pi^- 4\pi^0 \nu_\tau$ and $\tau^- \to K^- 3\pi^0 \nu_\tau$ are varied, only the branching fractions need to be re-calculated. Thus, 10000 iterations are performed.

6.5.11   Variation of the selection criteria

The event selection described in Chapter 4 is partially based on selection criteria that are applied to kinematic quantities, e.g., the thrust or the missing mass. A basic requirement for this method is the description of the data distributions in the region of the selection criterion by the Monte Carlo simulation. Otherwise, the resulting efficiency of the criterion may be different for data and simulated reactions. As the Monte Carlo simulation is used to estimate the selection efficiency for the data (Section 6.2), this would introduce an additional uncertainty of the measured branching fractions.

Since the agreement of data and simulated distributions is not always given within the statistical uncertainties (see, e. g., Figure 4.8), the resulting uncertainties of the branching fractions have to be quantified.

This is achieved by estimating how much the simulated distribution of a specific selection variable needs to be shifted to obtain a good description of the data in the region of the selection criterion. The analysis is then repeated with the selection criterion on the simulated events shifted by the estimated difference, while the criterion on the data is left at its nominal value. The resulting deviation of the branching fractions measured in this way with respect to their nominal values is taken as an estimate of the corresponding uncertainty. The method is illustrated in Figure 6.2 for the selection criterion on the thrust and the upper selection criterion on the missing mass. It has

(a) Criterion on the thrust T. (b) Upper criterion on m_{miss}.
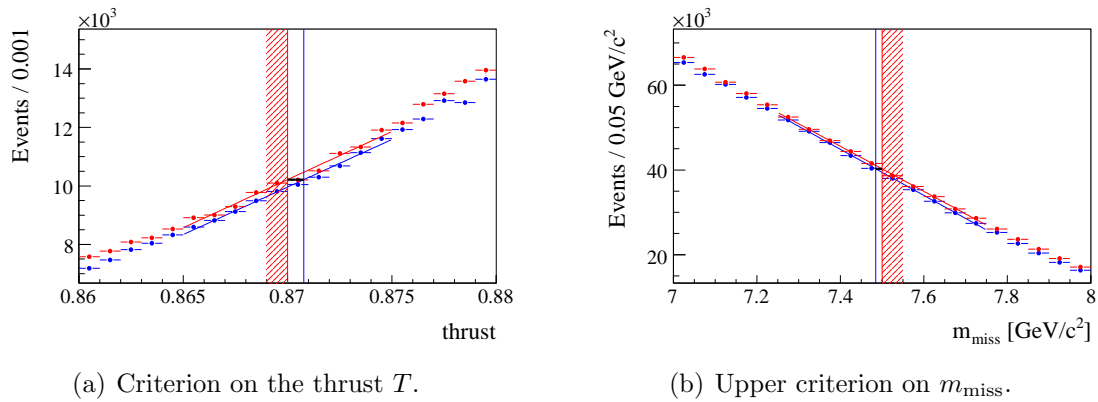
Figure 6.2: Illustration of the variation of the selection criteria. The histograms show a part of the **(a)** thrust and the **(b)** missing mass distributions (Figure 4.8) for the decay mode $\tau^- \to \pi^- \pi^0 \nu_\tau$ for data (red) and Monte Carlo simulation (blue) in the region of the selection criteria ($T > 0.87$, $m_{\mathrm{miss}} < 7.50\,\mathrm{GeV}/c^2$). Both values are indicated by the vertical red lines. The shift of the Monte Carlo simulation with respect to the data is estimated by fitting each distribution with a linear function as indicated by the red and blue curves. The difference between the values of the selection variable in data and Monte Carlo simulation (x-axis) that correspond to the number of events (y-axis) of the data distribution at the nominal value of the selection criterion is taken as a measure of the relative shift of the distributions. The resulting shifts are marked by horizontal black lines. The shifted selection criteria on the simulated events are indicated by the vertical blue lines.

been verified that all remaining distributions of the selection variables can also be approximated by a linear function in the region of the selection criterion. All deviations can be corrected by a shift of the Monte Carlo simulated distributions as exemplified in Figure 6.2.

Table 6.4 lists the resulting variations of the most important selection criteria. The distributions of the remaining selection criteria, i. e., the hadron-π^0 angle, the hadron-lepton acoplanarity and the invariant neutrino mass, agree between data and Monte Carlo simulation within the statistical uncertainties for the relevant decay modes. Hence, the selection criteria on these variables are not varied. The disagreement between

Table 6.4: Summary of the varied selection criteria. The table lists the changes of the selection criteria for the Monte Carlo simulation with respect to the nominal criteria (Tables 4.2, 4.3) as applied to the data.

Quantity		Variation
Thrust		0.0008
Missing mass	Lower boundary	$-0.015\,\mathrm{GeV}/c^2$
	Upper boundary	$-0.024\,\mathrm{GeV}/c^2$

data and Monte Carlo simulation with respect to the unassociated energy is discussed in Section 5.4. It is covered by the systematic uncertainty of the method of the π^0 efficiency correction. The unassociated energy is thus not varied separately.

The selection criteria on the missing mass are assumed to be fully correlated, i. e., the resulting uncertainties are added linearly. All remaining variations are treated as being independent, i. e., the uncertainties are added in quadrature. The resulting combined uncertainties from all variations of the selection criteria are listed in Table 6.5 for the measured decay modes. In principle, the variations would have to be performed several times to obtain the correlations of the uncertainties between the different decay channels. As each variation requires a large amount of computing power, they are only performed once. Due to the similarity of the selection criteria for the different decay modes, the resulting uncertainties are assumed to be fully correlated between the measured channels, i. e., $\rho_{ij}^{\mathcal{B}} = +1$ for all i, j.

6.5.12   Dependencies on the flavor of the tag lepton

Figure 6.3 shows the measured branching fractions as determined from electron-tagged and muon-tagged reactions as well as the entire event sample. The electron- and muon-tagged event samples are statistically independent and have partially different systematic uncertainties, e. g., the uncertainty due to the electron and muon identification. The systematic uncertainties caused by the charged particle identification are determined in a variation procedure simultaneously for all selected particle types (Section 6.5.5). Hence, the uncertainties plotted in Figure 6.3 only include the uncertainties that are of inherent statistical nature, i. e., those due to the statistical fluctuations of the numbers of selected data and simulated events (Sections 6.4, 6.5.6, 6.5.7). The contributions are added in quadrature. For completeness, the full set of the measured branching fractions for the different tag-lepton and run-period sub-samples is listed in Table D.1.

The consistency of the $N = 2$ branching fractions $\mathcal{B}_i$ measured with the different sub-samples is tested using a χ^2 variable [3]:

$$\chi^2 \equiv \sum_1^N \frac{\left(\overline{\mathcal{B}} - \mathcal{B}_i\right)^2}{\left(\Delta\mathcal{B}_i\right)^2} \,. \tag{6.63}$$

The $\Delta\mathcal{B}_i$ are the uncertainties and $\overline{\mathcal{B}}$ is the mean of the contributing measurements (cf.
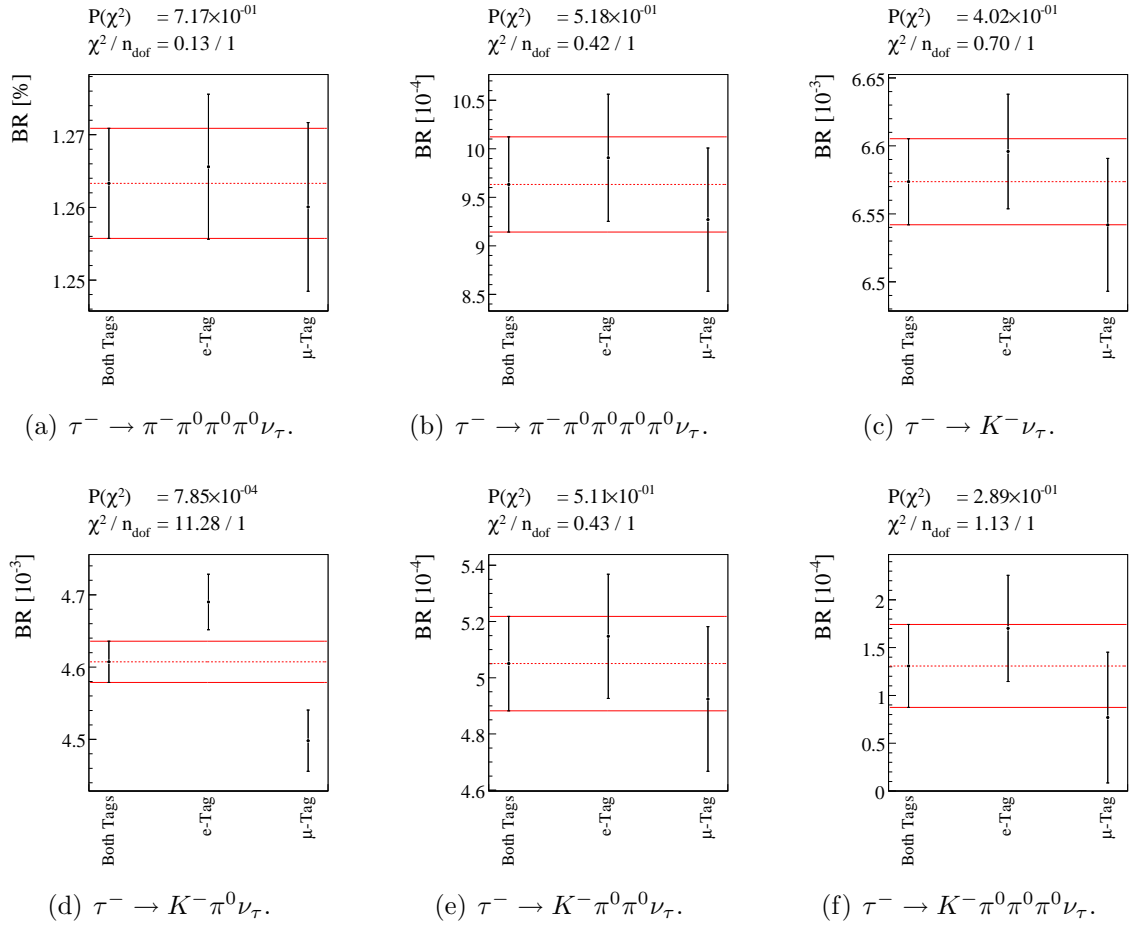
Figure 6.3: Measured branching fractions for electron-tagged and muon-tagged reactions as well as the entire event sample. The plotted uncertainties include all uncertainties that are of inherent statistical nature. All contributions are added in quadrature. The red lines mark the value (dashed) and the uncertainty band (solid) of the total measured branching fractions. The given χ^2 values are calculated according to Equation 6.63. Their expectation value is one if the measurements follow a Gaussian distribution. The values $P(\chi^2)$ are the corresponding probabilities that this is the case.

Equation 7.7). The resulting values are also specified in Figure 6.3. If the measurements follow a Gaussian distribution, the expectation value for χ^2 is $(N-1) = 1$. The corresponding probabilities $P(\chi^2)$ for a χ^2 value that is larger than the calculated one—if the contributing measurements follow a Gaussian distribution—are also given. They exhibit a good consistency for all decay modes but $\tau^- \to K^- \pi^0 \nu_\tau$. However, care needs to be taken since—as described above—the shown uncertainties do not include all uncertainties that are uncorrelated between the electron- and muon-tagged event samples. For the decay channel $\tau^- \to K^- \pi^0 \nu_\tau$, the uncertainty due to the electron and muon identification is comparable to the statistical one (Table 6.5). Thus, the agreement is acceptable also for this decay mode.

6.5.13   Dependencies on the run period

Similar to Figure 6.3, Figure 6.4 displays the $N = 6$ measured branching fractions and their total statistical uncertainties for the different run periods of data taking as well as the entire data set (Table 2.1). The χ^2 values as defined by Equation 6.63 as well as the
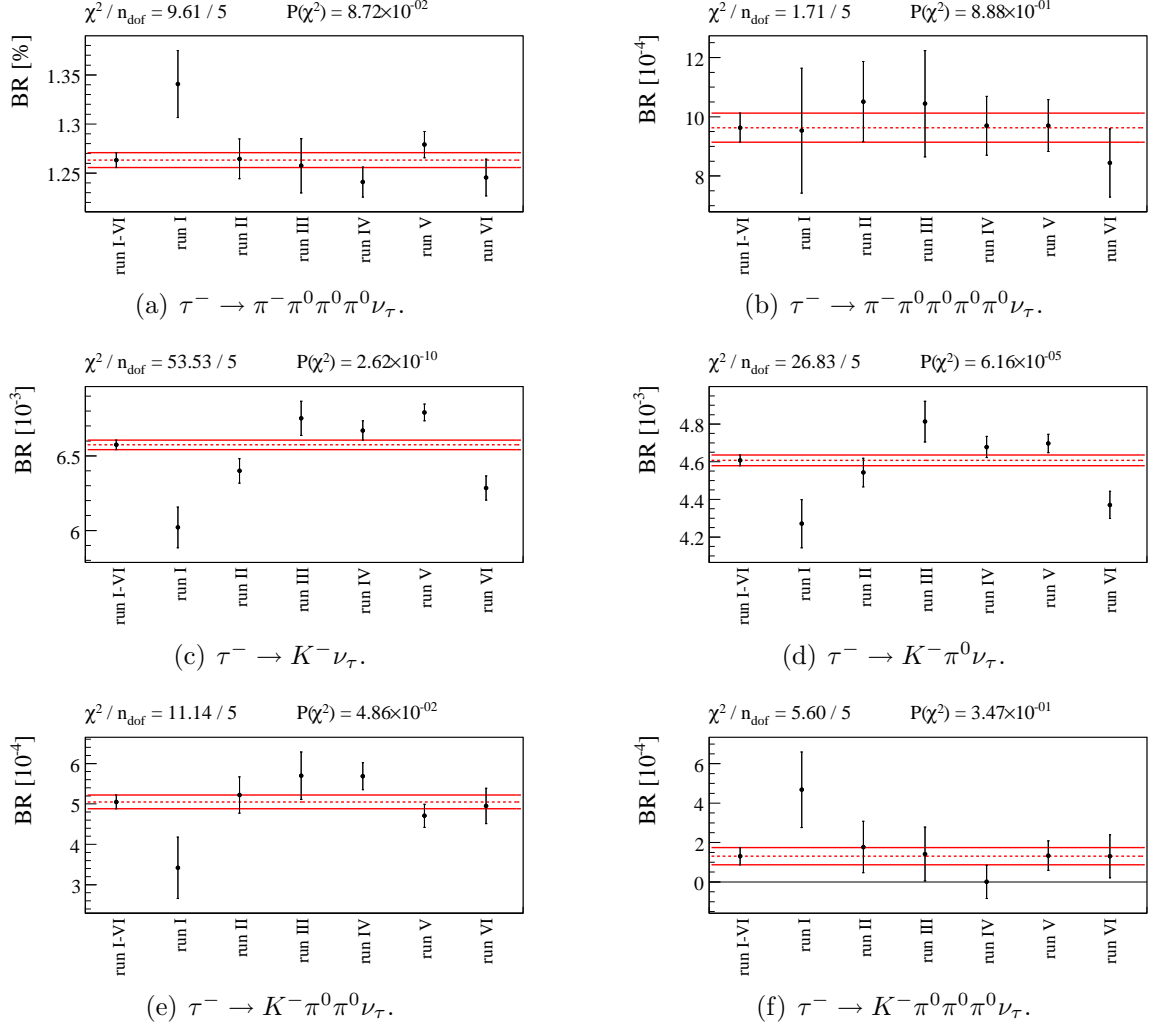
Figure 6.4: Measured branching fractions for the different run periods of data taking (Table 2.1). The plotted uncertainties include all uncertainties that are of inherent statistical nature. The red lines mark the value (dashed) and the uncertainty band (solid) of the total measured branching fractions. The given χ^2 values are calculated according to Equation 6.63. Their expectation value is five if the measurements follow a Gaussian distribution. The values $P(\chi^2)$ are corresponding the probabilities that this is the case.

resulting probabilities are also given. All six measurements of each branching fraction are statistically independent and have partially different systematic uncertainties. The particle identification uncertainties contain a significant fraction originating from the limited size of the control samples (Section 3.5), which is completely independent between all run periods. Additionally, the uncertainty of the luminosity is partially

independent between the run I–III and run IV–VI periods (Section 6.5.2).

All but the two decay modes $\tau^- \to K^- \nu_\tau$ and $\tau^- \to K^- \pi^0 \nu_\tau$ show a good agreement of the measurements for the different run periods. However, in case of the mode $\tau^- \to K^- \nu_\tau$, the uncertainty due to the luminosity is of the order of $1\,\%$ and by a factor of two bigger than the sum of the statistical uncertainties (Table 6.5). It can explain the deviation between the run I–III and run IV–VI measurements. The deviations within these two periods can be explained by the uncorrelated uncertainties of the particle identification. A similar argument holds for the mode $\tau^- \to K^- \pi^0 \nu_\tau$, where the uncertainty due to the particle identification is comparable to the statistical one.

The uncorrelated systematic uncertainties are especially significant for the decay modes $\tau^- \to K^- \nu_\tau$ and $\tau^- \to K^- \pi^0 \nu_\tau$, where the purely statistical uncertainties are small. As the former are not included in Figure 6.4, the deviations are acceptable. This is supported by the fact that the deviations exhibit different patterns for the different decay channels. E. g., run I is not always low, as in the case of the modes $\tau^- \to K^- \nu_\tau$ and $\tau^- \to K^- \pi^0 \nu_\tau$, and a systematic deviation of the run I data can be excluded.

6.6   Results

Table 6.5 summarizes the branching fractions and all contributions to the statistical and systematic uncertainties for the measured decay modes. Each uncertainty is defined as the standard deviation according to Equation 6.37. The listed statistical uncertainties include all uncertainties that are of inherent statistical nature, i. e., those due to the statistical fluctuations of the numbers of selected data and simulated events (Sections 6.4, 6.5.6, 6.5.7). In future, the statistical uncertainties as defined here could be reduced without further data taking by increasing the amount of available Monte Carlo simulated events. The remainder of the uncertainties are summarized into the total systematic uncertainties.

Assuming that statistical and systematic uncertainties are independent, the total statistical and systematic covariance matrices $\mathbf{V}^{\mathcal{B}}_{(\mathrm{stat})}$ and $\mathbf{V}^{\mathcal{B}}_{(\mathrm{syst})}$ are obtained as the sum of the matrices $\mathbf{V}^{\mathcal{B}}_i$ of all n contributions (see Appendix C):

$$\mathbf{V}^{\mathcal{B}}_{(\mathrm{stat})} = \sum_{i_{(\mathrm{stat})}}^{n_{(\mathrm{stat})}} \mathbf{V}_{i_{(\mathrm{stat})}} , \qquad \mathbf{V}^{\mathcal{B}}_{(\mathrm{syst})} = \sum_{i_{(\mathrm{syst})}}^{n_{(\mathrm{syst})}} \mathbf{V}_{i_{(\mathrm{syst})}} . \qquad (6.64)$$

The total statistical and systematic uncertainties $\sigma^{(\mathrm{stat})}_{\mathcal{B}_i}$ and $\sigma^{(\mathrm{syst})}_{\mathcal{B}_i}$ are defined as the corresponding standard deviations according to Equation 6.37. This is equivalent to adding all contributing uncertainties in quadrature. The resulting branching fractions are:

$$
\begin{aligned}
\mathcal{B}(\tau^- \to \pi^- \pi^0 \pi^0 \pi^0 \nu_\tau) &= (\, 1.263 \pm 0.008_{(\mathrm{stat})} \pm 0.078_{(\mathrm{syst})} \,) \times 10^{-2} \ , \\
\mathcal{B}(\tau^- \to \pi^- \pi^0 \pi^0 \pi^0 \pi^0 \nu_\tau) &= (\, 9.6 \ \ \pm 0.5_{(\mathrm{stat})} \ \ \ \pm 1.2_{(\mathrm{syst})} \ \ \ ) \times 10^{-4} \ , \\
\mathcal{B}(\tau^- \to K^- \nu_\tau) &= (\, 6.57 \ \ \pm 0.03_{(\mathrm{stat})} \ \ \pm 0.11_{(\mathrm{syst})} \ \ ) \times 10^{-3} \ , \\
\mathcal{B}(\tau^- \to K^- \pi^0 \nu_\tau) &= (\, 4.61 \ \ \pm 0.03_{(\mathrm{stat})} \ \ \pm 0.11_{(\mathrm{syst})} \ \ ) \times 10^{-3} \ , \\
\mathcal{B}(\tau^- \to K^- \pi^0 \pi^0 \nu_\tau) &= (\, 5.05 \ \ \pm 0.17_{(\mathrm{stat})} \ \ \pm 0.44_{(\mathrm{syst})} \ \ ) \times 10^{-4} \ , \\
\mathcal{B}(\tau^- \to K^- \pi^0 \pi^0 \pi^0 \nu_\tau) &= (\, 1.31 \ \ \pm 0.43_{(\mathrm{stat})} \ \ \pm 0.40_{(\mathrm{syst})} \ \ ) \times 10^{-4} \ .
\end{aligned}
\qquad (6.65)
$$

According to Equation 6.38, the corresponding correlation matrices are

$$
\rho^{\mathcal{B}}_{\text{(stat)}} \;=\;
\begin{array}{cccccc}
\pi 3\pi^0 & \pi 4\pi^0 & K & K\pi^0 & K2\pi^0 & K3\pi^0
\end{array}
\left(
\begin{array}{cccccc}
1.000 & -0.462 & 0.003 & -0.004 & 0.038 & -0.104 \\
-0.462 & 1.000 & 0.001 & -0.000 & 0.000 & 0.001 \\
0.003 & 0.001 & 1.000 & -0.063 & -0.006 & 0.006 \\
-0.004 & -0.000 & -0.063 & 1.000 & -0.100 & 0.017 \\
0.038 & 0.000 & -0.006 & -0.100 & 1.000 & -0.459 \\
-0.104 & 0.001 & 0.006 & 0.017 & -0.459 & 1.000
\end{array}
\right)
\begin{array}{l}
\pi 3\pi^0 \\
\pi 4\pi^0 \\
K \\
K\pi^0 \\
K2\pi^0 \\
K3\pi^0
\end{array}
\tag{6.66}
$$

for the total statistical uncertainties and

$$
\rho^{\mathcal{B}}_{\text{(syst)}} \;=\;
\begin{array}{cccccc}
\pi 3\pi^0 & \pi 4\pi^0 & K & K\pi^0 & K2\pi^0 & K3\pi^0
\end{array}
\left(
\begin{array}{cccccc}
1.000 & 0.724 & -0.531 & 0.826 & 0.891 & 0.381 \\
0.724 & 1.000 & -0.429 & 0.615 & 0.692 & 0.316 \\
-0.531 & -0.429 & 1.000 & -0.051 & -0.364 & -0.137 \\
0.826 & 0.615 & -0.051 & 1.000 & 0.860 & 0.402 \\
0.891 & 0.692 & -0.364 & 0.860 & 1.000 & 0.381 \\
0.381 & 0.316 & -0.137 & 0.402 & 0.381 & 1.000
\end{array}
\right)
\begin{array}{l}
\pi 3\pi^0 \\
\pi 4\pi^0 \\
K \\
K\pi^0 \\
K2\pi^0 \\
K3\pi^0
\end{array}
\tag{6.67}
$$

for the total systematic uncertainties. The uncertainties of the mode $\tau^- \to K^- \nu_\tau$ are anti-correlated with all other decay channels. This is due to the fact that the dominant uncertainty in decay modes with reconstructed π^0 mesons is due to the π^0 efficiency correction (Table 6.5). This uncertainty only enters the mode $\tau^- \to K^- \nu_\tau$ via the background modes that contain a π^0 meson. Since this background is subtracted, the uncertainty of the branching fraction that is caused by the uncertainty of the efficiency correction is anti-correlated with all other modes. The correlation matrices of the different statistical and systematic contributions are listed in Appendix C.

Adding the total statistical and systematic covariance matrices yields the final result of the measured branching fractions:

$$
\begin{aligned}
\mathcal{B}(\tau^- \to \pi^- \pi^0 \pi^0 \pi^0 \nu_\tau) &= (1.263 \pm 0.078) \times 10^{-2} \quad (\;6.2\,\%)\,, \\
\mathcal{B}(\tau^- \to \pi^- \pi^0 \pi^0 \pi^0 \pi^0 \nu_\tau) &= (9.6 \quad \pm 1.3 \quad) \times 10^{-4} \quad (13 \quad \%)\,, \\
\mathcal{B}(\tau^- \to K^- \nu_\tau) &= (6.57 \quad \pm 0.11 \quad) \times 10^{-3} \quad (\;1.7\,\%)\,, \\
\mathcal{B}(\tau^- \to K^- \pi^0 \nu_\tau) &= (4.61 \quad \pm 0.12 \quad) \times 10^{-3} \quad (\;2.5\,\%)\,, \\
\mathcal{B}(\tau^- \to K^- \pi^0 \pi^0 \nu_\tau) &= (5.05 \quad \pm 0.47 \quad) \times 10^{-4} \quad (\;9.4\,\%)\,, \\
\mathcal{B}(\tau^- \to K^- \pi^0 \pi^0 \pi^0 \nu_\tau) &= (1.31 \quad \pm 0.59 \quad) \times 10^{-4} \quad (45 \quad \%)\,,
\end{aligned}
\tag{6.68}
$$

where the numbers in brackets are the relative uncertainties. The corresponding total

correlation matrix is

$$
\rho^{\mathcal{B}} = \begin{array}{cccccc}
\pi 3\pi^0 & \pi 4\pi^0 & K & K\pi^0 & K2\pi^0 & K3\pi^0 \\
\end{array}
$$

$$
\rho^{\mathcal{B}} = \begin{pmatrix}
1.000 & 0.646 & -0.507 & 0.796 & 0.831 & 0.250 \\
0.646 & 1.000 & -0.379 & 0.548 & 0.595 & 0.198 \\
-0.507 & -0.379 & 1.000 & -0.051 & -0.327 & -0.088 \\
0.796 & 0.548 & -0.051 & 1.000 & 0.770 & 0.267 \\
0.831 & 0.595 & -0.327 & 0.770 & 1.000 & 0.122 \\
0.250 & 0.198 & -0.088 & 0.267 & 0.122 & 1.000
\end{pmatrix}
\begin{array}{l}
\pi 3\pi^0 \\
\pi 4\pi^0 \\
K \\
K\pi^0 \\
K2\pi^0 \\
K3\pi^0
\end{array}
\qquad (6.69)
$$

Since the total uncertainties are dominated by the systematic ones—except for the decay mode $\tau^- \to K^- \pi^0 \pi^0 \pi^0 \nu_\tau$—their correlation matrix is similar to the one from Equation 6.67. All measured branching fractions are the most precise measurements currently available for these decay modes [3]. A more detailed comparison with other measurements is provided in Chapter 8.

Table 6.5: Summary of the measured branching fractions and their uncertainties. All uncertainties are relative uncertainties in % with respect to the branching fractions. The statistical and systematic uncertainties are obtained by adding all statistical or systematic contributions in quadrature. The total uncertainty is obtained by adding the statistical and systematic uncertainties in quadrature.

	Section	$\tau^- \to \pi^- 3\pi^0 \nu_\tau$	$\tau^- \to \pi^- 4\pi^0 \nu_\tau$	$\tau^- \to K^- \nu_\tau$	$\tau^- \to K^- \pi^0 \nu_\tau$	$\tau^- \to K^- 2\pi^0 \nu_\tau$	$\tau^- \to K^- 3\pi^0 \nu_\tau$
Branching fraction	6.3	1.263×10^{-2}	9.63×10^{-4}	6.574×10^{-3}	4.607×10^{-3}	5.05×10^{-4}	1.31×10^{-4}
Total uncertainty [%]	6.6	6.2	13.0	1.72	2.51	9.4	45
Statistical uncertainty [%]	6.5.12	0.6	5.1	0.48	0.62	3.3	33
Data statistical uncertainty	6.4	0.5	4.5	0.34	0.44	2.6	26
Signal efficiencies	6.5.6	0.3	2.0	0.29	0.33	0.9	15
Background misidentification	6.5.7	0.2	1.5	0.19	0.29	1.9	14
Systematic uncertainty [%]	6.6	6.2	12.0	1.65	2.44	8.7	31
$\tau^+ \tau^-$ cross section	6.5.1	0.8	1.3	0.51	0.04	0.7	1.5
Luminosity	6.5.2	1.6	2.6	1.04	0.08	1.4	2.9
Background normalization	6.5.3	1.7	2.8	0.64	0.69	2.8	20
Tracking efficiency	6.5.4	1.0	1.7	0.68	0.05	0.9	1.9
Particle identification efficiency	6.5.5	0.2	0.5	0.52	0.89	2.4	12
π^0 efficiency correction	6.5.8	5.4	7.8	0.42	2.14	7.0	11
Split-offs	6.5.9	1.1	2.3	0.19	0.24	3.2	0.2
Additional π^0 mesons	6.5.10	0.4	7.5	0.00	0.00	0.6	13
Selection criteria	6.5.11	0.2	1.3	0.15	0.07	0.6	9.7

Chapter 7

Extraction of $|V_{us}|$

Within this work, $|V_{us}|$ is extracted from the total decay rate of the τ lepton into *strange* hadronic final states $R_{\tau,\mathrm{S}}$ following the method suggested in References [4, 5]. The context is described in Section 1.4.2 and results in the following formula:

$$|V_{us}| = \sqrt{\frac{R_{\tau,\mathrm{S}}}{\frac{R_{\tau,\mathrm{NS}}}{|V_{ud}|^2} - \delta R_\tau}} . \tag{7.1}$$

The symbol $R_{\tau,\mathrm{NS}}$ denotes the total decay rate of the τ lepton into *non-strange* hadronic final states and $|V_{ud}|$ is the corresponding CKM matrix element. The latter can be obtained from independent measurements. The quantity δR_τ is the (small) flavor-$\mathrm{SU}_F(3)$ breaking difference, which is dominated by the strange-quark mass and can be calculated theoretically (Section 1.4.2).

Experimentally, $R_{\tau,\mathrm{S}}$ is obtained from the total branching fraction of the τ lepton into hadronic final states with net strangeness $\mathcal{B}_\mathrm{S}$ and the lepton-universality improved electronic τ branching fraction $\mathcal{B}_e^{(\mathrm{uni})}$ (Section 1.2.3, [4, 5, 10]):

$$R_{\tau,\mathrm{S}} = \frac{\mathcal{B}_\mathrm{S}}{\mathcal{B}_e^{(\mathrm{uni})}} . \tag{7.2}$$

The most precise determination of $R_{\tau,\mathrm{NS}}$ is performed using $R_{\tau,\mathrm{S}}$ and the lepton-universality improved total hadronic branching fraction $\mathcal{B}_\mathrm{had}^{(\mathrm{uni})}$ (Section 1.2.1, [10]) with

$$\mathcal{B}_\mathrm{had}^{(\mathrm{uni})} = 1 - \mathcal{B}_e - \mathcal{B}_\mu = 1 - (1 + r_{\mu e}) \, \mathcal{B}_e^{(\mathrm{uni})} . \tag{7.3}$$

The symbols $\mathcal{B}_{e/\mu}$ are the measured leptonic τ branching fractions. Their ratio $r_{\mu e}$ can be calculated theoretically with high precision [10]. Thus, the branching fraction of the τ lepton into final states without net strangeness $\mathcal{B}_\mathrm{NS}$ is

$$\mathcal{B}_\mathrm{NS} = \mathcal{B}_\mathrm{had}^{(\mathrm{uni})} - \mathcal{B}_\mathrm{S} = 1 - (1 + r_{\mu e}) \, \mathcal{B}_e^{(\mathrm{uni})} - \mathcal{B}_\mathrm{S} . \tag{7.4}$$

The corresponding decay rate of the τ lepton $R_{\tau,\mathrm{NS}}$ is obtained from

$$R_{\tau,\mathrm{NS}} = \frac{\mathcal{B}_\mathrm{NS}}{\mathcal{B}_e^{(\mathrm{uni})}} = \frac{1}{\mathcal{B}_e^{(\mathrm{uni})}} - (1 + r_{\mu e}) - \frac{\mathcal{B}_\mathrm{S}}{\mathcal{B}_e^{(\mathrm{uni})}} . \tag{7.5}$$

In consequence, $|V_{us}|$ can be calculated from the experimental measurements according to

$$|V_{us}| = \sqrt{\frac{\mathcal{B}_{\mathrm{S}}}{\frac{1-(1+r_{\mu e})\mathcal{B}_e^{(\mathrm{uni})}-\mathcal{B}_{\mathrm{S}}}{|V_{ud}|^2} - \mathcal{B}_e^{(\mathrm{uni})}\delta R_\tau}}\,. \tag{7.6}$$

The biggest contribution to the final uncertainty of $|V_{us}|$ is due to the experimental uncertainty of the branching fraction of the τ lepton into final states with net strangeness $\mathcal{B}_{\mathrm{S}}$ (Section 1.4.2, [4, 5, 10]). This analysis has improved the branching fractions of the four decay modes $\tau^- \to K^- n\pi^0 \nu_\tau$ ($n = 0, 1, 2, 3$) that contribute to $\mathcal{B}_{\mathrm{S}}$ by factors of up to five with respect to the current world averages (Equation 6.68, Table 1.4, [3, 10]). In the following section, these measurements are combined with the current world averages to provide the most precise measurement of $\mathcal{B}_{\mathrm{S}}$. The resulting value is used in Section 7.2 to calculate $|V_{us}|$ according to Equation 7.6.

7.1   Branching fractions of strange τ decays

For all decay modes of the τ lepton into final states with net strangeness other than the four channels $\tau^- \to K^- n\pi^0 \nu_\tau$ ($n = 0, 1, 2, 3$), the current world averages are used as summarized in Table 7.1. The measurements described in this document (Equation 6.68) are combined with the current PDG world averages of the decay modes $\tau^- \to K^- n\pi^0 \nu_\tau$ into updated world averages using the method advocated by the PDG [3]. In this method, correlations between different decay modes and experiments are neglected, as they are not known for measurements other than the one performed within this work. However, *scale factors* are used to enlarge the experimental uncertainties if two or more measurements are inconsistent with each other.

In a first step, the contributing N measurements $\mathcal{B}_i$ with uncertainties $\Delta\mathcal{B}_i$ are averaged using a standard weighted least-squares procedure [3]. Assuming uncorrelated measurements, the average $\overline{\mathcal{B}}$ and its uncertainty $\Delta\overline{\mathcal{B}}$ are obtained as

$$\overline{\mathcal{B}} \pm \Delta\overline{\mathcal{B}} \equiv \frac{\sum_{i=1}^{N} \frac{1}{(\Delta\mathcal{B}_i)^2}\mathcal{B}_i}{\sum_{i=1}^{N} \frac{1}{(\Delta\mathcal{B}_i)^2}} \pm \left(\sum_{i=1}^{N} \frac{1}{(\Delta\mathcal{B}_i)^2}\right)^{-\frac{1}{2}}. \tag{7.7}$$

In a second step, the consistency of the calculated average and the single measurements is tested using a χ^2 variable:

$$\chi^2 \equiv \sum_{1}^{N} \frac{\left(\overline{\mathcal{B}} - \mathcal{B}_i\right)^2}{(\Delta\mathcal{B}_i)^2}\,. \tag{7.8}$$

It is compared with $(N-1)$—the expectation value of χ^2 if the measurements follow a Gaussian distribution. If $\chi^2 \leq (N-1)$, the result is accepted as it is. However, if $\chi^2 \gtrsim (N-1)$, the data is still averaged but the resulting uncertainty is increased by a *scale factor* S with

$$S \equiv \sqrt{\frac{\chi^2}{(N-1)}}\,. \tag{7.9}$$

Table 7.1: Updated averages for the branching fractions of τ decays into final states with net strangeness. The table lists the current world averages $\mathcal{B}_{\text{PDG}}$ from Table 1.4 as taken from References [7, 10]. These include recent measurements of the BABAR and Belle collaborations [24, 25]. The table also lists the measurements $\mathcal{B}_{\text{this}}$ of the decay modes $\tau^- \to K^- n\pi^0 \nu_\tau$ ($n = 0, 1, 2, 3$) performed in this analysis. The updated averages $\mathcal{B}_{\text{update}}$ and the corresponding scale factors S are obtained using the method of the PDG as described in the text. The value for the $\tau^- \to (\overline{K}\pi\pi)^- \nu_\tau$ branching fraction from Table 1.4 has been splitted into the measurement of the decay $\tau^- \to K^- \pi^0 \pi^0 \pi^0 \nu_\tau$ and the remaining contributions from the mode $\tau^- \to K^- \pi^+ \pi^- \pi^0 \nu_\tau$ as well as estimates for unseen final states using isospin relations. For the updated value, only the contributions from decays of the type $\tau^- \to K^- \pi^0 \pi^0 \pi^0 \nu_\tau$ are averaged.

Mode	$\mathcal{B}_{\text{PDG}}\,[10^{-3}]$	$\mathcal{B}_{\text{this}}\,[10^{-3}]$	$\mathcal{B}_{\text{update}}\,[10^{-3}]$	S
$\tau^- \to K^- \nu_\tau$	6.85 ± 0.23	6.57 ± 0.11	6.63 ± 0.11	1.1
$\tau^- \to K^- \pi^0 \nu_\tau$	4.54 ± 0.30	4.61 ± 0.12	4.60 ± 0.11	1
$\tau^- \to \pi^- \overline{K}^0 \nu_\tau$	8.31 ± 0.28			
$\tau^- \to K^- \pi^0 \pi^0 \nu_\tau$	0.58 ± 0.24	0.505 ± 0.047	0.508 ± 0.046	1
$\tau^- \to \pi^- \overline{K}^0 \pi^0 \nu_\tau$	3.6 ± 0.4			
$\tau^- \to K^- \pi^+ \pi^- \nu_\tau$	2.80 ± 0.16			
$\tau^- \to K^- \eta \nu_\tau$	0.27 ± 0.06			
$\tau^- \to K^- \pi^0 \pi^0 \pi^0 \nu_\tau$	0.37 ± 0.24	0.131 ± 0.059	0.144 ± 0.056	1
$\tau^- \to (\overline{K}\pi\pi)^- \nu_\tau{}^{\text{a}}$	0.37 ± 0.18			
$\tau^- \to K_1(1270)^- \nu_\tau{}^{\text{b}}$	0.67 ± 0.21			
$\tau^- \to (\overline{K}\pi\pi\pi)^- \nu_\tau{}^{\text{c}}$	0.40 ± 0.12			
$\tau^- \to K^- K^+ K^- \nu_\tau$	0.016 ± 0.002			
$\tau^- \to X_S^- \nu_\tau = \sum$	28.78 ± 0.79		28.31 ± 0.62	

[a] This value does not include the mode $\tau^- \to K^- \pi^0 \pi^0 \pi^0 \nu_\tau$.
[b] With a following decay into the final state $K^- \omega \nu_\tau$.
[c] This branching fraction also includes a small contribution from the mode $\tau^- \to K^{*-} \eta \nu_\tau$.

The reasoning is that the large value of χ^2 is likely to be caused by an underestimate of uncertainties in at least one of the experiments. Not knowing which of the uncertainties are underestimated, they are all scaled up by the common factor S such that their χ^2 becomes $(N-1)$ [3]. It is noted that the scaling only affects the uncertainties and leaves the central values of all averages unchanged.

Table 7.1 summarizes the contributing measurements to the updated world averages of the branching fractions $\mathcal{B}(\tau^- \to K^- n\pi^0 \nu_\tau)$ with $n = 0, 1, 2, 3$—the current PDG world averages and the measurements presented in this document. It also lists the resulting updated world averages of the branching fractions as well as their uncertainties and the calculated scale factors. The value for the $\tau^- \to (\overline{K}\pi\pi)^- \nu_\tau$ branching fraction

has been splitted into the measurement of the decay $\tau^- \to K^-\pi^0\pi^0\pi^0\nu_\tau$ and the remaining contributions from the mode $\tau^- \to K^-\pi^+\pi^-\pi^0\nu_\tau$ as well as estimates for unseen final states using isospin relations. For the updated world average, only the contribution from decays of the type $\tau^- \to K^-\pi^0\pi^0\pi^0\nu_\tau$ is averaged.

The resulting updated total branching fraction of the τ lepton into final states with net strangeness $\mathcal{B}_S$ and the corresponding decay rate $R_{\tau,S}$ (Equation 7.2) are listed in Table 7.2. The uncertainty of the total branching fraction is obtained by adding the

Table 7.2: Comparison of the updated total strange and non-strange branching fractions and decay rates of the τ lepton with previous measurements. The table lists the total strange branching fraction $\mathcal{B}_S$ and decay rate $R_{\tau,S}$ (Equation 7.2). They are determined from the *updated* world averages obtained in this analysis as well as the *current PDG* world averages (Table 7.1). The table also contains the corresponding total non-strange branching fraction $\mathcal{B}_{NS}$ and decay rate $R_{\tau,NS}$ according to Equations 7.4 and 7.5. The universality-improved values *(uni)* use the predicted branching fraction of the mode $\tau^- \to K^-\nu_\tau$ from Equation 7.11 instead of the measurements.

	$\mathcal{B}_S \, [10^{-3}]$	$\mathcal{B}_{NS} \, [10^{-2}]$	$R_{\tau,S}$	$R_{\tau,NS}$
Updated	28.31 ± 0.62	62.02 ± 0.09	0.1589 ± 0.0035	3.481 ± 0.010
PDG	28.78 ± 0.79	61.97 ± 0.10	0.1615 ± 0.0044	3.478 ± 0.011
Updated (uni)	28.84 ± 0.61	61.97 ± 0.09	0.1618 ± 0.0035	3.478 ± 0.010
PDG (uni)	29.08 ± 0.75	61.95 ± 0.10	0.1632 ± 0.0042	3.477 ± 0.011

single uncertainties in quadrature and the universality-improved electronic τ branching fraction

$$\mathcal{B}_e^{(\text{uni})} = (17.818 \pm 0.032)\,\% \tag{7.10}$$

is used to calculate the decay rate (Equation 1.21, [10]). Table 7.2 also lists the updated values for hadronic τ decays into final states without net strangeness according to Equations 7.4 and 7.5.

The updated results need to be compared to the values based on the current PDG world averages, which are also specified in Table 7.2. By including the measurements presented in this document, an improvement of 20 % has been achieved for the strange τ decay rate $R_{\tau,S}$.

If $\tau - \mu$ universality is assumed, the branching fraction $\mathcal{B}_K$ for the decay mode $\tau^- \to K^-\nu_\tau$ can be calculated from the precisely known branching fraction $\mathcal{B}(K^- \to \mu^-\overline{\nu}_\mu)$ (Section 1.2.2, [10]):

$$\mathcal{B}_K^{(\text{uni})} = (7.15 \pm 0.03) \times 10^{-3}\,. \tag{7.11}$$

Using this value instead of the measured average from Table 7.1 yields the universality-improved results as listed in Table 7.2. It is however noted that the measured and the universality-improved values of $\mathcal{B}_K$ differ by 4.6 standard deviations—a fact that could indicate new physics [7]. A more detailed discussion is provided in Chapter 8.

7.2 Calculation of $|V_{us}|$

Using the measured values of $\mathcal{B}_S$ and $\mathcal{B}_e^{(\text{uni})}$ from Table 7.2 as well as the theoretically calculated values (Sections 1.2.1, 1.4.2 [6, 10])

$$
\begin{aligned}
r_{\mu e}^{(\text{theo})} &= 0.972565 \pm 0.000009\,, \\
\delta R_\tau^{(\text{theo})} &= 0.216 \pm 0.016
\end{aligned}
\tag{7.12}
$$

and the world average [3]

$$
|V_{ud}| = (0.97418 \pm 0.00027)\,,
\tag{7.13}
$$

$|V_{us}|$ is calculated according to Equation 7.6:

$$
\begin{aligned}
|V_{us}| &= 0.2146 \pm 0.0005_{(\text{theo})} \pm 0.0025_{(\text{exp})} \\
&= 0.2146 \pm 0.0025 \quad (1.18\,\%)\,.
\end{aligned}
\tag{7.14}
$$

The uncertainties are of theoretical and experimental origin respectively. They are obtained using full Gaussian error propagation for the uncertainties of all ingredients of Equation 7.6. The total uncertainty is calculated by adding the two contributions in quadrature. The number in brackets is the relative uncertainty.

If the universality-improved branching fraction $\mathcal{B}_K^{(\text{uni})}$ is used, the values from Table 7.2 result in

$$
\begin{aligned}
|V_{us}|^{(\text{uni})} &= 0.2166 \pm 0.0005_{(\text{theo})} \pm 0.0024_{(\text{exp})} \\
&= 0.2166 \pm 0.0025 \quad (1.14\,\%)\,.
\end{aligned}
\tag{7.15}
$$

These are the most precise determinations of $|V_{us}|$ from hadronic τ decays to date. However, the difference of 4.6 standard deviations between the measured and the universality-improved branching fraction for the mode $\tau^- \to K^-\nu_\tau$ is directly propagated into the two values of $|V_{us}|$. It is only hidden by the total uncertainty of the $\mathcal{B}_S$. Considering that all but the measurements of the channel $\tau^- \to K^-\nu_\tau$ are identical in both cases, the two values of $|V_{us}|$ are as incompatible as the two branching fractions.

The determination using the current PDG world averages of the τ branching fractions without considering the results of this analysis yields

$$
\begin{aligned}
|V_{us}|_{\text{PDG}} &= 0.2164 \pm 0.0005_{(\text{theo})} \pm 0.0031_{(\text{exp})} \\
&= 0.2164 \pm 0.0031 \quad (1.45\,\%)\,, \\
|V_{us}|_{\text{PDG}}^{(\text{uni})} &= 0.2176 \pm 0.0005_{(\text{theo})} \pm 0.0030_{(\text{exp})} \\
&= 0.2176 \pm 0.0030 \quad (1.38\,\%)\,.
\end{aligned}
\tag{7.16}
$$

An improvement of $19\,\%$ has been achieved by the inclusion of the measurements presented in this thesis. The results in Equations 7.14 and 7.16 illustrate a general tendency. The determinations of $|V_{us}|$ that include new branching fraction measurements from the B factories result in considerably lower values than those which only consider the older LEP and CLEO measurements [7]. This is due to the fact that many

measurements of τ branching fractions at the B factories result in lower values than the corresponding averages of the LEP and CLEO results [7].

The new values from Equations 7.14 and 7.15 need to be compared to the current PDG world average of $|V_{us}|$ as obtained from semileptonic kaon decays (Section 1.4.1):

$$|V_{us}|_{K_{\ell 3}} = 0.2255 \pm 0.0019 \quad (0.84\,\%) \tag{7.17}$$

This measurement differs by 3.4 standard deviations from the fully measured value in Equation 7.14. The difference with respect to the universality-improved measurement (Equation 7.15) amounts to 2.8 standard deviations. A more detailed comparison of the most important measurements of $|V_{us}|$ that are currently available is provided in the following conclusion.

Chapter 8

Summary and conclusion

Within this thesis, the branching fractions of the decay modes $\tau^- \to K^- n\pi^0 \nu_\tau$ with $n = 0, 1, 2, 3$ and $\tau^- \to \pi^- n\pi^0 \nu_\tau$ with $n = 3, 4$ have been measured. The measurements are based on a data sample of approximately 427×10^6 $\tau\tau$ pairs that have been recorded with the $B\!A\!B\!A\!R$ detector in the years 1999–2007. The data sample corresponds to an integrated luminosity of $464.4\,\text{fb}^{-1}$.

All measured decay modes are mutual backgrounds. Thus, their branching fractions have been determined simultaneously, taking into account migrations in the form of a migration matrix. All correlations of the uncertainties between the different decay modes have been fully determined. The resulting correlation matrices are listed in Section 6.6 and Appendix C. The final results for the measured branching fractions are

$$
\begin{aligned}
\mathcal{B}(\tau^- \to K^- \nu_\tau) &= (\,6.57 \;\pm 0.03_{\text{(stat)}} \;\pm 0.11_{\text{(syst)}} \,)\times 10^{-3} \;,\\
\mathcal{B}(\tau^- \to K^- \pi^0 \nu_\tau) &= (\,4.61 \;\pm 0.03_{\text{(stat)}} \;\pm 0.11_{\text{(syst)}} \,)\times 10^{-3} \;,\\
\mathcal{B}(\tau^- \to K^- \pi^0 \pi^0 \nu_\tau) &= (\,5.05 \;\pm 0.17_{\text{(stat)}} \;\pm 0.44_{\text{(syst)}} \,)\times 10^{-4} \;,\\
\mathcal{B}(\tau^- \to K^- \pi^0 \pi^0 \pi^0 \nu_\tau) &= (\,1.31 \;\pm 0.43_{\text{(stat)}} \;\pm 0.40_{\text{(syst)}} \,)\times 10^{-4} \;,\\
\mathcal{B}(\tau^- \to \pi^- \pi^0 \pi^0 \pi^0 \nu_\tau) &= (\,1.263\pm 0.008_{\text{(stat)}} \pm 0.078_{\text{(syst)}} \,)\times 10^{-2} \;,\\
\mathcal{B}(\tau^- \to \pi^- \pi^0 \pi^0 \pi^0 \pi^0 \nu_\tau) &= (\,9.6 \quad\pm 0.5_{\text{(stat)}} \quad\pm 1.2_{\text{(syst)}} \,)\times 10^{-4} \;.
\end{aligned}
$$

For all decay modes whose final states contain multiple π^0 mesons, contributions from the intermediate resonances $K_S^0 \to \pi^0 \pi^0$ and $\eta \to \pi^0 \pi^0 \pi^0$ have been excluded or subtracted before the determination of the branching fractions.

The largest contribution to the uncertainty of the mode $\tau^- \to K^- \nu_\tau$ originates from the uncertainty of the luminosity measurement. For the channel $\tau^- \to K^- \pi^0 \pi^0 \pi^0 \nu_\tau$, the largest contribution is caused by the statistical fluctuations of the data and Monte Carlo simulated event samples. The uncertainties of all other modes are dominated by the unknown π^0 reconstruction efficiency (Table 6.5).

Within this analysis, the π^0 efficiency correction for simulated events has been determined by comparing the agreement of data and Monte Carlo simulation for the precisely measured decay mode $\tau^- \to \pi^- \pi^0 \nu_\tau$. This method in a way measures the decay mode $\tau^- \to K^- \pi^0 \nu_\tau$ relative to the channel $\tau^- \to \pi^- \pi^0 \nu_\tau$ and, to first order, many uncertainties cancel when evaluating the branching fraction. For the same reason, the uncertainties related to the π^0 reconstruction cancel in first order for the first π^0 in

all other modes. The correction derived from the channel $\tau^- \to \pi^- \pi^0 \nu_\tau$ has been tested using the description of the data by the Monte Carlo simulation in the precisely measured decay mode $\tau^- \to \pi^- \pi^0 \pi^0 \nu_\tau$. In this way, the uncertainty due to the reconstruction of π^0 mesons has been reduced by a factor of two in the framework of this analysis compared to previous measurements by the BABAR collaboration [72]. The precision of the measured branching fractions—which is still dominated by the uncertainty of the π^0 efficiency correction—illustrates the importance of this achievement.

Figure 8.1 shows a comparison of the results with earlier measurements and the current PDG world averages—if available [3]. All presented measurements are compatible
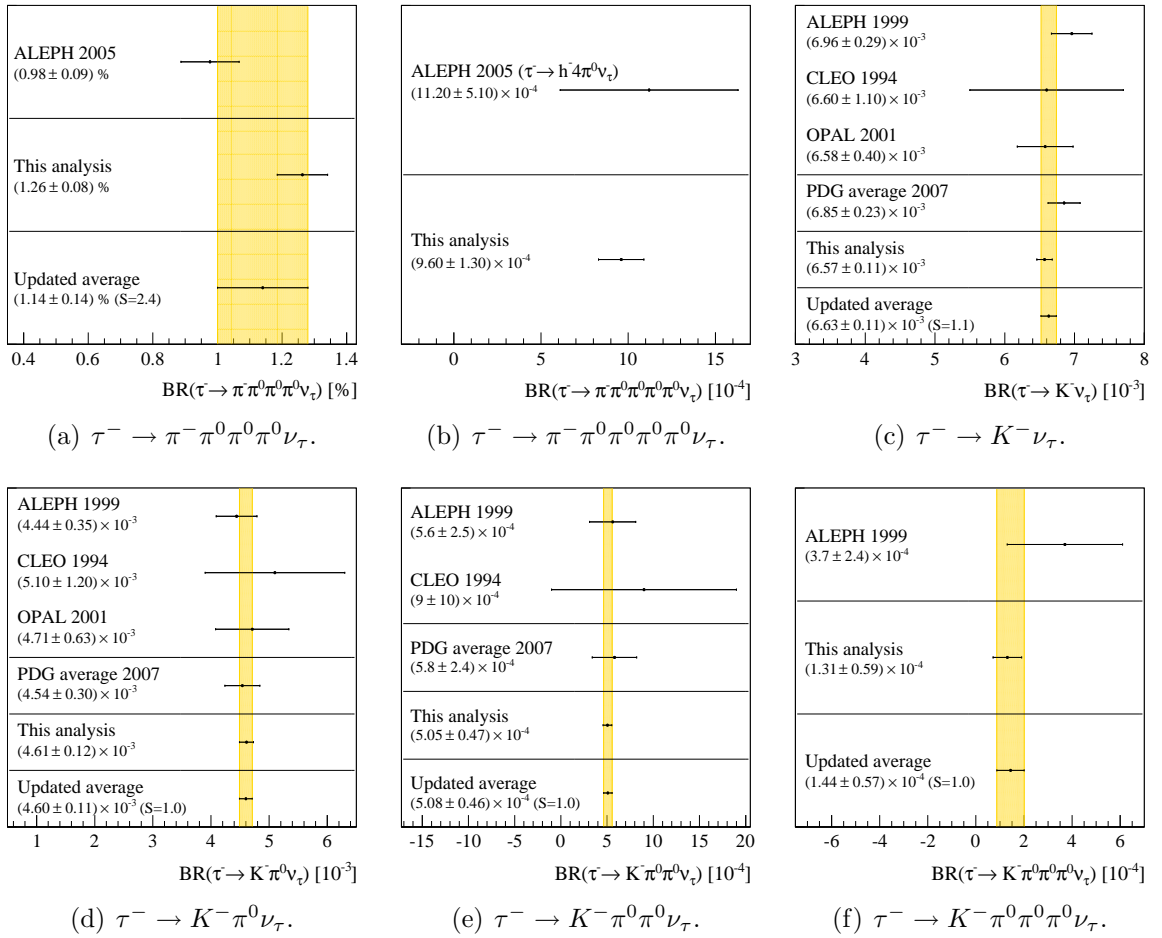
Figure 8.1: Comparison of the branching fractions measured within this work with earlier measurements and the current PDG world averages. The measurements of the ALEPH, CLEO and OPAL collaborations as well as the PDG world averages have been taken from Reference [3]. The updated averages, which include the results of this thesis, are indicated by the yellow bands. The corresponding scale factors S are also listed. They are used to enlarge the uncertainties according to the method of the PDG collaboration if the averaged measurements are not compatible within the given uncertainties [3]. In all analyses of final states containing multiple π^0 mesons, the intermediate resonances $K_S^0 \to \pi^0 \pi^0$ and $\eta \to \pi^0 \pi^0 \pi^0$ have been excluded.

with the results of other experiments and the PDG averages. The measurement of the mode $\tau^- \to \pi^- \pi^0 \pi^0 \pi^0 \pi^0 \nu_\tau$ is the first determination of this branching fraction. So far, only the combined mode $\tau^- \to h^- \pi^0 \pi^0 \pi^0 \pi^0 \nu_\tau$ with $h = \pi, K$ has been measured. The results of this analysis are the most precise measurements currently available and more precise than the existing PDG world averages by factors of up to five. On the basis of the presented measurements and the existing PDG averages, updated world averages have been calculated using the method of the PDG collaboration (Section 7.1, [3]). They are indicated by the yellow bands in Figure 8.1.

Due to a slight difference between the ALEPH measurement of the mode $\tau^- \to \pi^- \pi^0 \pi^0 \pi^0 \nu_\tau$ and the result of this analysis, the uncertainty of the combined value has been enlarged by a scale factor $S = 2.4$ according to the prescription of the PDG collaboration (Section 7.1, [3]). In case of the mode $\tau^- \to K^- \nu_\tau$ (Figure 8.1(c)), the scale factor is $S = 1.1$, while it is $S = 1.0$ for all remaining modes. This illustrates the good agreement of the presented with all previous measurements.

The measurement of the decay mode $\tau^- \to K^- \nu_\tau$ presented in this thesis has increased the deviation of the measured branching fraction from the prediction using the branching fraction $\mathcal{B}(K^- \to \mu^- \overline{\nu}_\mu)$ and $\tau - \mu$ lepton universality (Section 1.2.2). Using the updated world average, the difference amounts to 4.6 standard deviations, compared to 1.3 standard deviations for the current PDG world average. It is however noted that both the measurement of the OPAL and the one of the CLEO collaboration (Figure 8.1(c)) agree very well with the result of this analysis. The larger value of the PDG world average is solely caused by the measurement of the ALEPH collaboration. It dominates the PDG average due to its smaller uncertainty with respect to the measurements of the OPAL and CLEO collaborations.

Using the updated world averages of the measured decays into final states with net strangeness, $\tau^- \to K^- n \pi^0 \nu_\tau$ with $n = 0, 1, 2, 3$, the most precise determination of the total decay rate of the τ lepton into strange final states $R_{\tau,\mathrm{S}}$ and its non-strange counterpart $R_{\tau,\mathrm{NS}}$ (Section 1.2.3) has been performed:

$$
\begin{aligned}
R_{\tau,\mathrm{S}} &= 0.1589 \pm 0.0035 \,, \\
R_{\tau,\mathrm{NS}} &= R_\tau - R_{\tau,\mathrm{S}} = 3.481 \pm 0.010 \,.
\end{aligned}
$$

The symbol R_τ denotes the total hadronic decay rate of the τ lepton. The current PDG world averages and recent measurements of the $B\textsc{a}B\textsc{ar}$ and Belle collaborations have been used for the modes that were not measured in this analysis (Table 7.1, [3, 24, 25]). An improvement of 20 % has been achieved for $R_{\tau,\mathrm{S}}$ with respect to the determination based on the current PDG world averages and the recent measurements of the $B\textsc{a}B\textsc{ar}$ and Belle collaborations alone, $R_{\tau,\mathrm{S}}^{(\mathrm{PDG})} = 0.1615 \pm 0.0044$. Due to the lower values of the updated averages of the branching fractions of the modes $\tau^- \to K^- \nu_\tau$ and $\tau^- \to K^- \pi^0 \pi^0 (\pi^0) \nu_\tau$, the updated value for $R_{\tau,\mathrm{S}}$ is also smaller than the PDG-based value $R_{\tau,\mathrm{S}}^{(\mathrm{PDG})}$.

On the basis of these new values for $R_{\tau,\mathrm{S}}$ and $R_{\tau,\mathrm{NS}}$, an updated measurement of $|V_{us}|$ from hadronic τ decays (Equation 7.1) has been performed:

$$
\begin{aligned}
|V_{us}| &= 0.2146 \pm 0.0005_{\text{(theo)}} \pm 0.0025_{\text{(exp)}} \\
&= 0.2146 \pm 0.0025 \quad (1.18\,\%)\,.
\end{aligned}
$$

The total uncertainty is calculated by adding the experimental and theoretical contributions in quadrature. The number in brackets is the relative uncertainty. This is the most precise measurement of $|V_{us}|$ from hadronic τ decays. The uncertainty has been reduced by 19\% with respect to previous measurements, which have used the PDG world averages of the branching fractions as well as recent measurements of the BABAR and Belle collaborations [3, 24, 25], $|V_{us}|_{\mathrm{PDG}} = 0.2164 \pm 0.0005_{\text{(theo)}} \pm 0.0031_{\text{(exp)}}$. However, as discussed below, the new measurement differs by 3.5 standard deviations from the current world average of $|V_{us}|$ from semileptonic kaon decays, $|V_{us}|_{K\ell 3} = 0.2255 \pm 0.0019$ [3]. The uncertainties of the two determinations are comparable. While the measurement from semileptonic kaon decays is limited by its theoretical uncertainty [3], the uncertainty of the determinations from hadronic τ decays is dominated by the experimental uncertainty of $R_{\tau,\mathrm{S}}$.

Figure 8.2 provides a comparison of the measurement of $|V_{us}|$ performed within this work with the current world average from semileptonic kaon decays and other recent measurements. *Unitarity* refers to the determination from the unitarity condition for the first row of the CKM matrix and the world averages of $|V_{ud}|$ and $|V_{ub}|$. The measurements based on (semi)leptonic kaon decays $K\ell 3$ ($K\ell 2$) and hyperon decays use similar methods and are all dominated by their theoretical uncertainties. The current PDG world average is marked by a grey band in Figure 8.2 and the yellow band indicates the updated measurement from hadronic τ decays.

While the measurements based on kaon and hyperon decays are all compatible with unitarity, the updated measurement from hadronic τ decays differs by 4.0 standard deviations from unitarity. This deviation has been increased by the new smaller values for the branching fractions of the decay modes $\tau^- \to K^- \nu_\tau$ and $\tau^- \to K^- \pi^0 \pi^0 (\pi^0) \nu_\tau$ as presented in this thesis.

However, care needs to be taken when considering the unitarity condition for the first row of the CKM matrix. The PDG world average of $|V_{ud}|$ is solely based on measurements of superallowed $0^+ \to 0^+$ nuclear β-decays [3]. To extract $|V_{ud}|$ from the measurements, corrections for the structure of the nuclei and isospin breaking effects are needed. The central value of the current average obtained from these measurements has shifted upwards by 1.5 standard deviations compared to the average of the year 2006 due to a recent evaluation of the isospin breaking Coulomb corrections [3]. Moreover, determinations of $|V_{ud}|$ using neutron decays yield results that differ from the PDG world average by as much as 4.5 standard deviations. They range from $|V_{ud}| = 0.97092 \pm 0.00068$ [86] to $|V_{ud}| = 0.9786 \pm 0.0019$ [3], depending on the values of the neutron lifetime τ_n and the ratio of the axial-vector/vector coupling $g_\mathrm{A} \equiv G_\mathrm{A}/G_\mathrm{V}$ that are used to calculate $|V_{ud}|$. Both have been subject of discussions lately [3, 86]. A recent measurement of the neutron lifetime differs by 6.5 standard deviations from the PDG world average [3, 87]. In addition, a recent determination of g_A also differs from the world average by 1.9 standard deviations [3, 86]. In total, these observations show that the experimental and theoretical situation in the $|V_{ud}|$ sector is unclear.
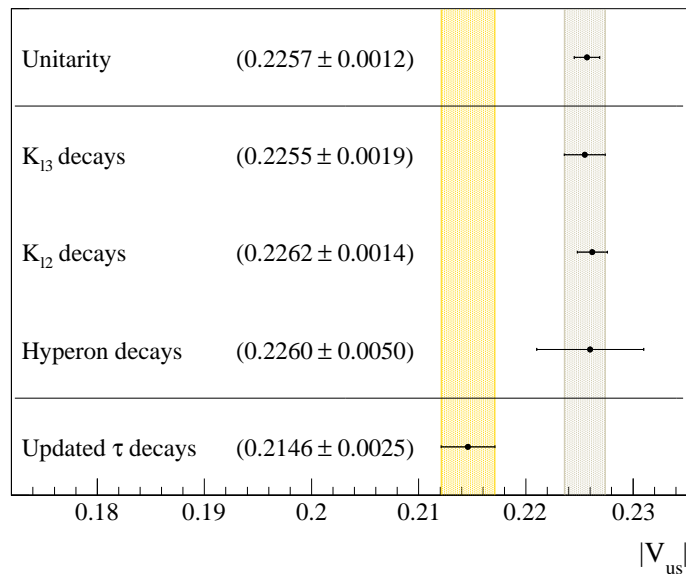
Figure 8.2: Comparison of the updated measurement of $|V_{us}|$ using hadronic τ decays with current measurements from other methods [3]. *Unitarity* refers to the value obtained from the world averages of $|V_{ud}|$ and $|V_{ub}|$ by imposing unitarity (Equation 1.63). The measurement using $K_{\ell 3}$ *decays* is described in Section 1.4.1. *Hyperon* [31] and $K_{\ell 2}$ *decays* [32] provide similar methods to determine $|V_{us}|$. All three measurements are dominated by theoretical uncertainties [3, 31, 32]. The independent measurement using τ *decays* has been performed within this work and is described in Section 7.2. It includes the updated world averages of the decay modes $\tau^- \to K^- n\pi^0 \nu_\tau$ with $n = 0, 1, 2, 3$ (Equation 6.68). This measurement is dominated by experimental uncertainties. The current world average—which does not include the measurement using $K_{\ell 2}$ decays [3]—is marked by the grey band. The yellow band indicates the updated measurement from τ decays.

Finally, the deviations of the measured branching fraction $\mathcal{B}(\tau^- \to K^- \nu_\tau)$ from the predicted value using $\tau - \mu$ lepton universality and of the measured value of $|V_{us}|$ using τ decays from determinations on the basis of kaon and hyperon decays also need to be considered in a wider context. While they could indicate new physics beyond the Standard Model, they also add to a growing list of deviations between measurements in the τ lepton sector and other experimental areas [10]. One example is the comparison of τ vector spectral functions (Section 1.2.4), e.g., in the mode $\tau^- \to \pi^- \pi^0 \nu_\tau$, with the $e^+ e^-$ annihilation cross section of the corresponding isovector final state, i.e., $e^+ e^- \to \pi^+ \pi^-$, via the conservation of vector currents [10]. Correcting for all identified sources of isospin breaking, e.g., the π^--π^0 mass splitting, a significant deviation is observed between the τ and the $e^+ e^-$ data [10]. Integrating the τ spectral function and the annihilation cross section up to the τ mass results in a difference of 2.9 standard deviations between the measured rates in τ decays and in $e^+ e^-$ data [10]. Similarly, the hadronic vacuum polarization contribution to the anomalous magnetic moment of the muon also shows significant deviations between τ and $e^+ e^-$ based calculations [10].

In summary, the results of this analysis—in conjunction with the outlined findings of other experiments and calculations—underline the necessity for a careful review of the theoretical understanding of τ decays and for precise measurements of hadronic τ decays. Considering hadronic τ decays into final states with net strangeness, updated measurements of the modes

$$\tau^- \to \pi^- \overline{K}^0 \nu_\tau \,,$$
$$\tau^- \to \pi^- \overline{K}^0 \pi^0 \nu_\tau \,,$$
$$\tau^- \to K^- \pi^+ \pi^- \pi^0 \nu_\tau \,,$$
$$\tau^- \to K^- \omega \nu_\tau$$

would be most valuable. These four modes contribute a large fraction to the total uncertainty of $R_{\tau,\mathrm{S}}$ and $|V_{us}|$ as determined from hadronic τ decays. In addition, precise measurements of the spectral functions of hadronic τ decays with net strangeness would allow further tests of the theoretical description of τ decays [4, 5, 10].

Appendix A

Distributions of selection variables

Figures A.1–A.12 show the distributions of the selection variables (Tables 4.2, 4.3) for the remaining decay modes that are not displayed in Chapter 4.

(a) $\tau^- \to \pi^- \pi^0 \nu_\tau$.

(b) $\tau^- \to \pi^- \pi^0 \pi^0 \nu_\tau$.

(c) $\tau^- \to \pi^- \pi^0 \pi^0 \pi^0 \nu_\tau$.

(d) $\tau^- \to \pi^- \pi^0 \pi^0 \pi^0 \pi^0 \nu_\tau$.
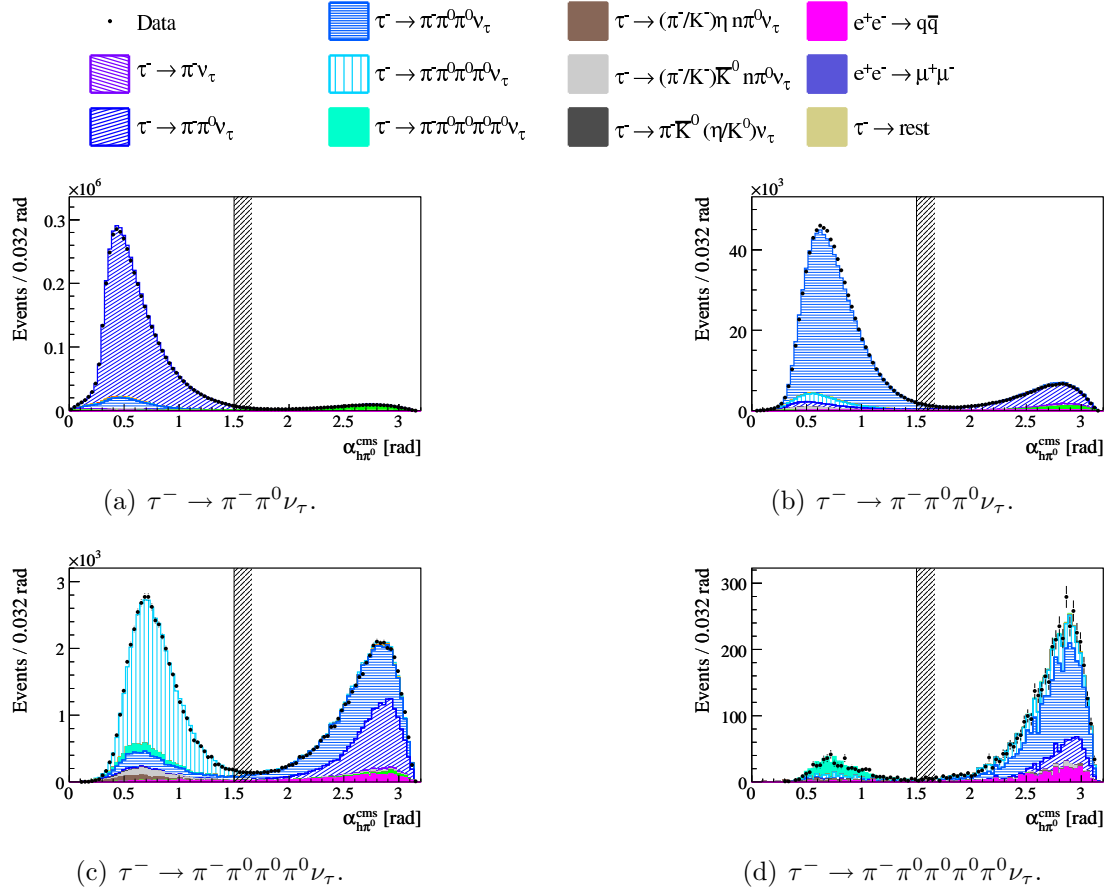
Figure A.1: Distributions of the maximal hadron-π^0 angle in the center-of-mass system $\alpha_{h\pi^0}^{\mathrm{cms}}$ for the different event categories without net strangeness, $\tau^- \to \pi^- n\pi^0 \nu_\tau$ with $n = 1, 2, 3, 4$, using muon tagged reactions. The selection criteria on this variable are indicated by the vertical lines.
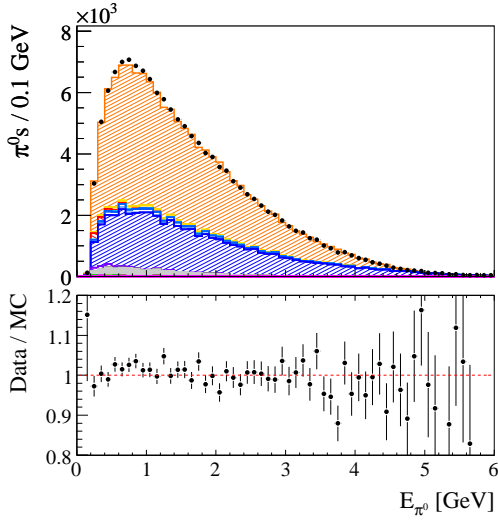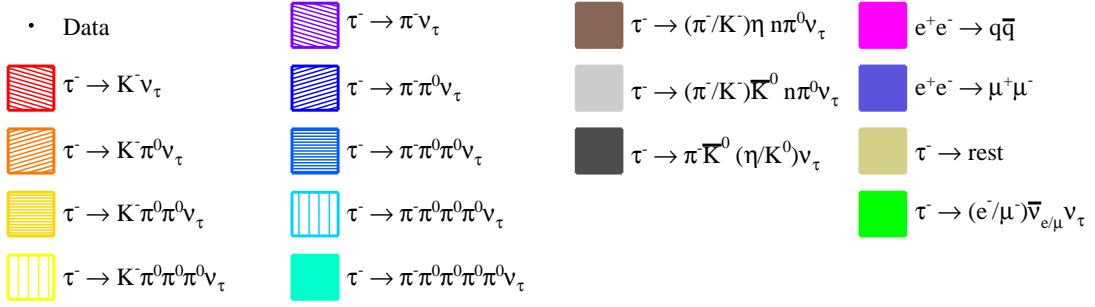
(a) $\tau^- \to K^- \pi^0 \nu_\tau$.

(b) $\tau^- \to K^- \pi^0 \pi^0 \nu_\tau$.

(c) $\tau^- \to K^- \pi^0 \pi^0 \pi^0 \nu_\tau$.
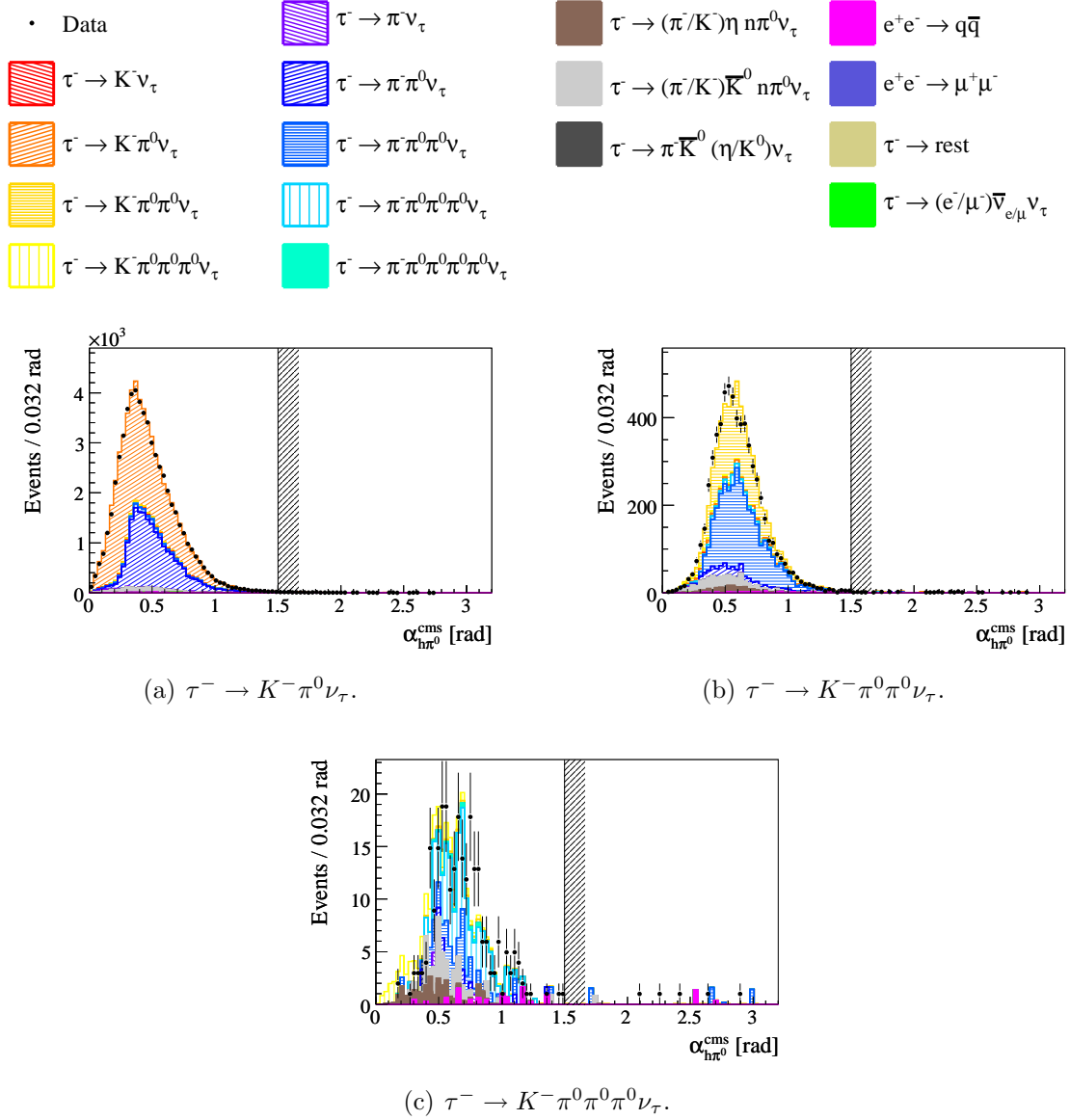
Figure A.2: Distributions of the maximal hadron-π^0 angle in the center-of-mass system $\alpha_{h\pi^0}^{\mathrm{cms}}$ for the different event categories with net strangeness, $\tau^- \to K^- n\pi^0 \nu_\tau$ with $n = 1, 2, 3$, using muon tagged reactions. The selection criteria on this variable are indicated by the vertical lines.
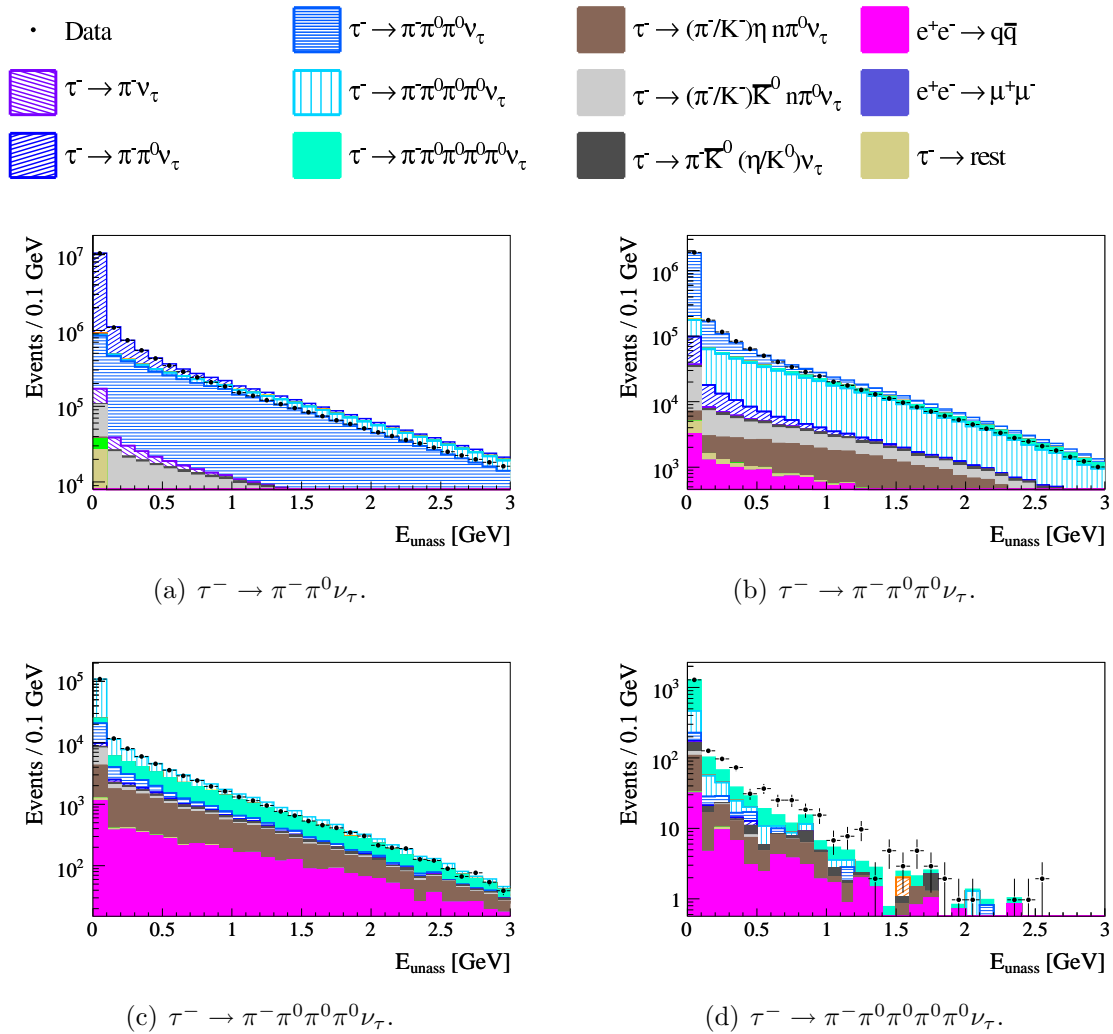
Figure A.3: Distributions of the unassociated energy in the signal event hemisphere E_{unass} for the different event categories without net strangeness, $\tau^- \to \pi^- n\pi^0 \nu_\tau$ with $n = 1, 2, 3, 4$.
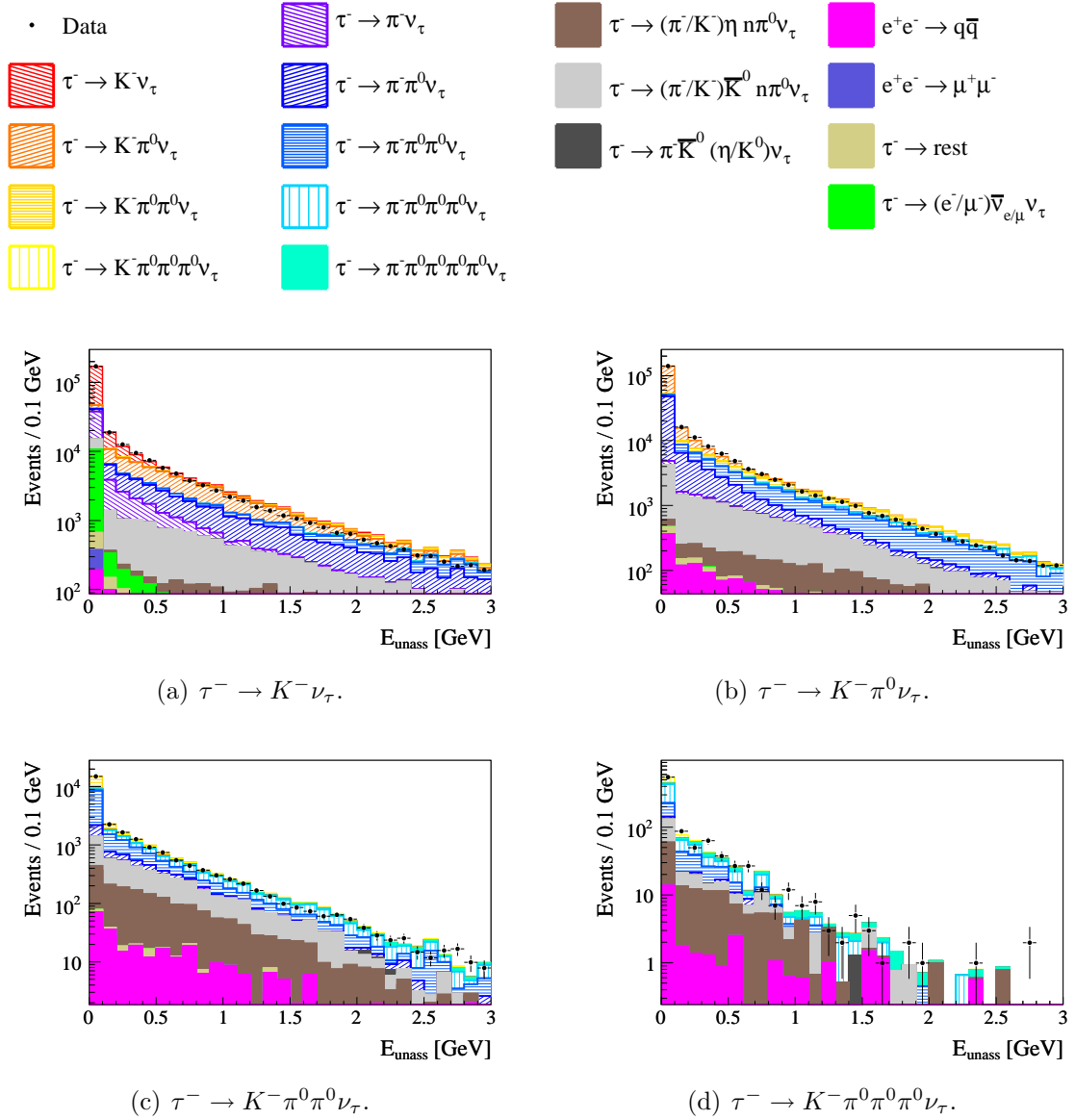
Figure A.4: Distributions of the unassociated energy in the signal event hemisphere E_{unass} for the different event categories with net strangeness, $\tau^- \to K^- n\pi^0\nu_\tau$ with $n = 0, 1, 2, 3$.
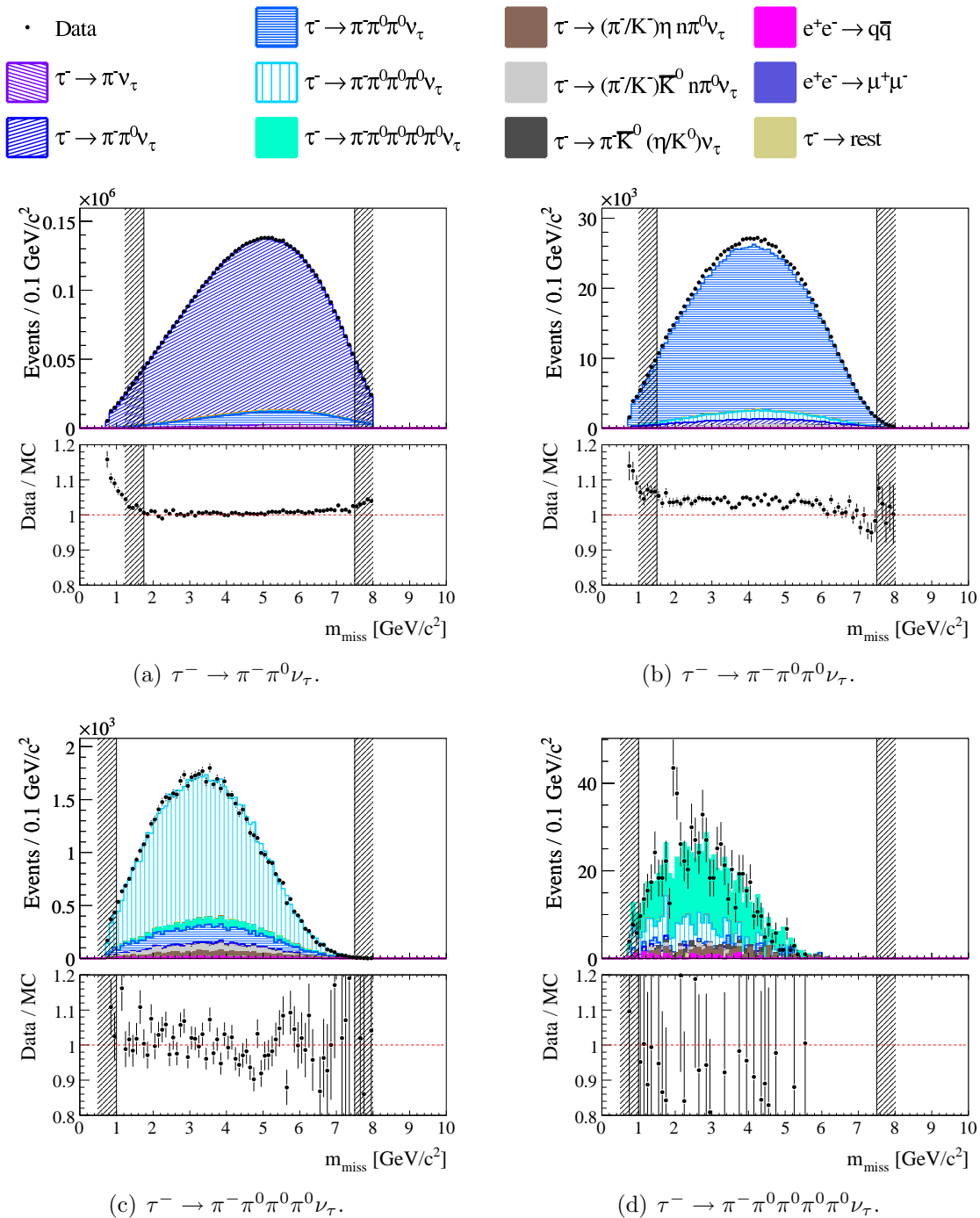
Figure A.5: Distributions of the missing mass m_{miss} for the different event categories without net strangeness, $\tau^- \to \pi^- n\pi^0 \nu_\tau$ with $n = 1, 2, 3, 4$, using electron tagged reactions. The selection criteria on this variable are indicated by the vertical lines.

(a) $\tau^- \to K^- \nu_\tau$.

(b) $\tau^- \to K^- \pi^0 \nu_\tau$.

(c) $\tau^- \to K^- \pi^0 \pi^0 \nu_\tau$.

(d) $\tau^- \to K^- \pi^0 \pi^0 \pi^0 \nu_\tau$.
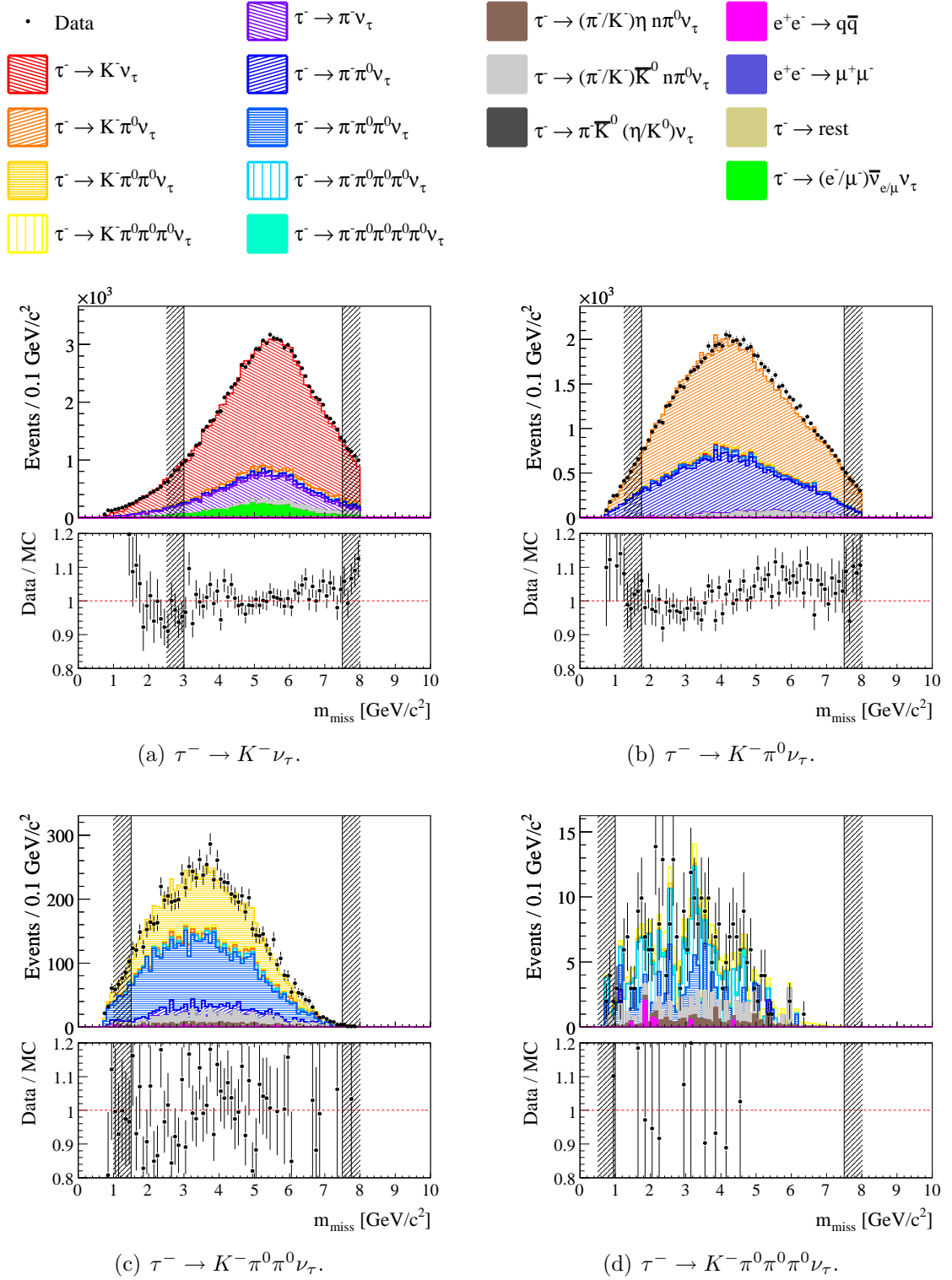
Figure A.6: Distributions of the missing mass m_{miss} for the different event categories with net strangeness, $\tau^- \to K^- n\pi^0 \nu_\tau$ with $n = 0, 1, 2, 3$, using electron tagged reactions. The selection criteria on this variable are indicated by the vertical lines.
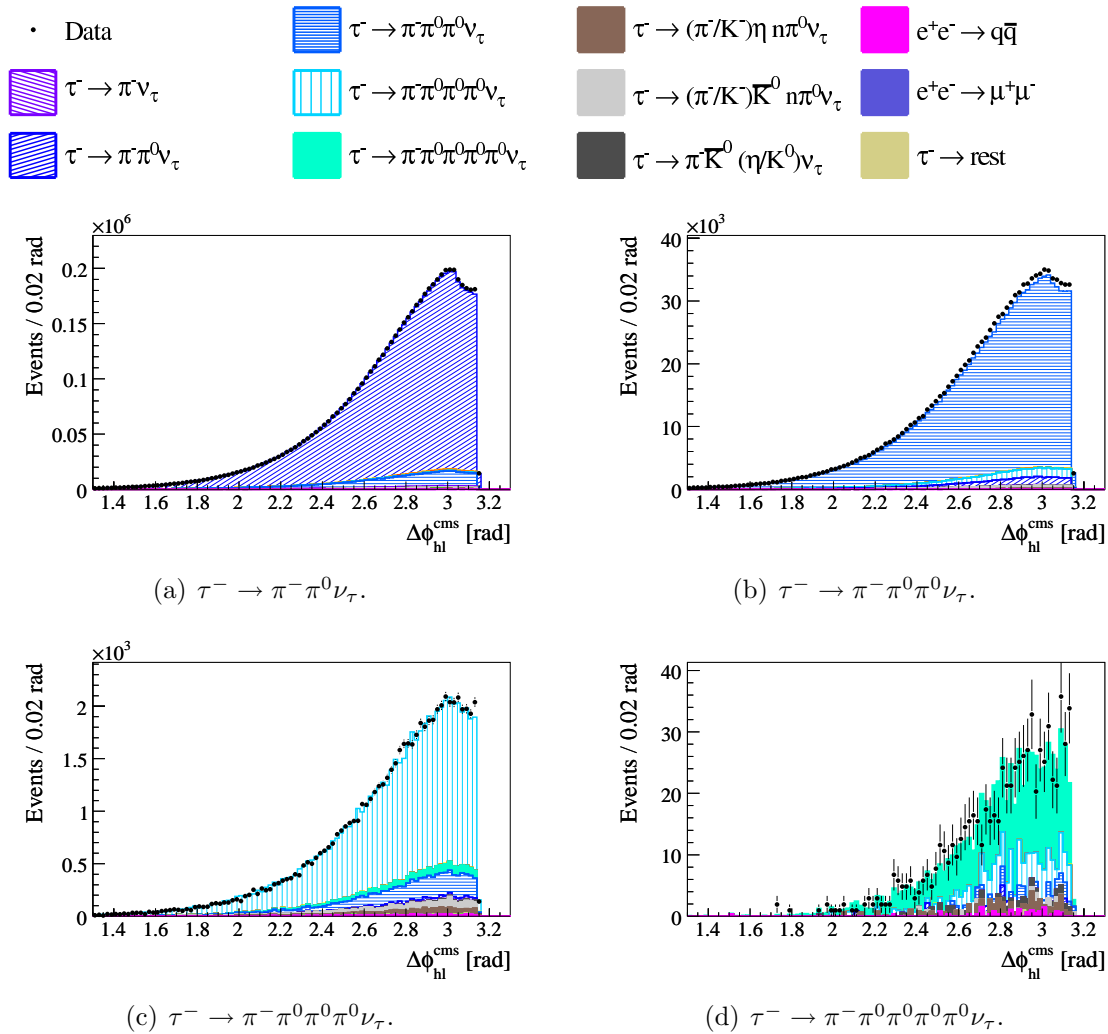
Figure A.7: Distributions of the hadron-lepton acoplanarity $\Delta\phi_{h\ell}^{\mathrm{cms}}$ in the center-of-mass system for the different event categories without net strangeness, $\tau^- \to \pi^- n\pi^0 \nu_\tau$ with $n = 1, 2, 3, 4$, using electron tagged reactions.
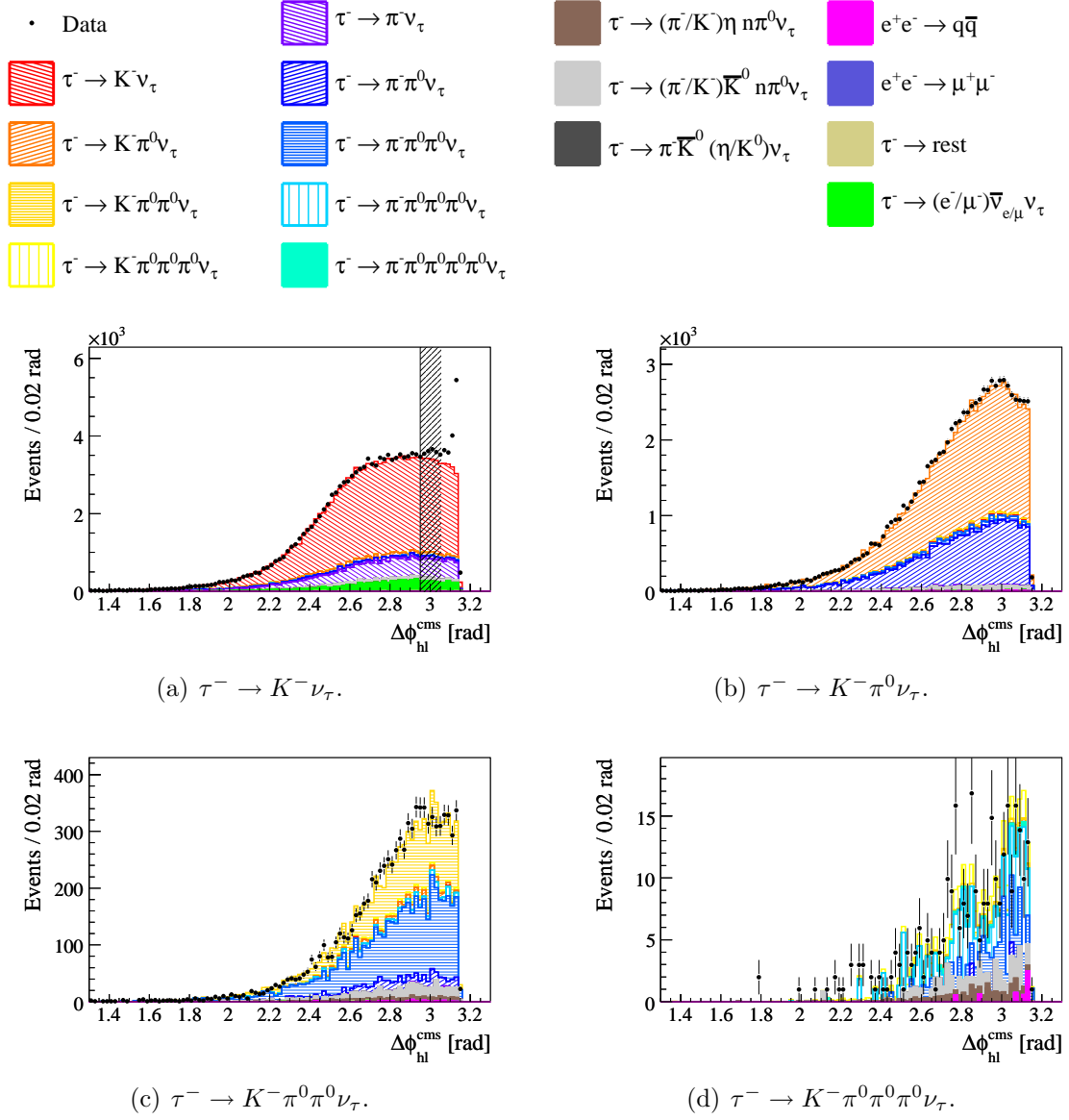
Figure A.8: Distributions of the hadron-lepton acoplanarity $\Delta\phi_{h\ell}^{\mathrm{cms}}$ in the center-of-mass system for the different event categories with net strangeness, $\tau^- \to K^- n\pi^0\nu_\tau$ with $n = 0, 1, 2, 3$, using electron tagged reactions. The selection criterion on this variable is indicated by the vertical line.

(a) $\tau^- \to \pi^- \pi^0 \nu_\tau$.

(b) $\tau^- \to \pi^- \pi^0 \pi^0 \nu_\tau$.

(c) $\tau^- \to \pi^- \pi^0 \pi^0 \pi^0 \nu_\tau$.

(d) $\tau^- \to \pi^- \pi^0 \pi^0 \pi^0 \pi^0 \nu_\tau$.
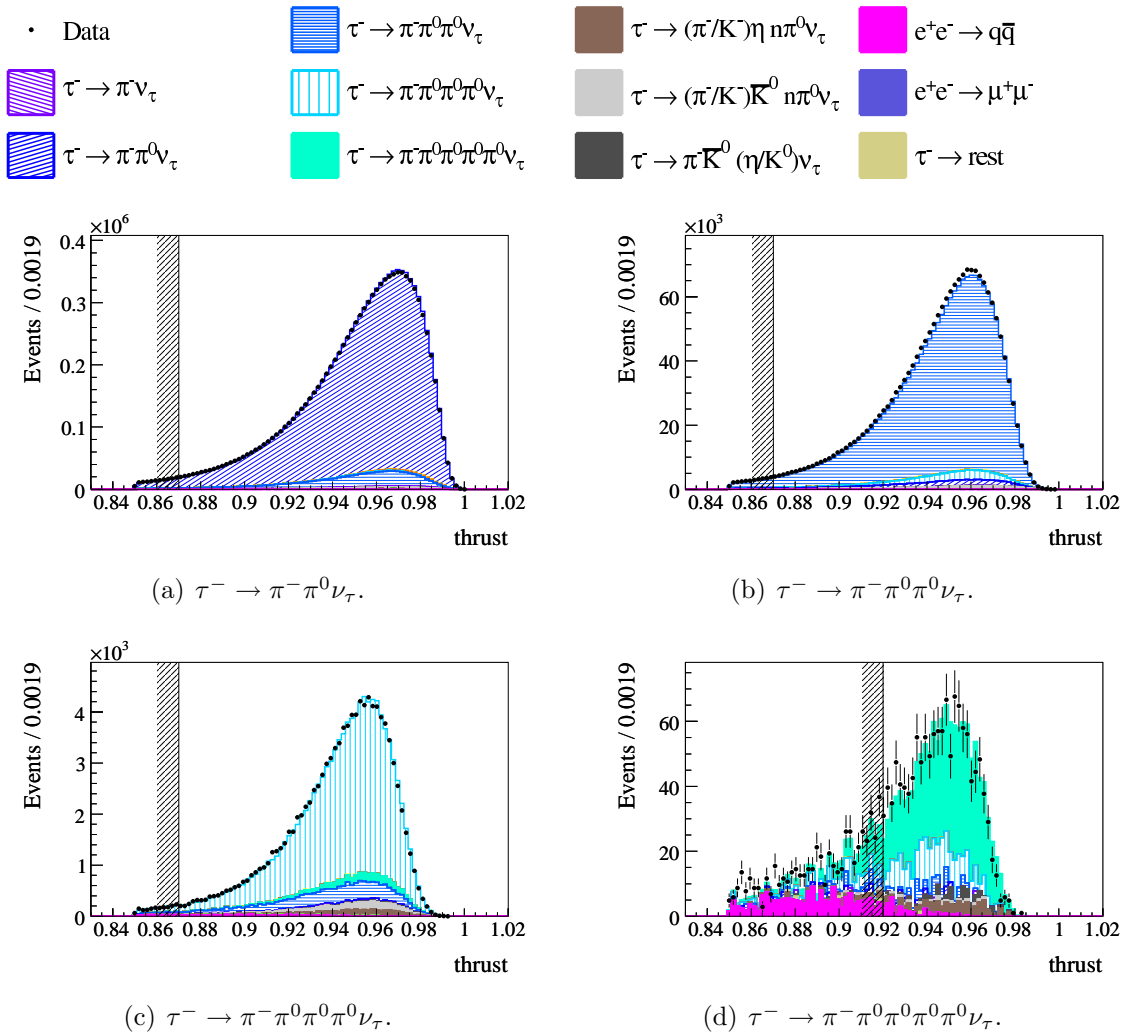
Figure A.9: Distributions of the thrust for the different event categories without net strangeness, $\tau^- \to \pi^- n\pi^0 \nu_\tau$ with $n = 1, 2, 3, 4$. The selection criteria on this variable are indicated by the vertical lines.
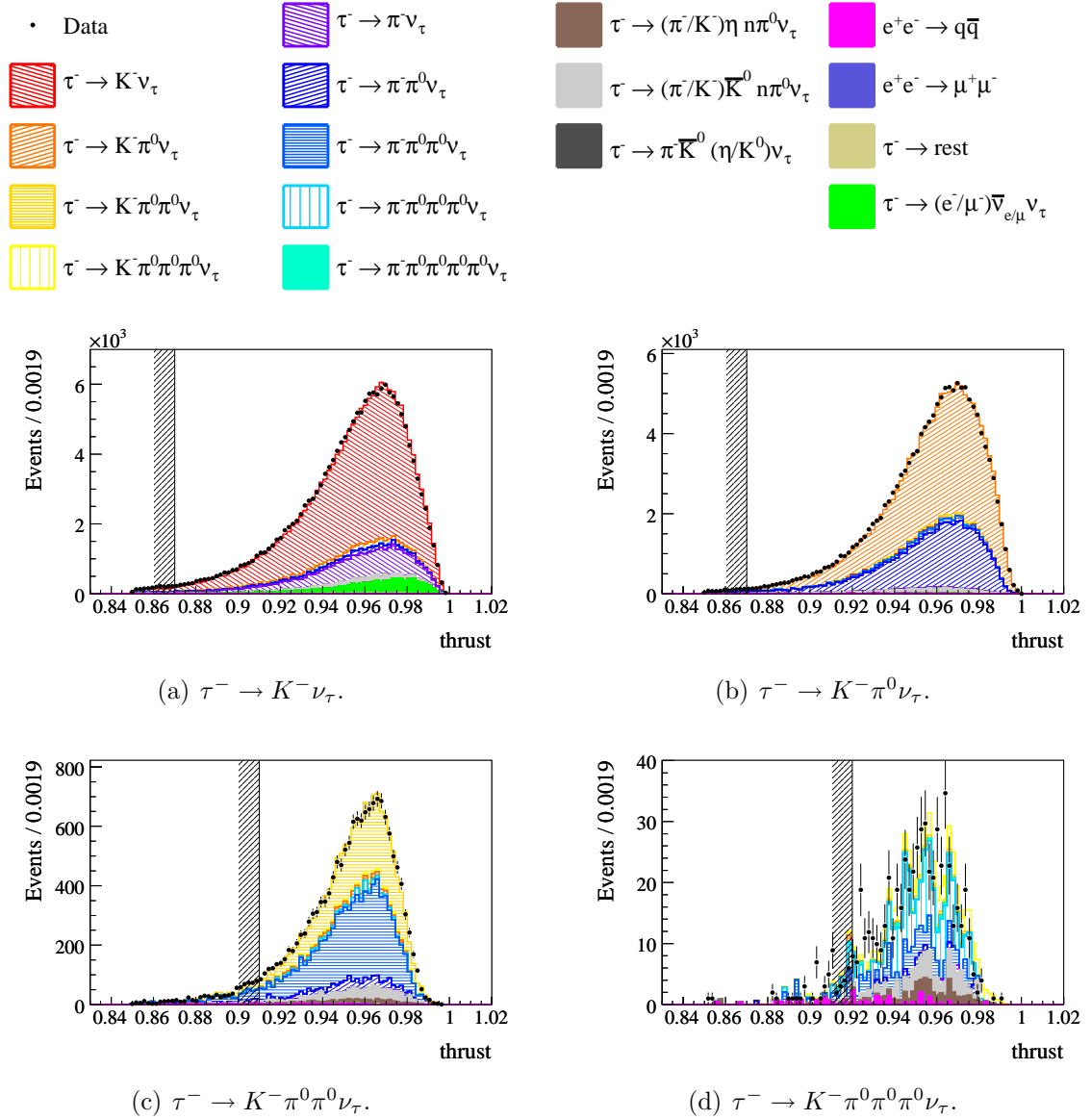
Figure A.10: Distributions of the thrust for the different event categories with net strangeness, $\tau^- \to K^- n\pi^0 \nu_\tau$ with $n = 0, 1, 2, 3$. The selection criteria on this variable are indicated by the vertical lines.
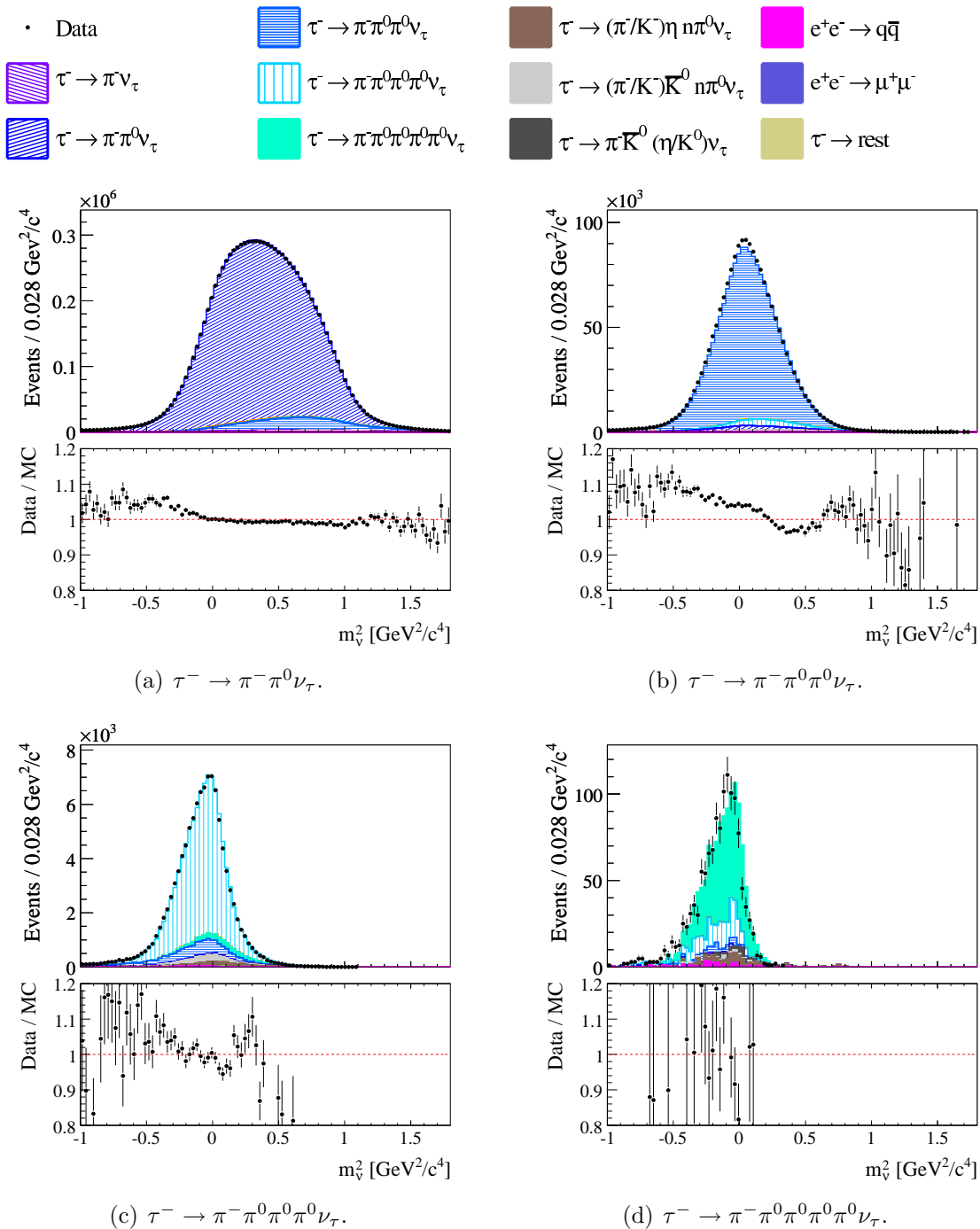
Figure A.11: Distributions of the squared invariant neutrino mass m_ν^2 for the different selected event categories without net strangeness, $\tau^- \to \pi^- n\pi^0 \nu_\tau$ with $n = 1, 2, 3, 4$. Negative values occur because of the finite detector resolution and due to the rough estimate of the τ direction using the thrust direction.
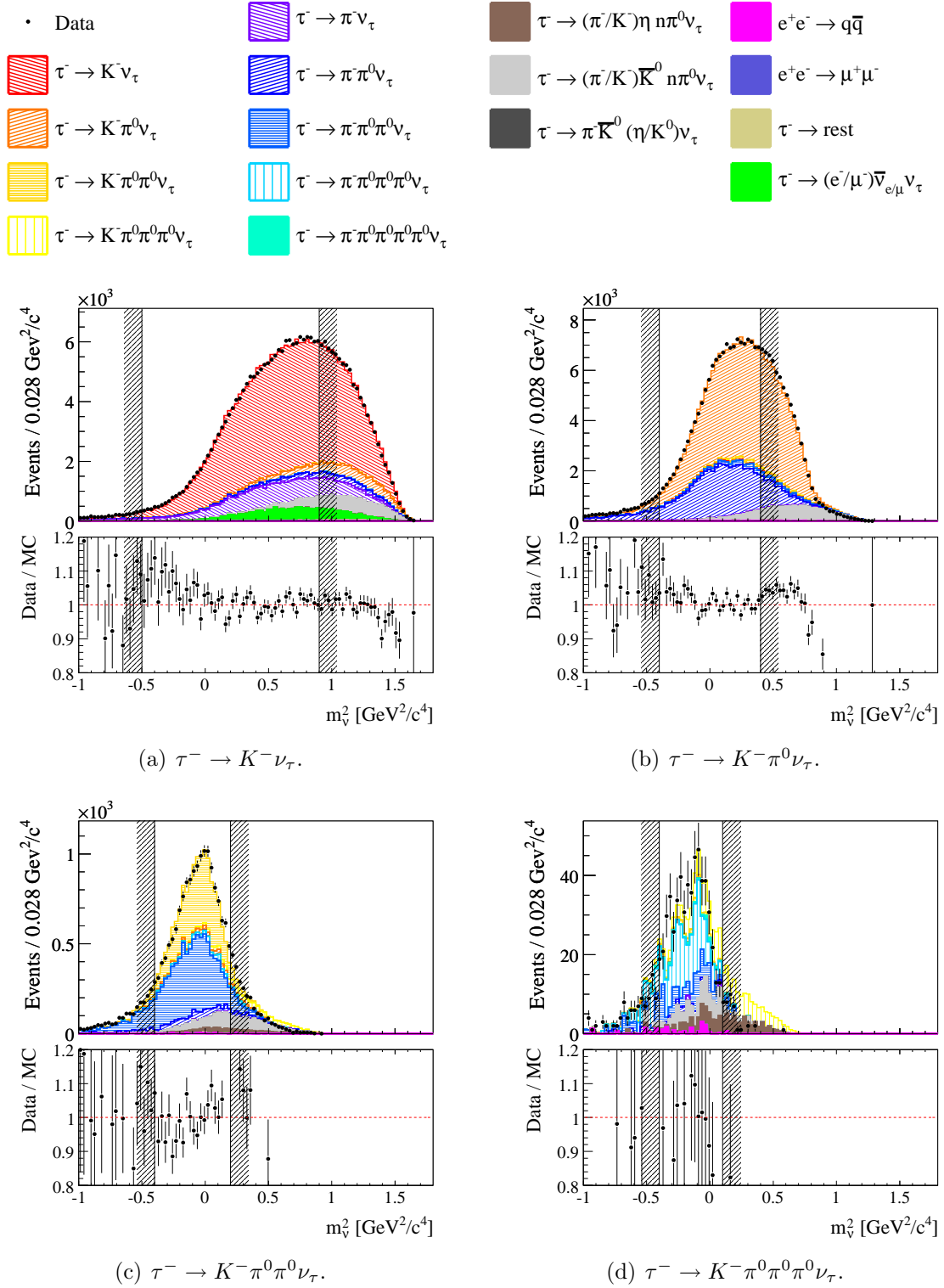
Figure A.12: Distributions of the squared invariant neutrino mass m_ν^2 for the different selected event categories with net strangeness, $\tau^- \to K^- n\pi^0 \nu_\tau$ with $n = 0, 1, 2, 3$. Negative values occur because of the finite detector resolution and due to the rough estimate of the τ direction using the thrust direction. The selection criteria on this variable are indicated by the vertical lines.

Appendix B

Distributions of kinematic variables

Figures B.1 and B.2 show the π^0 energies E_{π^0} for all decay channels with final state π^0 mesons.

(a) $\tau^- \to \pi^- \pi^0 \nu_\tau$.

(b) $\tau^- \to \pi^- \pi^0 \pi^0 \nu_\tau$.

(c) $\tau^- \to \pi^- \pi^0 \pi^0 \pi^0 \nu_\tau$.

(d) $\tau^- \to \pi^- \pi^0 \pi^0 \pi^0 \pi^0 \nu_\tau$.
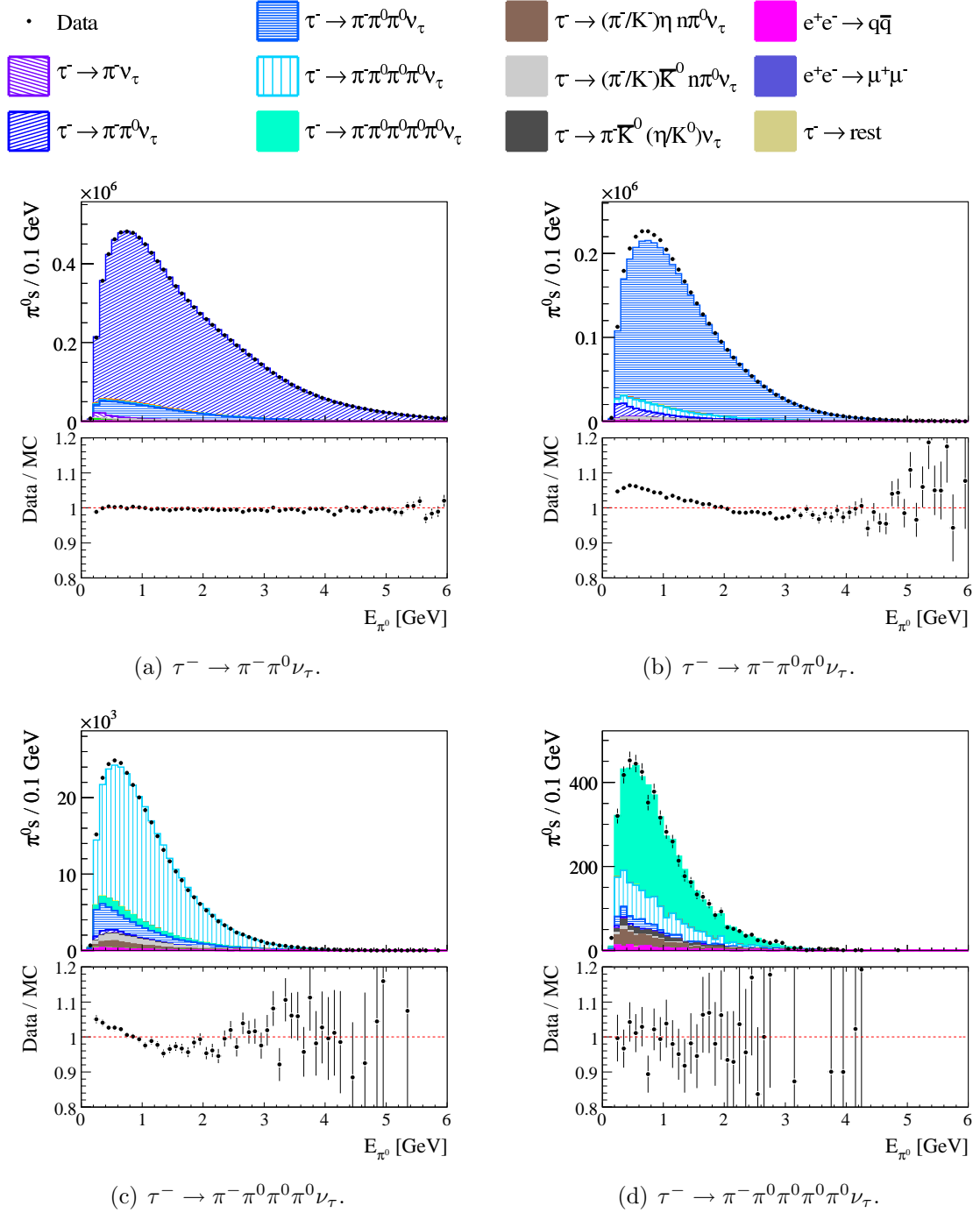
Figure B.1: Distributions of the π^0 energies E_{π^0} for the different event categories without net strangeness, $\tau^- \to \pi^- n\pi^0 \nu_\tau$ with $n = 1, 2, 3, 4$.

(a) $\tau^- \rightarrow K^-\pi^0\nu_\tau$.

(b) $\tau^- \rightarrow K^-\pi^0\pi^0\nu_\tau$.

(c) $\tau^- \rightarrow K^-\pi^0\pi^0\pi^0\nu_\tau$.
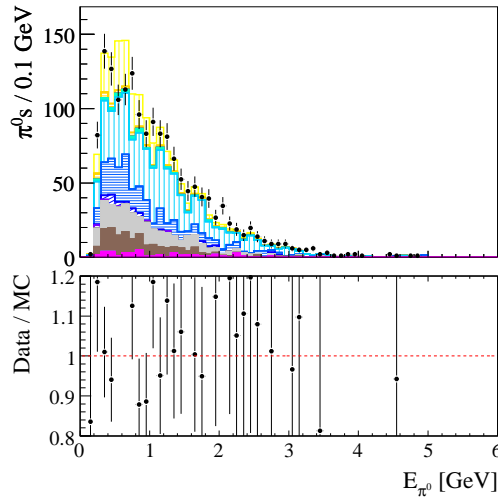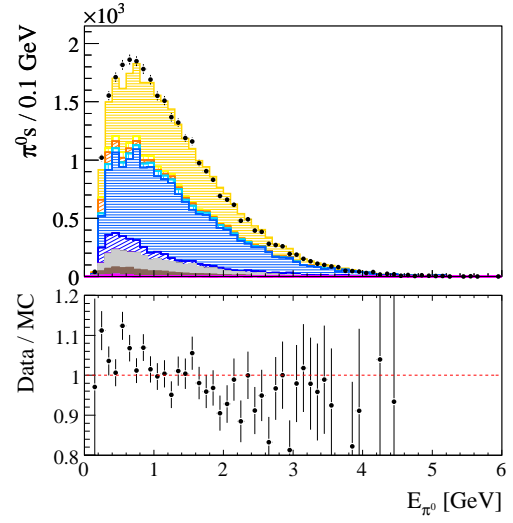
Figure B.2: Distributions of the π^0 energies E_{π^0} for the different event categories with net strangeness, $\tau^- \rightarrow K^- n\pi^0\nu_\tau$ with $n = 1, 2, 3$.

Appendix C

Correlation matrices

Equations C.1–C.10 list the correlation matrices for the individual contributions to the statistical and systematic uncertainties that are not listed in Chapter 6.

$\tau\tau$ production cross section $\sigma(e^+e^- \to \tau^+\tau^-)$

$$
\rho^{\mathcal{B}}_{\sigma_{\tau\tau}} =
\begin{array}{c}
\begin{array}{cccccc}
\pi 3\pi^0 & \pi 4\pi^0 & K & K\pi^0 & K2\pi^0 & K3\pi^0
\end{array} \\
\left(
\begin{array}{cccccc}
1.000 & 1.000 & -1.000 & -1.000 & 1.000 & 1.000 \\
1.000 & 1.000 & -1.000 & -1.000 & 1.000 & 1.000 \\
-1.000 & -1.000 & 1.000 & 1.000 & -1.000 & -1.000 \\
-1.000 & -1.000 & 1.000 & 1.000 & -1.000 & -1.000 \\
1.000 & 1.000 & -1.000 & -1.000 & 1.000 & 1.000 \\
1.000 & 1.000 & -1.000 & -1.000 & 1.000 & 1.000
\end{array}
\right)
\begin{array}{l}
\pi 3\pi^0 \\
\pi 4\pi^0 \\
K \\
K\pi^0 \\
K2\pi^0 \\
K3\pi^0
\end{array}
\end{array}
\qquad (\text{C.1})
$$

All decay channels are fully correlated with respect to the uncertainty of the $\tau\tau$ production cross section. This is due to the fact that background from reactions other than $e^+e^- \to \tau^+\tau^-$ is negligible in this analysis (Figures 4.13, 4.14). Thus, the $\tau\tau$ cross section enters in the same way into all branching fractions. The anti-correlation of events of the type $\tau^- \to K^-\nu_\tau$ with respect to all modes containing multiple π^0 mesons is caused by the treatment of the π^0 efficiency correction. The decay mode $\tau^- \to K^-\pi^0\nu_\tau$ is also anti-correlated with all modes containing multiple π^0 mesons. It is however noted that the uncertainty of the branching fraction $\mathcal{B}(\tau^- \to K^-\pi^0\nu_\tau)$ due to the uncertainty of the $\tau\tau$ production cross section is very small (Table 6.5). This is caused by the method of the π^0 efficiency correction, which in a way is a relative measurement of the mode $\tau^- \to K^-\pi^0\nu_\tau$ with respect to the channel $\tau^- \to \pi^-\pi^0\nu_\tau$. Hence, many uncertainties cancel in first order. The same arguments hold for the luminosity and the tracking efficiency, which enter the calculation of the branching fractions in the same way as the $\tau\tau$ production cross section.

Luminosity

$$
\boldsymbol{\rho}_{\mathcal{L}}^{\mathcal{B}} \;=\;
\begin{matrix}
 & \pi3\pi^0 & \pi4\pi^0 & K & K\pi^0 & K2\pi^0 & K3\pi^0 & \\
\left(\vphantom{\begin{matrix}1\\1\\1\\1\\1\\1\end{matrix}}\right.
\begin{matrix}
1.000 & 1.000 & -0.999 & -0.948 & 1.000 & 1.000 \\
1.000 & 1.000 & -1.000 & -0.952 & 1.000 & 1.000 \\
-0.999 & -1.000 & 1.000 & 0.957 & -0.999 & -1.000 \\
-0.948 & -0.952 & 0.957 & 1.000 & -0.945 & -0.950 \\
1.000 & 1.000 & -0.999 & -0.945 & 1.000 & 1.000 \\
1.000 & 1.000 & -1.000 & -0.950 & 1.000 & 1.000
\end{matrix}
\left.\vphantom{\begin{matrix}1\\1\\1\\1\\1\\1\end{matrix}}\right)
&
\begin{matrix}
\pi3\pi^0 \\ \pi4\pi^0 \\ K \\ K\pi^0 \\ K2\pi^0 \\ K3\pi^0
\end{matrix}
\end{matrix}
\tag{C.2}
$$

Background normalization

$$
\boldsymbol{\rho}_{\mathcal{B}_{i_{\mathrm{BG}}}}^{\mathcal{B}} \;=\;
\begin{matrix}
 & \pi3\pi^0 & \pi4\pi^0 & K & K\pi^0 & K2\pi^0 & K3\pi^0 & \\
\left(\vphantom{\begin{matrix}1\\1\\1\\1\\1\\1\end{matrix}}\right.
\begin{matrix}
1.000 & 0.886 & -0.202 & 0.569 & 0.596 & 0.139 \\
0.886 & 1.000 & -0.207 & 0.504 & 0.497 & 0.140 \\
-0.202 & -0.207 & 1.000 & 0.600 & 0.071 & 0.009 \\
0.569 & 0.504 & 0.600 & 1.000 & 0.553 & 0.179 \\
0.596 & 0.497 & 0.071 & 0.553 & 1.000 & 0.229 \\
0.139 & 0.140 & 0.009 & 0.179 & 0.229 & 1.000
\end{matrix}
\left.\vphantom{\begin{matrix}1\\1\\1\\1\\1\\1\end{matrix}}\right)
&
\begin{matrix}
\pi3\pi^0 \\ \pi4\pi^0 \\ K \\ K\pi^0 \\ K2\pi^0 \\ K3\pi^0
\end{matrix}
\end{matrix}
\tag{C.3}
$$

Tracking efficiency

$$
\boldsymbol{\rho}_{\eta_{\mathrm{track}}}^{\mathcal{B}} \;=\;
\begin{matrix}
 & \pi3\pi^0 & \pi4\pi^0 & K & K\pi^0 & K2\pi^0 & K3\pi^0 & \\
\left(\vphantom{\begin{matrix}1\\1\\1\\1\\1\\1\end{matrix}}\right.
\begin{matrix}
1.000 & 1.000 & -1.000 & -1.000 & 1.000 & 1.000 \\
1.000 & 1.000 & -1.000 & -1.000 & 1.000 & 1.000 \\
-1.000 & -1.000 & 1.000 & 1.000 & -1.000 & -1.000 \\
-1.000 & -1.000 & 1.000 & 1.000 & -1.000 & -1.000 \\
1.000 & 1.000 & -1.000 & -1.000 & 1.000 & 1.000 \\
1.000 & 1.000 & -1.000 & -1.000 & 1.000 & 1.000
\end{matrix}
\left.\vphantom{\begin{matrix}1\\1\\1\\1\\1\\1\end{matrix}}\right)
&
\begin{matrix}
\pi3\pi^0 \\ \pi4\pi^0 \\ K \\ K\pi^0 \\ K2\pi^0 \\ K3\pi^0
\end{matrix}
\end{matrix}
\tag{C.4}
$$

Charged particle identification efficiency

$$
\boldsymbol{\rho}_{\eta_{\mathrm{PID}}}^{\mathcal{B}} \;=\;
\begin{matrix}
 & \pi3\pi^0 & \pi4\pi^0 & K & K\pi^0 & K2\pi^0 & K3\pi^0 & \\
\left(\vphantom{\begin{matrix}1\\1\\1\\1\\1\\1\end{matrix}}\right.
\begin{matrix}
1.000 & 0.657 & -0.250 & -0.043 & 0.048 & -0.038 \\
0.657 & 1.000 & -0.169 & -0.023 & 0.017 & -0.007 \\
-0.250 & -0.169 & 1.000 & 0.727 & 0.377 & 0.151 \\
-0.043 & -0.023 & 0.727 & 1.000 & 0.781 & 0.407 \\
0.048 & 0.017 & 0.377 & 0.781 & 1.000 & 0.341 \\
-0.038 & -0.007 & 0.151 & 0.407 & 0.341 & 1.000
\end{matrix}
\left.\vphantom{\begin{matrix}1\\1\\1\\1\\1\\1\end{matrix}}\right)
&
\begin{matrix}
\pi3\pi^0 \\ \pi4\pi^0 \\ K \\ K\pi^0 \\ K2\pi^0 \\ K3\pi^0
\end{matrix}
\end{matrix}
\tag{C.5}
$$

While the uncertainties of all decay modes comprising a kaon in their final state are positively correlated, they are negatively correlated with the ones of the two modes that contain a charged pion. This is due to the identification of charged pions as "not being kaons" (Section 3.3.2). If an event of true type $\tau^- \to \pi^-\pi^0\pi^0\pi^0\nu_\tau$ is spuriously identified as an event of the type $\tau^- \to K^-\pi^0\pi^0\pi^0\nu_\tau$, the event is not counted in the decay mode $\tau^- \to \pi^-\pi^0\pi^0\pi^0\nu_\tau$ while the number of reconstructed $\tau^- \to K^-\pi^0\pi^0\pi^0\nu_\tau$ events increases. Thus, the two modes are anti-correlated.

Signal selection efficiencies

$$
\rho^{\mathcal{B}}_{\varepsilon_{\text{sig}}} =
\begin{array}{cccccc}
\pi3\pi^0 & \pi4\pi^0 & K & K\pi^0 & K2\pi^0 & K3\pi^0
\end{array}
\left(
\begin{array}{cccccc}
1.000 & -0.343 & 0.009 & -0.011 & 0.075 & -0.110 \\
-0.343 & 1.000 & 0.004 & 0.005 & -0.003 & 0.002 \\
0.009 & 0.004 & 1.000 & -0.076 & -0.015 & 0.021 \\
-0.011 & 0.005 & -0.076 & 1.000 & -0.043 & 0.005 \\
0.075 & -0.003 & -0.015 & -0.043 & 1.000 & -0.756 \\
-0.110 & 0.002 & 0.021 & 0.005 & -0.756 & 1.000
\end{array}
\right)
\begin{array}{l}
\pi3\pi^0 \\
\pi4\pi^0 \\
K \\
K\pi^0 \\
K2\pi^0 \\
K3\pi^0
\end{array}
\tag{C.6}
$$

Background misidentification probabilities

$$
\rho^{\mathcal{B}}_{\varepsilon_{\text{BG}}} =
\begin{array}{cccccc}
\pi3\pi^0 & \pi4\pi^0 & K & K\pi^0 & K2\pi^0 & K3\pi^0
\end{array}
\left(
\begin{array}{cccccc}
1.000 & -0.464 & -0.001 & 0.002 & 0.039 & -0.123 \\
-0.464 & 1.000 & -0.003 & -0.010 & -0.006 & 0.001 \\
-0.001 & -0.003 & 1.000 & -0.067 & -0.012 & -0.002 \\
0.002 & -0.010 & -0.067 & 1.000 & -0.129 & 0.018 \\
0.039 & -0.006 & -0.012 & -0.129 & 1.000 & -0.366 \\
-0.123 & 0.001 & -0.002 & 0.018 & -0.366 & 1.000
\end{array}
\right)
\begin{array}{l}
\pi3\pi^0 \\
\pi4\pi^0 \\
K \\
K\pi^0 \\
K2\pi^0 \\
K3\pi^0
\end{array}
\tag{C.7}
$$

π^0 efficiency correction

$$
\rho^{\mathcal{B}}_{\eta_{\pi^0}} =
\begin{array}{cccccc}
\pi3\pi^0 & \pi4\pi^0 & K & K\pi^0 & K2\pi^0 & K3\pi^0
\end{array}
\left(
\begin{array}{cccccc}
1.000 & 1.000 & -1.000 & 1.000 & 1.000 & 1.000 \\
1.000 & 1.000 & -0.999 & 0.999 & 1.000 & 1.000 \\
-1.000 & -0.999 & 1.000 & -1.000 & -1.000 & -0.999 \\
1.000 & 0.999 & -1.000 & 1.000 & 1.000 & 0.999 \\
1.000 & 1.000 & -1.000 & 1.000 & 1.000 & 1.000 \\
1.000 & 1.000 & -0.999 & 0.999 & 1.000 & 1.000
\end{array}
\right)
\begin{array}{l}
\pi3\pi^0 \\
\pi4\pi^0 \\
K \\
K\pi^0 \\
K2\pi^0 \\
K3\pi^0
\end{array}
\tag{C.8}
$$

Split-offs

$$\boldsymbol{\rho}^{\mathcal{B}}_{\text{split-offs}} \;=\; \begin{array}{c} \begin{array}{cccccc} \pi 3\pi^0 & \pi 4\pi^0 & K & K\pi^0 & K2\pi^0 & K3\pi^0 \end{array} \\ \left(\begin{array}{cccccc} 1.000 & 1.000 & -1.000 & 1.000 & 1.000 & -1.000 \\ 1.000 & 1.000 & -1.000 & 1.000 & 1.000 & -1.000 \\ -1.000 & -1.000 & 1.000 & -1.000 & -1.000 & 1.000 \\ 1.000 & 1.000 & -1.000 & 1.000 & 1.000 & -1.000 \\ 1.000 & 1.000 & -1.000 & 1.000 & 1.000 & -1.000 \\ -1.000 & -1.000 & 1.000 & -1.000 & -1.000 & 1.000 \end{array} \right) \begin{array}{l} \pi 3\pi^0 \\ \pi 4\pi^0 \\ K \\ K\pi^0 \\ K2\pi^0 \\ K3\pi^0 \end{array} \end{array} \quad \text{(C.9)}$$

Background with additional π^0 mesons

$$\boldsymbol{\rho}^{\mathcal{B}}_{(\text{n}+1)\pi^0} \;=\; \begin{array}{c} \begin{array}{cccccc} \pi 3\pi^0 & \pi 4\pi^0 & K & K\pi^0 & K2\pi^0 & K3\pi^0 \end{array} \\ \left(\begin{array}{cccccc} 1.000 & -0.999 & -0.288 & -0.022 & 0.023 & -0.045 \\ -0.999 & 1.000 & 0.247 & -0.020 & 0.019 & 0.003 \\ -0.288 & 0.247 & 1.000 & 0.964 & -0.964 & 0.969 \\ -0.022 & -0.020 & 0.964 & 1.000 & -1.000 & 1.000 \\ 0.023 & 0.019 & -0.964 & -1.000 & 1.000 & -1.000 \\ -0.045 & 0.003 & 0.969 & 1.000 & -1.000 & 1.000 \end{array} \right) \begin{array}{l} \pi 3\pi^0 \\ \pi 4\pi^0 \\ K \\ K\pi^0 \\ K2\pi^0 \\ K3\pi^0 \end{array} \end{array} \quad \text{(C.10)}$$

Appendix D

Dependencies on the tag lepton and the run period

Table D.1 lists the measured branching fractions for the different tag lepton types and run periods of data taking. All listed branching fractions are statistically independent and have partially independent systematic uncertainties (Sections 6.5.12, 6.5.13).

Table D.1: Measured branching fractions for the different tag lepton types and run periods of data taking (Table 2.1). The listed uncertainties include all uncertainties that are of inherent statistical nature, i.e., those due to the statistical fluctuations of the numbers of selected data and simulated events (Sections 6.4, 6.5.6, 6.5.7). All three contributions are added in quadrature.

Electron and muon tagged events

		run I	run II	run III	run IV	run V	run VI	run I–VI
$\mathcal{B}(\tau^- \to \pi^-\pi^0\pi^0\pi^0\nu_\tau)$	$[\times 10^{-2}]$	1.341 ± 0.034	1.264 ± 0.020	1.257 ± 0.028	1.241 ± 0.015	1.279 ± 0.013	1.246 ± 0.019	1.263 ± 0.008
$\mathcal{B}(\tau^- \to \pi^-\pi^0\pi^0\pi^0\pi^0\nu_\tau)$	$[\times 10^{-4}]$	9.5 ± 2.1	10.5 ± 1.4	10.4 ± 1.8	9.70 ± 0.99	9.70 ± 0.88	8.4 ± 1.2	9.63 ± 0.5
$\mathcal{B}(\tau^- \to K^-\nu_\tau)$	$[\times 10^{-3}]$	6.02 ± 0.14	6.399 ± 0.081	6.75 ± 0.11	6.670 ± 0.064	6.791 ± 0.056	6.285 ± 0.081	6.574 ± 0.032
$\mathcal{B}(\tau^- \to K^-\pi^0\nu_\tau)$	$[\times 10^{-3}]$	4.27 ± 0.13	4.542 ± 0.076	4.81 ± 0.11	4.678 ± 0.057	4.697 ± 0.049	4.370 ± 0.072	4.607 ± 0.029
$\mathcal{B}(\tau^- \to K^-\pi^0\pi^0\nu_\tau)$	$[\times 10^{-4}]$	3.42 ± 0.76	5.22 ± 0.45	5.70 ± 0.59	5.67 ± 0.33	4.71 ± 0.29	4.95 ± 0.44	5.05 ± 0.17
$\mathcal{B}(\tau^- \to K^-\pi^0\pi^0\pi^0\nu_\tau)$	$[\times 10^{-4}]$	4.7 ± 1.9	1.8 ± 1.3	1.4 ± 1.4	0.01 ± 0.84	1.34 ± 0.75	1.3 ± 1.1	1.31 ± 0.43

Electron tagged events

		run I	run II	run III	run IV	run V	run VI	run I–VI
$\mathcal{B}(\tau^- \to \pi^-\pi^0\pi^0\pi^0\nu_\tau)$	$[\times 10^{-2}]$	1.342 ± 0.046	1.257 ± 0.027	1.217 ± 0.037	1.259 ± 0.020	1.260 ± 0.017	1.289 ± 0.024	1.266 ± 0.010
$\mathcal{B}(\tau^- \to \pi^-\pi^0\pi^0\pi^0\pi^0\nu_\tau)$	$[\times 10^{-4}]$	10.5 ± 2.8	10.7 ± 1.8	13.2 ± 2.5	9.2 ± 1.3	10.3 ± 1.2	8.0 ± 1.5	9.91 ± 0.66
$\mathcal{B}(\tau^- \to K^-\nu_\tau)$	$[\times 10^{-3}]$	5.95 ± 0.18	6.59 ± 0.11	6.71 ± 0.15	6.621 ± 0.085	6.734 ± 0.073	6.45 ± 0.11	6.596 ± 0.042
$\mathcal{B}(\tau^- \to K^-\pi^0\nu_\tau)$	$[\times 10^{-3}]$	4.42 ± 0.18	4.74 ± 0.11	4.85 ± 0.15	4.641 ± 0.075	4.796 ± 0.066	4.500 ± 0.096	4.690 ± 0.038
$\mathcal{B}(\tau^- \to K^-\pi^0\pi^0\nu_\tau)$	$[\times 10^{-4}]$	3.66 ± 0.99	5.05 ± 0.63	5.84 ± 0.78	5.64 ± 0.44	4.54 ± 0.38	5.80 ± 0.57	5.15 ± 0.22
$\mathcal{B}(\tau^- \to K^-\pi^0\pi^0\pi^0\nu_\tau)$	$[\times 10^{-4}]$	4.1 ± 2.6	2.1 ± 1.9	1.0 ± 1.6	0.2 ± 1.1	2.36 ± 0.92	1.6 ± 1.4	1.70 ± 0.56

Muon tagged events

		run I	run II	run III	run IV	run V	run VI	run I–VI
$\mathcal{B}(\tau^- \to \pi^-\pi^0\pi^0\pi^0\nu_\tau)$	$[\times 10^{-2}]$	1.339 ± 0.052	1.275 ± 0.030	1.313 ± 0.42	1.216 ± 0.023	1.296 ± 0.021	1.185 ± 0.029	1.260 ± 0.012
$\mathcal{B}(\tau^- \to \pi^-\pi^0\pi^0\pi^0\pi^0\nu_\tau)$	$[\times 10^{-4}]$	8.3 ± 3.2	10.2 ± 2.1	6.68 ± 2.6	10.4 ± 1.5	8.9 ± 1.3	8.9 ± 1.7	9.27 ± 0.74
$\mathcal{B}(\tau^- \to K^-\nu_\tau)$	$[\times 10^{-3}]$	6.12 ± 0.21	6.14 ± 0.12	6.81 ± 0.17	6.74 ± 0.10	6.874 ± 0.088	6.05 ± 0.13	6.542 ± 0.049
$\mathcal{B}(\tau^- \to K^-\pi^0\nu_\tau)$	$[\times 10^{-3}]$	4.09 ± 0.18	4.31 ± 0.11	4.76 ± 0.16	4.729 ± 0.087	4.571 ± 0.074	4.19 ± 0.11	4.498 ± 0.042
$\mathcal{B}(\tau^- \to K^-\pi^0\pi^0\nu_\tau)$	$[\times 10^{-4}]$	3.1 ± 1.2	5.43 ± 0.65	5.53 ± 0.90	5.77 ± 0.52	3.54 ± 0.47	3.82 ± 0.69	4.92 ± 0.26
$\mathcal{B}(\tau^- \to K^-\pi^0\pi^0\pi^0\nu_\tau)$	$[\times 10^{-4}]$	5.2 ± 2.8	1.4 ± 1.8	1.9 ± 2.3	-0.3 ± 1.4	8.0 ± 1.5	0.9 ± 1.8	0.77 ± 0.68

List of Figures

169

List of Tables

Bibliography

[1] Cabibbo, N. *Phys. Rev. Lett.* **10** , 531–532 (1963).

[2] Kobayashi, M. and Maskawa, T. *Prog. Theor. Phys.* **49** , 652–657 (1973).

[3] Yao, W.-M. et al. *J. Phys.* **G33** , 1–1232 (2006, and 2007 partial update for the 2008 edition available on the PDG WWW pages (URL: `http://pdg.lbl.gov/`)).

[4] Gamiz, E., Jamin, M., Pich, A., Prades, J., and Schwab, F. *J. High En. Phys.* **01** , 060 (2003).

[5] Gamiz, E., Jamin, M., Pich, A., Prades, J., and Schwab, F. *Phys. Rev. Lett.* **94** , 011803 (2005).

[6] Gamiz, E., Jamin, M., Pich, A., Prades, J., and Schwab, F. *Theoretical progress on the V_{us} determination from tau decays*, (2007). arXiv:0709.0282 [hep-ph].

[7] Banerjee, S. *Measurement of $|V_{us}|$ using hadronic tau decays from BaBar & Belle*, (2007). arXiv:0707.3058 [hep-ex].

[8] Aubert, B. et al. *Nucl. Instr. Methods Phys. Res., Sect. A* **479** , 1–116 (2002).

[9] Banerjee, S., Pietrzyk, B., Roney, J. M., and Was, Z. *Tau and Muon Pair Production Cross-Sections in Electron- Positron Annihilations at $\sqrt{s} = 10.58\,\mathrm{GeV}$*, (2007). arXiv:0706.3235 [hep-ph].

[10] Davier, Michel and Hocker, Andreas and Zhang, Zhiqing. *Rev. Mod. Phys.* **78** , 1043–1109 (2006).

[11] Halzen, F. and Martin, A. D. *Quarks and Leptons: An Introductory Course in Modern Particle Physics*. John Wiley & Sons Inc., (1984).

[12] Nachtmann, O. *Phänomene und Konzepte der Elementarteilchenphysik*. Friedr. Vieweg & Sohn, (1986).

[13] Perkins, D. H. *Introduction to High Energy Physics*. Cambridge University Press, 4th edition, (2000).

[14] Glashow, S. *Nucl. Phys.* **22** , 579 (1961).

[15] Salam, A. and Ward, J. C. *Phys. Lett.* **13** , 168 (1964).

[16] Weinberg, S. *Phys. Rev. Lett.* **19** , 1264 (1967).

[17] Wolfenstein, L. *Phys. Rev. Lett.* **51** , 1945 (1983).

[18] Eidelman, S. et al. *Phys. Lett. B* **592** , 1 (2004).

[19] Barate, R. et al. *Eur. Phys. Jour. C* **11** , 599–618 (1999).

[20] Abbiendi, G. et al. *Eur. Phys. Jour. C* **35** , 437–455 (2004).

[21] Bishai, M. et al. *Phys. Rev. Lett.* **82** , 281 (1999).

[22] Briere, R. A. et al. *Phys. Rev. Lett.* **90** , 181802 (2003).

[23] Arms, K. et al. *Phys. Rev. Lett.* **94** , 241802 (2005).

[24] Aubert, B. et al. *Exclusive branching fraction measurements of semileptonic tau decays into three charged hadrons, $\tau^- \to \phi\pi^-\nu_\tau$ and $\tau^- \to \phi K^-\nu_\tau$*, (2007). arXiv:0707.2981 [hep-ex].

[25] Epifanov, D. et al. *Study of $\tau^- \to K_S^0\pi^-\nu_\tau$ decay at Belle*, (2007). arXiv:0706.2231 [hep-ex].

[26] Aubert, B. et al. *Phys. Rev. D* **76** , 051104 (2007).

[27] The values have been calculated using the branching fractions from References [7, 10] as listed in Table 1.4 and Equations 1.24, 1.25. (2008).

[28] Davier, M. and Descotes-Genon, S. and Höcker, A. and Malaescu, B. and Zhang, Z. *The Determination of α_S from τ Decays Revisited*, (2008). arXiv:0803.0979 [hep-ph].

[29] Ambrosino, F. et al. *$|V_{us}|$ and lepton universality from kaon decays with the KLOE detector*, (2008). arXiv:0802.3009 [hep-ex].

[30] Leutwyler, H. and Roos, M. *Z. Phys. C* **25** , 91 (1984).

[31] Mateu, V. and Pich, A. *J. High En. Phys.* **10** , 041 (2005).

[32] Follana, E., Davies, C. T. H., Lepage, G. P., and Shigemitsu, J. *Phys. Rev. Lett.* **100** , 062002 (2008).

[33] Harrison, P. F., ed. and Quinn, Helen R., ed. *The BABAR Physics Book: Physics at an Asymmetric B Factory*. Papers from Workshop on Physics at an Asymmetric *B* Factory (*BABAR* Collaboration Meeting), Rome, Italy, 11-14 Nov 1996, Princeton, NJ, 17-20 Mar 1997, Orsay, France, 16-19 Jun 1997 and Pasadena, CA, 22-24 Sep 1997.

[34] PEP-II. *An asymmetric B Factory*, (1993). SLAC-418, LBL-5379.

[35] The *BABAR* Collaboration. *The Pub Board Page of Official Plots*, (2008). http://www.slac.stanford.edu/BFROOT/www/Organization/PubBoard/OfficialPlots/index.html.

[36] The PEP-II Group at the Stanford Linear Accelerator Center. *PEP-II Records*, (2004). `http://www.slac.stanford.edu/grp/ad/pep-ii/stat/PEPEII_lum_record.pdf`.

[37] Dubitzky, R. S. *Measurement of the CKM Matrix Element $|V_{cb}|$ with Exclusively Reconstructed Decays $B \to D^* e\nu$ at the BABAR Experiment*. PhD thesis, Technische Universität Dresden, (2003).

[38] The BABAR Collaboration. *Accelerator and Detector Performance Data*, (2008). `http://bbr-onlwww.slac.stanford.edu:8080/babarrc/BaBarRecords.html`, `http://bbr-onlwww.slac.stanford.edu:8080/babarrc/LumInt-Run_1-7.gif`.

[39] Banerjee, S. *Tau Cross-Sections*, (2007). Personal Communications.

[40] Schenk, S. *Data Luminosities*, (2008). Output from the Lumi Script.

[41] Banerjee, S. and Lusiani, A. *TauQED AWG: notes on systematics studies*, (2007). `http://www.slac.stanford.edu/BFROOT/www/Physics/Analysis/tauqed/systematics.html`.

[42] Gamet, R. and Touramanis, C. BABAR Analysis Document **1312**, SLAC, (2005).

[43] Gamet, R. *Run 4 and Run 5 Luminosity Measurement using R18d*, (2007). Talk at June 2007 BABAR Collaboration Meeting, `http://www.slac.stanford.edu/BFROOT/www/Organization/CollabMtgs/2007/detJun07/Tues3/gamet.pdf`.

[44] Jadach, S., Ward, B. F. L., and Was, Z. *Comput. Phys. Commun.* **130** , 260–325 (2000).

[45] Jadach, S., Was, Z., Decker, R., and Kuhn, J. H. *Comput. Phys. Commun.* **76** , 361–380 (1993).

[46] Hagiwara, K. et al. *Phys. Rev. D* **66** , 010001 (2002).

[47] Lange, D. J. *Nucl. Instr. Methods Phys. Res., Sect. A* **462** , 152–155 (2001).

[48] Agostinelli, S. et al. *Nucl. Instr. Methods Phys. Res., Sect. A* **506** , 250–303 (2003).

[49] Kleinknecht, K. *Detectors for particle radiation*. Cambridge University Press, 2nd edition, (1998).

[50] Billoir, P. *Nucl. Instr. Methods Phys. Res., Sect. A* **225** , 352–366 (1984).

[51] Billoir, P. and Qian, S. *Nucl. Instr. Methods Phys. Res., Sect. A* **311** , 139–150 (1992).

[52] Brown, D. N., Lopes Pegna, D., Lynch, G., Prencipe, E., Tackmann, K., and Tanabe, T. BABAR Analysis Document **1628**, SLAC, (2007).

[53] The Charged Particles Reconstruction Working Group. *Tracking Efficiency for Run 1 - Run 5 in R22*, (2007). `http://www.slac.stanford.edu/BFROOT/www/Physics/TrackEfficTaskForce/TrackingTaskForce-2007-R22.html`.

[54] Bowerman, D., Dallapiccola, C., Xuanzhong, L., and Nikolich, M. *BaBar* Analysis Document **917**, SLAC, (2004).

[55] Adam, I. et al. *Nucl. Instr. Methods Phys. Res., Sect. A* **538** , 281–357 (2005).

[56] Brandt, T. *BaBar* Analysis Document **391**, SLAC, (2002).

[57] Mohapatra, A., Hollar, J., and Band. *BaBar* Analysis Document **474**, SLAC, (2004).

[58] The Charged Particles Identifcation Working Group. *Inventory of PidSelectors*, (2007). `http://www.slac.stanford.edu/BFROOT/www/Physics/Tools/Pid/Selectors/r22a/selectors.html`.

[59] Electron Identification Analysis Working Group. *BaBar* Analysis Document **060**, SLAC, (2001).

[60] Mancinelli, G. and Spanier, S. *BaBar* Analysis Document **116**, SLAC, (2001).

[61] The *BaBar* Collaboration. *Instrumented Flux Return*, (2006). `http://www.slac.stanford.edu/BFROOT/www/Detector/IFR/IFR.html`.

[62] Dujmic, D. *BaBar* Analysis Document **514**, SLAC, (2002).

[63] The Charged Particles Identifcation Working Group. *What are PidTables?*, (2005). `http://www.slac.stanford.edu/BFROOT/www/Physics/Tools/Pid/PidTables/WhatArePT.html`.

[64] Bartoldus, R. et al. *BaBar* Analysis Document **194**, SLAC, (2002).

[65] Hojeong, K. *BaBar trigger scheme*, (2007). `http://www.slac.stanford.edu/BFROOT/www/Detector/Trigger/operations/trigdef.html`.

[66] The *BaBar* Workbook Team. *Background Filter Information*, (2007). `http://www.slac.stanford.edu/BFROOT/www/doc/workbook/eventinfo/TagInfo/BGF+DigiF_Flags.html`.

[67] Banerjee, S. *BaBar* Analysis Document **1265**, SLAC, (2005).

[68] Banerjee, S. et al. *BaBar* Analysis Document **760**, SLAC, (2003).

[69] Lyon, A. and Salvatore, F. *BaBar* Analysis Document **972**, SLAC, (2006).

[70] Banerjee, S., Nugent, I., and Roney, M. *BaBar* Analysis Document **930**, SLAC, (2006).

[71] Berger, E. L. and Lipkin, H. J. *Phys. Lett. B* **189** , 226 (1987).

[72] Allen, M., Naisbit, M., Roodman, A., and Banerjee, S. *BaBar* Analysis Document **870**, SLAC, (2004).

[73] Allmendinger, T., Bhuyan, B., Cavoto, G., Covarelli, R., Hamano, K., Kowalewski, R., and Nugent, I. *BaBar* Analysis Document **867**, SLAC, (2004).

[74] The *BaBar* Collaboration. *EMC calibration page*, (2006). `http://www.slac.stanford.edu/BFROOT/www/Detector/Calorimeter/software/calib_mtg/general_calib.html`.

[75] Gámiz, E., Jamin, M., Pich, A., Prades, J., and Schwab, F. *Nucl. Phys. Proc. Suppl.* **169** , 85–89 (2007).

[76] Gámiz, E., Jamin, M., Pich, A., Prades, J., and Schwab, F. $|V_{us}|$ *from Strange Hadronic τ Data*, (2006). [hep-ph/0610246].

[77] Gámiz, E., Jamin, M., Pich, A., Prades, J., and Schwab, F. *Determination of $|V_{us}|$ from Hadronic τ Decays*, (2005). [hep-ph/0505122].

[78] Gámiz, E., Jamin, M., Pich, A., Prades, J., and Schwab, F. *Nucl. Phys. Proc. Suppl.* **144** , 59–64 (2005).

[79] The *BaBar* Collaboration. *Branching fractions of the TAUOLA library*, (2008). `http://babar-hn.slac.stanford.edu:5090/cgi-bin/internal/cvsweb.cgi/tauola/TauolaDecayModes.txt`.

[80] The *BaBar* Collaboration. *Branching fractions of the EvtGen package*, (2008). `http://babar-hn.slac.stanford.edu:5090/cgi-bin/internal/cvsweb.cgi/EvtGen/DECAY.DEC`.

[81] Asner, D. M. et al. *Phys. Rev. D* **61** , 012002 (2000).

[82] Hartert, J. *Messung der Verzweigungsverhältnisse von τ-Zerfällen in Endzustände mit drei geladenen Hadronen mit dem BaBar-Experiment.* Diplom thesis, Ruprecht-Karls-Universität Heidelberg, (2007).

[83] Hohler, R. *Messung des Verzweigungsverhältnisses $\mathcal{B}(\tau^- \to K^- \pi^+ \pi^- \nu_\tau)$ mit dem BaBar-Experiment.* Diplom thesis, Ruprecht-Karls-Universität Heidelberg, (2007).

[84] Nekrassov, D. *Messung des Verzweigungsverhältnisses $\mathcal{B}(\tau^- \to K^0 \pi^- \nu_\tau)$ mit dem BaBar-Experiment.* Diplom thesis, Ruprecht-Karls-Universität Heidelberg, (2006).

[85] Barlow, R. *Statistics – A Guide to the Use of Statistical Methods in the Physical Sciences.* Wiley, (1989).

[86] Mund, D. *Messung der Betaasymmetrie A im Neutronenzerfall.* PhD thesis, Ruprecht-Karls-Universität Heidelberg, (2006).

[87] Serebrov, A. et al. *Phys. Lett. B* **605** , 72 (2005).

Acknowledgments

Stufen

Wie jede Blüte welkt und jede Jugend
Dem Alter weicht, blüht jede Lebensstufe,
Blüht jede Weisheit auch und jede Tugend
Zu ihrer Zeit und darf nicht ewig dauern.
Es muß das Herz bei jedem Lebensrufe
Bereit zum Abschied sein und Neubeginne,
Um sich in Tapferkeit und ohne Trauern
In andre, neue Bindungen zu geben.
Und jedem Anfang wohnt ein Zauber inne,
Der uns beschützt und der uns hilft, zu leben.

Wir sollen heiter Raum um Raum durchschreiten,
An keinem wie an einer Heimat hängen,
Der Weltgeist will nicht fesseln uns und engen,
Er will uns Stuf' um Stufe heben, weiten.
Kaum sind wir heimisch einem Lebenskreise
Und traulich eingewohnt, so droht Erschlaffen,
Nur wer bereit zu Aufbruch ist und Reise,
Mag lähmender Gewöhnung sich entraffen.

Es wird vielleicht auch noch die Todesstunde
Uns neuen Räumen jung entgegen senden,
Des Lebens Ruf an uns wird niemals enden...
Wohlan denn, Herz, nimm Abschied und gesunde!

Hermann Hesse (1941)